

Carbon dots based nanomaterials for biomedical applications

by

Ruqiya Dheea Ismael Al-Jaafar

A thesis submitted in partial fulfillment for the requirements for the degree of
Doctor of Philosophy at the University of Central Lancashire

March 2023

RESEARCH STUDENT DECLARATION FORM

Type of Award PhD Doctor of Philosophy

School School of Natural Sciences

1. Concurrent registration for two or more academic awards

I declare that while registered as a candidate for the research degree, I have not been a registered candidate or enrolled student for another award of the University or other academic or professional institution.

2. Material submitted for another award

I declare that no material contained in the thesis has been used in any other submission for an academic award and is solely my own work.

3. Use of a Proof-reader

No proof-reading service was used in the compilation of this thesis.

Signature of Candidate:



Print name: Ruqiya Dheea Ismael Al-Jaafar

Abstract

Carbon dots (C-dots) are an emerging class of photoluminescent (PL) materials that are mainly composed of carbon, hydrogen, and oxygen, along with heteroatoms such as N, P, and S. C-dots are spherical in shape with a diameter between 1-20 nm, they demonstrate excitation wavelength-dependent emission with minimum photobleaching, while showing low toxicity levels for humans and the environment.

In this project C-dots were synthesized via hydrothermal decomposition of a mixture of CA and ethanolamine, and they were subjected to surface treatment with nitric acid followed by purification via dialysis against water. Moreover, the heptapeptide (lysine)₇ (referred hereafter as K7) was synthesized by means of solid phase peptide synthesis and was subsequently purified and characterized via High-Performance Liquid Chromatography (HPLC) and by Liquid Chromatography–Mass Spectrometry (LC-MS). In addition, a quaternary ammonium salt (QAS) was synthesized and was covalently attached to polyethyleneimine (PEI) (Figure 1 A), giving rise to PEI/QAS (Figure 1B).

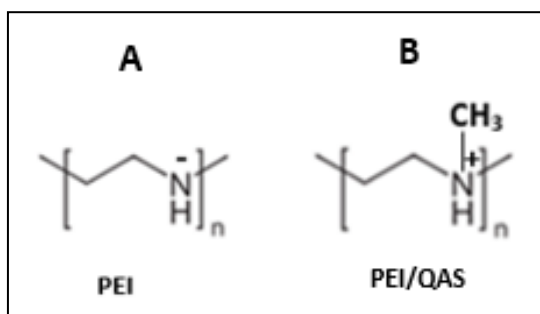


Figure 1: Chemical structure of: A) polyethyleneimine (PEI), B) quaternary ammonium salt attached to the polyethyleneimine (PEI/QAS).

Finally, C-dots were conjugated with K7, Arginine-Glycine-Aspartic acid (RGD, a commercially available peptide), PEI/QAS, Jeffamine D-230 (Figure 2, a commercially available polymer) to generate a family of conjugates denoted as C-K7, C-RGD, C-PEI/QAS and C-J, respectively.

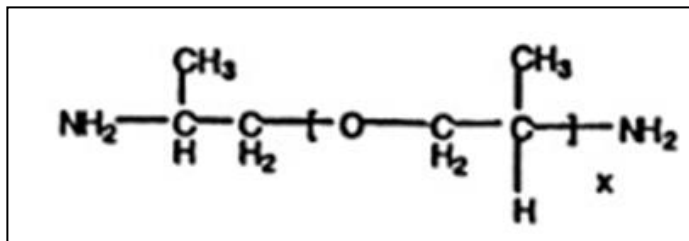


Figure 2: Chemical structure of Jeffamine D-230. $x=33$.

This project aims to explore the structure-property relationships within this family of novel nanomaterials. To that end, the conjugates were characterized by TEM, FTIR, elemental analysis, TGA, UV-vis, fluorescence and time-resolved fluorescence spectroscopy.

TEM imaging indicated that all types of conjugates are spherical with an average diameter 11 ± 2 nm. The quantum yield (QY) at excitation wavelength $\lambda_{ex} = 345$ nm (using 4',6-diamidino-2-phenylindole as the standard) was calculated 4.2%, 5.4%, 7.4%, 7.3% and 5.1% for C-dots, C-K7, C-RGD, C-PEI/QAS, and C-J respectively. Interestingly, the fluorescence spectra of the conjugates, while maintaining the characteristic excitation-wavelength emission mode, they showed pronounced blue shifts compared to C-dots. The average fluorescence lifetime decay (τ_{avg}) of the conjugates is close to 8 ns and 5.5 ns at $\lambda_{ex} = 375$ nm and 450 nm, respectively, in line with the behavior observed for C-dots, with only C-J showing significant deviation from those τ_{avg} values possibly due to pronounced modifications of the local electronic environment.

MTT and PrestoBlue assays indicated that the viability of HeLa, U87, T96G and GC-1 SPG cells when incubated with the conjugates remain consistently at levels above 83% at 100 $\mu\text{g}/\text{mL}$ loading, while haemolysis tests confirmed that the conjugates do not cause rupturing of the blood cells. Fluorescence microscope imaging showed that all conjugates are able to penetrate the HeLa cells, rendering the cytoplasm highly fluorescent, thus showing promise for *in vivo*

bioimaging applications. However, only the C-K7 can effectively illuminate the Hela cells at concentrations as low as 10 $\mu\text{g}/\text{mL}$, while for the other conjugates much higher concentrations are required to induce similar effects.

Additionally, all conjugates show significant antibacterial activity against *Escherichia coli* (*E. coli*) and *Staphylococcus aureus* (*S. aureus*) with the most effective being C-PEI/QAS that eliminates the population of *E. coli* and the *S. aureus* by 99.9% and 99.96%, respectively. For comparison, it was found that C-dots suppress the growth *E. coli* and the *S. aureus* by 94.4% and 96.7%, respectively.

The release profiles of ibuprofen and temozolomide dispersed in hydrogels of copolymer $[\text{HO}(\text{CH}_2\text{CH}_2\text{O})_{20}(\text{CH}_2\text{CH}(\text{CH}_3)\text{O})_{70}(\text{CH}_2\text{CH}_2\text{O})_{20}\text{H}]$ (otherwise known as Pluronic 123) in the presence of the conjugates were monitored at 25 °C. Incorporation of C-PEI/QAS, C-RGD and C-J to hydrogels facilitates the release of ibuprofen to 95% after 100 h, compared to only 60% release for the conjugate-free counterparts over the same period of time. Interestingly, introduction of C-RGD can facilitate an almost linear ibuprofen release as a function of time for 100 h, an effect that is highly desirable for controlled and sustained drug release applications. The C-dot and conjugate-enriched hydrogels showed a faster release of temozolomide compared to their nanoparticle-free counterparts.

In conclusion, this project contributes novel insights into the synthesis of non-toxic peptide/C-dots and polymer/C-dots conjugates that combine the supreme photoluminescent properties of C-dots with the cell-penetrating nature of K7 and RGD peptides and the biocompatible nature of PEI/QAS and Jeffamine, ultimately giving rise to a new generation of advanced materials that show great promise for a series of challenging applications related to bioimaging, controlled drug release and antimicrobial treatment.

Table of Contents

Abstract.....	3
Table of Contents.....	6
Acknowledgments.....	9
List of figures.....	11
List of tables.....	20
List of Abbreviations.....	21
Chapter 1: Introduction.....	23
1.1 The aim of the project:.....	24
1.2 The objectives of this project are:.....	24
1.3 System design:.....	24
1.4 Carbon nanodots overview.....	25
1.4.1 Structure of C-dots.....	28
1.4.2 Graphene Carbon Dots, synthesis, and structure.....	31
1.4.3 C-dots Synthesis methods.....	36
1.4.4 Optical properties of C-dots.....	50
1.4.5 Other properties.....	61
1.4.6 General applications of C-dots.....	70
1.4.7 Biomedical applications of C-dots.....	81
1.5 Peptides, proteins, and polymers overview.....	99
1.5.1 Peptides:.....	99
1.5.2 Proteins.....	132
1.5.3 Polymers.....	133
Chapter 2: Experimental section.....	150
2.1 Materials.....	151
2.2 Synthesis and purification section.....	152
2.2.1 Synthesis and purification of C-dots.....	152
2.2.2 Synthesis and purification of K7.....	155
2.2.3 Synthesis and purification of PEI/QAS.....	159
2.3 Conjugation section.....	161
2.3.1 Conjugation of C-dots with K7.....	161
2.3.2 Conjugation of C-dots with RGD.....	162

2.3.3	Conjugation of C-dots with PEI/QAS	163
2.3.4	Conjugation of C-dots with Jeffamine.....	163
2.4	Characterization of K7.....	164
2.4.1	High-performance liquid chromatography (HPLC)	164
2.4.2	Liquid chromatography–mass spectrometry (LC-MS)	166
2.5	Characterization of C-dots and their conjugates	167
2.5.1	Transmission electron microscopy (TEM).....	167
2.5.2	Fourier transform infrared spectroscopy (FTIR)	169
2.5.3	Elemental analysis.....	170
2.5.4	Thermogravimetric analysis (TGA).....	170
2.6	Photophysical analysis	171
2.6.1	Ultraviolet-visible spectroscopy (UV-vis).....	171
2.6.2	Fluorescence spectroscopy.....	172
2.6.3	Quantum yield (QY).....	173
2.6.4	Fluorescence lifetime.....	175
2.7	The biological analysis.....	176
2.7.1	Cytotoxicity	176
2.7.2	Cell culture processes	178
2.7.3	Media preparation	178
2.7.4	Thawing cells.....	179
2.7.5	Counting cell viability.....	179
2.7.6	Haematocytometer.....	180
2.7.7	Cell countess	181
2.7.8	Growing cells.....	182
2.7.9	Splitting cells	183
2.7.10	Freezing cells.....	184
2.8	MTT assay.....	184
2.8.1	Plating the cells	184
2.8.2	MTT procedure.....	185
2.9	PrestoBlue assay	187
2.10	Haemolysis assay	188
2.11	Fluorescence microscopy on HeLa cells.....	188
2.12	Antimicrobial study.....	190

2.12.1	<i>Escherichia coli</i> K12	190
2.12.2	<i>Staphylococcus aureus</i> ATCC 25923.....	190
2.12.3	Antimicrobial process	191
2.13	Drug delivery study	192
Chapter 3: Results and discussion.....		195
3.1	Characterization of materials.....	196
3.1.2	Purification and characterisation of K7.....	196
3.1.3	TEM of C-dots, the C-K7, the C-RGD, and the C-PEI/QAS	200
3.1.4	FTIR spectroscopy	201
3.1.5	Elemental analysis.....	209
3.1.6	TGA.....	209
3.2	Photophysical properties	214
3.2.1	UV-vis	214
3.2.2	Photoluminescence.....	215
3.2.3	Quantum yield.....	218
3.2.4	Lifetime	220
3.3	Biological analysis	224
3.3.1	MTT results	224
3.3.2	PrestoBlue assay	229
3.3.3	Haemolysis	234
3.4	Fluorescence microscopy on HeLa cells.....	236
3.5	Microbiology	243
3.6	Drug release	244
Conclusion.....		247
References		248

Acknowledgments

I would like to express my deepest appreciation to my first supervisor Dr. Antonios Kellarakis for all the help, the unaverred support, and the time in making this project possible, and before that for giving me this great opportunity to be your student. For all of that, I am and will always be indebted to you.

I would also like to extend my sincere gratitude to my second supervisor Dr. Marta Krysmann for all your help in the lab, and the great support you provided. Furthermore, I'd like to thank you for believing in me and making this journey possible, your help cannot be overestimated.

During my journey at UCLan, I have met many kind people who always supported me and helped in the lab. Therefore, I am grateful to Dr. Claire Mellor for your invaluable help and continuous support. I cannot begin to express my thanks to the lab technicians at UCLan who always been there for help and support, especially Tamar Garcia, Sameera Mahmood, Dr. Peter Bentley, Elinor Clayton, and Beth Milnes, thank you very much for your valuable experience, help and support.

I am also grateful to my research team members who always were there to help, support, discuss lab techniques, and not to forget the laughs and long list of complains that things are not working. Therefore, special thanks to Spyridon Gavalas, Yang Chen, and Alexander Ejsmont. I would like to extend my sincere thanks to the research team member Dr. Ella Nicole Gibbons for her help in the Microbiology studies, and for being a real friend.

Thanks should be also go to my best friends, who always were there for me since day one, many thanks to Saja Falah, Aisha Ahmed, and Nawfal Alabbasi. Thank you ever so much for being part of my life.

I am extremely grateful for my beloved family who never let me down, always believed in me, and never left a day without giving me a push to make this work possible. Therefore, many thanks to my mother Dr. Asmaa Adnan who always inspired me to do a PhD and always

supported me in my education. I am also grateful to my beloved sisters Khansaa, Sumaia, and Aeshah, in addition to my brother Dr. Ahmet, your support cannot be overestimated, thank you ever so much for being in my life. I would also like to thank my nephew Zeyad Abdulrahman for his invaluable technical help that made this thesis look the way it is. Finally, I would like to express my deepest gratitude to my beloved husband Ali, who has been very supportive, there is not enough words to thank you for the help, love, and support you showed during this journey, and not to forget the nice countless meals you made me while I am doing my PhD, in addition to your patience that cannot be underestimated, thank you ever so much.

List of figures

Figure 1: Chemical structure of : A) polyethyleneimine (PEI), B) quaternary ammonium salt attached to the polyethyleneimine (PEI/QAS)	3
Figure 2: Chemical structure of Jeffamine D-230. $x=33$	4
Figure 3: C-dots carrying drug molecule (a): Pore-loaded C-dots, (b): drug physically adsorbed on the C-dots surface. The ligand can be: K7, RGD, PEI/QAS, or Jeffamine.	25
Figure 4: Cell viability by MTT assay for HeLa cells were treated with C-dots (3).....	26
Figure 5: Antimicrobial activity of C-dots in a comparison with Water and a solution of CA plus β -alanine, against <i>S. enterica</i> , <i>E. coli</i> , <i>P. syringae</i> , <i>A. rhizogenes</i> , <i>A. tumefaciens</i> , and <i>P. carotovorum</i> (4).....	27
Figure 6: a) TEM image of synthesized C-dots; scale bar: 20 nm (inset: high-resolution TEM image of a C-dot; scale bar: 5 nm). b) XRD patterns of C-dots, c) Raman spectrum of C-dots, and d) ^{13}C NMR spectrum of C-dots in D ₂ O (40 mg/mL), e) FTIR spectrum of C-dots in the dry state, and f) UV-vis absorption and PL spectra of a dilute aqueous solution of C-dots at various λ_{ex} (12).....	30
Figure 7: Illustration of the synthesis of GC-dots following the cage opening of fullerenes; a) adsorption of C_{60} molecules to the terraces of Ru crystals, b) temperature-dependent growth of GC-dots with triangular and hexagonal equilibrium shape, c) and d) scanning tunneling microscope images of the triangular and hexagonal GC-dots, respectively (18).....	31
Figure 8: Illustration of the synthesis of GC-dots following the organic and chemical method; a) structure of Quantum C-dots, b) bulky moieties chemically attached to the edges of the C-dot to enhance colloidal stability, c) an energy-minimized configuration of Quantum C-dots (20).	32
Figure 9: Illustration of the synthesis of GC-dots following the electrochemical method (24). .	33
Figure 10: GC-dots synthesized following the electrochemical oxidation of a graphene film: a) and b) TEM images, c) size distribution, d) XRD pattern compared to the initial graphene film, e) Raman spectrum, f) C 1s peak compared to paternal film; the inset refers to the C 1s of GC-dots, and g) FTIR spectrum (26).....	35
Figure 11: Schematic diagram of the two synthesis methods of C-dots. A) top-down methods and B) bottom-up methods (30).....	36
Figure 12: Schematic diagram of reaction to synthesize C-dots using SWNTs by Tao et al. (35).	38
Figure 13: Schematic diagram of apparatus for preparing C-dots following the Arc discharge method (40).	39
Figure 14: a) λ_{ex} dependent emission behavior, and b) TEM image of the C-dots synthesized by Zhu et al. (49).	42
Figure 15: a) λ_{ex} dependent emission behavior, b) TEM images, and c) corresponding particle size distribution histograms of the C-dots synthesized by Zhang et al. (50).....	43
Figure 16: a) TEM image, b) particle size distribution, and c) λ_{ex} dependent emission behavior of the C-dots synthesized by Sahu et al. (51).....	44

Figure 17: Schematic diagram of the synthesis of C-dots following the thermal treatment of crude biomass by Krysmann et al. (6).....	45
Figure 18: Schematic diagram of the synthesis of C-dots following the thermal treatment of crude biomass by Wang et al. (53).	46
Figure 19: Stability of C-dots synthesized by Jiang et al., as a function of: a) Time, b) pH (63)..	48
Figure 20: Photoluminescence emission spectra of the C-dots were synthesized by Liu et al. (64).	49
Figure 21: Absorption spectra of C-dots (red), and surface passivated C-dots (black) (68).....	51
Figure 22: a) TEM images, and b) emission spectra at λ_{ex} ranging from 220 nm to 380 nm of C-dots synthesized by Zhang et al, (78).	53
Figure 23: Luminescence images of C-dots synthesized by Cao t al., using confocal microscope (all scale bars 20 μ m) with a) argon ion laser λ_{ex} = 458 nm, b) femtosecond pulsed laser λ_{ex} = 800 nm, and c) is an overlay of (a) and (b) (82).	54
Figure 24: Up-conversion PL properties of C-dots synthesized by Yin et al. (83).....	55
Figure 25: in vivo near infrared up conversion luminescence image of a mouse before (left) and after (right) subcutaneous injection of C-dots synthesized by Li et al. (84).	55
Figure 26: Proposed mechanism of the up conversion photoluminescent in the near infrared C-dots (84).	56
Figure 27: Schematic illustration of the synthesis of reduced state C-dots with blue luminescence from original carbon dots. Inset: photographs of aqueous solutions of the C-dots (left) and the reduced C-dots (right) obtained under UV light (360 nm) (86).	57
Figure 28: TEM images of the A) C-dots, and B) the reduced C-dots (86).	57
Figure 29: Photoluminescence spectra of the C-dots (dashed line), the λ_{ex} = 470 nm, and the λ_{em} of the excitation spectrum was 520 nm. The reduced C-dos (solid line), the λ_{ex} of the emission spectrum was 280 nm, and the λ_{em} of the excitation spectrum was 440 nm (86).	58
Figure 30: PL lifetimes of the C-dots (the λ_{ex} = 470 nm, and the λ_{em} = 520 nm), and the reduced C-dots (the λ_{ex} = 280 nm and the λ_{em} is 440 nm) (86).	59
Figure 31: Schematic illustration of the mechanism of the two-photon absorption (88).	60
Figure 32: Cell viability of NIH-3T3 cells incubated with C-dots at different concentrations for 12 h, 24 h and 48 h (90).	62
Figure 33: Cell viability of HT-92 cells incubated with C-dots (black), and PEG1500N (white) at different concentrations for 24 h (91).	63
Figure 34: Blood hematology analysis of rats treated with C-dots at doses of 0.2, 2, and 20 mg/kg, samples obtained in 1, 3, 7 and 28 days of exposure. (A) White blood cells, (B) red blood cells, (C) hemoglobin, (D) HCT, (E) platelets, (F) lymphocytes, (G) neutral cells, and (H) other cells (93).	65
Figure 35: Changes of the blood biochemical data of rats treated with C-dots at doses of 0.2, 2, and 20 mg/kg and samples obtained in 1, 3, 7, and 28 days of exposure. (A) GPT, (B) GOT, (C) urea, (D) cholesterol, (E) TG, (F) blood glucose, (G) Cr, (H) total protein, and (I) albumin (93)...	67
Figure 36: Results of histopathological analyses of rats were treated with C-dots at the dose of 20 mg/kg at 30 days of exposure (93).	68

Figure 37: Blood samples of mice were injected with C-dot synthesized by Huang et al., after three injection routes obtained in different times; (A) (Top) i.v. injection, (Middle) s.c. injection, and (Bottom) i.m. injection. (B) Fluorescence time-activity curves derived from signals in (A) (95).....	69
Figure 38: Possible strategies of C-dots (yellow spheres) in a photocatalytic application, a) as electron acceptor (electron sink) from the semiconductor, and b) as electron donor creating a cascade of electrons from C-dots lowest unoccupied molecule orbital to semiconductors (99).	70
Figure 39: Schematic diagram of the setup used for the detection of photo catalytically generated H ₂ (100).....	72
Figure 40: Schematic illustration of (A) conventional and (B) inverted organic solar cells (OSC) (105).....	73
Figure 41: Energy band diagram of p–n junction solar cell (109).....	74
Figure 42: Schematic illustration of piezoelectric inkjet printing. Inset: the as-prepared fluorescent C-dots ink (111).....	76
Figure 43: a) Photograph of the fluorescent pattern representing blue and white porcelain by inkjet printing, b) pattern created by C-dots/SA ink, c) Illustration of the pen-on-paper process of writing words “carbon dots @ paper”, and c) Digital photos of “carbon dots @ paper” (111).....	77
Figure 44: a) Different graphic patterns on paper using C-dots as ink, under the UV, b) Inks in multiple colors, made by different C-dots concentrations, and c) different graphic pattern obtained by C-dots ink creating a multicolor effect (112).....	78
Figure 45: Fluorescence microscopy images of PVA/C-dots a) at 0 minutes time, and b) after 30 minutes with exposure to 2000 W UV (112).....	78
Figure 46: Fluorescence microscopy images of fingerprints developed with (0.7 wt% C-dot) on a glass slide under a) violet, b) blue and c) green λ_{ex} . The magnification is 100 \times (114).....	79
Figure 47: Latent fingerprints on aluminum foil surface developed using C-dots, TiO ₂ , C-dots@TiO ₂ (coat-I), C-dots@TiO ₂ (coat-II), and C-dots@TiO ₂ (coat-III) respectively (115).....	80
Figure 48: Schematic representation of an Hg ²⁺ /Cys biosensor based on C-dots synthesized by Lu et al. The photoluminescence analysis shows the λ_{em} of: a) C-dots, b) C-dots after interaction with Hg ²⁺ , and c) C-dots after interaction with Cys (117).....	82
Figure 49: Schematic illustration of a Cu ²⁺ biosensor using C-dots (119).....	83
Figure 50: a) Overlay of bright-field and fluorescence images of HeLa cells incubated with 0.05 mg/ mL of C-dots. b) confocal fluorescence images of HeLa cells before the enhancement of the endocytic activity, and c) after the enhancement of the endocytic activity. d) A bar graph showing the integrated intensity from 480–580 nm over the integrated fluorescence intensity from 600–680 nm. e) the confocal fluorescence images obtained from 480–580 nm before the enhancement of the endocytic activity, and g) after the enhancement of the endocytic activity. f) the confocal fluorescence images obtained from 600–680 nm before the enhancement of the endocytic activity, and h) after the enhancement of the endocytic activity. The scale bar is 25 μ m (120).....	84



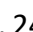


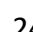

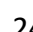




Figure 51: Images of female DBA/1 subcutaneously injected with passivated C-dots by PEG ₁₅₀₀ N: (a) in bright field, (b) under $\lambda_{\text{ex}} = 470$ nm with (d) 525 nm emission, (c) under $\lambda_{\text{ex}} = 545$ nm with, (e) $\lambda_{\text{em}} = 620$ nm (122).....	85
Figure 52: Confocal microscope images of starfish embryos were exposed to C-dots, the images were taken at different times of hours post fertilization (hpf) 2, 9, 24, 32, 48, and 72. Upper: bright field, and lower fluorescence images (123).	86
Figure 53: Antibacterial activity of C-dots (10-100 μL) dictated by the zone of inhibition on three bacterial strains. (a) <i>Staphylococcus aureus</i> , (b) <i>Klebsiella pneumoniae</i> and (c) <i>Pseudomonas aeruginosa</i> (127).	88
Figure 54: (a) UV-vis and (b) emission spectra of boldine-loaded C-dots at different time intervals from 0 to 60 h in PBS. Boldine responses for 327.27 $\mu\text{g}/\text{mL}$ boldine-loaded C-dots under $\lambda_{\text{ex}} = 430$ nm (129).	90
Figure 55: Profiles for release of DOX by DOX/C-dots within environments with pH 5.0, and 7.4 (132).	92
Figure 56: Schematic illustration of the intracellular release of DOX from the DOX/C-dots drug delivery system (132).	92
Figure 57: Confocal microscopic images of MGC-803 cells incubated with Cdots@PEI or Cy ₃ -siRNA for 2 h, Cy ₃ -siRNA-Cdots@PEI complexes for 2 and 5 h (134).....	95
Figure 58: Synthetic scheme for C-dots/Oxa(IV) and its applications in bioimaging and theragnostic (135).....	96
Figure 59: <i>in vivo</i> fluorescence images of mouse bearing H22 liver cancer after the first intralesional injection of C-dots/Oxa(IV); a) 0 minutes (taken under white light, b) 2 minutes, c) 6 h, d) 24 h, e) 24 h 20 minutes (the second injection), f) 48 h, and g) 72 h. All taken under blue light unless otherwise stated (a). Semiquantitative fluorescence intensities of the tumor area determined at different times. Red arrow indicates the 2 nd injection. i–m) Photographs of the tumor area after intralesional injection of C-dots/Oxa after i) 2 minutes, j) 18 h, k) 24 h, l) 48 h, and m) 72 h. n) Tumor sizes of H22 xenograft model as a function of time (135).	98
Figure 60: Mechanism of reaction of the formation of the peptide bond (139).	99
Figure 61: Genal chemical structure of amino acids, in which the R is different from amino acid to another (139).	100
Figure 62: Mechanisms of CPPs uptake, direct translocation through the cellular membrane, which requires no energy, and endocytosis, an energy-dependent process (146).	102
Figure 63: Mechanisms of endocytic entry into the cell including both classes phagocytosis and pinocytosis (154).	105
Figure 64: Principle of solid phase peptide synthesis, (P) is the permanent side chain protecting group, (T) is the temporary urethane N $^{\alpha}$ protecting group, (A) activating group, (X) NH or O, (SPPS) solid phase peptide synthesis (164).	109
Figure 65: Epimerization by oxazolone formation (164).	110
Figure 66: Schematic surface modification of nanoparticles with CPPs using electrostatic or covalent coupling strategies and their major advantages and disadvantages (176).	114

Figure 67: Schematic illustration of the DOX-C-dots-NLS accumulating at the tumor site and releasing DOX into the cell nucleus (183).....	116
Figure 68: One-photon cell imaging of mouse melanoma B16-F10 cancer cells under (a) bright field, λ_{ex} = (b) 405 nm, (c) 488 nm, (d) 543 nm and (e) merger image of (b), (c) and (d) with C-dots. One-photon cell imaging of mouse melanoma B16-F10 cancer cells under (f) bright field, λ_{ex} = (g) 405 nm, (h) 488 nm, (i) 543 nm and (j) merger of (g), (h) and (i) with TAT-C-dots. One-photon cell imaging of mouse melanoma B16-F10 cancer cells under (k) bright field, λ_{ex} = (l) 405 nm, (m) 488 nm, (n) 543 nm and (o) merger of (l), (m) and (n) stained with PI (185).	118
Figure 69: Schematic illustration of the synthesis of functionalized supra-C-dots with MLS and RGD, and the use of the complex in the cancer treatment following the PTT rout (187).	120
Figure 70: (A1-A3 and C1–C3) Super-resolution fluorescence images of HepG2 cells and L02 cells treated with functionalized supra-C-dots (green), while the mitochondria were stained in red. B1 and D1 of the panorama simulation images of A3 and C3. B2, B3 and D2, D3 show the enlarged regions from B1 and D1 (187).....	121
Figure 71: Images of HepG2 treated with functionalized supra-C-dots (top row), L02 cells treated with functionalized supra-C-dots (middle row), and HepG2 treated with supra-C-dots followed by irradiation for 3, 7, and 10 mins. The viable cells were stained as green, while the dead cells were stained as red. The scale bar is 50 μ m (187).	123
Figure 72: Cell viabilities of L02 cells and HepG2 cells treated with functionalized supra-C-dots using WST-1 cell viability assay (187).	124
Figure 73: Amine-functionalized QDs were activated with sulfo-SMCC, subsequently followed by reaction with the thiol group of the peptide (197).....	126
Figure 74: RNA delivery mediated by the QD-k7 conjugate. Delivery of the 83 base long RNA in HeLa (top row), and HEK 293 cells (bottom row). RNA in red, QD-K7 green, and the nucleus was stained with blue. Both cell lines were incubated for 1.5 h, and 6 h (197).....	127
Figure 75: Chemical structure of the RGD peptide (198).	128
Figure 76: Schematic illustration of the modification of the GQD with RGD and loading the system with DOX (201).	129
Figure 77: Confocal microscope images for the intracellular uptake and localization of DOX, GQD, GQD@DOX, and RGD–GQD@DOX in H460 cells with incubation for 2 h (scale bar: 50 μ m) (201).....	130
Figure 78: confocal microscope images for the intracellular uptake and localization of DOX, GQD, GQD@DOX, and RGD–GQD@DOX in SK-mel-5 cells with incubation for 1 h (scale bar: 50 μ m) (201).	131
Figure 79: Skeletal structures representative of polymers (208).	133
Figure 80: Skeletal structures representative of dendrimers and hyperbranched polymers (208).	135
Figure 81: Composition of the homopolymers and copolymers.	136
Figure 82: Classification of polymers (208).....	137
Figure 83: Illustration of the mechanism of action of the chain reaction polymerization of polyetylenglykol.	139

Figure 84: Illustration of the step growth polymerization strategy with the possible products.	141
Figure 85: Illustration of polymerization of polyethylene oxide following the ring opening approach (214).	142
Figure 86: C-dots synthesized by Sun et al.: a) TEM images, b) the passivated C-dots with PEG _{1500N} exhibit better photoluminescence properties, and c) absorption of photoluminescence spectra of the passivated C-dots under different wavelength starting with 400 nm and increment of 20 nm (22).	143
Figure 87: TPL images of A431 cells: a) were treated with conjugated C-dots attached to Ab _{EGFR} antibody, and b) cells treated with the conjugated C-dots (217).	145
Figure 88: Illustration of the chemical structure of the quaternary ammonium salt conjugated with Polyethyleneimine PEI/QAS.	146
Figure 89: Schematic representation of the synthesis of methylated PEI-cloth. Step 1: the acylation of the cloth with 4-bromobutylchloride, step 2: the attachment of PEI, step 3: the methylation of the PEI-cloth using iodomethane (219).	146
Figure 90: Bactericidal activities against air borne <i>S. aureus</i> , using PEI-cloths of different PEI molecular weights (219).	147
Figure 91: Illustration of the chemical structure of the Jeffamine D-230. $x=33$ (223).	148
Figure 92: Illustration of the chemical reaction for the synthesis of C-dots, A) the generation of the precursor (230), and B) the full synthesis of the C-dots (231).	152
Figure 93: Illustration of the hydrothermal synthesis of C-dots. a) the mixture of the starting materials b) the generation of the precursor under reflux c) the precursor material, d) the generation of the C-dots230, e) the C-dots230 material, f) the generation of the C-dots.	153
Figure 94: TEM images and size histograms of (a) C-dots230 and (b) the C-dots (7).	154
Figure 95: Passivation of the C-dots using nitric acid with reflux.	154
Figure 96: Purification of the C-dots using dialysis a) at zero-time, b) after a 3 h of the dialysis, c) completely purified C-dots.	155
Figure 97: Chemical structure of the protected Lysine used for the synthesis of K7. The Fmoc is the temporary protecting group that protects the terminal NH ₂ of the Lysine. The Boc is the permanent protecting group that protects the NH ₂ of the R group of the Lysine.	156
Figure 98: Deprotection of the Lysine using the peptide synthesizer, removing the Fmoc that makes the Lysine ready to be attached to the next Lysine via peptide bond as shown in Figure 60.	156
Figure 99: Filtration of the K7 after the resin was cleaved, showing the beds of the resin.	158
Figure 100: Illustration of the chemical reaction for the synthesis of PEI/QAS.	160
Figure 101: Illustration of the conjugation reaction of C-dots with K7.	161
Figure 102: Illustration of the conjugation reaction of C-dots with RGD.	162
Figure 103: Illustration of the conjugation reaction of C-dots with PEI/QAS.	163
Figure 104: Illustration of the conjugation reaction of C-dots with Jeffamine.	164
Figure 105: A diagram of a transmission electron microscope (233).	167

Figure 106: Schematic diagram of the FTIR instrument, (1) moving mirror, (2) fixed mirror, (3) beam splitter, and ADC analog digital converter (239).	169
Figure 107: Illustration of the Jablonski diagram (245).	172
Figure 108: A schematic illustration of the fluorescence decays after pulsed excitation (254).	176
Figure 109: Grids of one chamber on the haemocytometer under the microscope (263).	181
Figure 110: Process of loading the slide with the cell suspension using the cell countess method.	182
Figure 111: HeLa cells under the microscope, A) 20% confluent, B) 70% confluent, and C) 85% confluent.	183
Figure 112: Layout of the 96-well plate.	186
Figure 113: Illustration of the fluorescence microscope (271).	189
Figure 114: Illustration of the dissolution enhancer cell (284).	194
Figure 115: HPLC chromatogram of the K7 right after the cleaving of the resin showing the two separated peaks.	196
Figure 116: Molecular structure of K7 showing the locations around the carbonyl bonds where fragments occur. The R group represents the side groups (288).	197
Figure 117: Mass spectrum for Peak 1 of K7 as shown in Figure 115.	198
Figure 118: Mass spectrum for Peak 2 of K7 as shown in Figure 115.	199
Figure 119: TEM images of: C-dots, C-K7, C-RGD, and C-PEI/QAS.	200
Figure 120: FTIR spectra of: A) C-dots, B) K7, C) C-K7, and D) a comparison of A, B, and C. All the samples were tested in solid state.	202
Figure 121: FTIR spectra of: A) C-dots, B) RGD, C) C-RGD, and D) a comparison of A, B, and C. All the samples were tested in solid state.	204
Figure 122: FTIR spectra of: A) C-dots, B) PEI/QAS, C) C-PEI/QAS, and D) a comparison of A, B, and C. All the samples were tested in solid state.	206
Figure 123: FTIR spectra of: A) C-dots, B) PEI/QAS, C) C-PEI/QAS, and D) a comparison of A, B, and C. All the samples were tested in solid state, except Jeff where it was tested in a liquid state (as approached by the provider).	208
Figure 124: TGA curve of C-dots.	210
Figure 125: TGA curves of A) C-dots, B) K7, and C) C-K7.	211
Figure 126: TGA curve of A) C-dots, and B) C-RGD.	212
Figure 127: TGA curves of A) PEI/QAS, and B) C-PEI/QAS.	213
Figure 128: TGA curve of A) C-dots, and B) C-J.	Error! Bookmark not defined.
Figure 129: UV-vis spectra of 0.1 mg/mL aqueous solutions of C-dots, C-K7, C-RGD, C-PEI/QAS, C-J, K7, RGD, PEI/QAS, and Jeffamine.	215
Figure 130: PL spectra of 0.085 mg/mL aqueous solution of C-dots λ_{ex} range of 440-600 nm with 20 nm increment. The dashed line indicates the λ_{ex} -independent emission that is apparent at low λ_{ex}	216
Figure 131: PL spectra of 0.085 mg/mL aqueous solution of C-K7 λ_{ex} range of 440-600 nm with 20 nm increment.	216

Figure 132: PL spectra of 0.085 mg/mL aqueous solution of C-RGD λ_{ex} range of 440-600 nm with 20 nm increment.....	217
Figure 133: PL spectra of 0.085 mg/mL aqueous solution of C-PEI/QAS λ_{ex} range of 440-600 nm with 20 nm increment.....	217
Figure 134: PL spectra of 0.085 mg/mL aqueous solution of C- λ_{ex} range of 440-600 nm with 20 nm increment.....	218
Figure 135: Fluorescence lifetime decay at λ_{ex} =375 nm of 0.085 mg/mL aqueous solution of: A) C-Dots, B) C-K7, C) C-RGD, D) C-PEI/QAS, and E) C-J. The points represent the experimental data, and the lines correspond to the cumulative fitting curves.....	223
Figure 136: Fluorescence lifetime decay at λ_{ex} =450 nm of 0.085 mg/mL aqueous solutions of: A) C-Dots, B) C-K7, C) C-RGD, D) C-PEI/QAS, and E) C-J. The points represent the experimental data, and the lines correspond to the cumulative fitting curves.	224
Figure 137: Viability of HeLa, U87, T98G and GC-1SPG cells following incubation with C-dots for 24h, using MTT assay.	225
Figure 138: Viability of HeLa, U87, T98G and GC-1SPG cells following incubation with C-K7 for 24h, using MTT assay.	226
Figure 139: Viability of HeLa, U87, T98G and GC-1SPG cells following incubation with C-RGD for 24h, using MTT assay.	227
Figure 140: Viability of HeLa, U87, T98G and GC-1SPG cells following incubation with C-PEI/QAS for 24h, using MTT assay.	227
Figure 141: Viability of HeLa, U87, T98G and GC-1SPG cells following incubation with C-J for 24h, using MTT assay.	228
Figure 142: Viability of HeLa, U87, T98G and GC-1SPG cells following incubation with K7 for 24h, using MTT assay.	228
Figure 143: Viability of HeLa, U87, T98G and GC-1SPG cells following incubation with PEI/QAS for 24h, using MTT assay.	228
Figure 144: Viability of HeLa, U87, T98G and GC-1SPG cells following incubation with C-dots for 24h, using PrestoBlue assay.....	230
Figure 145: Viability of HeLa, U87, T98G and GC-1SPG cells following incubation with C-K7 for 24h, using PrestoBlue assay.....	231
Figure 146: Viability of HeLa, U87, T98G and GC-1SPG cells following incubation with C-RGD for 24h, using PrestoBlue assay.....	232
Figure 147: Viability of HeLa, U87, T98G and GC-1SPG cells following incubation with C-PEI/QAS for 24h, using PrestoBlue assay.	232
Figure 148: Viability of HeLa, U87, T98G and GC-1SPG cells following incubation with C-J for 24h, using PrestoBlue assay.....	233
Figure 149: Viability of HeLa, U87, T98G and GC-1SPG cells following incubation with K7 for 24h, using PrestoBlue assay.....	233
Figure 150: Viability of HeLa, U87, T98G and GC-1SPG cells following incubation with PEI/QAS for 24h, using PrestoBlue assay.	234

Figure 151: Positive control (to the left), and negative control (to the right) of the haemolysis assay.....	234
Figure 152: Haemolysis test of 100 µg/mL aqueous solution of: C-dots, C-K7, C-RGD, C-PEI/QAS, and C-J. All the samples were incubated for 24 h in a premade hole in blood agar.....	235
Figure 153: Fluorescence microscope images of HeLa cells incubated with 10 µg/mL of C-dots, C-K7, C-RGD, C-PEI/QAS, and C-J for 24 hours, under UV, blue, green λ_{ex} . Scale bar 100 µm... ..	236
Figure 154: HeLa cells images under the fluorescence microscope after incubation with 30 µg/mL of C-dots, C-K7, C-RGD, C-PEI/QAS, and C-J for 24 hours, under UV, blue, green λ_{ex} . Scale bar 100 µm.....	237
Figure 155: HeLa cells images under the fluorescence microscope after incubation with 100 µg/mL of C-dots, C-K7, C-RGD, C-PEI/QAS, and C-J for 2 hours, under UV, blue, green λ_{ex} . Scale bar 100 µm.....	238
Figure 156: HeLa cells images under the fluorescence microscope after incubation with 100 µg/mL of C-dots, C-K7, C-RGD, C-PEI/QAS, and C-J for 4 hours, under UV, blue, green λ_{ex} . Scale bar 100 µm.....	239
Figure 157: HeLa cells images under the fluorescence microscope after incubation with 100 µg/mL of C-dots, C-K7, C-RGD, C-PEI/QAS, and C-J for 6 hours, under UV, blue, green λ_{ex} . Scale bar 100 µm.....	240
Figure 158: HeLa cells images under the fluorescence microscope after incubation with 100 µg/mL of C-dots, C-K7, C-RGD, C-PEI/QAS, and C-J for 8 hours, under UV, blue, green λ_{ex} . Scale bar 100 µm.....	241
Figure 159: HeLa cells images under the fluorescence microscope after incubation with 100 µg/mL of C-dots, C-K7, C-RGD, C-PEI/QAS, and C-J for 24 hours, under UV, blue, green λ_{ex} . Scale bar 100 µm.....	242
Figure 160: Average percentage reduction in colony formation units of <i>E. coli</i> , and <i>S. aureus</i> incubated for 20 h with: C-dots, C-K7, C-RGD, C-PEI/QAS, and C-J. *: these data obtained at 0.5mg/mL, while the rest at 5mg/mL.	243
Figure 161: Drug release profile of the Ibuprofen against PBS at 25±1 °C initially loaded in:  P123 gel system,  P123 and C-dots system,  P123 and C-K7 system,  P123 and C-RGD system,  P123 and C-PEI/QAS system, and  P123 and C-J system.	245
Figure 162: Drug release profile of the Temozolomide against PBS at 25±1 °C initially loaded:  P123 gel system,  P123 and C-dots system,  P123 and C-K7 system,  P123 and C-RGD system,  P123 and C-PEI/QAS system, and  P123 and C-J system.	246

List of tables

Table 1: The HPLC method for separation the K7, A: water with 0.1% trifluoroacetic acid, B: Acetonitrile with 0.1% trifluoroacetic acid, with a flow rate is 3 mL/ minutes.	159
Table 2: The three methods that were suggested by Agilent technologies for the separation of the K7.	164
Table 3: Elemental analysis for C-dots, C-K7, C-RGD, C-PEI/QAS, and C-J.....	209
Table 4: the percentage of weight loss of the samples using the TGA analysis.	214
Table 5: QY values of the C-dots, the C-K7, the C-RGD, the C-PEI/QAS, and the C-J, in an aqueous solution $\lambda_{ex} = 345$ in correspondence to DAPI dye.	218
Table 6: UV-vis and PL measurements used to calculate the QY of the nanoparticles.....	219
Table 7: τ_{avg} values of the C-dots, C-K7, C-RGD, C-PEI/QAS, and C-J. All the samples were tested in an aqueous solution of 0.085 mg/mL.	220

List of Abbreviations

C-dots	Carbon dots
PL	Photoluminescence
K7	Heptapeptide (lysine) ₇
RGD	Tripeptide Arginine-Glycine-Aspartic acid
QAS	Quaternary ammonium salt
PEI	Polyethyleneimine
PEI/QAS	Quaternary ammonium salt conjugated with polyethyleneimine
C-K7	C-dots conjugated with K7
C-RGD	C-dots conjugated with RGD
C-PEI/QAS	C-dots conjugated with PEI/QAS
C-J	C-dots conjugated with Jeffamine D-230
HPLC	High-Performance Liquid Chromatography
LC-MS	Liquid Chromatography–Mass Spectrometry
TEM	Transmission Electron Microscopy
FTIR	Fourier Transform InfraRed spectroscopy
TGA	Thermal Gravimetric Analysis
UV-vis	Ultraviolet-visible spectroscopy
QY	Quantum Yield
λ_{ex}	Excitation wavelength
λ_{em}	Emission wavelength
τ_{avg}	Average fluorescence lifetime decay
CPPs	Cell-Penetrating Peptides
Boc	Butyloxycarbonyl
Fmoc	Fluorenylmethoxycarbonyl

NMP	1-methyl-2-Pyrrolidone
DMF	N,N-dimethylformamide
DCM	Dichloromethane
DIEA	N-EthylDiisopropyleamine
HBTU	2-(1H-benzotriazol-1-yl)-1,1,3,3-tetramethyluronium hexafluorophosphate
NHC	N-hydroxysuccinimide
EDC	N-(3-dimethylaminopropyl)-N'-ethylcarbodiimide hydrochloride
DMSO	Dimethyl sulfoxide
<i>E. coli</i>	<i>Escherichia coli</i>
<i>S. aureus</i>	<i>Staphylococcus aureus</i>
PBS	Phosphate-buffered saline
P123	Copolymer [HO(CH ₂ CH ₂ O) ₂₀ (CH ₂ CH(CH ₃)O) ₇₀ (CH ₂ CH ₂ O) ₂₀ H], Pluronic 123
MTT	(3-[4,5-di-methylthiazol-2yl]-2,5-diphenyl-tetrazolium bromide)
CA	Citric acid
EA	Ethanolamine

Chapter 1: Introduction

1.1 The aim of the project:

To develop a new generation of non-toxic nanomaterials that show potential as bioimaging agents and drug carries.

1.2 The objectives of this project are:

- 1- To synthesize and characterize a new series of multifunctional conjugates based on C-dots, bearing peptides or polymeric groups.
- 2- Investigate structure-properties relationships in those conjugates.
- 3- To explore the performance of C-dots as drug carriers, in which two model systems have been made, Ibuprofen (a nonsteroidal anti-inflammatory medication) as a model and Temozolomide (a chemotherapeutic medication). The interaction between the drug and the carrier is based on the physical adsorption of the drug within the corona of the C-dots (Figure 3).
- 4- To evaluate the nanomaterials with respect to their bioimaging capabilities.
- 5- To assess the toxicity and the antimicrobial performance of the conjugates.

1.3 System design:

This project focuses on developing new types of C-dots in the light that previous studies have shown that C-dots exhibit remarkable photoluminescent (PL) properties combined with low level of toxicity (1). Therefore, in this project the synthesised systems being tested and shown to be one of the promising classes of nanomaterials emerging that are suitable for medical applications, such as bioimaging and advanced drug delivery are studied. Furthermore, it is well known that the conventional chemotherapeutic medicines are causing many side effects,

mainly due to the lack of the specificity of the drugs (2). One way to overcome this challenge is to use a drug carrier with the ability to penetrate the cancer cells. C-dots could potentially act as drug carriers with an elevated level of specificity, as shown in Figure 3.

This project focusses on designing peptide functionalised C-dots and polymers functionalised C-dots. The peptide functionalised C-dots are a) C-dots combined with K7 peptide (composed of 7 Lysine amino acids) to produce C-K7, and b) C-dots combined with RGD peptide (composed of Arginine, Glycinin, and Aspartic acid) to produce C-RGD. The polymer functionalised C-dots are C-dots combined with PEI/QAS (Quaternary ammonium salt functionalised PEI polymer) to produce C-PEI/QAS, and C-dots combined with Jeffamine polymer to produce C-J.

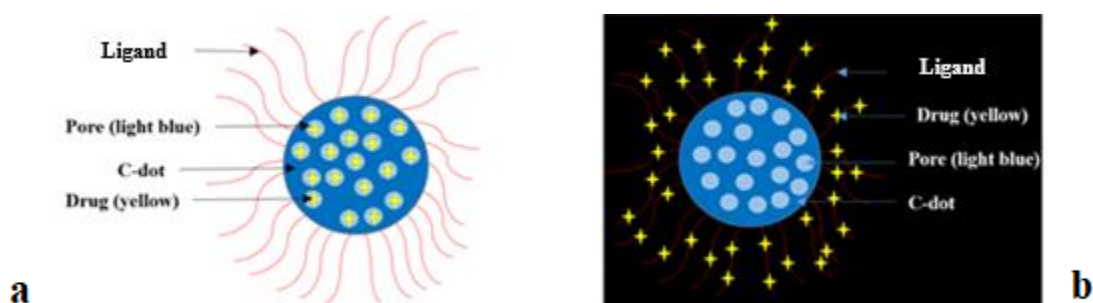


Figure 3: C-dots carrying drug molecule (a): Pore-loaded C-dots, (b): drug physically adsorbed on the C-dots surface. The ligand can be: K7, RGD, PEI/QAS, or Jeffamine.

1.4 Carbon nanodots overview

The carbon nanoparticles of interest in this project are the Carbon dots (C-dots), they are a fairly new class of materials. They are exceedingly small size of a range between 1 nm and up to 100 nm and have remarkable PL properties. They are also considered biocompatible with very low levels of toxicity. An MTT (3-[4,5-di-methylthiazol-2yl]-2,5-diphenyl-tetrazolium bromide) cell proliferation assay undertaken by Tong et al. showed that HeLa cells (cervical cancer cells)

treated with C-dots shows high level of cells viability (Figure 4). In Figure 4, Tong et al., synthesized C-dots following the hydrothermal method by using citric acid (CA) and hyperbranched poly (amino amine) as the surface passivation agent (3). The toxicity of the synthesized C-dots was tested using MTT assay, with HeLa cells being incubated in a 96-well plate for 24 h in an incubator at 37 °C and 5% CO₂. Then different concentrations of the C-dots were added to the cells (10, 20, 50, 100, 200, and 400 µg/ml), incubated in the same previous conditions for 24 h, then the MTT assay was done by adding the MTT reagent to the C-dots treated HeLa cells. Cells were then incubated for 2-4 hours, followed by the addition of the lysis buffer after which the cells were kept in the dark at room temperature for 2-4 h, and finally the absorption was measured using a plate reader (3). The MTT assay results shown in Figure 4 shows very high cell viability results especially at low concentration. Furthermore, the higher the C-dots concentration the lower the cell viability. Yet, the lowest cell viability is greater than 80% in which can be seen at 400 µg/mL concentration (3).

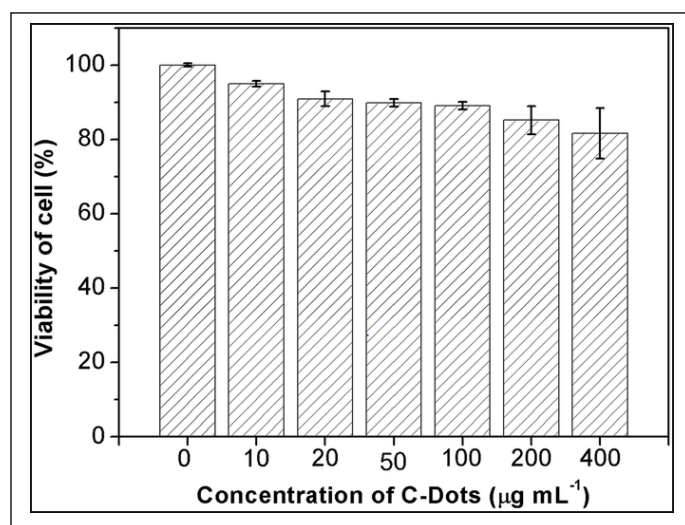


Figure 4: Cell viability by MTT assay for HeLa cells were treated with C-dots (3).

In addition to the low toxicity, C-dots exhibit antimicrobial activities against gram negative bacteria such as: *Salmonella enterica* (*S. enterica*), *Escherichia coli* (*E. coli*), *Pseudomonas syringae* (*P. syringae*), *Pseudomonas tomato* (*pv. Tomato*), *Rhizobium rhizogenes* (*A.*

rhizogenes), *Agrobacterium tumefaciens* (*A. tumefaciens*), and *Pectobacterium carotovorum* (*P. carotovorum*) (4).

Pandy et al., assessed the antimicrobial activity of C-dots synthesized following the microwave method using CA plus β -alanine. They followed the agar plate disc diffusion method to evaluate the antimicrobial activity. In this method they spread 50 μ l of bacterial suspension on the agar surface and incubated at temperatures suitable for the growth of the different bacterial species (28 °C to 37 °C), then with a cork borer 3 wells of 0.6 mm were made in the agar to be filled with 40 μ L of C-dots, water, and a solution of CA and β -alanine, then incubated at the same previous incubation conditions overnight, and finally the exclusion zone was measured (4). The results in Figure 5 shows different response to the C-dots in which the C-dots are most effective against *P. syringae* pv. *Tomato*, *A. rhizogenes*, and *A. tumefaciens*, less effective against *S. enterica*, and the least against *E. coli* (4).

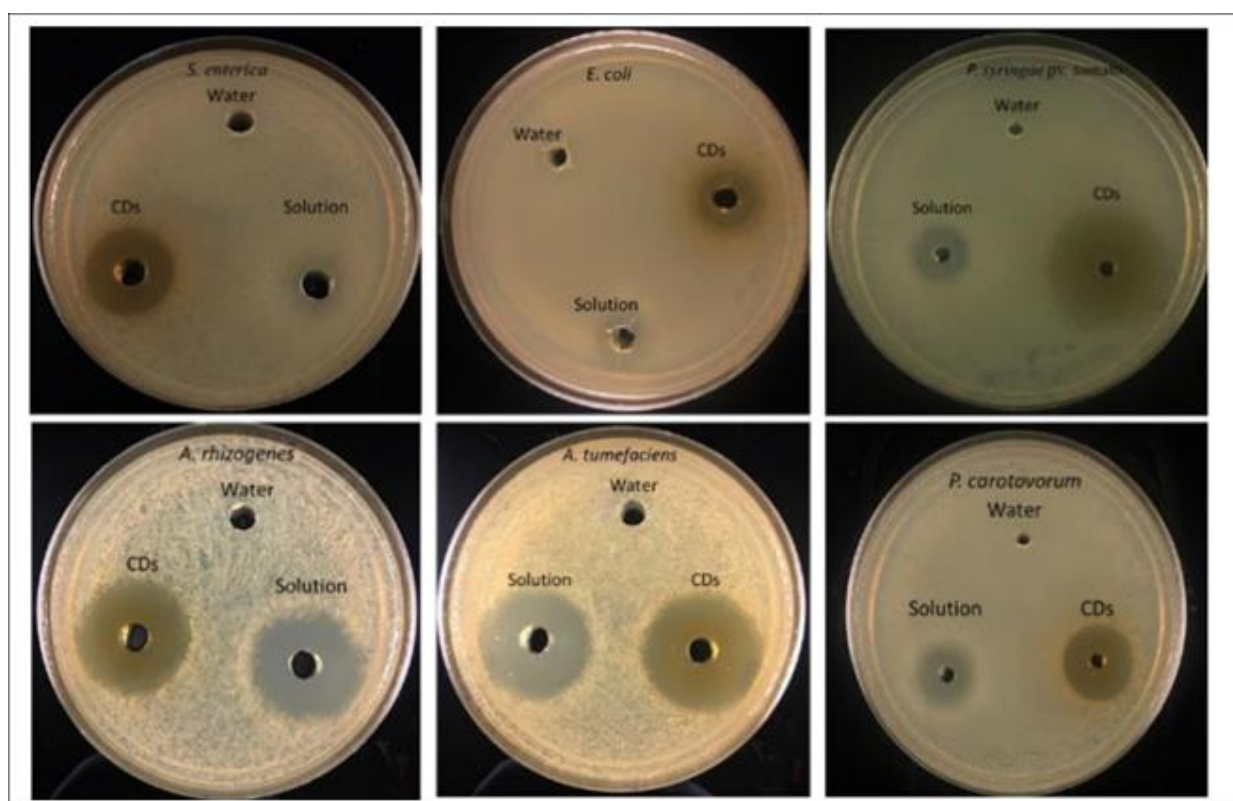


Figure 5: Antimicrobial activity of C-dots in a comparison with Water and a solution of CA plus β -alanine, against *S. enterica*, *E. coli*, *P. syringae*, *A. rhizogenes*, *A. tumefaciens*, and *P. carotovorum* (4).

C-dots can be made using different precursors depending on the required properties of the final products, including polymers, carbohydrates, organic acids, ionic liquids, and crude biomass (5), (6), (7). In this project, C-dots were synthesized following the hydrothermal treatment by Krysmann et al. due to the remarkable optical properties and a high QY (7).

Throughout the last decade, the synthesis methods and the characterization techniques of C-dots have been developed depending on the precursors used and the required properties of the yield (8). The vast majority of synthesis methods are time and cost effective, yielding product with high-water solubility, low toxicity, and are both biocompatible and eco-friendly (9). Furthermore, the C-dots have the ability to penetrate cells (10).

In conclusion, the remarkable PL properties in addition to the particle size of the C-dots, make them viable candidates in many *in vivo* applications.

1.4.1 Structure of C-dots

In the past several years, much research has been carried out to define the structure of C-dots (11), (12). Most research illustrated that the general structure of C-dots is a spherical shaped nanoparticle with a carbonized core, which is surrounded by functional groups (11). In addition to the carbon, elemental analysis results show that the C-dots are often surrounded by large number of functional groups including oxygen, hydrogen, and nitrogen. These are known as defects in the surface of the C-dots and contribute to the PL properties of the C-dots (11) (12).

The Transmission Electron Microscopy (TEM) images show that the C-dots have a well-defined spherical shape with a narrow size distribution of 1- 5 nm in diameter as shown in Figure 6 a (12).

The C-dots exhibit a high level of disordered carbon atoms which are shown in the X-ray Diffraction (XRD), the XRD patterns illustrated two broad peaks at 6.8 Å and 3.4 Å in which indicate that the C-dots exhibit a small core with disordered surface, as shown in Figure 6 b.

The Raman spectra shows that the C-dots display two peaks, one at 1365 cm^{-1} which corresponds to the D band (sp_3 -hybridized), and the other peak is at 1575 cm^{-1} which corresponds to the G band (sp_2 -hybridisation), as shown in Figure 6 c. The intensity ratio of D band to the crystalline G band (I_D/I_G) is 0.86 (12).

Supporting the Raman spectroscopy results, ^{13}C Nuclear Magnetic Resonance (NMR) spectroscopy shows signals in the range 30-40 ppm which represents the aliphatic sp^3 -hybridized carbon atoms and signals in the range 90-185 ppm which corresponds to the sp^2 -hybridized carbon atoms. Furthermore, signals in the range 170-185 ppm indicate the presence of carboxyl and amide groups, as shown in Figure 6 d (12).

As stated above, on the C-dots surface there are various defects/ functional groups in addition to the carboxyl and amide. The C-dots also have $\nu(\text{O-H})$ and $\nu(\text{N-H})$ is shown as a broad absorption bands at $3100\text{-}3500\text{ cm}^{-1}$ in Fourier Transform Infrared Spectroscopy (FTIR) analysis. These functional groups improve the hydrophilicity of the C-dots and the stability in an aqueous solution. Furthermore, the FTIR analysis shows absorption bands at $1600\text{-}1700\text{ cm}^{-1}$ which correspond to $\nu(\text{C=O})$, and absorption bands at $1350\text{-}1460\text{ cm}^{-1}$ which correspond to $\delta(\text{CH}_2)$, as shown in Figure 6 e. Furthermore, the functional groups on the surface of C-dots allows further functionalization with other molecules (13). Supporting the FTIR, the zeta potential of the C-dots in an aqueous solution are +88.1 mV, which demonstrates that the C-dots are highly dispersed and stable in an aqueous solution (12).

The UV-vis and photoluminescence spectra displayed in Figure 6 f, show that the C-dots have quite wide absorbance spectra in which have peaks at 270 nm, 340 nm, and 405 nm which are related to the absorption of an aromatic pi region. Furthermore, Figure 6 f shows that the C-dots exhibit an excitation wavelength (λ_{ex}) dependent emission behavior in which $\lambda_{\text{ex}} = 340\text{ nm}$ shows emission at 445 nm, and the emission wavelength (λ_{em}) keep shifting to longer wavelengths as the λ_{ex} increase, showing maximum $\lambda_{\text{em}} = 525\text{ nm}$ when excited with 380 nm (12).

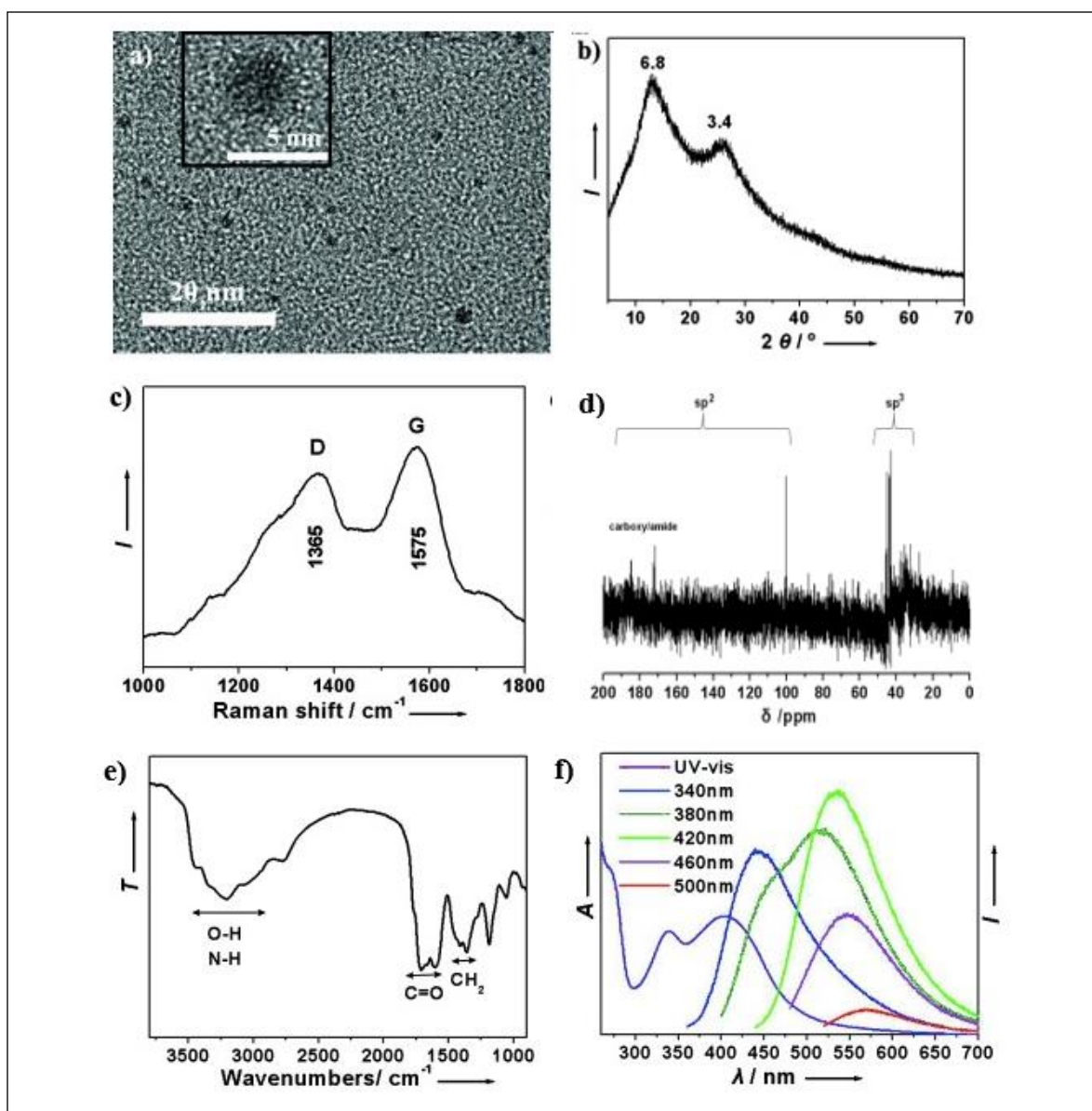


Figure 6: a) TEM image of synthesized C-dots; scale bar: 20 nm (inset: high-resolution TEM image of a C-dot; scale bar: 5 nm). b) XRD patterns of C-dots, c) Raman spectrum of C-dots, and d) ^{13}C NMR spectrum of C-dots in D₂O (40 mg/mL), e) FTIR spectrum of C-dots in the dry state, and f) UV-vis absorption and PL spectra of a dilute aqueous solution of C-dots at various λ_{ex} (12).

1.4.2 Graphene Carbon Dots, synthesis, and structure

The graphene carbon dots are another class of carbogenic nanoparticles well known as GC-dots, the GC-dots are considered as disks of single layer of graphene (14). The main important properties of the GC-dots are the remarkable electronic conductivity as well as the stability of the structure, regardless of the breaking down of the GC-dots into few aromatic groups (15).

The GC-dots can be synthesized following the hydrothermal etching of carbon nanotubes (CNTs) (16), graphene treatment with oxygen plasma (17), or via high resolution electron beam lithography (15). The cage opening of fullerenes is considered as a unique method while the C_{60} -Ru attractive forces resulting vacancies in the Ru crystal to take in the C_{60} particles (14). At very high temperatures, the embedded molecules will be diffused and aggregated to produce GC-dots (18) as shown in Figure 7.

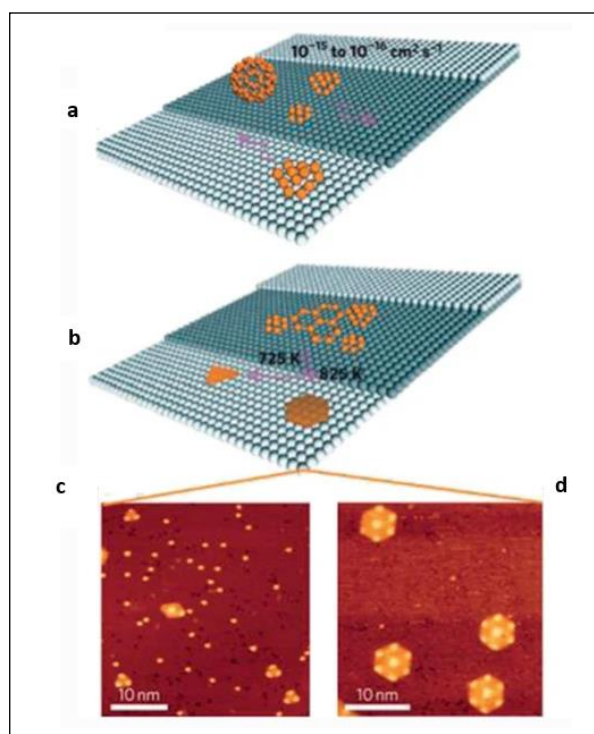


Figure 7: Illustration of the synthesis of GC-dots following the cage opening of fullerenes; a) adsorption of C_{60} molecules to the terraces of Ru crystals, b) temperature-dependent growth of GC-dots with triangular and hexagonal equilibrium shape, c) and d) scanning tunneling microscope images of the triangular and hexagonal GC-dots, respectively (18).

Furthermore, the organic and chemical synthesis methods produce GC-dots with relatively large size, but colloidal and stable alongside uniformity in size and tunable dimensions (19), (20). The organic and chemical synthesis methods based on the oxidation of polyethylene dendritic precursors to produce graphene moieties which are more stable against self-aggregation via attaching bulky 2,4,6-trialkyl phenyl groups to their edges (20), Figure 8 demonstrate the synthesis methods of GC-dots following the organic and chemical process.

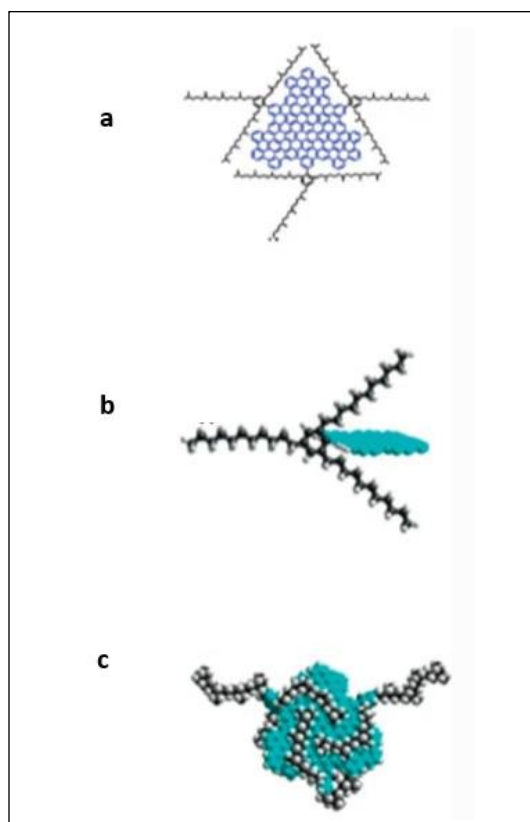


Figure 8: Illustration of the synthesis of GC-dots following the organic and chemical method; a) structure of Quantum C-dots, b) bulky moieties chemically attached to the edges of the C-dot to enhance colloidal stability, c) an energy-minimized configuration of Quantum C-dots (20).

Moreover, GC-dots can be synthesized following the solvothermal method, which is based on the hydrothermal fragmentation of sucrose under high pressure, which opens the ring of the hydrolyzed compounds, to form dehydrated furfural compounds, then polymerization via hydronium catalysis, and finally carbonization to produce the GC-dots (21).

In addition, GC-dots can be synthesized following the laser ablation method, which is based on directing a laser on graphitic powder, then oxidation step using HNO_3 , this method requires surface passivation amine terminated oligomers or polymers otherwise, the produced GQ-dots will not show any photoactivity (22).

Furthermore, the GC-dots can be synthesized via electrochemical oxidation of CNTs (23) or graphite (24), in which they represent the working electrodes in a traditional electrochemical cell as illustrated in Figure 9. The electrode of choice should include ultrapure water, phosphate buffer solution, ionic liquid water, NaOH with ethanol, and acetonitrile (23). The reaction starts with extensive electrode exfoliation, to facilitate the release the GC-dots. Mechanically determined, the electrooxidation event is related to the production of hydroxyl as well as the oxygen radicals (which are naturally produced by the electrolysis of the solvent) and which attack the graphitic anode on defect and edge sites, in which resulting the electrolyte to intercalate the layers of the graphite causing electrode chipping and production of the GC-dots (25).

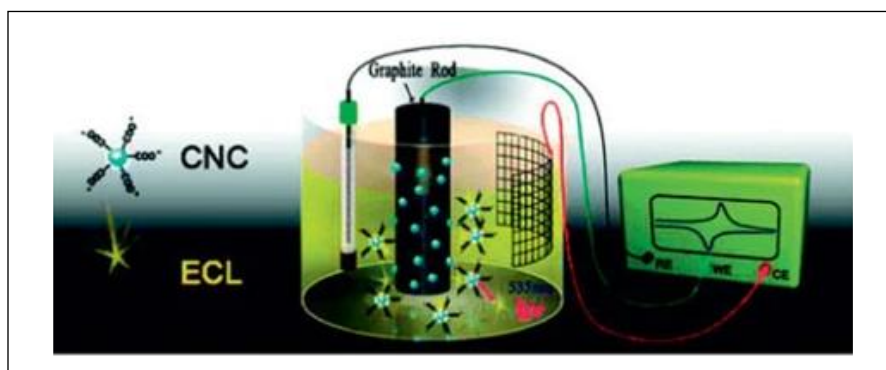


Figure 9: Illustration of the synthesis of GC-dots following the electrochemical method (24).

Following the electrochemical oxidation method, Li et al., synthesized GC-dots using graphene film as the working electrode, Pt wire as the counter electrode, Ag/AgCl as the reference electrode and phosphate buffer solution of 6.7 pH as the electrolyte, with cycling voltammetry window ± 3 V (26).

The GC-dots produced by Li et al., have a narrow size distribution with diameters of 3-5 nm as shown in the TEM images in Figure 10 a, b, and c. The XRD pattern of GC-dots display a broad peak at 3.4 Å compared to 3.7 Å for the source of carbon (the graphene electrode) as shown in Figure 10 d.

The Raman spectrum of GC-dots presents two peaks located at 1365 cm^{-1} and 1596 cm^{-1} , which correspond to the D and G bands of the graphitic and amorphous carbon respectively. The G peak is related to the E_{2g} vibration mode of the sp^2 bonded carbon, while the D peak represent the A_{1g} (zone-edge), in which breathing vibration photon that activated in close proximity to the sp^3 defect only (27). $I_D/I_G = 0.5$, as shown in Figure 10 e.

The analysis of C1s peak of the GC-dots (presented in Figure 10 f) shows the presence of C=C at 284.8 eV, a C–O which is at 286.8 eV, C=O at 287.8 eV and COOH at 289 eV bonds, due to the hydroxyl, the carbonyl, and the carboxylic acid groups respectively. Those surface functional groups are responsible for the colloidal stability of the GC-dots. Supporting the C1s analysis, the FTIR analysis shows the presence of -OH at 3500 cm^{-1} and C=O at 1750 cm^{-1} as shown in Figure 10 g (26).

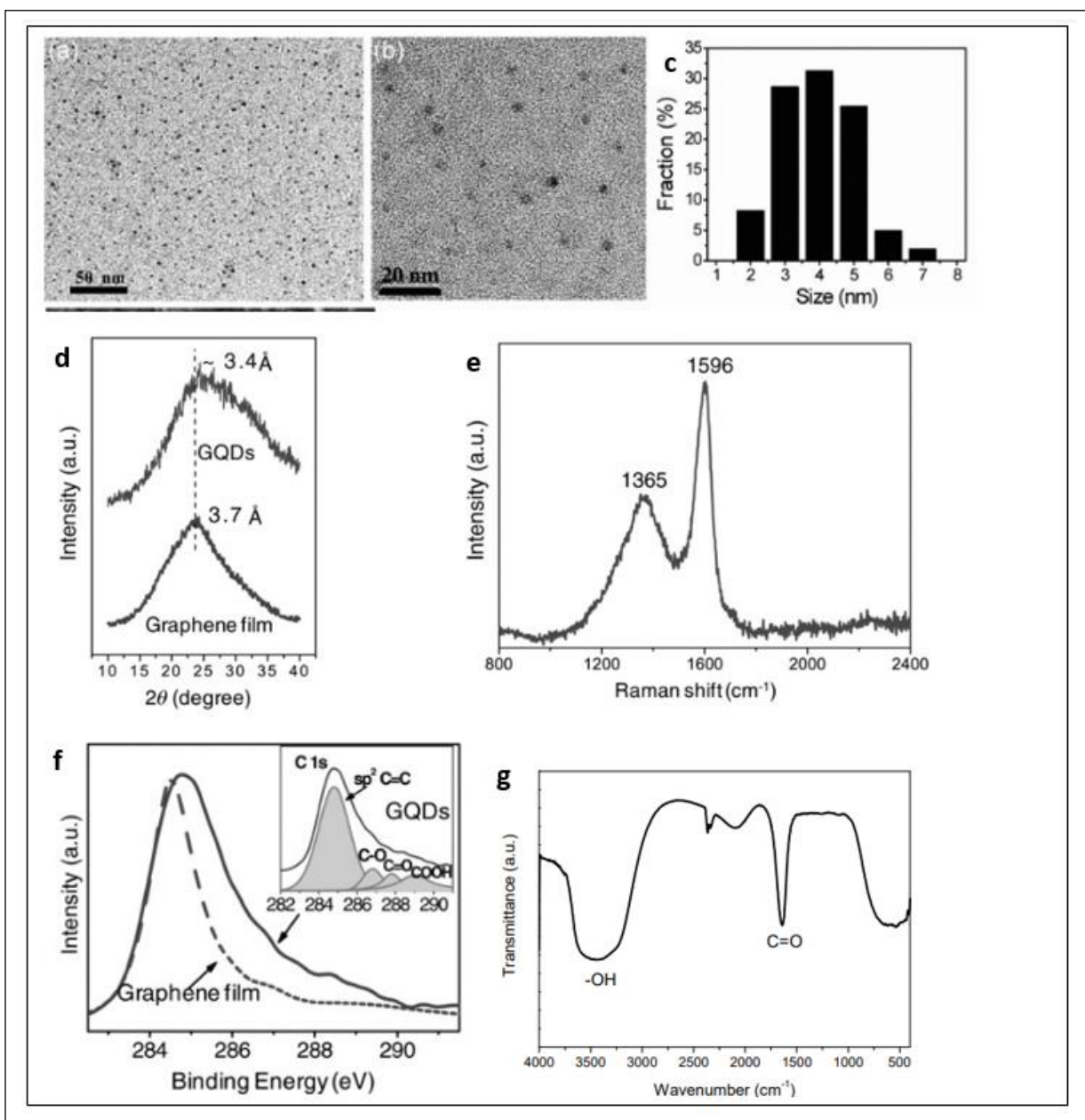


Figure 10: GC-dots synthesized following the electrochemical oxidation of a graphene film: a) and b) TEM images, c) size distribution, d) XRD pattern compared to the initial graphene film, e) Raman spectrum, f) C 1s peak compared to paternal film; the inset refers to the C 1s of GC-dots, and g) FTIR spectrum (26).

1.4.3 C-dots Synthesis methods

Following up on what has been explained earlier, C-dots have been an interesting field of research in the last decade for many scientists, and the synthesis methods have been developed and modified (28). To summarize the synthesis methods, they have been classified into two main approaches which are top-down and bottom-up methods depending on the synthesis procedure (29) as shown in Figure 11.

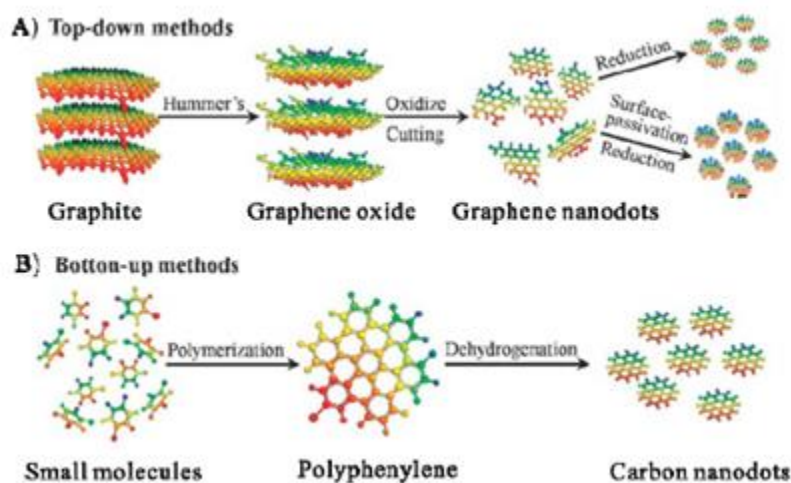


Figure 11: Schematic diagram of the two synthesis methods of C-dots. A) top-down methods and B) bottom-up methods (30).

1.4.3.1 The top-down methods

They are based on the breaking down of the bulky carbon source such as CNTs, carbon fibers, graphene oxide, graphene sheets, or the other organic source to produce nanosized C-dots (29). The top-down methods include;

1.4.3.2 Decomposition of graphene-based material via oxidation

This method is based on using graphene-based materials to produce C-dots, in which to be oxidized to produce C-dots (31), (32).

Vinci et al., synthesized C-dots using carbon fibers as the source of carbon which was mixed with H_2SO_4 and HNO_3 , the mixture was sonicated for 1 hour then heated at $120\text{ }^\circ\text{C}$ for 1 hour to form a solution of C-dots which were then neutralized using ammonium carbonate (32). The synthesized C-dots exhibit an average diameter of 7 nm with blue λ_{em} when excited at 325 nm, and a quantum yield (QY) = 4%.

Yang et al. reported a large-scale synthesis of three species of heteroatom doped C-dots as well as C-dots using carbon quantum dots (CQDs) obtained from Chinese ink (which is made of a mixture of soot and animal glue (33)) (34). They oxidized the CQDs using nitric acid, sulfuric acid, and sodium chlorate, followed by a hydrothermal reaction with dimethylformamide as the nitrogen source, sodium hydrosulfide as sulfur source, and sodium selenide as selenium source (34). The synthesized classes of C-dots are C-dots, nitrogen C-dots (N-C-dots), sodium C-dots (S-C-dots), and selenium C-dots (Se-C-dots), which had a sizes ranging from 1 nm to 7 nm. They reported that the doped C-dots exhibit higher QY than the pure C-dots (C-dots 6%, N-C-dots 39%, S-C-dots 24%, and Se-C-dots 19%), as well as a longer lifetime. They also exhibit different PL properties as C-dots are blue, N-C-dots are violet, and S-C-dots are green. Furthermore, Se-C-dots are also exhibit green λ_{em} when exciting at 275, 324, 360, and 485 with non- λ_{ex} dependent emission behavior (34). These species also all possess good photostability.

Tao et al. synthesized C-dots following the oxidation of graphene-based material. They used single walled carbon nanotubes (SWNTs) which was mixed in a 3:1 ratio of H_2SO_4 : HNO_3 (as shown in Figure 12) and refluxed for 24 h to make a transparent solution of C-dots that are photostable at room temperature for up to one year (35). The synthesized C-dots are with spherical shape with a nearly uniform diameter size of 2-3 nm, with a QY = 6% and green λ_{em} = 530 nm at an excitation range of 350-650 nm with 50 nm increment.

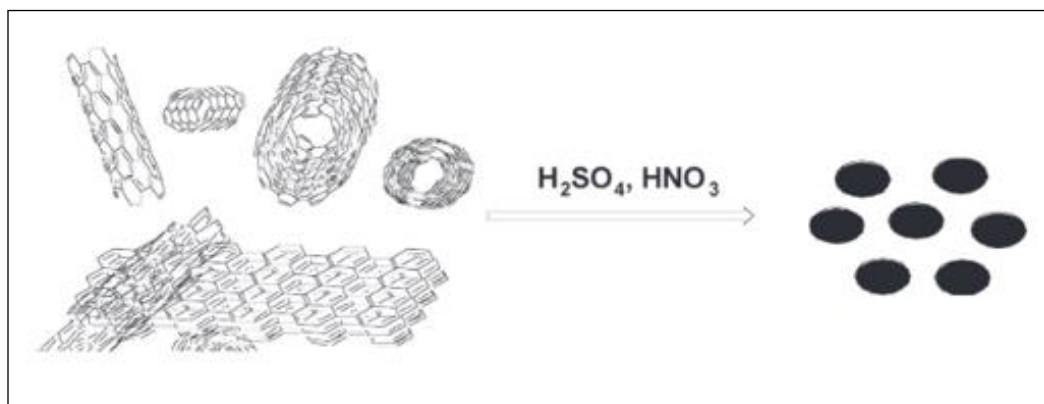


Figure 12: Schematic diagram of reaction to synthesize C-dots using SWNTs by Tao et al. (35).

1.4.3.2.1 Arc discharge method

This method is based on using an arc discharge, a carbon source, a cathode, an anode, and an ambient gas (36) as shown in Figure 13.

Shi et al. synthesized C-dots following the arc discharge method, in which they used a pure graphite rod which had a hole drilled into it and was filled with 1:1 molar ratio of graphite and Y-Ni alloy powder as the anode (37). The Y-Ni powder was used instead of their metal mixture because they are stable in the atmosphere pressure. The cathode they used was a graphite rod in the presence of helium atmosphere under a pressure of 100-700 torr. The obtained C-dots had a narrow range of distribution with an average diameter of 1.3 nm (37).

Hutchison et al. synthesized C-dots using the arc discharge method, in which they used metal-graphite electrodes, a graphite rod with a drilled channel which was filled with the catalyst (the catalyst was made of a mixture of Ni, Co, and Fe powder metals) as the anode, a graphite rod as the cathode, and an inert gas atmosphere (38) The obtained C-dots have varied sizes with diameters between 2 and 5 nm (38).

Jiang et al. synthesized C-dots using Benzene (99%) and ethylenediamine (99%, anhydrous) as carbon source following the arc discharge method in the presence of helium gas under atmospheric pressure (39). The obtained nanoparticles had a size range of 5-20 nm (39).

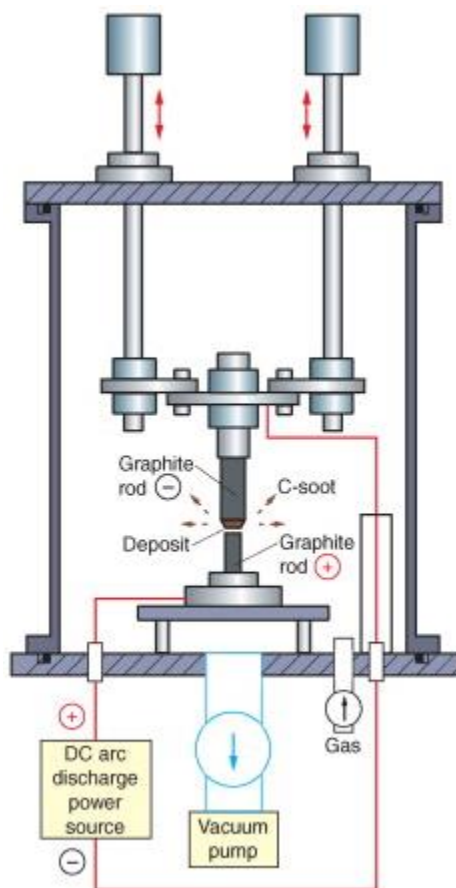


Figure 13: Schematic diagram of apparatus for preparing C-dots following the Arc discharge method (40).

1.4.3.2.2 Acidic oxidation

This method can be called chemical ablation, it involves the use of a carbonaceous carbon source such as: carbohydrates, carbogenic quantum dots, CA, grass, or orange peels (41), (42). This method is based on the decomposition of the carbon source into nano-sized particles, concomitantly initiating hydrophilic groups on the surface of the synthesized C-dots such as hydroxyl and carboxyl groups which improve the water solubility properties as well as the

fluorescence characterization (41), (42). The oxidation step is achieved by using an acid such as: sulfuric or nitric acid (41), (42).

Zhang et al., synthesized C-dots following the oxidation method using fullerene carbon soot (FCS) which was treated with 1:1 ratio of $\text{HNO}_3:\text{H}_2\text{SO}_4$ (pre sonicated for 40 min) for the oxidation (43). The mixture of the FCS and the acid were sonicated for an hour then heated at $120\text{ }^\circ\text{C}$ whilst stirring for 12 hours. The product was cooled down and neutralized with K_2CO_3 . The synthesized C-dots exhibit a diameter size of 2-3 nm, with a QY = 5.47% and green emission.

Qiao et al. synthesized C-dots following the oxidation process by using activated carbon, which was treated with HNO_3 , followed with passivated using amine (44). The synthesized C-dots exhibit a spherical shape with narrow distribution size of 2-6 nm, and QY = 1.25% with purple emission.

1.4.3.2.3 Laser ablation

This method is based on targeting a source of carbon using a laser in the presence of gas as a carrier such as argon, helium, or water vapor (22). This method is considered as a flexible method as the source of carbon can be either solid or dissolved in a solution (22).

Sun et al. synthesized C-dots following the laser ablation method using a solid precursor which was obtained by applying hot pressure at a mixture of graphite and cement. Before being backed, cured and finally annealed under argon flow (22). Once the solid precursor was ready, laser was used for ablation of the carbon target in the presence of argon and water vapor as carrier gas, which a water bubbler was used for this purpose at $900\text{ }^\circ\text{C}$ and 75 kPa (22). The ablated sample was refluxed with HNO_3 (up to 2.6 M) for 12 h, then polyethylene glycol 1500N (PEG 1500N) was used for surface passivation, in which the final product was tested to show diameter size of less than 5 nm, with QY = 10% and λ_{ex} dependent emission that shows different colors (22).

On the other hand, Hu et al. synthesized C-dots following the laser ablation method using a carbon source in suspension in an organic solvent rather than the solid state (45). They used graphite powder with an average thickness of 2 μm , in which were suspended in a solution of diamine hydrate, diethanolamine, or poly (ethylene glycol) (PEG200N), and then targeted by laser (45). The produced C-dots have a wide range of particle size between 1 and 8 nm, yet most of the particles have between 2-4 nm, with QY = 5% and showing blue λ_{em} (45).

1.4.3.3 The bottom-up methods

The bottom-up approach is based on the principle of using an organic precursor as the carbon source, which includes the polymerization and carbonization processes of the carbon source such as CA, amino acids, carbohydrates, and so on, into C-dots via chemical reactions (28), (46). The bottom-up methods include;

1.4.3.2.1 Hydrothermal synthesis/ Solvothermal

This method is considered the most popular method for the synthesis of C-dots, due to many reasons including simple synthesis steps, relatively narrow size distribution of the final product, high QY (47), low cost, and environmentally friendly (48). This method is based on the small organic molecules, polymers molecules, a combination of both, or any carbon rich precursors, a solvent is required to dissolve the precursor(s) which can be water (hydrothermal synthesis), or organic solvent (solvothermal synthesis), then transfer the mixture into stainless-steel autoclave or simply using a round bottom flask heated at high temperature (46). Throughout the heating process at elevated temperature, the precursors will be going through series of chemical reactions and resulting carbon seeding cores, after that they will grow into C-dots with nearly uniform size of less than 10 nm (46).

Zhu et al. synthesized C-dots following the hydrothermal method, they used CA and ethanolamine (EA) as precursors in an aqueous solution, the solution then transferred to stainless steel autoclave and heated 300 °C for 5 h (49). During the heating process the precursors formed polymer like C-dots, followed by carbonization in order to form the C-dots with spherical shape (30). The synthesized C-dots have a nearly uniform particle diameter of 2-6 nm (Figure 14 b), and interesting PL properties (49). The resulting C-dots exhibit blue color under portable UV lamp, and the fluorescence spectra shows optimal λ_{ex} and λ_{em} at 360 nm and 443 nm respectively (49). Furthermore, it was reported that the resulting C-dots have λ_{ex} dependent emission behavior. This behavior was tested by preparing an aqueous of 0.01 mg/mL of C-dots, in which excited by different wavelengths between 300-420 nm with 20 nm increase, as shown in Figure 14 a (49).

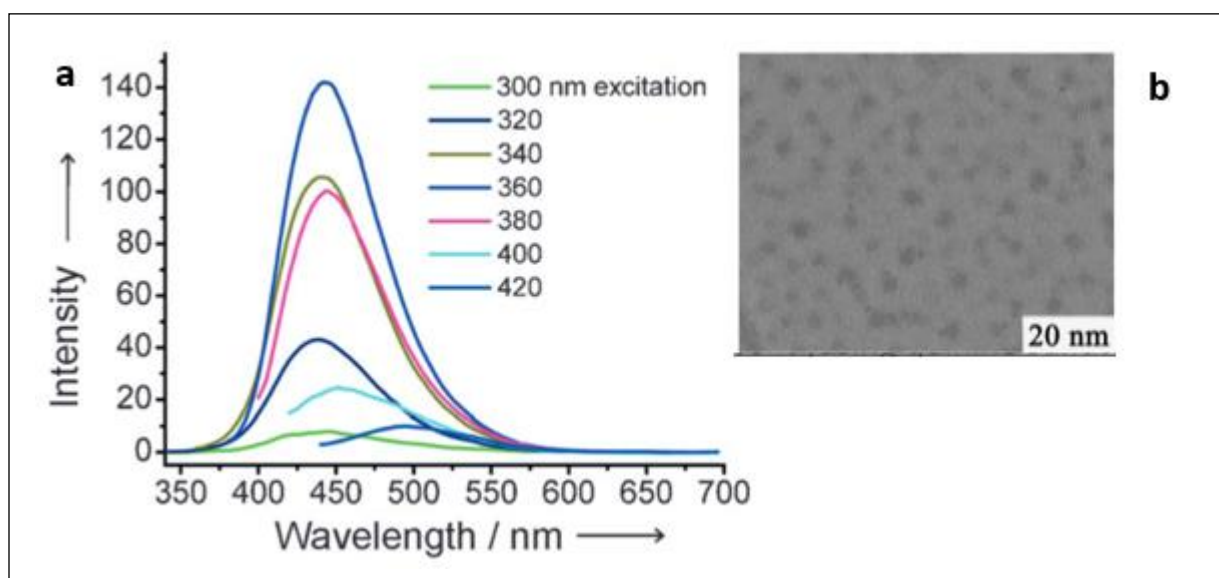


Figure 14: a) λ_{ex} dependent emission behavior, and b) TEM image of the C-dots synthesized by Zhu et al. (49).

Zhang et al. synthesized C-dots following the hydrothermal method using bovine serum albumin as the precursor, in which were dissolved in water and the mixture was stirred for 30 minutes then 4,7,10-trioxa,1,13-tridecanediamine (TTDDA) was added as a passivation agent, the mixture was transferred into stainless steel autoclave and then heated at 180 °C for 12 h (50). The heating process firstly carbonized the bovine serum albumin followed by surface

passivation of the C-dots (50). The produced C-dots have a narrow range size distribution of 2-6 nm as shown in Figure 15 b and c, with QY = 11%, and blue emission, in addition to interesting λ_{ex} dependent emission behavior as shown in Figure 15, the C-dots were excited using wavelengths from 320 nm to 420 nm with 20 nm increase as shown in Figure 15 a (50).

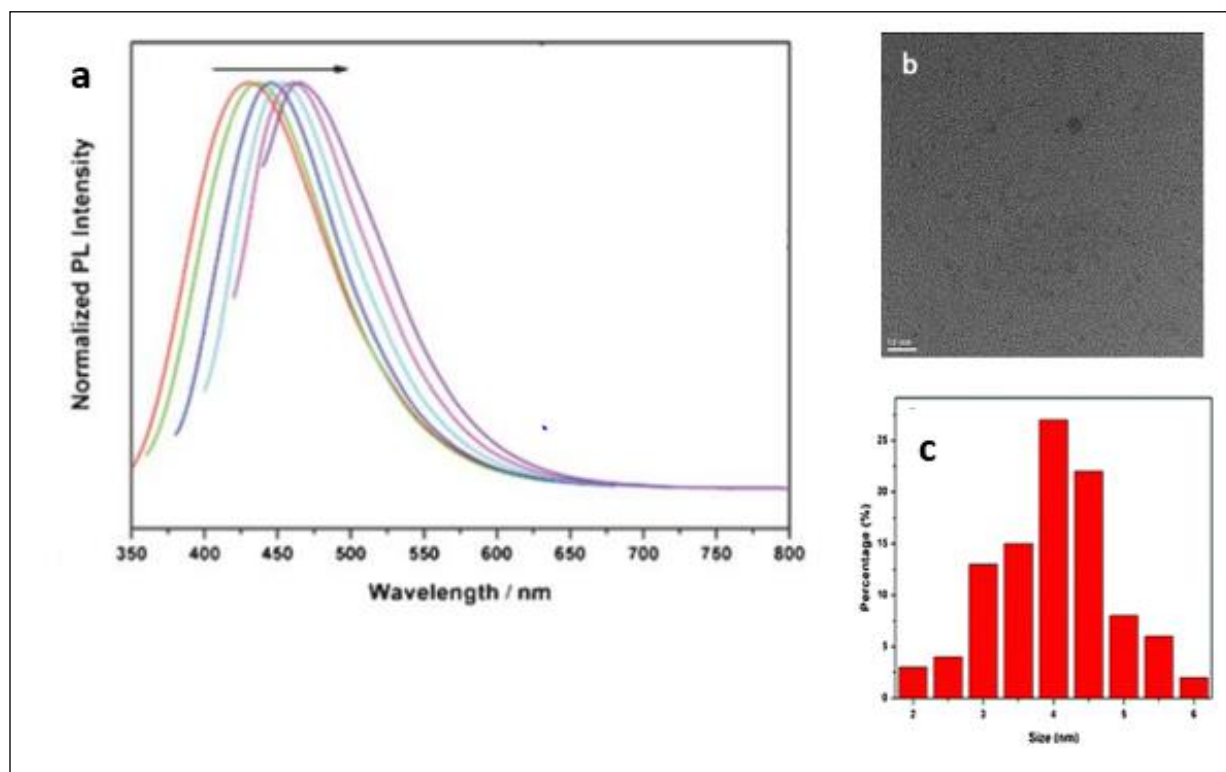


Figure 15: a) λ_{ex} dependent emission behavior, b) TEM images, and c) corresponding particle size distribution histograms of the C-dots synthesized by Zhang et al. (50).

Sahu et al. synthesized C-dots using biomass following the solvothermal synthesis method, they used pulp-free orange juice as a precursor and ethanol as solvent, the mixture was transferred into stainless-steel autoclave and heated at 120 °C (constant temperature) for 2.5 h (51). During the reaction the carbohydrates and the acids in the juice are carbonized to produce the C-dots with narrow distribution size of 1.5-4.5 nm (51). The produced C-dots exhibit high QY = 26%, and interesting PL properties with λ_{ex} dependent emission, as shown in Figure 16 (51).

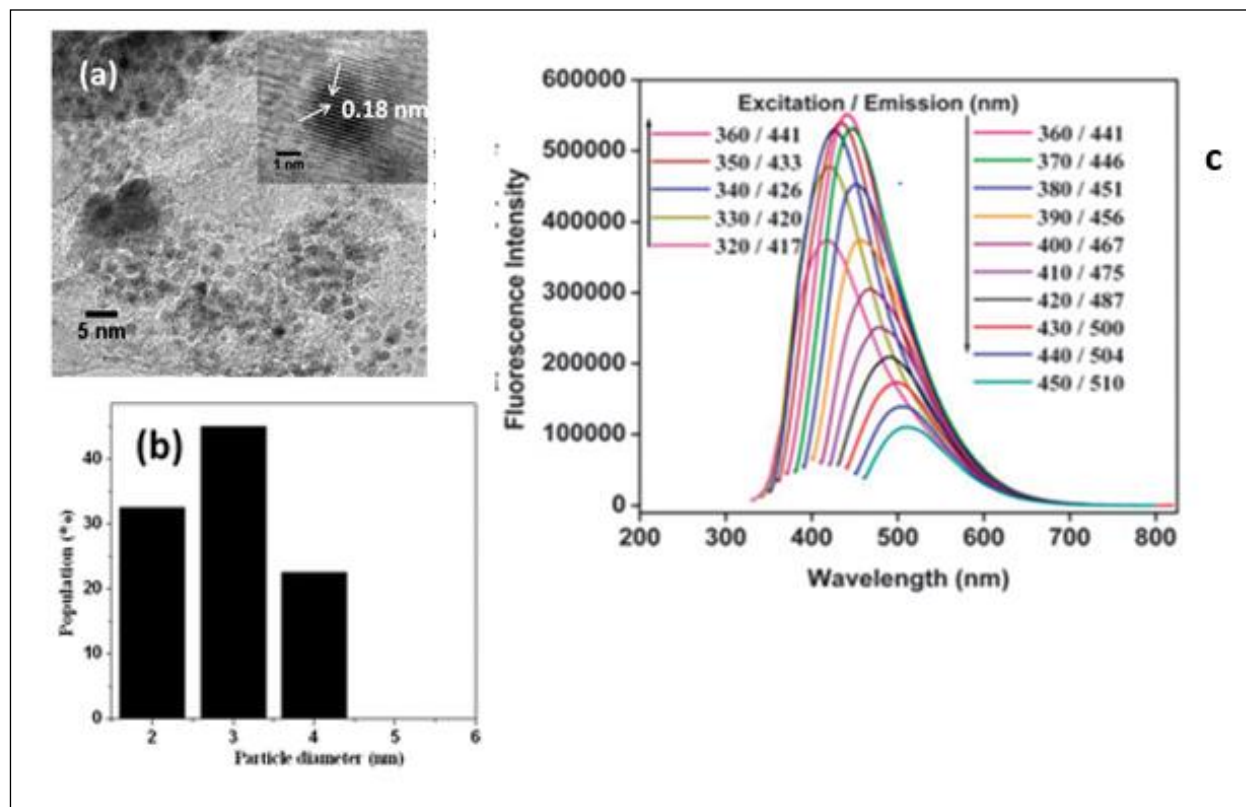


Figure 16: a) TEM image, b) particle size distribution, and c) λ_{ex} dependent emission behavior of the C-dots synthesized by Sahu et al. (51).

Bhunia et al. fabricated various species of C-dots following the solvothermal synthesis process where they used carbohydrates such as sucrose and ascorbic acid as precursors in which they were dissolved in organic solvent such as octadecene, they used sulfuric acid and phosphoric acid as dehydrating agents, the mixture was heated at a wide range of temperatures between 80 and 300 °C (52). The mixtures were carbonized at relatively low temperature 80-120 °C to produce C-dots that exhibit wide range diameter of 1-10 nm, with blue, green, yellow, and red λ_{em} (52). On the other hand, the mixture was carbonized at higher temperatures 150-300 °C showed increased the carbonization rate and promote restrictions over the size in which the produced C-dots exhibit diameter of less than 4 nm, they also limited the emission color to blue and green only (52). The synthesized C-dots exhibits high QY UP to 30% (52).

1.4.3.2.2 Thermal treatment of crude biomass

This method might be considered as a derivative from the hydrothermal method, yet it is more environmentally friendly, it is based on using crude biomass as the source of the carbon in which they are thermally carbonated to produce C-dots (6).

Krysmann et al. synthesized C-dots using an environmentally friendly synthesis process following acid oxidation method using crude biomass as a carbon precursor (6). They simply blended fresh grass completely with water, the mixture was heated in an oven at 300 °C for 4 hours, then the obtained carbogenic material was disseminated in water and refluxed with nitric acid of (3 M) aqueous solution for 4 h (6) as seen in Figure 17.

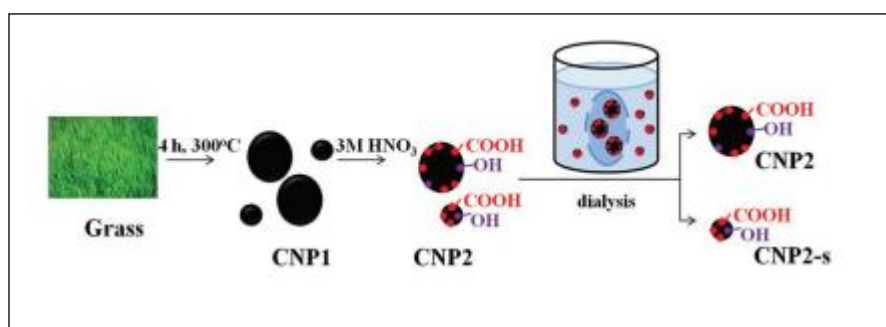


Figure 17: Schematic diagram of the synthesis of C-dots following the thermal treatment of crude biomass by Krysmann et al. (6).

Wang et al. synthesized C-dots following the crude biomass hydrothermal, they used dehydrated shiitake mushrooms as the source of carbon, in which was soaked and washed with distilled water to remove any impurities and ashes, then freeze-dried and grounded into powder. The mushroom powder mixed with deionized water and transferred into an autoclave to be heated at 200 °C for 12 h to obtain C-dots, as shown in Figure 18 (53). The synthesized C-dots exhibit a narrow diameter size distribution of 2-6 nm, with QY = 5.5% and blue color λ_{em} with λ_{ex} = 365 nm excitation.

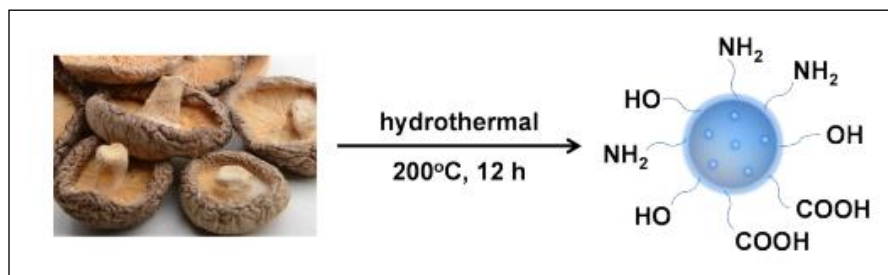


Figure 18: Schematic diagram of the synthesis of C-dots following the thermal treatment of crude biomass by Wang et al. (53).

1.4.3.2.3 Combustion routes

This method is also known as the thermal decomposition method, it is considered to be one of the most cost-effective methods, environmentally friendly, and easy to scale up for the production of C-dots (46). This method is based on the thermal decomposition of the precursor(s), followed by the functionalization of the C-dots by passivation using a suitable passivating agent (54). The passivation process enables fabricating C-dots with specific surface chemical properties by selecting a suitable passivating agent and precursor(s) (55). The synthesis of C-dots following the combustion routes have tunable optical properties, alongside controlled morphology (55).

The synthesis of the functionalized C-dots following the combustion routes can be done in two steps rather than one step as discussed in Bourlinos et al., i.e., a synthesis step followed by a functionalization step which gives the flexibility to produce varied species of the C-dots (56).

Ludmerczki et al. synthesized C-dots following the combustion routes by using CA monohydrate as a precursor, in which they heated the CA in an oil bath at 180 °C with continuous stirring at 100 rpm for 120 minutes until the colorless liquid turned into an orange-yellow sticky liquid (56). An aqueous solution of the synthesized C-dots was made and aminopropyl triethoxysilane was added to the C-dots solution, then kept in a closed vessel and heated at 25 °C with continuous stirring for 24 h at 500 rpm (56). The functionalizing of the C-dots has an effect in many aspects such as; the pH of the non-functionalized C-dots is 4.5 while the pH of the

functionalized C-dots is 11.5, the emission spectra has greatly changed in which resulting a new intense violet emission band peak around 410 nm in addition to a second fluorescent component with a maximum around 480 nm. Furthermore, the UV/Vis reflected change in the emission spectra in which the absorption band 335 nm has disappeared in the functionalized C-dots, and the UV band at 220 intensity has increased. The synthesized C-dots exhibit a wide range of particle sizes distribution of 1 to 20 nm, yet the majority of the population are between 5 and 15 nm (56).

Dong et al. synthesized C-dots following the combustion route. They used CA which was heated in a beaker on the hotplate at 200 °C, the CA turned to liquid after 5 minutes of the reaction, then the color of the liquid had changed from colorless to light yellow and finally orange within 30 minutes, which means that the C-dots were formed (57). The synthesized C-dots exhibit an average size of 15 nm with QY = 9% and blue emission PL properties.

1.4.3.2.4 Microwave-assisted hydrothermal synthesis

This method is considered to be a rapid and cost-effective method (58), which is based on the homogenous heating of the precursor using microwave irradiation for a predetermine time (59). In the microwave-assisted method, the precursor absorbs the microwave irradiation in which generate heat (dielectric heating), which is a unique behavior for this method as it directly targets the molecule instead of conductively in comparison to other methods (60).

Shen et al. synthesized C-dots following the microwave-assisted hydrothermal synthesis, they used CA and cyclen as precursors which they dissolved in water and heated in a 750 W microwave for 5minutes, until the liquid mixture turned into solid, during the heating process the precursors condensed and dehydrated each other to form a crosslinking intermediate, followed by carbonization to produce the C-dots (61). The C-dots obtained have an average diameter of 5 nm with blue color emission, they also exhibit a high QY = 27.6% and blue emission PL properties when excited at 350 nm wavelength (61).

Jiang et al. synthesized C-dots following microwave-assisted hydrothermal synthesis, they used EA and phosphoric acid aqueous solution, in which the solution was heated for 5 minutes in a 750 W microwave (62). The synthesized C-dots have a narrow size distribution between 2.5 nm and 4 nm, with QY = 20.5% and blue color λ_{em} (62).

In another report, Jiang *at al.*, synthesized C-dots following the microwave-assisted hydrothermal synthesis using glycerol and EA as precursors, in which glycerol is the carbon source and ethylenediamine is a nitrogen doped molecule, the precursors were heated in 1kW microwave for 2,5,10,15, and 20 minutes (63). The synthesized C-dots have range size of 1-15 nm with the majority of the population between 1 nm to 5 nm, with blue color and QY = 7.5% (63). The obtained C-dots show stability up to 1 month as shown in Figure 19 a, and against the pH change between 4 and 10 pH, hence the C-dots were dissolved in different pH levels solutions 1-13, and the λ_{em} is nearly stable, as shown in Figure 19 b (63).

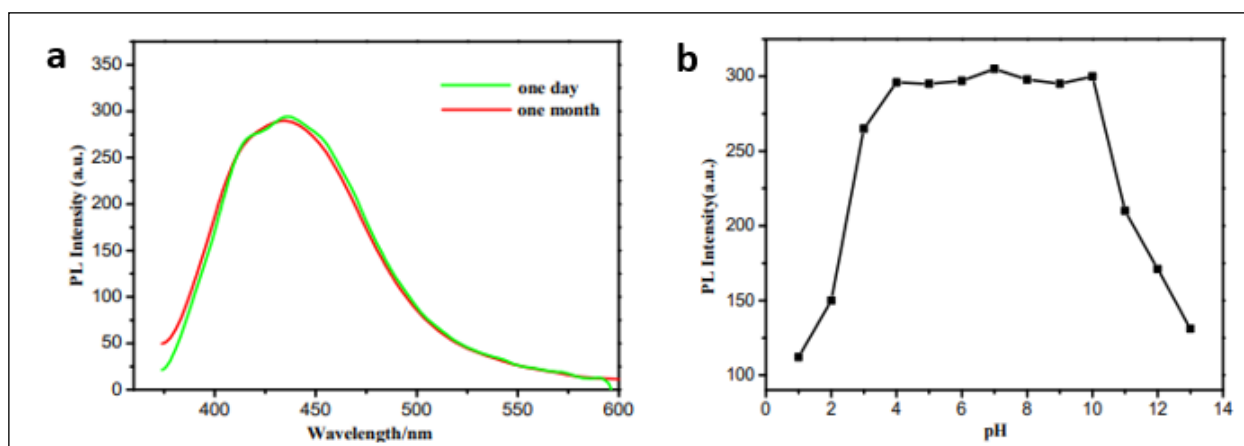


Figure 19: Stability of C-dots synthesized by Jiang et al., as a function of: a) Time, b) pH (63).

1.4.3.2.5 Template

This method is based on using a template and it is done in two phases, the first phase calcining in the mesoporous template of choice or silicon ball, and the second phase is etching to remove the carrier and produce the C-dots (48).

Liu et al. synthesized C-dots following the template method, they used polymer/F127/silica composites as a template or carrier, and resols (phenol and formaldehyde resins) as carbon precursor, the carrier-precursor was heated at 350-400 °C, then the carrier was etched using sodium hydroxide solution at 40 °C for 48 h to produce the C-dots (64). To increase the hydrophilicity of the produced C-dots, acid treatment and a simple surface passivation step can be done (64). The obtained C-dots exhibit spherical shape with diameter of 1.5-2.5 nm, with QY = 14.7% and an λ_{ex} dependent emission photoluminescence spectrum, see Figure 20 (64).

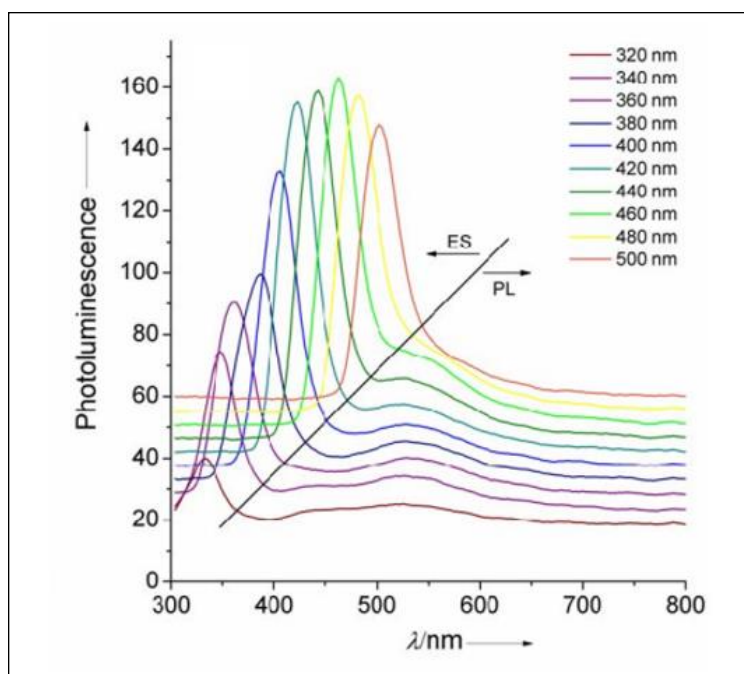


Figure 20: Photoluminescence emission spectra of the C-dots were synthesized by Liu et al. (64).

Zong et al. synthesized C-dots following the template method, they used mesoporous silica as the template and CA as the precursor, in which the mesoporous silica was soaked in a mixed solution of CA and complex salt (65). The mixture was sonicated then calcined at 300 °C for 2 h in the air, the carrier was etched using 2M sodium hydroxide solution at 40 °C for 24 h (65). The synthesized C-dots exhibit a narrow size distribution of 1.5-2.5 nm, with blue λ_{em} and QY = 23%, it has been realized that the use of the mesoporous silica prevent the aggregation of the C-dots during the pyrolysis process (65).

Yang et al. synthesized C-dots following the template method, in this report they used soft template and hard template in which the soft template is the copolymer P123 while the ordered mesoporous silica represent the hard template, and a mixture of organic molecules (including 1, 3, 5-tritoluene, diphenylamine, pyrene, and phenroline) as the precursor (66). The mixture of the soft template, the hard template, and the organic molecules were stirred at 40 °C for 4 hours, then the mixture was transferred into hydrothermal reactor in which were heated at 100 °C for 24 hours, followed by a calcination process was done at 900 °C for 2 h with the presence of nitrogen gas (66). For releasing the C-dots from the carrier, 2 M of sodium hydroxide solution was used at 40 °C for 48 h (66). The obtained C-dots exhibit a narrow range particle size distribution of 8 nm, and QY = 3.3-4.7 with green λ_{em} (66).

1.4.4 Optical properties of C-dots

1.4.4.1 UV-vis absorbance

The C-dots exhibit strong light absorption in the ultraviolet region between 230 nm and 350 nm, which can be shifted towards the visible region around 400 nm. Furthermore, the absorption spectrum of C-dots is composed of two main bands, a peak centered around 250 nm and the other peak at 350 nm (48), (67). The two bands are related to the π -conjugated electrons in the sp^2 atomic framework and the functional groups on the surface of the C-dots, in more detail the peak at 250 nm region is caused by the π - π^* transition of aromatic C=C bond or the C=O bond which are part of the carbon network, while the peak at 350 region is caused by the n - π^* transitions of N or O containing structure at the edge of the carbon structure (67). As mentioned earlier, the C-dots absorption might be shifted towards the visible region, this is caused by the functionalization of the C-dots in which the molecules on the surface of the C-dots can cause this absorption(48), (67).

As shown in Figure 21, the C-dots were synthesized following the hydrothermal synthesis using CA as the source of carbon and was doped with nitrogen. The absorption of the non-functionalized C-dots (red) has peaks centered at 250 nm which is attributed to represent the

core band including $\pi-\pi^*$ transition from the sp^2 networked carbogenic domains, and 350 nm which represents the edge/ molecular band including $n-\pi^*$ transition of nitrogen and oxygen containing groups.

On the other hand, the absorption of the functionalized C-dots (black) shows the same peaks with higher intensity at the 250 nm peak and the appearance a shift at 450 nm to higher wavelength which represent the surface band, with lower intensity that was caused by the presence of the surface functional groups (68).

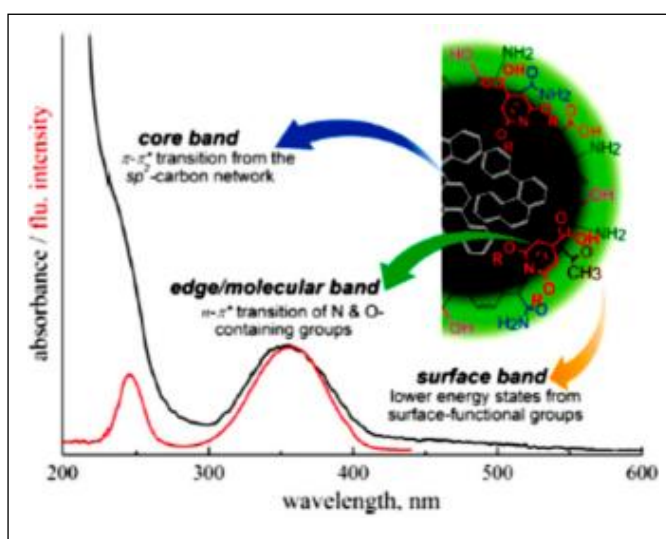


Figure 21: Absorption spectra of C-dots (red), and surface passivated C-dots (black) (68).

1.4.4.2 Photoluminescence

The photoluminescence spectrum is created when the electron transition from the highest occupied molecular orbital (HOMO) into the lowest energy unoccupied molecular orbital (LUMO) occurs (69). The PL properties of C-dots were derived from the electronic band gap surface state and the edge effect (48). Furthermore, the surface passivation of C-dots can substantially increase the QY in which, non passivated C-dots obtain a maximum QY = 10%

(usually less than that), while the surface passivated C-dots exhibit higher QY therefore the passivation process is common to enhance the brightness of the C-dots (70).

Furthermore, in principle the photoluminescence spectra of the C-dots are usually broad and the emission dependent on the λ_{ex} (71).

Liu et al. synthesized C-dots using epoxy resin as a precursor and surfactant modified silicon dioxide as the carrier to produce C-dots with diameter of 1.5-2.5 nm and blue λ_{em} under $\lambda_{ex} = 365$ nm wavelength (72). After the passivation process using PEG_{1500N} the obtained C-dots exhibit wide emission spectra range from 430nm to 580 nm with λ_{ex} dependent emission (73).

Moreover, the strong photoluminescence might be caused by the quantum confinement effect of the surface energy trap during the passivation process, Sun et al. synthesized high luminescence C-dots with an average diameter of 1.54 nm with λ_{ex} dependent emission, and a QY = 47% (74), (75). The quantum confinement effect describes the free electron behavior in terms of the energy levels, the potential wells, the valence bands, the conduction bands, and the electron energy band gap, in which is created when the size of the particle is too small (in nano scale) to be compared to the wavelength of the electron, which is obvious in quantum dots (76).

In addition, it was found that the emission spectrum of the C-dots have a good correlation between the λ_{em} and the λ_{ex} , Li, et al. synthesized C-dots following the arc discharge method and rapid passivation process using laser targeting the C-dots in an organic solvent (48), (77). Additionally, the particle size of the C-dots and the vary oxygen containing functional groups on the surface of the C-dots (which were formed after the rapid laser passivation process) are reasons to create the tunable photoluminescence (77).

On the other hand, reports have also shown that the C-dots fluorescence λ_{em} is independent to the λ_{ex} this might be because of the uniform size of the synthesized C-dots, as shown in Figure 22 a (48). Additional reason for the absence of the λ_{ex} dependent emission behavior of the C-dots might be due to the synthesis method, for example Zhang et al. synthesized C-dots following the hydrothermal method using cysteine and CA as precursors in which resulting C-dots with stable and bright blue $\lambda_{em} = 418$ nm regardless the λ_{ex} and diameter of 4 nm, as

shown in Figure 22 b, the C-dots were excited with a range of wavelength between 220 nm and 380 nm, with incasement of 20 nm (78). The lack of λ_{ex} dependent emission behavior might be due to the fact that the hydrothermal method is a non-radiative transition, it is thermal relaxation/electron transfer between the carbogenic core of the C-dots and the surface state (78). However, the fluorescence intensity had changed with different λ_{ex} , which shows λ_{ex} dependent intensity behavior (78).

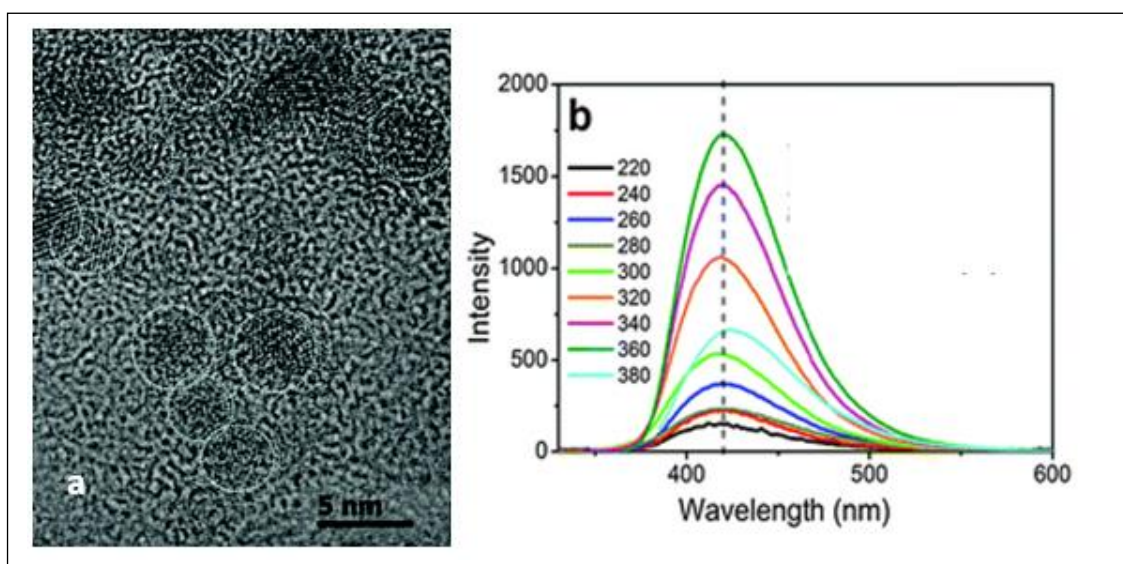


Figure 22: a) TEM images, and b) emission spectra at λ_{ex} ranging from 220 nm to 380 nm of C-dots synthesized by Zhang et al, (78).

Furthermore, reports shown that the λ_{ex} independent emission behavior can be a result of the presence of fluorophores, i.e., the fluorophores create an λ_{ex} independent emission behavior (79), (80).

Finally, it has been reported that the increase in the surface oxidation degree will lead to λ_{em} shift towards the red region, and the higher the surface oxidation degree will cause higher surface defect and brighter red emission, which make the C-dots good candidate for bioimaging prob under the IR range or it can be applied as an energy collector (81).

1.4.4.3 Up-conversion photoluminescence

It has been reported that adjusting the λ_{ex} or the particle size of the C-dots, enables to select different λ_{em} in order to meet the needs of the optical labeling and the fluorescence (48). Furthermore, some C-dots have an interesting up-conversion photoluminescence which means that they show shorter λ_{em} than the λ_{ex} (48). This phenomenon was first discovered by Cao et al., as they used excited the C-dots at 800nm femtosecond and two photon excitation using argon ion laser at 458 nm to get pictures of C-dots via the confocal microscope, as shown in Figure 23 (82).

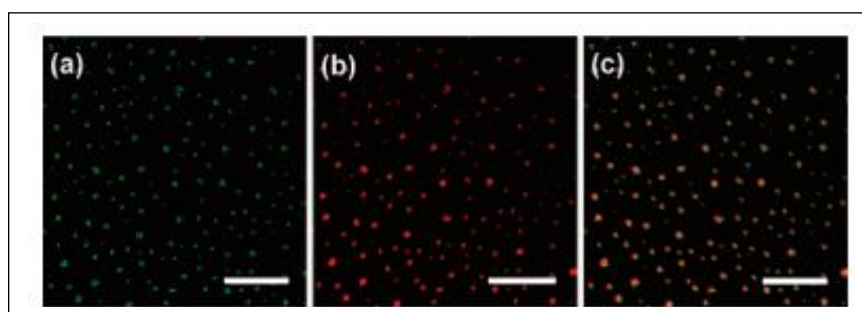


Figure 23: Luminescence images of C-dots synthesized by Cao et al., using confocal microscope (all scale bars 20 μm) with a) argon ion laser $\lambda_{ex} = 458 \text{ nm}$, b) femtosecond pulsed laser $\lambda_{ex} = 800 \text{ nm}$, and c) is an overlay of (a) and (b) (82).

Yin et al. synthesized C-dots via carbonization at 160 °C using sweet pepper as the precursor, the produced C-dots exhibit QY = 16.8% with strong up conversion fluorescence when they were excited at 740-900 nm, the fluorescence $\lambda_{em} = 400-600 \text{ nm}$, as shown in Figure 24 (83).

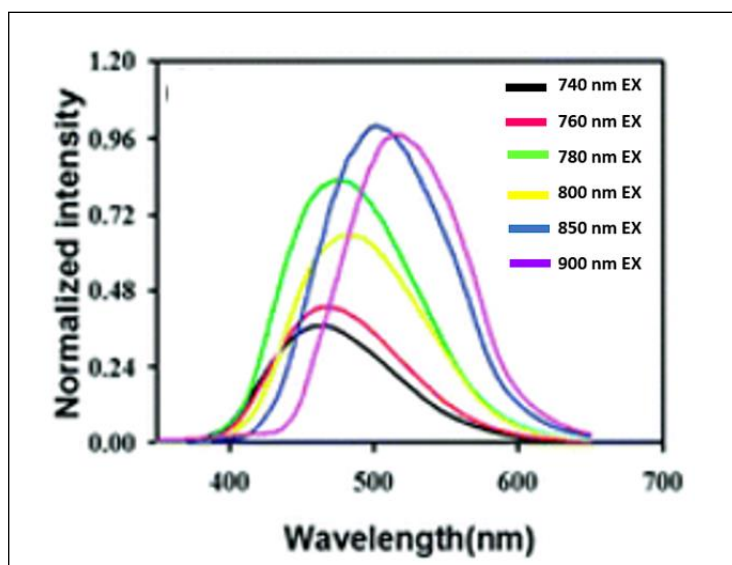


Figure 24: Up-conversion PL properties of C-dots synthesized by Yin et al. (83).

The up-conversion behavior of the C-dots makes them good candidate for *in vivo* fluorescence imaging, this is due to the λ_{ex} of the C-dots is nearly in the infrared region, in which gives them the ability to penetrate the tissue deeply and reduced fluorescence background interference (48). Li et al. synthesized C-dots following the microwave assisted method using N,N-dimethylformamide (DMF) solution. The produced C-dots are with near infrared absorption/emission and show up conversion PL at 784 nm when excited at 808 nm using continuous wave laser. Which is suitable for bioimaging, as shown in Figure 25, which shows a mouse was injected subcutaneously with C-dots, the λ_{ex} = 808 nm and λ_{em} = 770 nm (84).

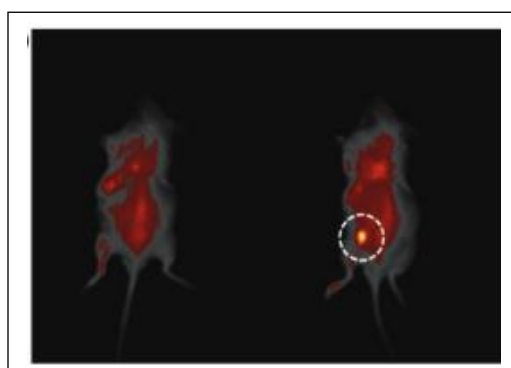


Figure 25: *in vivo* near infrared up conversion luminescence image of a mouse before (left) and after (right) subcutaneous injection of C-dots synthesized by Li et al. (84).

The multi-photon activation system is considered to be the principal cause for the up conversion PL of C-dots, particularly the simultaneous absorption of a couple of photons (or greater photons) (85). The structural capabilities of the near infrared C-dots now no longer most effective make contributions to the red-shifted optical spectra of near infrared C-dots with their most important absorption/emission within the near infrared region, however, are also accountable for the occurrence of near infrared of up conversion PL, see Figure 26 for the proposed mechanism of the up conversion photoluminescent in the near infrared C-dots (48).

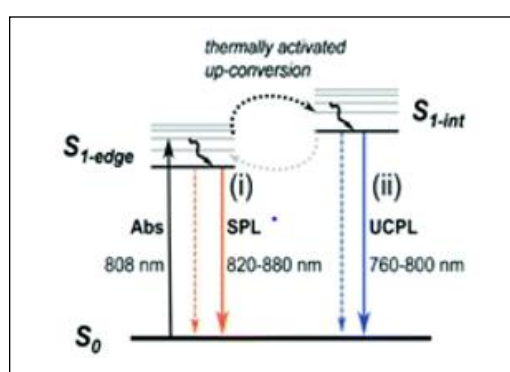


Figure 26: Proposed mechanism of the up conversion photoluminescent in the near infrared C-dots (84).

In Figure 26, when a laser energy directed the electron (808 nm laser was used), the electron will absorb the energy and will be excited to the S_1 edge state. Only two pathways for the excited electrons for their radioactive deactivation, the first pathway is; the relaxation from the S_1 edge state into the ground state by SPL, and the second pathway is; thermally activated up conversion from S_1 edge state, then followed by radiative relaxation from S_{1-int} into the ground state by Upconversion photoluminescence (UCPL) (84).

It has been reported that the synthesis method of C-dots can increase the quantum yield, Zheng et al. synthesized C-dots following the acid oxidation method then reduction reaction in order to increase the QY(86). They collected candle soot from a glass plate which was suspended above on a smoldering candle, the elemental analysis of the collected soot shows 91.69% C, 1.75% H, 0.12% N, and 4.36% O, so the main element is carbon, and it was

hydrophobic and insoluble in the common solvents (87). The soot then was oxidized using a reflux of 5 M of HNO_3 to form a homogenous black suspension of C-dots with an average size of 3 nm and exhibit green photoluminescence properties with $\text{QY} = 2\%$. Zheng et al. used sodium borohydride as a reduction agent to reduce the weak green luminescence synthesized C-dots, in which results string blue photoluminescence properties. Although the reduction reaction did not cause an obvious decrease in the size of the C-dots, yet it shows a remarkable increase in the $\text{QY} = 24\%$ as shown in Figure 27 (86).

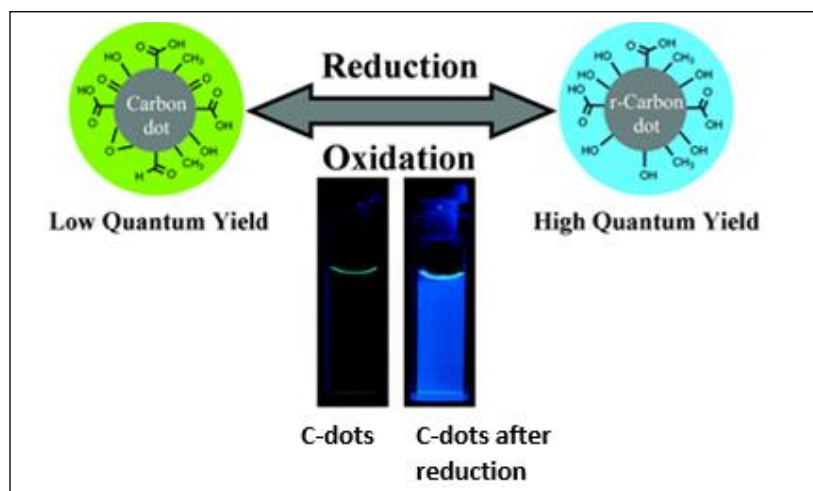


Figure 27: Schematic illustration of the synthesis of reduced state C-dots with blue luminescence from original carbon dots. Inset: photographs of aqueous solutions of the C-dots (left) and the reduced C-dots (right) obtained under UV light (360 nm) (86).

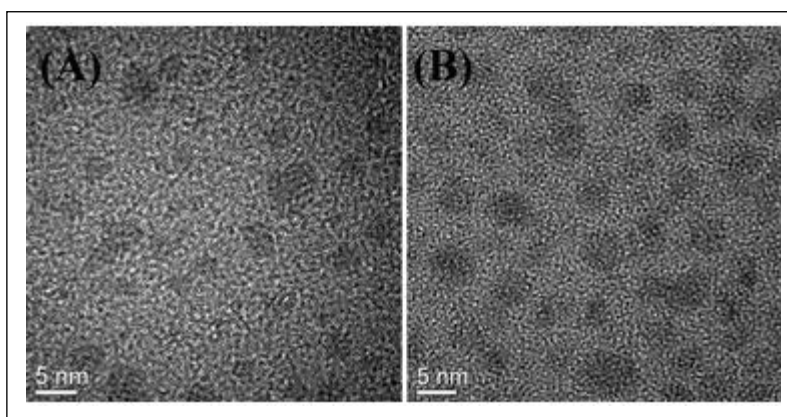


Figure 28: TEM images of the A) C-dots, and B) the reduced C-dots (86).

Figure 28 A shows less contrast on the edges of the particle and lattice fringes which is caused by the low electron density of the carbon and the small size of the C-dots, while Figure 28 B shows that the C-dots after reduction are well dispersed yet, the particle size has not reduced (86).

The comparison of the UV-vis absorption spectra and the photoluminescence spectra for the C-dots and the reduced C-dots in Figure 29 shows that a new peak appears at 230 nm in the UV-vis of the reduced C-dots, while the C-dots has no observed peak under 300 nm. The appearing of the new peak is thought to be due to the surface structural change because of the reduction reaction. The most remarkable change is the blue shift of the λ_{em} of the reduced C-dots, in which shows a bright blue photoluminescence appeared when excited at 280 nm with $\lambda_{em} = 440\text{nm}$, while the original C-dots obtained maximum $\lambda_{ex} = 470\text{ nm}$ and maximum $\lambda_{em} = 520\text{ nm}$ (86).

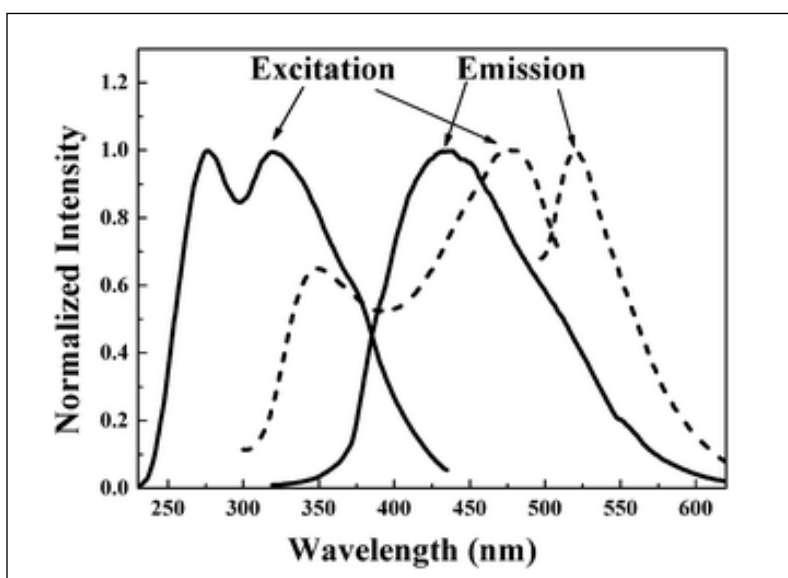


Figure 29: Photoluminescence spectra of the C-dots (dashed line), the $\lambda_{ex} = 470\text{ nm}$, and the λ_{em} of the excitation spectrum was 520 nm. The reduced C-dots (solid line), the λ_{ex} of the emission spectrum was 280 nm, and the λ_{em} of the excitation spectrum was 440 nm (86).

Moreover, the widths at half maximum of the λ_{em} created by the C-dots and the reduced C-dots were about 100 nm together, which indicates the presence of impurities, also the irregular

photoluminescence spectra support that. It is believed that the impurities affecting the quantum yield, as the purification process using column chromatography shows an increase in the QY of the C-dots to 6% after purification and the reduced C-dots up to 60% after purification. In addition to that, the luminescence lifetime of the C-dots have been improved after the reduction reaction, as the C-dots lifetime is 2.71 ns with $\lambda_{\text{ex}} = 470$ nm and $\lambda_{\text{em}} = 520$ nm, while the lifetime of the reduced C-dots is 6.08 ns with $\lambda_{\text{ex}} = 280$ nm and $\lambda_{\text{em}} = 440$ nm as shown in Figure 30 (86).

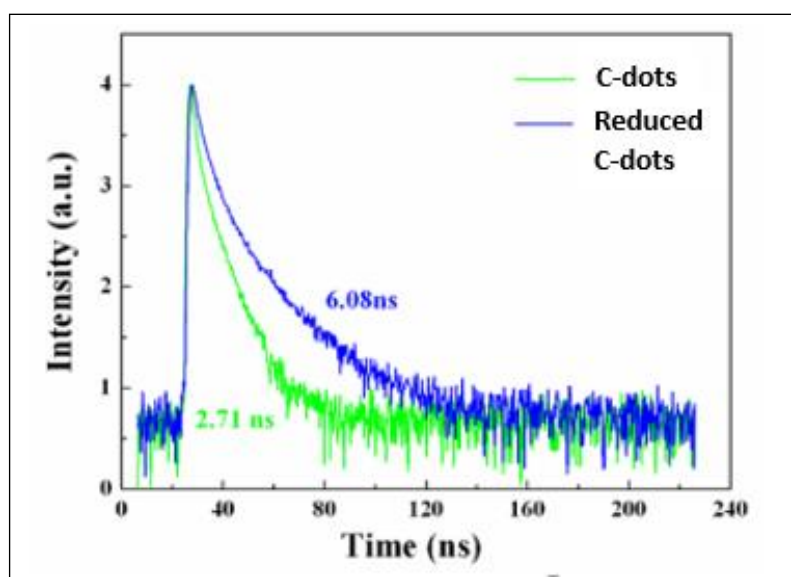


Figure 30: PL lifetimes of the C-dots (the $\lambda_{\text{ex}} = 470$ nm, and the $\lambda_{\text{em}} = 520$ nm), and the reduced C-dots (the $\lambda_{\text{ex}} = 280$ nm and the λ_{em} is 440 nm) (86).

1.4.4.4 Two-photons absorption

The two photons absorption phenomenon is a behavior that most of the photoluminescence particles can acquire, it is based on exciting the electrons from the ground state to the S_1 stage using two photons instead of one photon, each of the two photons have nearly half of the energy of the one photon, with longer wavelength (near the infrared region) (88). The two-photon absorption can obtain interference minimum determined by the location of the intermediate states as well as by the relationship of the dipole matrix element to the detuning.

Therefore, the interference minimum in two-photon absorption is controlled by the intrinsic properties of the medium (88). Figure 31 shows a proposed mechanism of the two-photon absorption. Where, the 2γ 's represent the rates of spontaneous decay, the field transition $|2\rangle \leftrightarrow |4\rangle$ is the control field, ω represent the photon, and Δ_i is the detuning. The Figure 31 proposed that the absorption probability depends on the intermediate level $|2\rangle \leftrightarrow |4\rangle$, in which makes the medium transparent to two-photon transition between $|2\rangle \leftrightarrow |3\rangle$ (88).

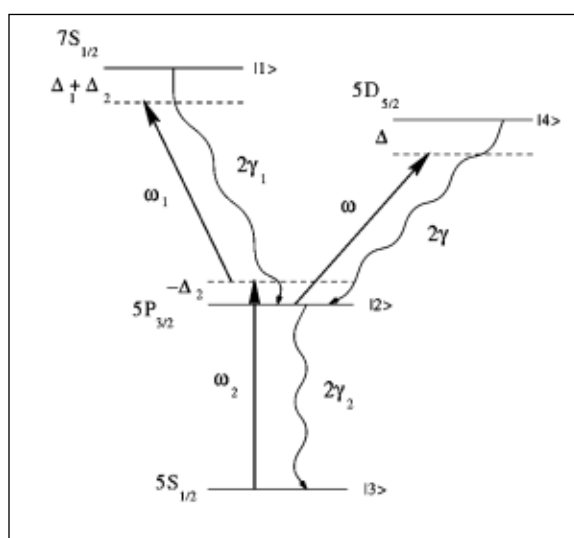


Figure 31: Schematic illustration of the mechanism of the two-photon absorption (88).

Because the two-photon absorption behavior of the C-dots the light is emitted in the visible region (near infrared region), it makes them good candidates for biomedical imaging purpose, more than the conventional methods by using heavy metals due to the low toxicity of the C-dots and the fact that they are environmentally friendly materials (89).

Cao et al. synthesized C-dots following the laser ablation method using solid precursor which was obtained by applying a hot pressure at a mixture of graphite and cement, the mixture was backed then annealed under argon flow (82). The synthesized C-dots have a spherical shape with an average diameter of 5 nm (size distribution of <5-5 nm) with strong λ_{em} in the visible

region when excited using argon ion laser at 458 nm, and the femtosecond pulsed laser for two-photon excitation in the near infrared region (800 nm), Figure 23 shows images of the C-dots λ_{em} with each laser individually and a combined image of the λ_{em} with both lasers (82).

1.4.5 Other properties

1.4.5.1 Cytotoxicity

Due to the significant PL properties of C-dots and the ability to emit light near the infrared region and the possibility to use them in bioimaging applications, many studies have been carried out to assess the cytotoxicity of the C-dots against various human cells, in which cells were incubated with different concentrations of C-dots to test the cell viability (48).

Li et al. synthesized C-dots following the solvothermal method using o-phenylenediamine in which was mixed with ethanol and heated at 180 °C for 12 hours, the synthesized C-dots exhibit an average diameter size of 8 nm and multicolored emission (90). Li et al. tested the synthesized C-dots against fibroblast cell line that was isolated from a mouse NIH/Swiss embryo (NIH-3T3), they grew the cells in a 96-well plate for 24 h at 37 °C and 5% CO₂ so they can adhere, then they added different concentrations of C-dots (5 µg/ml, 10 µg/ml, 20 µg/ml, and 40 µg/ml), then incubated at 37 °C and 5% for 12 hours, 24 hours, and 48 h (90). They used cell counting kit 8 (CCK-8) assay to test the viability by measuring the absorption value at 490 nm, the results show the longer the incubation time the lower the cell viability yet, the minimum cell viability is 90% which is considered very low toxicity. Furthermore, the higher the concentration the lower the viability level, as the 5 µg/mL concentration show nearly 100% cell viability as shown in Figure 32 (90).

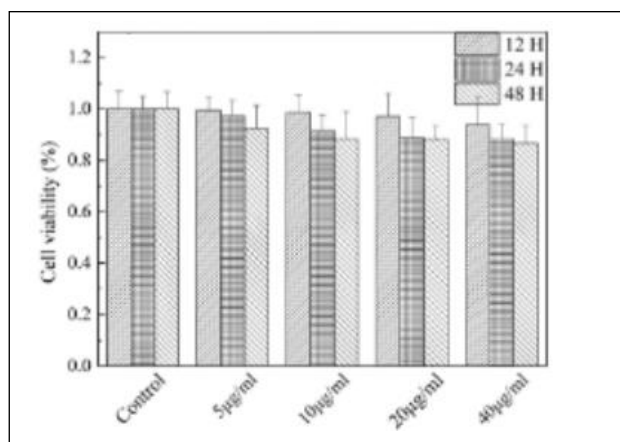


Figure 32: Cell viability of NIH-3T3 cells incubated with C-dots at different concentrations for 12 h, 24 h and 48 h (90).

Wang et al. synthesized C-dots following the laser ablation method using pyrrole as the source of carbon then functionalized the C-dots with O,O'-bis(3-aminopropyl) polyethylene glycol (PEG1500N), the synthesized C-dots exhibit a diameter size of 10 nm. They tested the toxicity of the synthesized C-dots against human colon adenocarcinoma grade II cell line (HT-29) in a comparison with the PEG1500N using MTT assay (91). They incubated the HT-29 in a 96 well plate for 24 h at 37 °C and 5% CO₂, then added 0.1 µg/ml, 1 µg/ml, 5 µg/ml, 25 µg/ml, and 25 µg/mL of the synthesized C-dots, incubated for 24 h at 37 °C and 5% CO₂, after that the MTT assay was done, the same process was done in another 96 well plate for the PEG1500N instead of the C-dots. The results show quite high cell viability especially at low concentration of the C-dots, reduced as the concentration increases yet the minimum viability levels are around 90%. Although at lower concentrations the C-dots show slightly less cell viability than the PEG1500N, at the highest concentration the C-dots show better viability levels as shown in Figure 33 (C-dots in black, and PEG1500N in white) (91).

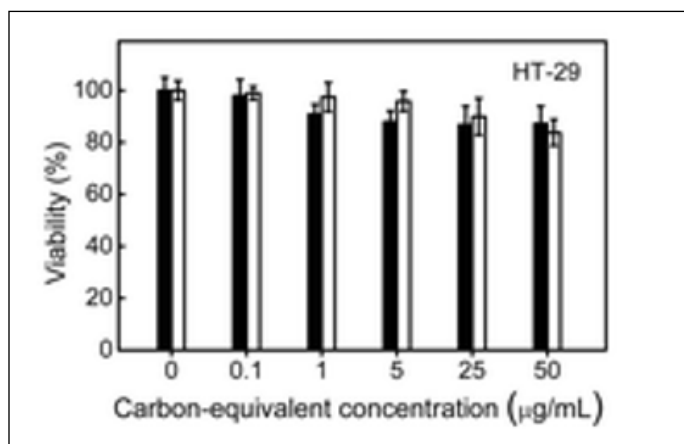


Figure 33: Cell viability of HT-92 cells incubated with C-dots (black), and PEG1500N (white) at different concentrations for 24 h (91).

Ray et al. synthesized C-dots following the acid oxidation method using carbon soot as the source of carbon in which was oxidized by HNO_3 , the synthesized C-dots exhibit a narrow distribution particle size of 2-6 nm, with QY = 3% and green PL properties (92). The results shows that the synthesized C-dots successfully penetrate the hepatocellular carcinoma cells, and the cell viability is 90-100% after incubation 24 h of incubation with various concentrations reaches up to 0.5 g/ml, which is quite high concentration, and it is about 1000 times the required concentration for bioimaging (92).

1.4.5.2 Biocompatibility

It has been proven that the C-dots are considered as a class of nanoparticles that have a very low toxicity levels, it is important to investigate the fate of the C-dots after they have been administered to the cells and assess the biocompatibility. A study by Wang *et al*, was done to synthesis C-dots and evaluate the safety of the synthesized C-dots. They synthesized C-dots following acid oxidation method using carbon soot as the source of carbon and HNO_3 as the oxidation agent, in which were heated at 120 °C for 18 hours, the synthesized C-dots exhibit a narrow size distribution of 4-8 nm and blue PL properties (93). They did different *in vivo* tests in

which they used 64 Wistar rats (weight 177 to 224 g), they were divided into three groups and each rat was injected a single intravenously injection via the tail with 0.2 mg/kg (group A), 2 mg/kg (group B), and 20 mg/kg (group C), and a control group of rats were injected with 0.9% normal saline. Blood samples were taken from each rat at day 1, day 3, day 7, and day 28 for hematology test and biochemical test (which will be discussed after the hematology test), in which they tested the white blood cells, red blood cells, platelets, lymphocytes, neutral cells, other cells, hemoglobin, and hematocrit (HCT) as shown in Figure 34.

The results show that the parameters levels are normal in a comparison to the control group, except for the HTC level after 7 days of exposure to 0.2 mg/kg with ($p < 0.05$) (93).

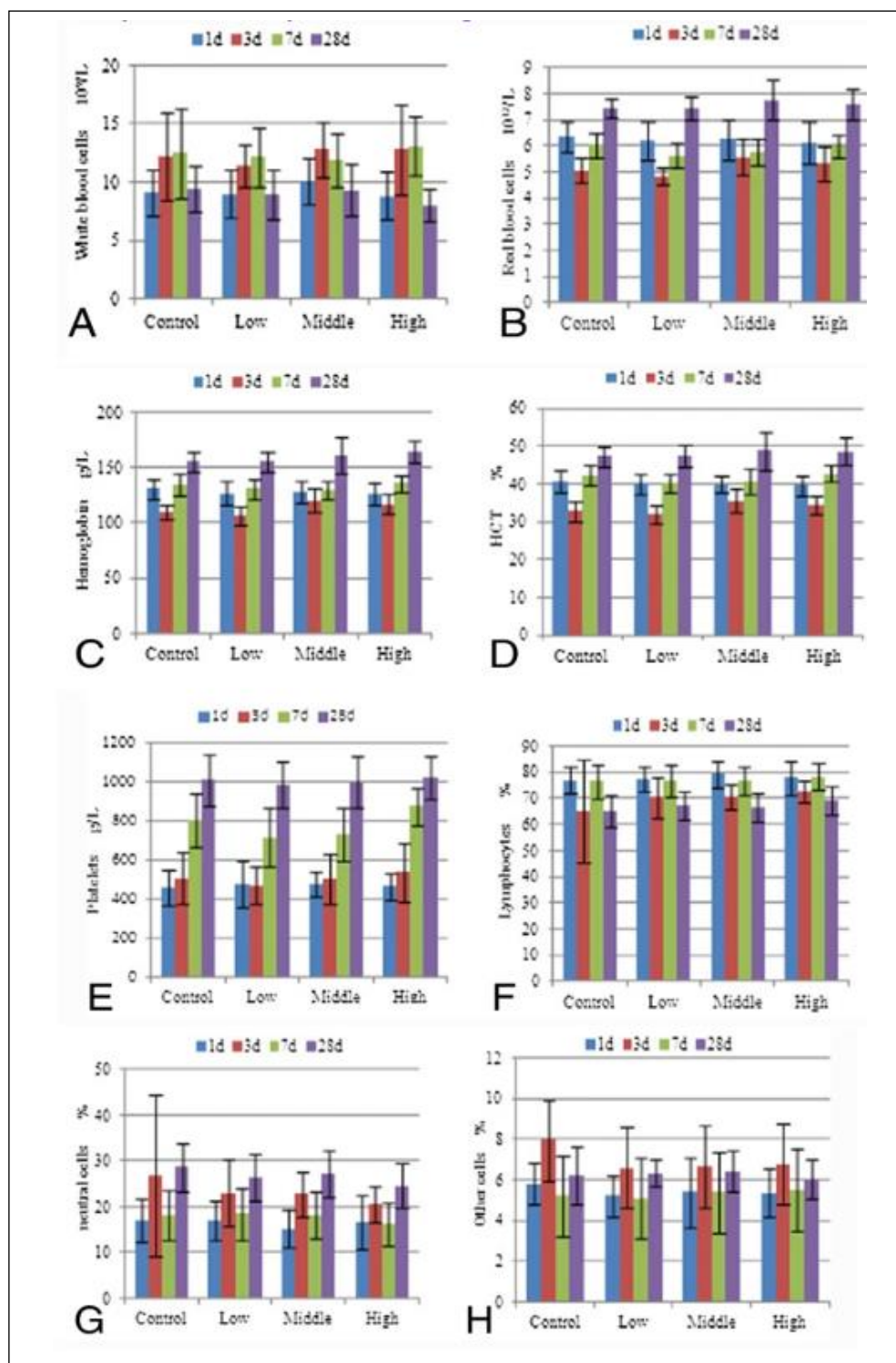


Figure 34: Blood hematology analysis of rats treated with C-dots at doses of 0.2, 2, and 20 mg/kg, samples obtained in 1, 3, 7 and 28 days of exposure. (A) White blood cells, (B) red blood cells, (C) hemoglobin, (D) HCT, (E) platelets, (F) lymphocytes, (G) neutral cells, and (H) other cells (93).

Furthermore, biochemical tests were done in order to investigate any possibility of subacute C-dots poisoning occurring because if the C-dots cause subacute poisoning, the biochemical parameters should change. The biochemical parameters tested were; glutamic pyruvate transaminase (GPT), glutamic oxaloacetic transaminase (GOT), urea, cholesterol, triacyl glyceride (TG), blood glucose, creatinine (Cr), total protein, and albumin (93). The results shown in Figure 35 shows that after one day of exposure the TG levels decreases ($p < 0.01$) in the group injected with 20 mg/kg in a comparison to the control group. Yet, after 30 days all the biochemical parameter seems to be in normal levels throughout various times in a comparison to the control group, as shown in Figure 35.

Despite the statistical differences in the hematological parameters and the biochemical parameters of the injected groups, compared to the control group, the differences are not biologically significant (93).

Moreover, histopathological analysis was done to the rats that were injected with 20mg/kg, by harvesting their organs, in which includes the hearts, the livers, the spleens, the lungs, the kidneys, the brains, the stomachs, the intestines, the ovaries, and the testes. The histopathological tests show that there no obvious organ damage, and no histopathological abnormality in the tested tissues, as well as no lesion were observed. Furthermore, the cardiac muscle fibers structure in the test group were normal in a comparison to the control group. The hepatic sections show no steatosis, no necrosis, and no hydropic degeneration in addition to normal liver lobule with few collagen fibers located in the portal area and the central vein. The splenic capsule is completed with clear red and white pulps. There were no signs of infection in the lungs and the structure of the lungs are normal. The kidneys' structure was normal, and the glomerular structure was easily distinguished. The intestine shows no bleeding, and no differentiation was observed in the gastric mucosa, Figure 36 shows the histopathological analysis of the injected rats in a comparison with the control group (93). In conclusion, Wang et al. had concluded that the synthesized C-dots have not shown any significant toxicity to mice and rats. They also shown that they have not caused any abnormalities or lesions in the organs of rats that were treated with the C-dots. In addition to no gene toxicity, which make the

synthesized C-dots good candidate to be used in *in vivo* bioimaging due to the good compatibility (93).

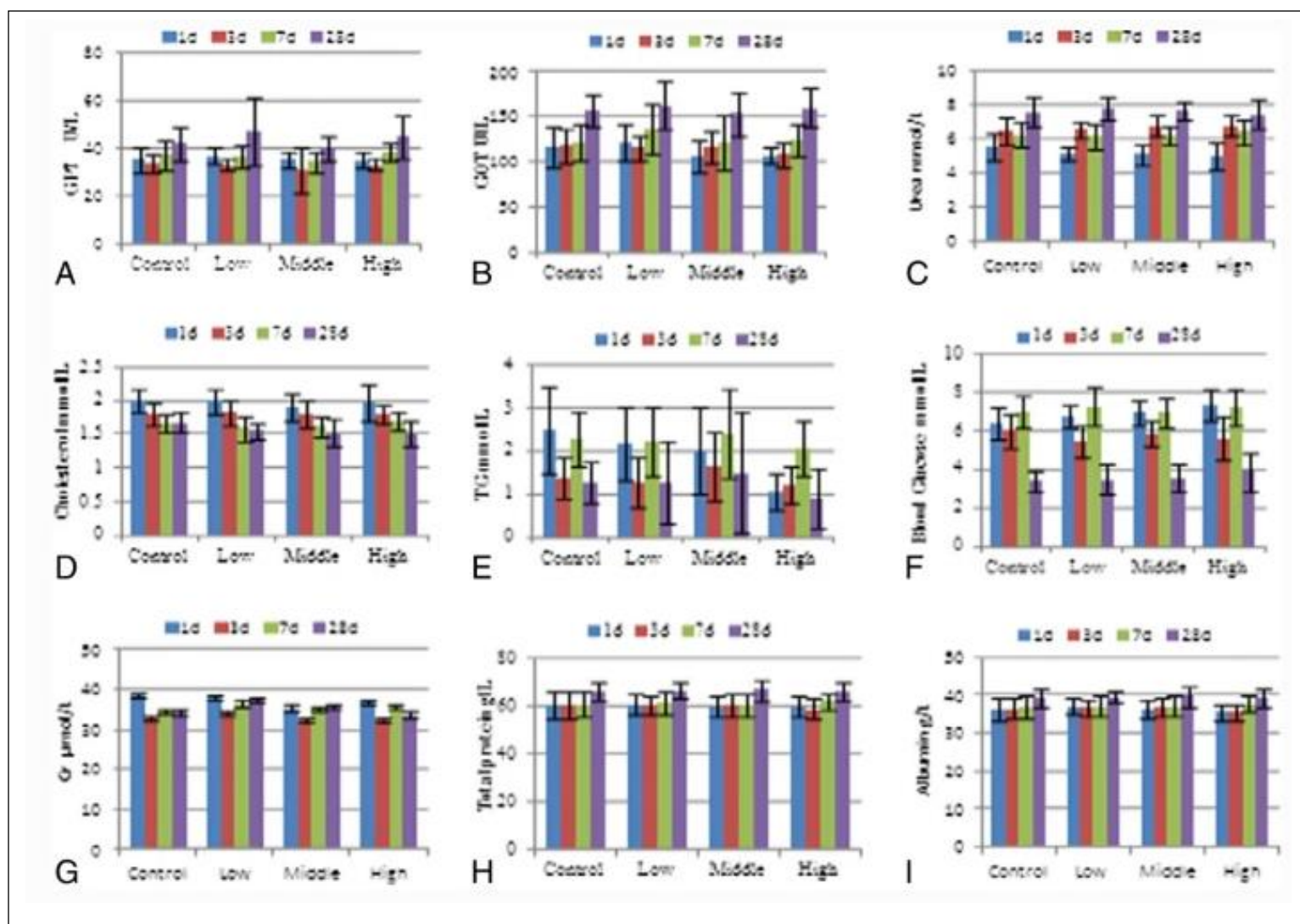


Figure 35: Changes of the blood biochemical data of rats treated with C-dots at doses of 0.2, 2, and 20 mg/kg and samples obtained in 1, 3, 7, and 28 days of exposure. (A) GPT, (B) GOT, (C) urea, (D) cholesterol, (E) TG, (F) blood glucose, (G) Cr, (H) total protein, and (I) albumin (93).

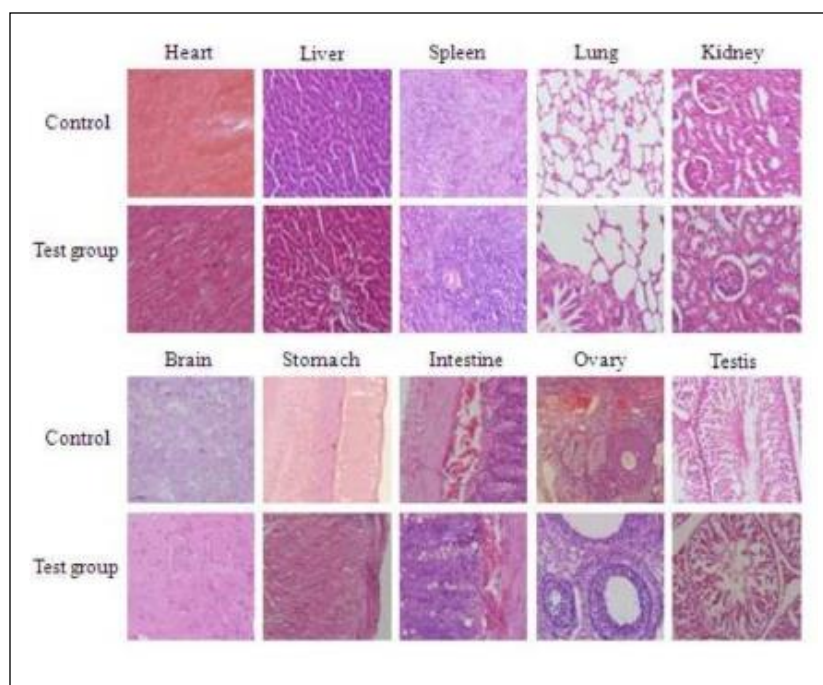


Figure 36: Results of histopathological analyses of rats were treated with C-dots at the dose of 20 mg/kg at 30 days of exposure (93).

The US food and drug administration (FDA) has demanded that any agents injected into the human body for diagnostic purposes should completely cleared after a reasonable time of the injection, and they should not be accumulated in the body, as well as minimize the exposure time as much as possible (94).

Huang et al. reported a study that assessing the clearance of the C-dots, in which they synthesized C-dots following the laser ablation method where they used solid precursor which was obtained by applying a hot pressure at a mixture of graphite and cement, the mixture was backed then annealed under argon flow (95). The synthesized C-dots exhibit an average diameter size of 3 nm with λ_{em} near the infrared region. They assessed the clearance of the C-dots by studying the effect of injecting the C-dots via three different routes, intravenous (i.v.), subcutaneous (s.c.), and intramuscular (i.m.). They used 3 groups of athymic nude mice, group one was injected with 50 μ L of 2.5 mg/kg of C-dots in a vein the tail (i.v.), group two was injected with 50 μ L of 2.5 mg/kg of C-dots under the skin of left leg (s.c.), and group three was

injected with 50 μL of 2.5 mg/kg of C-dots in the left muscle (i.m.). 5 μL of blood samples were obtained from tail vein at different time slots (1, 2, 5, 10, 20, 25, 30, 45, and 60 minutes) in Eppendorf tubes contain μL of heparin to be analyzed by measuring the fluorescence using Maestro all optical imaging system (95).

Figure 37 shows the fluorescence of the blood after collection, the clearance rate of C-dots is different with in each injection route, the i.v. injection route has dramatically decreased (Figure 37 A top, and B) while the s.c. route has increased with time then plateaued after 20 minutes (Figure 37 A middle, and B), and the i.m. injection route has increased up to 30 minutes then plateaued (Figure 37 A bottom, and B) (95). In conclusion, the C-dots are good candidates for biomedical applications, due to the fast clearance from the blood as determined by the FDA as mentioned above (94).

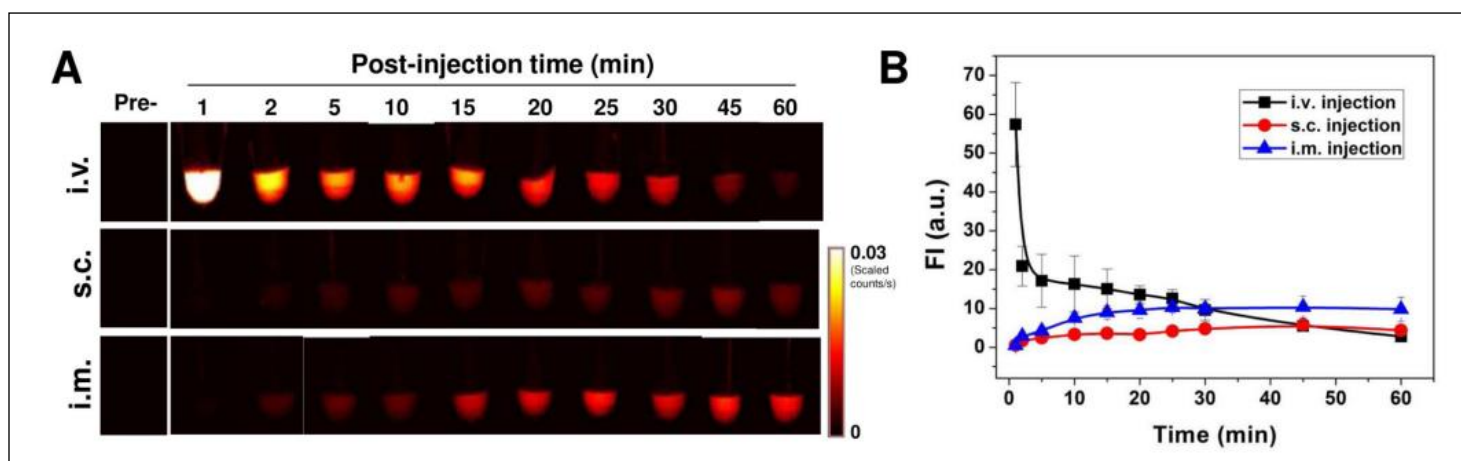


Figure 37: Blood samples of mice were injected with C-dot synthesized by Huang et al., after three injection routes obtained in different times; (A) (Top) i.v. injection, (Middle) s.c. injection, and (Bottom) i.m. injection. (B) Fluorescence time-activity curves derived from signals in (A) (95).

1.4.6 General applications of C-dots

1.4.6.1 Photocatalysts

A photocatalyst is any material that has the ability to speed up a chemical reaction after photo excitation (96). Due to the optical properties of the C-dots, the electron transfer properties, and the ability to coupling with other materials such as titanium oxide (TiO_2) (97), and Fe_2O_3 (98), make them good candidates for photocatalysis applications (96).

The C-dots can work in two different mechanisms, the first mechanism is demonstrated in Figure 38 a, in which the C-dots can be good photocatalyst via acting as acceptors of charge carriers from the photoexcited semiconductor, so the recombination of the electrons and the holes will be suppressed, or slowed resulting in an increase in the possibility of the chemical reactions as well enhancing the photocatalytic properties. The second mechanism demonstrated in Figure 38 b, the C-dots can act as a photosensitizer in which the C-dots absorb the light then transfer a photogenerated electron to an attached semiconductor which is normally absorb only in the UV region, which resulting the catalytic action of the composite to extend into the visible region (96), (99).

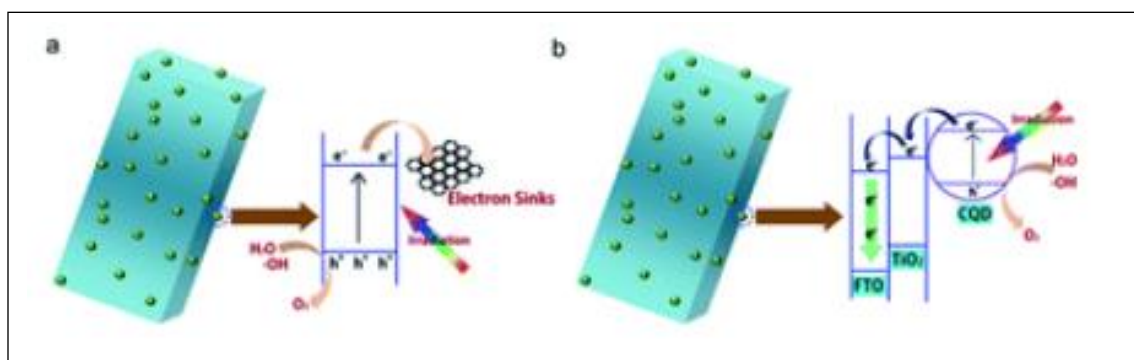


Figure 38: Possible strategies of C-dots (yellow spheres) in a photocatalytic application, a) as electron acceptor (electron sink) from the semiconductor, and b) as electron donor creating a cascade of electrons from C-dots lowest unoccupied molecule orbital to semiconductors (99).

Cao et al. used functionalized C-dots as photocatalyst for CO₂ conversion and water splitting. They functionalized the C-dots with a coat of gold or platinum and used them to collect visible photons (100). The role of C-dots can be summarized by the photoexcitation of the surface passivated C-dots cause charge separation which resulting surface confined electrons and holes (101). The bright fluorescence λ_{em} can be enhanced to radiative recombination on the surface of the particles can be quenched by electron acceptors and electron donors (101). In addition, the gold or platinum coating diminishes the emission, because they designed to soak up the surface confined electrons resulting disrupting of the radiative recombination. As a result, the functionalized C-dots seem to serve the harvesting of the visible photons to initiate the photoreduction process, alongside the particle surface defect driving the charge separation via trapping the separated electrons and holes (101).

They prepared an aqueous solution functionalized C-dots, in which was added to an optical cell in the photolysis setup, then the solution was purged with CO₂ gas until it has been saturated at room temperature. The solution then was photo irradiated using visible light at 425-720 for 5 h until the reduction reaction results formic acid in form of volatile photoproduct in the aqueous solution which was simply collected by distillation.

Cao et al. did the same experiment with the same condition but without purging the functionalized C-dots with CO₂, as they designed this experiment to split hydrogen in the water. The only difference in this experiment is that they connected the top of the sealed optical cell into H₂ detector containing an aqueous solution of CuSO₄ as shown in Figure 39. The color of the CuSO₄ had changed and precipitations in the H₂ indicator was formed due to the reduction of the Cu⁺² to Cu⁺, then Cu as a result of the formation of H₂ (100).

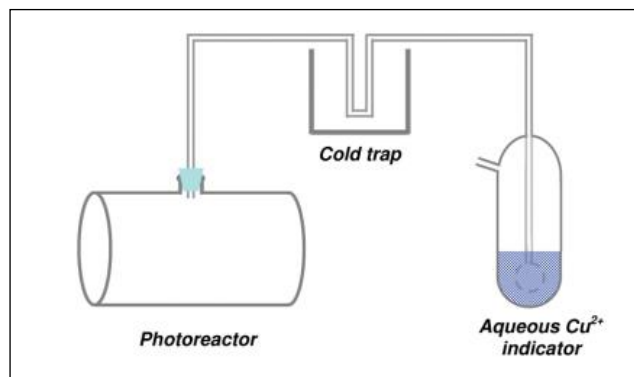


Figure 39: Schematic diagram of the setup used for the detection of photo catalytically generated H₂ (100).

Li et al. used C-dots as photocatalyst for the degradation reaction of methyl blue, they followed the electrochemical method to synthesis C-dots using two graphite rods as the anode and the cathode with a solution of ethanol, water, and NaOH as the electrolyte. The synthesized C-dots exhibit narrow distribution size of 1.2-3.8 nm, with interesting up conversion PL properties (102). As mentioned before, the C-dots have the ability to couple with different materials, herein Li, et al. attached the C-dots to TiO₂ to produce TiO₂/C-dots composite photocatalyst. When the C-dots absorb the visible light, it'll emit shorter wavelength energy at 325-425 nm, due to the up-conversion behavior in which will excite the TiO₂ to form electron/hole (e⁻/h⁺) pairs, then the (e⁻/h⁺) pairs will react with the adsorbed oxidant/reducer in which is O₂/OH⁻ to form oxygen radical such as ·O²⁻ or ·OH, and the oxygen radical will cause degradation of the methyl blue (102). It has been reported that the TiO₂/C-dots can be used in photocatalytic degradation of organic pollutant and dyes such as methylene blue (103).

1.4.6.2 Organic photovoltaics devices

The sun provides the surface off the earth with about 120,000 terawatts, which is nearly equal to 6000 folds of the world's consumption of energy (104). It is believed that the solar energy is a sustainable, clean, abundant, and ecofriendly source of energy which could be stored and

converted into consumable energy via organic photovoltaics effect, which based on converting the illumination of a material to provide an electric current using the p-n junction (105). Due to the PL properties of the C-dots and the other properties such as; tunable color, high photostability, light weight, very good electron acceptor materials, and low cost, are considered as good candidates for the organic photovoltaics applications (106). It has been demonstrated that the power conversion efficiency of the tandem solar cells can reach up to 17% in a comparison to 14% in the state of the art (105).

The conventional solar cells are composed of a cathode which can be such as Al, an active doner/ acceptor layer in which can be polymers such as poly(3-hexylthiophene) (P3HT), and fullerene derivative (6,6)-phenylC61 butyric acid methyl ester (PCBM), the problem with this layer is that the organic semiconductor limits the size of it in which resulting an undesirable charge recombination that cause low power conversion efficiency (107). The conventional solar cells also composed of a hole extraction layer (HEL) which usually initialize the facilitation of the charge separation and avoid interfacial recombination within the cell to provide service with high level of performance, the HEL is commonly made of Poly(3,4-ethylenedioxythiophene):poly(styrene sulfonate) (PEDOT:PSS), and finally an electron transfer layer made of ITO/FTO on a glass which acts as a buffer layer to improve the sustained separation of charges and subsequent extraction of charge carriers as shown in Figure 40 A (105).

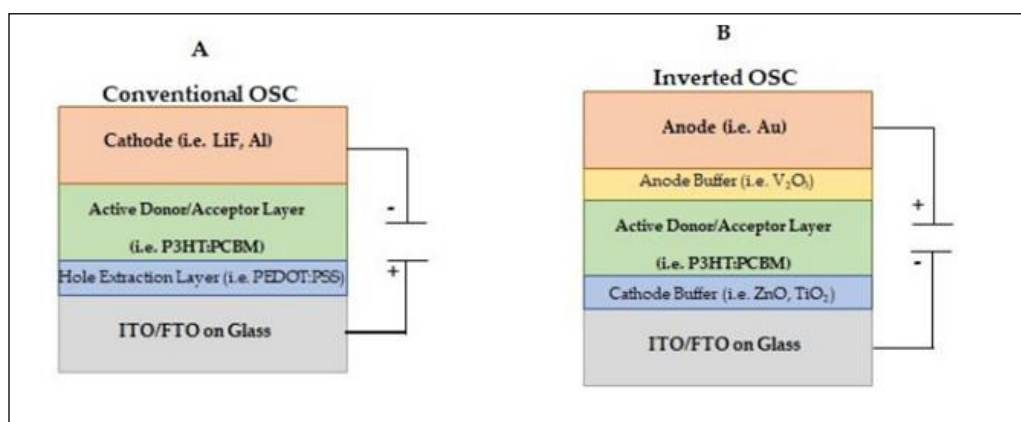


Figure 40: Schematic illustration of (A) conventional and (B) inverted organic solar cells (OSC) (105).

Another class of solar cells is the inorganic solar cells or as commonly known silicon solar cells, based on using p-n junction with energy conversion efficiency of 24% (108), formed on a 300-500 μm thick p type silicon layers (109). Phosphorous is usually used as the n type dopant, diffused on to the p type wafer resulting a thin emit layer (109). Furthermore, the diffusion of the holes to the n region and electrons to the p region resulting in a non-equilibrium status, in which create the space charge region between the p and the n type semiconductors as shown in Figure 41. The electron-hole pairs formed when the incident photons have an energy greater than the semiconductor band gap ($h\nu > E_g$), the asymmetry in the device structure driving the flow of electrons towards the n type region and the holes are collected at the p type region (109). Due to the existence of the electrons and the holes in the same bulk volume, photovoltaic performance of the device is sensitive to the bulk properties of the materials. A disadvantage of the silica solar cells is that they are expensive due to the need to use a defect free semiconductor for efficient carrier collection (109).

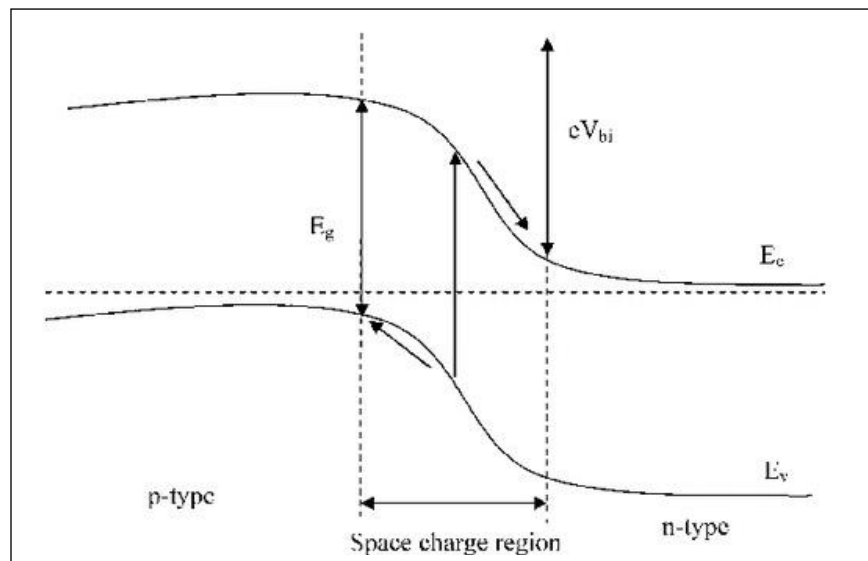


Figure 41: Energy band diagram of p-n junction solar cell (109).

More recent research was done to improve the efficiency of the solar cells in which includes inverting few parts as shown in Figure 40 B, the inverted called dye sensitized solar cells (DSSC) which are composed of a sensitized photoelectrode (dye-TiO₂ or dye-ZnO/sensitizer), electrolyte (I³⁻/I⁻), and counter electrode (CE) (105). The DSSC offers way better performance than the conventional solar cells, yet they need very long synthesis time because they require a Ru metal center which is very expensive and replacing it with lower price material is required (107).

On the other hand, the C-dots can provide solar cells with way better performance because they can replace the sensitized photoelectrode dye (D-dots- TiO₂) due to the remarkable photoluminescence properties they exhibit, and they also can act as the electron donor/acceptor agent due to their properties (110). Furthermore, the tunability, the high quantum yield, the photostability, the low cost and the ecofriendly properties of the C-dots make them a very good candidate in the production of the organic photovoltaics applications in order to produce more sustainable consumable energy (105).

1.4.6.3 Latent printing

Due to the significant PL properties of the C-dots in addition to the high quantum yield, the solubility and the reality that they are non-toxic, made them good candidates for use in printing application as an ink.

Wang et al. synthesized C-dots using chicken eggs as the source of the carbon which was carbonized using low temperature plasma beam with high energy for 3 minutes (111). The synthesized C-dots exhibit a narrow diameter size distribution of 2-5 nm, with QY = 7% and bright blue fluorescence λ_{em} under $\lambda_{ex} = 302$ nm. To produce the ink, 10 g of aqueous solution of the C-dots was blended magnetically with 6 g of glycol to form a homogeneous solution, the solution then encapsulated into the ink cartridge of the inkjet printer to be used at room temperature, the use of helps in preventing the clogging of the nozzle by acting as humectant. Figure 42 shows the mechanism of using the fluorescent C-dots ink in the inkjet printer, in

which an electrical field applied to the piezoelectric materials resulting change in their shape which create a pressure pulse and activate the connecting pump to inject fluorescent C-dots ink droplets out of the nozzle (111).

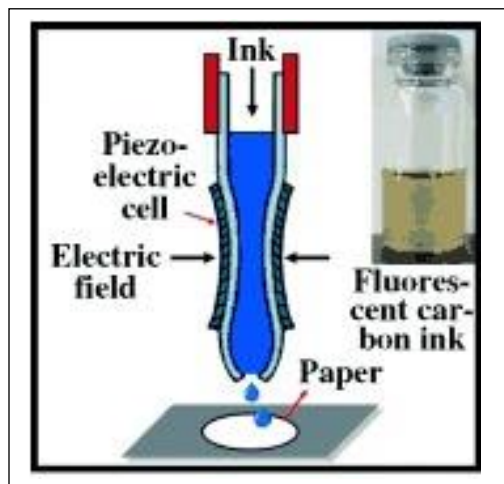


Figure 42: Schematic illustration of piezoelectric inkjet printing. Inset: the as-prepared fluorescent C-dots ink (111).

The optimal surface tension of the fluorescent C-dots ink is 44 mN/m, and the viscosity is 3.51 cP as well as high electrical conductivity about 6.76 S/m which making them promising materials for optoelectronic devices (111). The synthesized fluorescent C-dots ink was used in two methods, the first is shown in Figure 43 a, which a fluorescent image of blue and white porcelain on a paper substrate in 20 min. The other process is considered as cheaper and simpler one, as silk screen was used to create fluorescent patterns.

Furthermore, they used sodium alginate (SA) as a matrix due to its affinity to the C-dots in which the C-dots/SA was screened through woven mesh onto a paper substrate via extrusion using scraper blade which was transferred as a bright blue emitting pattern as shown in Figure 43 b. The fluorescent C-dots ink is also showing success with the open-on-paper technique as shown in Figure 43 c and 41 d (111).

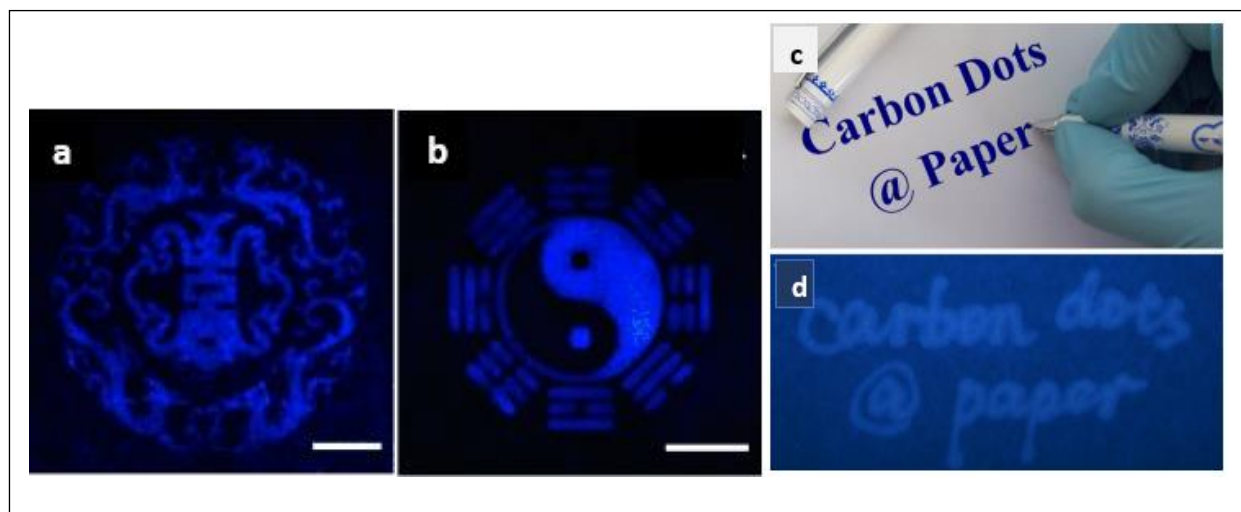


Figure 43: a) Photograph of the fluorescent pattern representing blue and white porcelain by inkjet printing, b) pattern created by C-dots/SA ink, c) Illustration of the pen-on-paper process of writing words “carbon dots @ paper”, and d) Digital photos of “carbon dots @ paper” (111).

Zhue et al. synthesized C-dots following the hydrothermal method by using CA as the source of carbon in which was mixed with ethylenediamine, and the mixture dissolved in deionized water, then the solution was transferred into an autoclave which was heated at 300 °C for 5 h (112). The synthesized C-dots exhibit an average diameter of 5 nm, with blue PL properties and a QY = 58% (112).

The printing process was done by using a 1 µg/mL of colorless C-dots solution and a commercially available papers in which the C-dots are easily adhere on them, the C-dots solution were injected into a vacant cartridge of a commercial inkjet printer. The very low concentration of the C-dots was enough to produce strong fluorescence with obvious words under the UV lamp as shown in Figure 44 a. It has been noted that the increase in the concentration of the C-dots, increase the intensity of the fluorescence as shown in Figure 44 b, in which can be used to produce different colors using different concentrations of C-dots as shown in Figure 44 c (112).

Furthermore, mixing C-dots with some polymers such as polyvinyl alcohol resulting a composite ink (PVA/C-dots) with multiple colors under UV, blue and green light excitation as shown in

Figure 45 a. Finally, the photoluminescence intensity did not change after a prolonged, exposure to the UV, as shown in Figure 45 b, furthermore the printing patterns and the prepared composites retained the stability after four months at room temperature (112).

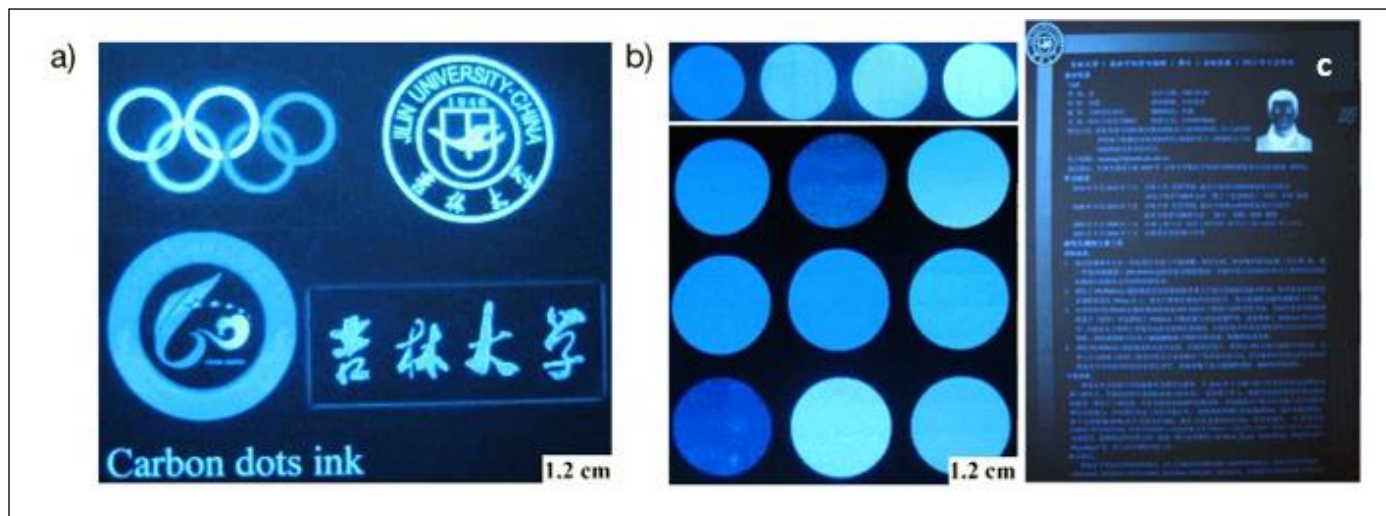


Figure 44: a) Different graphic patterns on paper using C-dots as ink, under the UV, b) Inks in multiple colors, made by different C-dots concentrations, and c) different graphic pattern obtained by C-dots ink creating a multicolor effect (112).

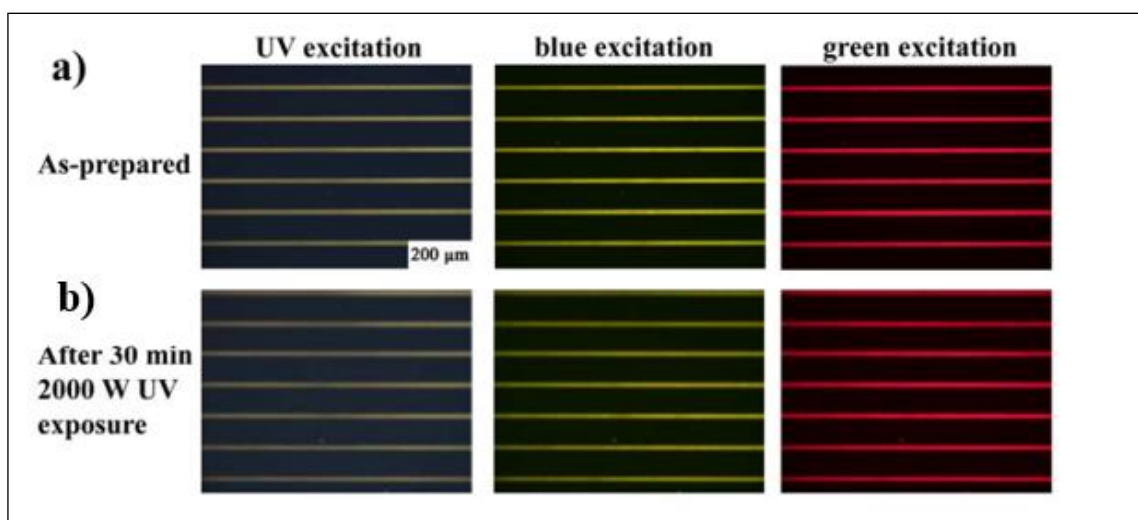


Figure 45 Fluorescence microscopy images of PVA/C-dots a) at 0 minutes time, and b) after 30 minutes with exposure to 2000 W UV (112).

1.4.6.4 Fingerprint development

Fingerprints are marks and signs in form of lines and curves that caused by pressing the figure on a solid surface due to the sweat and oily sebum that is naturally produced by the body, which are unique for each person that makes them very important in identification a person in forensic examination, law enforcement, medical diagnosis, and access security control (113).

In 2015, Fernandes et al. reported using the C-dots powder in latent fingerprint application for the first time (114), they synthesized C-dots following the thermal decomposition method using CA as the source of carbon in which was mixed with EA and heated at 180 °C for 30 min, the synthesized C-dots exhibit an average diameter of 19 nm with multicolored λ_{ex} dependent emission PL properties and QY = 50% (7).

Fernandes et al. used the C-dots powder that homogeneously dispersed on silica to dilute the C-dots powder in which to prevent the quenching effect that may create by the C-dots, a (0.7 wt%) of C-dots/ silica powder was applied using a brush on a glass slide with a fingerprint on, the florescence microscope images show bright obvious fingerprints as shown in Figure 46 a, b, and c, with excitation using different wavelengths (violet, blue, and green (114).

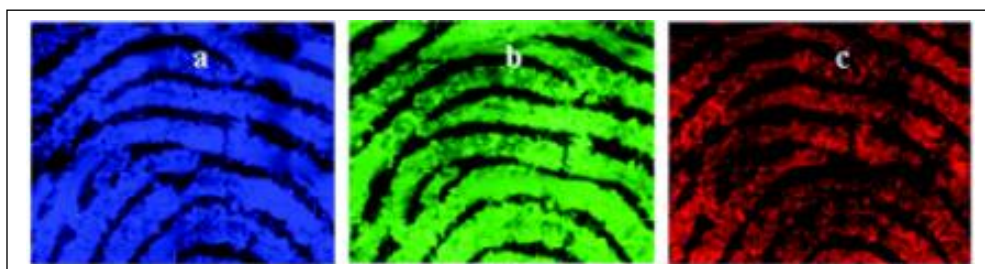


Figure 46: Fluorescence microscopy images of fingermarks developed with (0.7 wt% C-dot) on a glass slide under a) violet, b) blue and c) green λ_{ex} . The magnification is 100 \times (114).

Yadav et al. synthesized C-dots following the hydrothermal method using biomass (pomegranate peels) as the source of carbon, in which the pomegranate peels were dried by heating at 150 °C for 12 hours, following by addition of sodium hydrochloride solution to be oxidated for 6 h then the mixture was transferred into an autoclave to be heated at 180 °C for 12 h (115). The synthesized C-dots exhibit an average diameter size of 500 nm with blue PL properties. Titanium oxide was used for coating C-dots to produce a stable dispersion of nanoparticles in which proven to be useful in many applications such as; photography, catalysis, biological labeling (115). A group of C-dots were coated with titanium oxide by single coated (C-dots@TiO₂ I), a second group of C-dots were coated with double coated (C-dots@TiO₂ II), and a third group of C-dots were coated with triple coated (C-dots@TiO₂ III), which will be used for fingerprinting (115).

Yadav, et al. tested the stability of the C-dots@TiO₂ as fingerprint detector by creating a fingerprint on an aluminum foil surface, in which the C-dots powder were brushed on the aluminum foil and tested in a comparison with the TiO₂, I coat of C-dots@TiO₂, II coats of C-dots@TiO₂, and III coats of C-dots@TiO₂ as shown in Figure 47 (115).

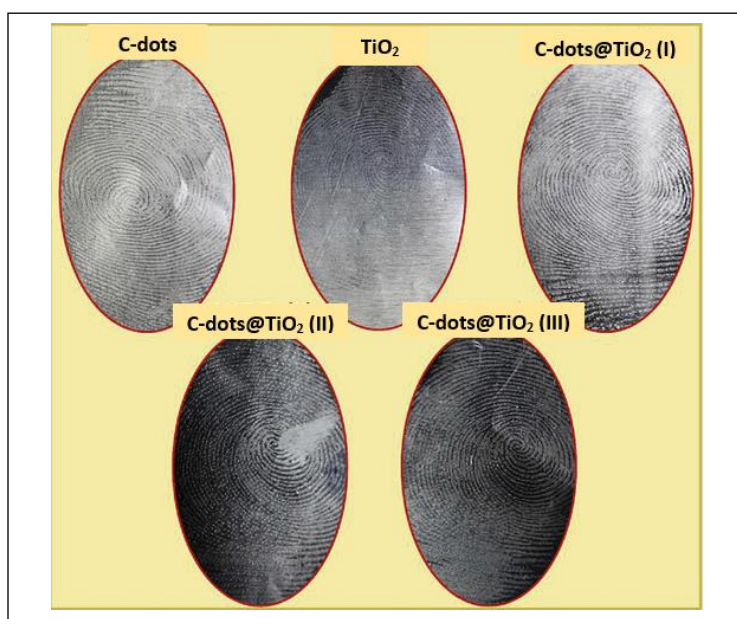


Figure 47: Latent fingerprints on aluminum foil surface developed using C-dots, TiO₂, C-dots@TiO₂ (coat-I), C-dots@TiO₂ (coat-II), and C-dots@TiO₂ (coat-III) respectively (115).

By observing Figure 47, the latent fingerprint of C-dots@TiO₂ (III coat) obtain well defined characters on most of the selected area, with good contrast which showing clear pattern and significant brightness which make them good candidate for detecting fingerprints using brushing method in forensic investigation science (115).

1.4.7 Biomedical applications of C-dots

1.4.7.1 Biochemical sensor

The field of sensing has been attracting a lot of interest and has developed many chemical and biological sensors depending on their florescence properties as well as the surface functional groups (116). Therefore, C-dots considered a good candidate for the chemical/ biological sensors applications because of the effect on the florescence properties of the C-dots, which appear in the form of quenching or enhancement when they interact with chemical substances (116), in addition to their biocompatibility and the ability to penetrate cells (48).

Lu et al. synthesized C-dots following the hydrothermal method using an ecofriendly and low-cost source of carbon which was pomelo peel, to produce water soluble C-dots with blue PL properties and QY = 6.9% (117). They used the synthesized C-dots for fluorescent detection of Hg⁺² and thiol such as cystine (Cys), in which they discovered that when the C-dots interact with Hg⁺² the florescence quenches. On the other hand, the Cys proves to restore the florescence properties of the C-dots which was obvious by interacting the florescence quenched C-dots with thiol resulting enhancement in the florescence properties resulting a “Turn-on” (created by the Hg⁺²) and “Turn-off” (created by the Cys) effect as shown in Figure 48, in which the photoluminescence graph shows that the C-dots have high intensity (black peak), the C-dots after interacting with Hg⁺² (red peak), and C-dots after interaction with Cys (blue peak). The sensitivity of the C-dots as sensor is high as the florescence quenching effect occurs by using very low concentration of Hg⁺² which is only 0.23 nM (117).

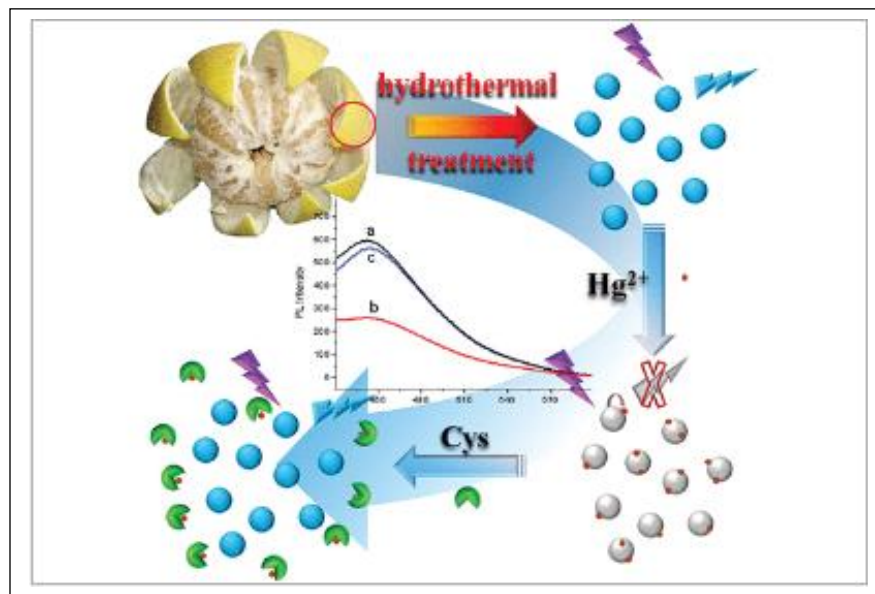


Figure 48: Schematic representation of an Hg^{2+} /Cys biosensor based on C-dots synthesized by Lu et al. The photoluminescence analysis shows the λ_{em} of: a) C-dots, b) C-dots after interaction with Hg^{2+} , and c) C-dots after interaction with Cys (117).

Dong et al. synthesized C-dots following the hydrothermal method using CA, which was mixed with branched polyethyleneimine, dissolved in water and at 200 °C for 3 h (118). The synthesized C-dots exhibit an average diameter size of 6.2 nm with blue λ_{em} under $\lambda_{\text{ex}} = 365$ nm and a QY = 42.5%.

Dong *et al*, used the synthesized C-dots as a chemical sensor for Cu^{+2} , they observed that the Cu^{+2} attached to the C-dots by being captured by the amino groups on the surface of the C-dots resulting an absorbent complex on the surface which causes strong quenching in the fluorescence of the C-dots (119). This method is rapid and sensitive, it can detect the Cu^{+2} with as low concentration as 6 nM, the mechanism is shown in Figure 49.

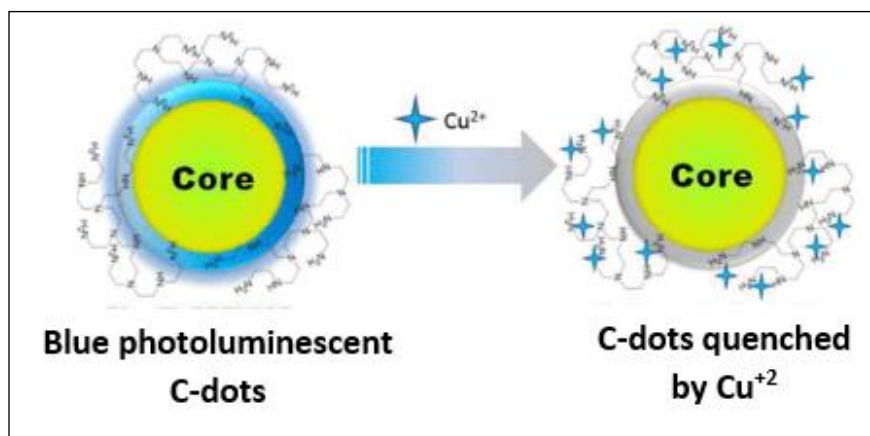


Figure 49: Schematic illustration of a Cu^{2+} biosensor using C-dots (119).

A development in using C-dots for detecting Cu^{2+} was reported by Zhu et al., in which they used the C-dots as biosensor for the Cu^{2+} in intracellular activities (120). They synthesized C-dots following the electrochemical oxidation method by using graphite rods as the anode and the cathode, with NaOH dissolved in ethanol/water (99.5:0.5) as the electrolyte and current intensity 40 mA cm^{-2} for 12 h. The synthesized C-dots exhibit an average diameter size of 5 nm with blue λ_{em} when excited at 400nm and QY = 10%.

They assessed the biosensor activity of C-dots using HeLa cells in which were incubated with phorbol-12,13-dibutyrate (PDBu, a compound that increase the endocytic activity, in which represents the activity of the cells to uptake particles and molecules, i.e. increase the uptake of Cu^{2+} by cells) in Phosphate Buffered Saline (PBS) (pH7.4) for 2 h at 37°C and 5% CO_2 , then 0.05 mg/mL of C-dots were added to the HeLa, the cells were imaged using confocal microscope before and after the enhancement of the endocytic activity and at different λ_{ex} as shown in Figure 50 (120).

As shown in Figure 50 (a) the C-dots managed to penetrate the cells. In image 50 (b), the cells were tested before the enhancement of the endocytic activity (low level of Cu^{2+}) and show a strong λ_{em} in a comparison to Figure 50 (c) which was taken after the enhancement of the

endocytic activity (high level of Cu^{2+}). Figure 50 (d) represents the integrated intensity from 480–580 nm over the integrated fluorescence intensity from 600–680 nm, the values are the mean ratio generated from the intensity from three randomly selected fields in both channels. Figures 50 (e) and (g) represent the images of HeLa obtained from 480–580 nm before the enhancement of the endocytic activity (low level of Cu^{2+}) and after the enhancement of the endocytic activity (high level of Cu^{2+}) respectively, in which (g) is dimmer than (e) due to the quenching effect of Cu^{2+} . The image (f) shows the HeLa cells before the enhancement of the endocytic activity (low level of Cu^{2+}) obtained from 600–680 nm, in which is brighter than (h) which is after the enhancement of the endocytic activity (high level of Cu^{2+}) due to the quenching effect of Cu^{2+} . Therefore, the C-dots is considered as a good candidate for the biosensor applications (120).

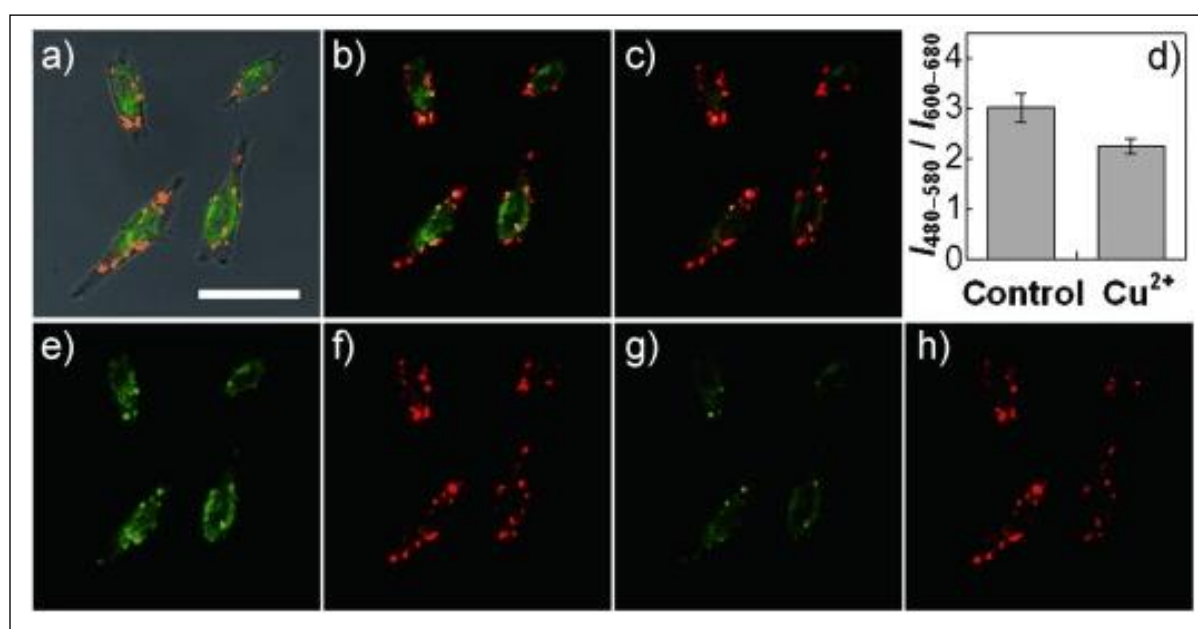


Figure 50: a) Overlay of bright-field and fluorescence images of HeLa cells incubated with 0.05 mg/ mL of C-dots. b) confocal fluorescence images of HeLa cells before the enhancement of the endocytic activity, and c) after the enhancement of the endocytic activity. d) A bar graph showing the integrated intensity from 480–580 nm over the integrated fluorescence intensity from 600–680 nm. e) the confocal fluorescence images obtained from 480–580 nm before the enhancement of the endocytic activity, and g) after the enhancement of the endocytic activity. f) the confocal fluorescence images obtained from 600–680 nm before the enhancement of the endocytic activity, and h) after the enhancement of the endocytic activity. The scale bar is 25 μm (120).

1.4.7.2 Bioimaging

Due to the significant optical properties, in addition to the biocompatibility, low level of toxicity, solubility in water, and the resistance to photobleaching, made them good candidates for using in bioimaging applications (121).

C-dots were used for *in vivo* for the first time by Yang et al., in which they synthesized C-dots following the laser ablation method, they used a solid precursor which was obtained by applying a hot pressure at a mixture of graphite and cement, then the mixture was backed following by curing and finally annealing under argon flow (22). Then they surface passivated the synthesized C-dots with PEG_{1500N}, with total average size of 4-5 nm and green λ_{em} (122). Female DBA/1 mice (around 25 g) were used for subcutaneous injection, in which they were shaved in the back area surrounding the injection site, where 30 μ L of (30 μ g/ μ L) C-dots were injected. The mice then were imaged with λ_{ex} = 470 nm and the λ_{em} = 525 nm, and λ_{ex} = 545 nm with λ_{em} = 620 nm as shown in Figure 51. The diffusion of the injected C-dots is quite slow, and the florescence faded after 24 h (122).

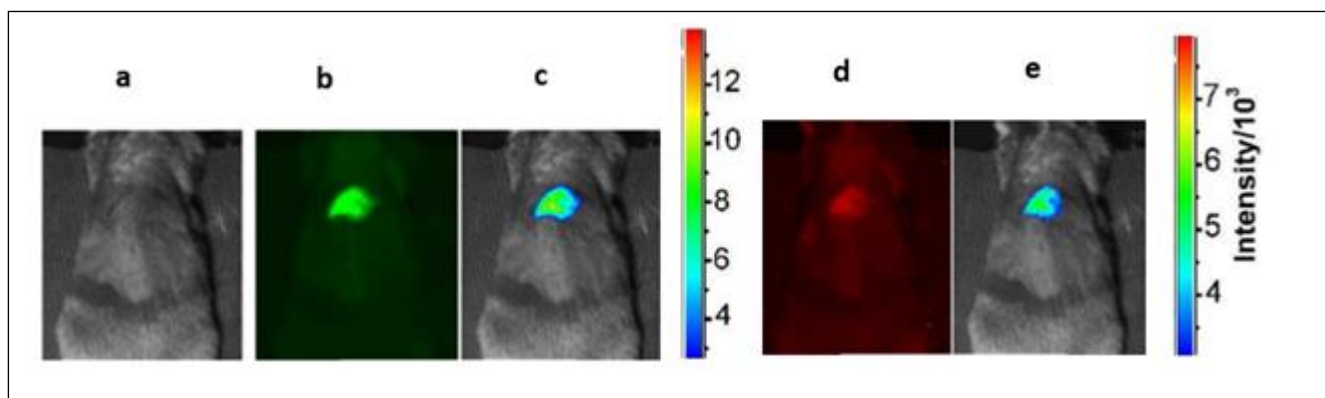


Figure 51: Images of female DBA/1 subcutaneously injected with passivated C-dots by PEG_{1500N}: (a) in bright field, (b) under λ_{ex} = 470 nm with (d) 525 nm emission, (c) under λ_{ex} = 545 nm with, (e) λ_{em} = 620 nm (122).

Wei et al. synthesized C-dots for the purpose of bioimaging in which they followed the acid oxidation synthesis process using glucose as the source of carbon, which was mixed with EA and phosphoric acid, the mixture was stirred vigorously at low temperature to produce C-dots with narrow size distribution of 2-6 nm, in addition to bright blue λ_{em} PL properties and QY = 48% (123).

Wei et al. used embryos of zebrafish to assess the C-dots in bioimaging, they exposed the embryos to a solution of 1.2 mg/mL C-dots, and fluorescence was tested using the confocal microscope in different stages of growth which started at 2 h post fertilization (hpf), 9, 24, 32, 48, and 72 hpf as shown in Figure 52. Images at 2 hpf show very bright color of the embryos (lower), at 24 and 48 hpf the C-dots seem to attach to the chorions because the fluorescence is on the edges of the embryos. Then the fluorescence starts fading at 48 and 73 hpf, due to the structure decomposition of the C-dots. Furthermore, the exposure to C-dots did not affect the development of the embryos and more than 85% of zebrafish embryo viability were recorded due to the low toxicity of the C-dots (123).

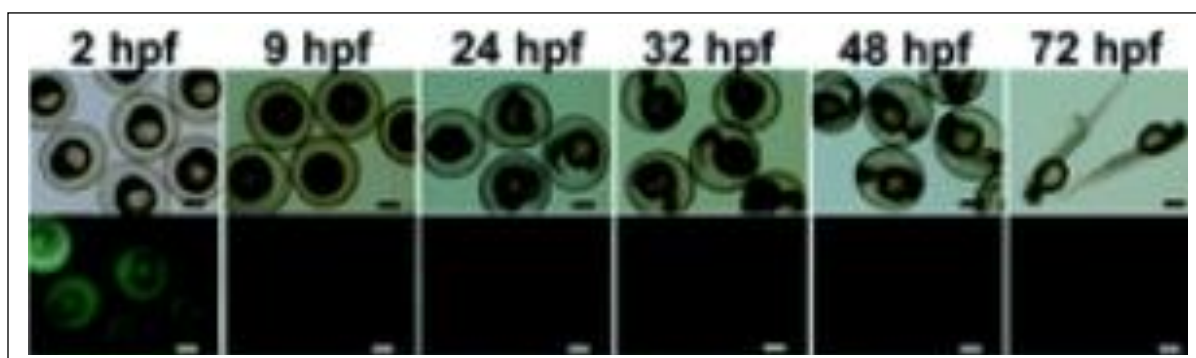


Figure 52: Confocal microscope images of starfish embryos were exposed to C-dots, the images were taken at different times of hours post fertilization (hpf) 2, 9, 24, 32, 48, and 72. Upper: bright field, and lower fluorescence images (123).

1.4.7.3 Antimicrobial agents

It has been reported that the use of antibiotics can cause antibiotic resistance, therefore there is a need to develop classes of antibacterial agents that do not cause antibiotic resistance (124). Some classes of C-dots can act as antimicrobial agents, especially the doped C-dots, as it has been demonstrated that the doping of the C-dots resulting boost in the antimicrobial activity of the C-dots (125).

Kumar et al., synthesized C-dots following the ultrasonic irradiation method using polyethylene glycole-400 as the source of the carbon and gallium as the doping agent. The resulting Ga@C-dots obtained an average diameter of 9 nm, that shows enhancement of the antibacterial activity in a comparison to the C-dots against *Pseudomonas aeruginosa*, an opportunistic Gram-negative pathogen (126). Kumar et al., evaluated the antimicrobial activity of the Ga@C-dots by calculating the minimum inhibitory concentration (MIC) value for *Pseudomonas aeruginosa*. They found out that the MIC of the Ga@C-dots is 0.34 ppm while the MIC of the C-dots is 57.5 ppm (126).

Boobalan et al., synthesized C-dots following the hydrothermal carbonization of oyster mushroom, resulting C-dots with blue/green fluorescent. Boobalan et al., evaluated the antibacterial activity of the synthesized C-dots against *Staphylococcus aureus*, *Klebsiella pneumoniae* and *Pseudomonas aeruginosa* using the disc method (127). They used different concentrations of the C-dots (10-100 μ L), and the results show that the C-dots inhibit the growth of the bacteria as shown in Figure 53.

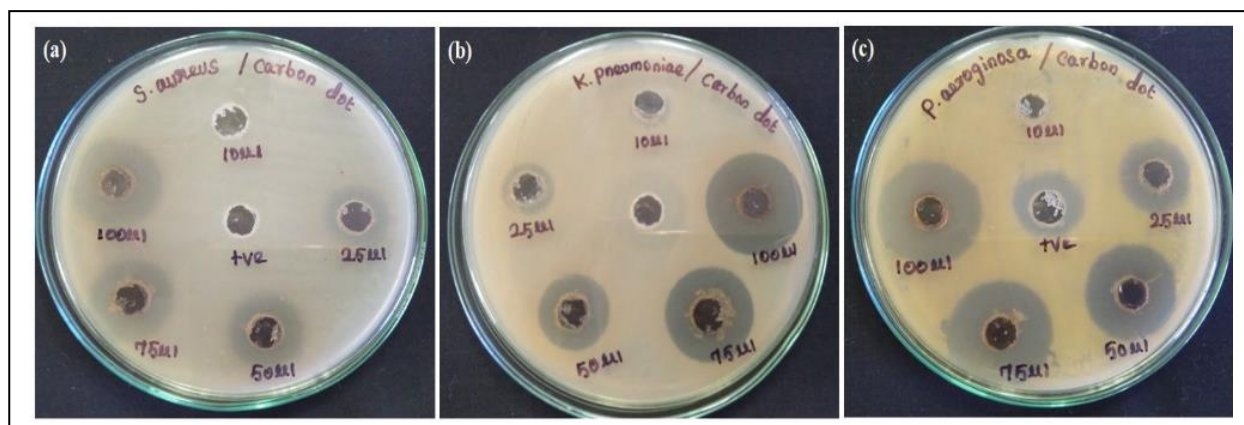


Figure 53: Antibacterial activity of C-dots (10-100 μ L) dictated by the zone of inhibition on three bacterial strains. (a) *Staphylococcus aureus*, (b) *Klebsiella pneumoniae* and (c) *Pseudomonas aeruginosa* (127).

1.4.7.4 Drug delivery

As it has been reported earlier, the surface passivation of C-dots provides supreme structure properties including variety of functional groups such as amino, hydroxyl, and carboxyl groups which enhance the ability of the C-dots to form covalent bond or hydrogen bond with different compounds (drugs) (48). Combining with the properties were reported earlier, the low levels of toxicity, the biocompatibility, and the PL properties, makes them good candidates to be used as drug carriers (48).

D'souza et al. synthesized C-dots to be used as drug carrier for boldine (an alkaloid drug known for its anti-inflammatory and antioxidant activity, which can be considered as anti-tumor promoter (128)), they followed the hydrothermal method using dried shrimp as the source of carbon, in which was mixed with 1:1 ethanol: H₂O then transferred into an autoclave to be heated 170 °C for 12 h (129). The synthesized C-dots exhibit an average diameter size of 6 nm, with blue λ_{em} under $\lambda_{ex} = 365$ nm with 54% quantum yield.

The C-dots loading boldine process was done by mixing a stock solution of 1mM of boldine with different ratios of C-dots: boldine (from 10:0 to 0:10) in which the boldine was attached on the surface of the C-dots by hydrogen bond. The boldine drug release was assessed by adding 10

mL of boldine-loaded C-dots in a dialysis tube (MWCO ~ 70 kDa) against PBS (pH 5.2, 7.4 and 9.2) bath at 37 °C. In order to quantify the amount of the drug that is released from the dialysis tubing, the UV-visible spectroscopy and fluorescence spectroscopic techniques have been used by taking a determined sample of the dialysis PBS at intervals of 180 minutes for the first 24 hours, and then intervals of 24 h for three days, in which the samples were replaced with equal amount of PBS each time (129).

The UV-vis absorption and the fluorescence λ_{em} of the samples are shown in Figure 54 (a) and (b) respectively, as well as a graph of the drug release in Figure 54 (c). As shown in Figure 54 c, the boldine had not been released by the same amount in different pH, this is due to the increase of the hydrophilicity and the solubility of boldine at pH 5.2, as well as different degrees of hydrogen bonding interaction between the C-dots and the boldine at different pH conditions (130). In the acidic solution, the hydrogen bonding interaction between the H⁺ in the solution and the hydroxyl, the carboxylic, and the amin groups of the C-dots as well as the hydroxyl group in the boldine are weaker than those forming at pH 7.4 (129).

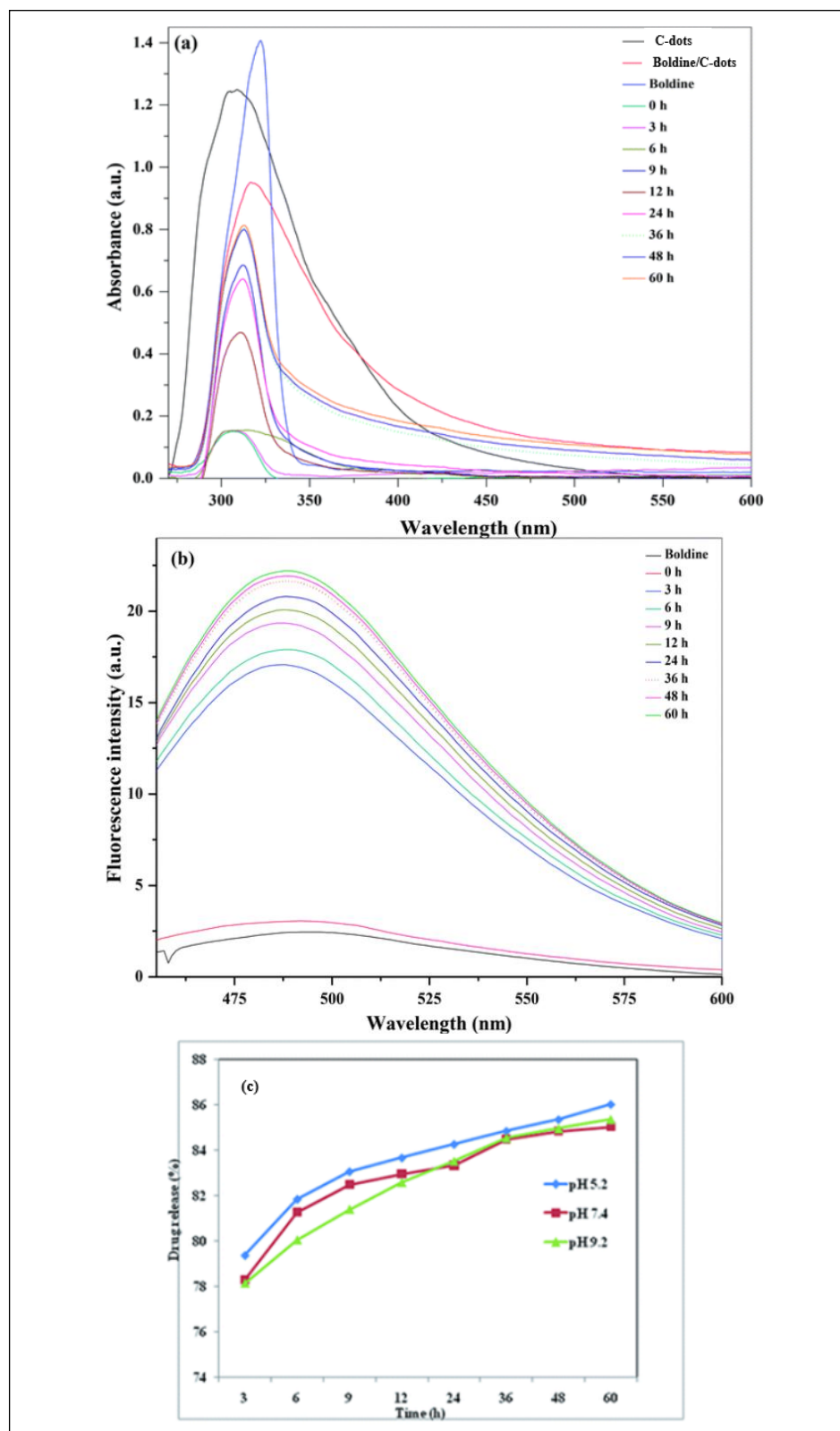


Figure 54: (a) UV-vis and (b) emission spectra of boldine-loaded C-dots at different time intervals from 0 to 60 h in PBS. Boldine responses for 327.27 $\mu\text{g}/\text{mL}$ boldine-loaded C-dots under $\lambda_{\text{ex}} = 430 \text{ nm}$ (129).

Wang et al. synthesized C-dots as drug carriers for doxorubicin (DOX) an anthracycline anticancer drug which is known to be effective and commonly used chemotherapeutic agent for various malignancies (131)) (132). They synthesized the C-dots following the hydrothermal synthesis method using bovine serum albumin as the source of carbon in which was dissolved in ultrapure water then ethanol (1:1) were added and the mixture was sonicated until the formation of a homogeneous solution which then transferred into an autoclave and heated at 180 °C for 12 h. The synthesized C-dots exhibit a narrow distribution size of 3-9 nm, with blue PL properties and QY = 7% (132).

The loading of C-dots with DOX was achieved by adding 0.1 mg/mL DOX in a solution of C-dots in the darkness due to the photosensitivity of the DOX, then stirred overnight. The drug release study was done by dialyzing 10 mL of the DOX/C-dots in 500 mL of PBS at pH 7.4 and 5.0 and the dialysis bags were taken out of the system every 4 h for 20 hours in order to be measured using the fluorescence spectroscopy at $\lambda_{\text{ex}} = 245$ nm as shown in Figure 55. The solubility of the DOX increases under an acidic condition, therefore the release at pH 5 is faster than the release at pH 7.4. The dialysis system was kept in the darkness during the process (132). They suggested a mechanism of cell uptake of DOX loaded C-dots based on the endocytosis as shown in Figure 56, in which the drug will be released inside the cell. Therefore, C-dots considered to be biocompatible, with very low levels of toxicity nanoparticles can be used in drug release applications.

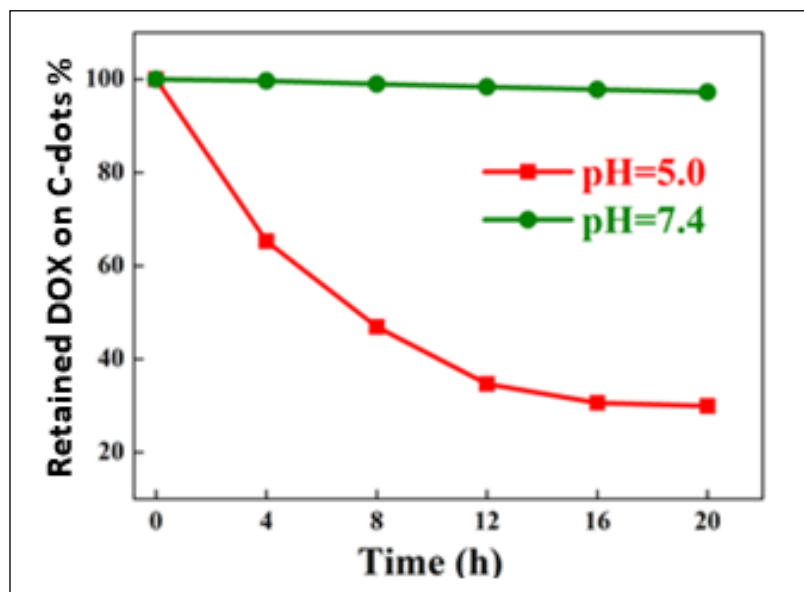


Figure 55: Profiles for release of DOX by DOX/C-dots within environments with pH 5.0, and 7.4 (132).

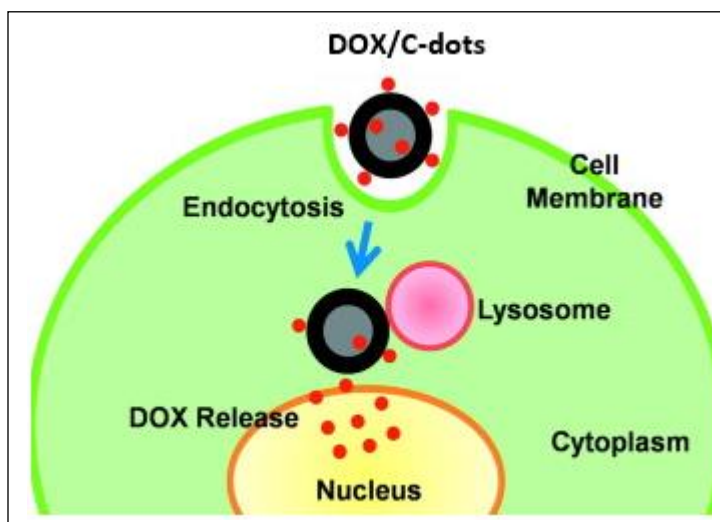


Figure 56: Schematic illustration of the intracellular release of DOX from the DOX/C-dots drug delivery system (132).

1.4.7.5 Cancer theragnostic

Theragnostic is a term used to describe the combination of diagnosis of the disease and the treatments which have been significant in promoting the development of the precision medicine (48). As reported earlier, the C-dots exhibit many properties that give them high potential to be used for cancer theragnostic applications such as; remarkable PL properties, biocompatible, very low level of toxicity, easy functionalization, and large surface to volume ratio. Especially, C-dots excited by red light or near infrared area due to the ability of penetrating tissues deeply, which provides a variety mechanisms for effective treatment of tumors (48). The enhancement of the cellular uptake of particles can be achieved, either by coupling some tumor biomarker on the surface of C-dots which can be done due to the variety of the functional groups on the surface of C-dots, or by enhancing the permeability and retention effect of the tumor microvascular system which also can be achieved by using particles bellow 100 nm in size to work as drug carriers (133).

Wang et al. synthesized C-dots to be used as gene vector to deliver Survivin siRNA into human gastric cancer cell line MGC-803, following the microwave assisted hydrothermal method using citrate which was mixed with L-Tryptophan and dissolved in ultrapure water and stirred for 1 hour to form homogeneous solution. Then the solution was then carbonized via a domestic microwave oven (700 W) for 3 minutes (134). The synthesized C-dots exhibit an average diameter size of 2.6 nm with blue λ_{em} under λ_{ex} range of 340-380 nm, and red λ_{em} under λ_{ex} range of 515-560 nm, as well as 45%.

For the gene delivery, a C-dots based complex was synthesized via interactions electrostatically between the negatively charged of C-dots and the and the positively charged polyethyleneimine (PEI). The gene to be delivered is siRNA which was labeled with Cy3 (which is a traditional orange-red label for protein and nucleic acid used for imaging, flow cytometry, and genomic applications). Then the negatively charged phosphate backbone of the Cy3-siRNA attached to the C-dots@PEI complex to form Cy3-siRNA-C-dots@PEI in which to be exposed to the MGC-803 cells (134).

The gene delivery process was done by growing the MGC-803 in a 6-well plate for 48 hours, then plating them onto 14 mm coverslips and allowed to adhere well. Then the different samples of C-dots@PEI complex (the functionalized C-dots), Cy3-siRNA (the gene to be transferred into the cell with a dye), and Cy3-siRNA-C-dots@PEI complex (the gene loaded functionalized C-dots) were added to each well, in order to be compared to each other. For the imaging, the confocal microscope was used, in which blue and red fluorescence images were collected under $\lambda_{\text{ex}} = 340\text{--}380$ nm resulting blue $\lambda_{\text{em}} = 450\text{--}490$ nm and Cy3 specific $\lambda_{\text{ex}} = 515\text{--}560$ nm resulting $\lambda_{\text{em}} = 590$ nm as shown in Figure 57. Figure 57 shows that the MGC-803 treated with C-dots@PEI exhibit blue PL properties with low red signal as the C-dots used exhibit blue PL properties, while the cells treated with Cy3-siRNA show no blue λ_{em} and red photoluminescence due to the nature of the Cy3, and the MGC-803 Cy3-siRNA-C-dots@PEI show bright λ_{em} in the blue as well as the red region furthermore, the signal is stronger after 5 h of incubation, i.e. the longer the incubation time the brighter the image. Which proves that the C-dots succeeded to deliver the gene into the cells (134).

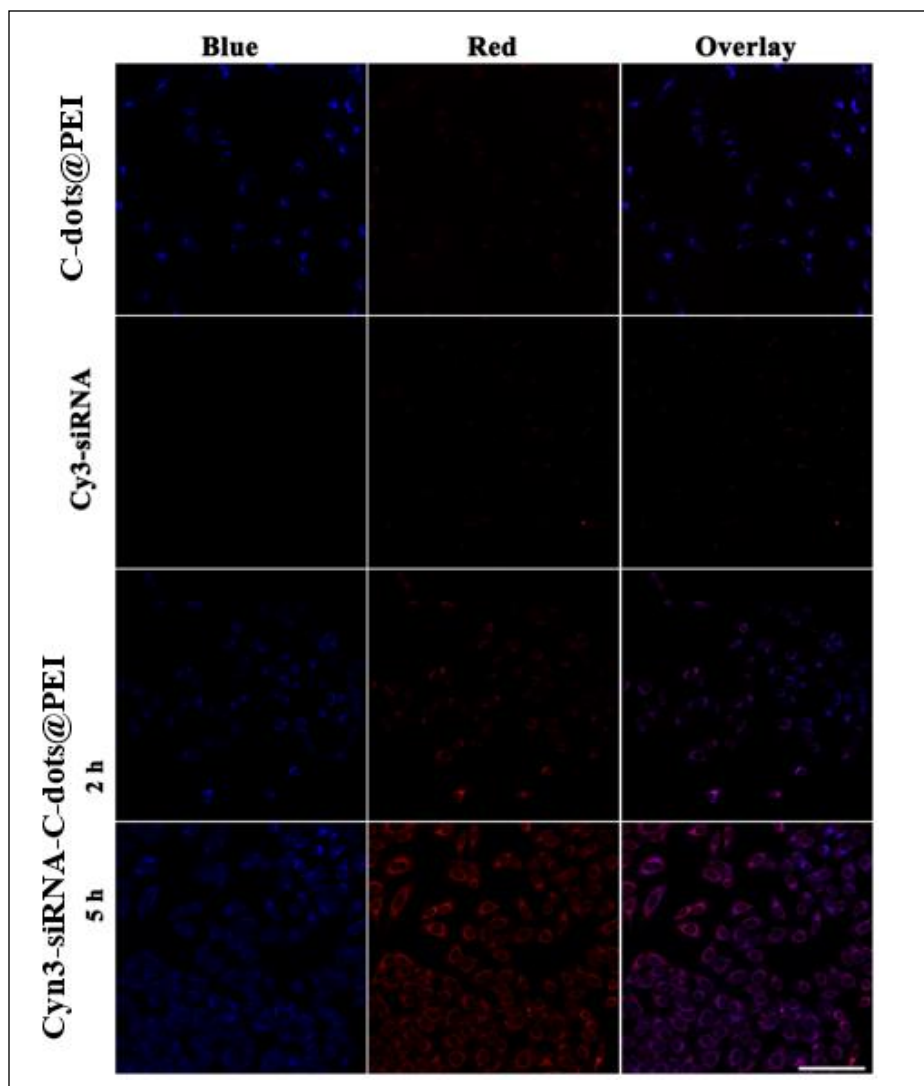


Figure 57: Confocal microscopic images of MGC-803 cells incubated with Cdots@PEI or Cy₃-siRNA for 2 h, Cy₃-siRNA-Cdots@PEI complexes for 2 and 5 h (134).

Zheng et al. synthesized C-dots for the purpose of cancer theragnostic following the solvothermal synthesis method using CA as the source of the carbon which was mixed with polyene polyamine and then heated at 170 °C in an oil bath for 2 h (135). The synthesized C-dots exhibit an average diameter of 2.5 nm, with multicolor PL properties, in which emit bright

green, orange, and red colors under λ_{ex} of blue, green, and yellow light, respectively, with QY = 21%.

Curly et al. attached the synthesized C-dots to oxaliplatin (Oxa(IV), which is a platinum derivative chemotherapeutic medication that inhibits synthesis of the DNA via causing intrastrand cross-links in DNA (136)) by mixing 1-Ethyl-3-(3-dimethylaminopropyl) carbodiimide (EDC) and N-hydroxysulfosuccinimide (self-NHS) which were added into a solution of Oxa(IV)-COOH, the reaction's pH was adjusted to 5.3 using NaOH. Then after stirring the chemicals for 2 hours, the synthesized C-dots were added, and the pH was adjusted at 7.4 and let to stir overnight. The mechanism of the reaction based on the formation of covalent bond between the carboxyl functional group of the Oxa(IV) and the amin functional group on the surface of the C-dots as shown in Figure 58 (135).

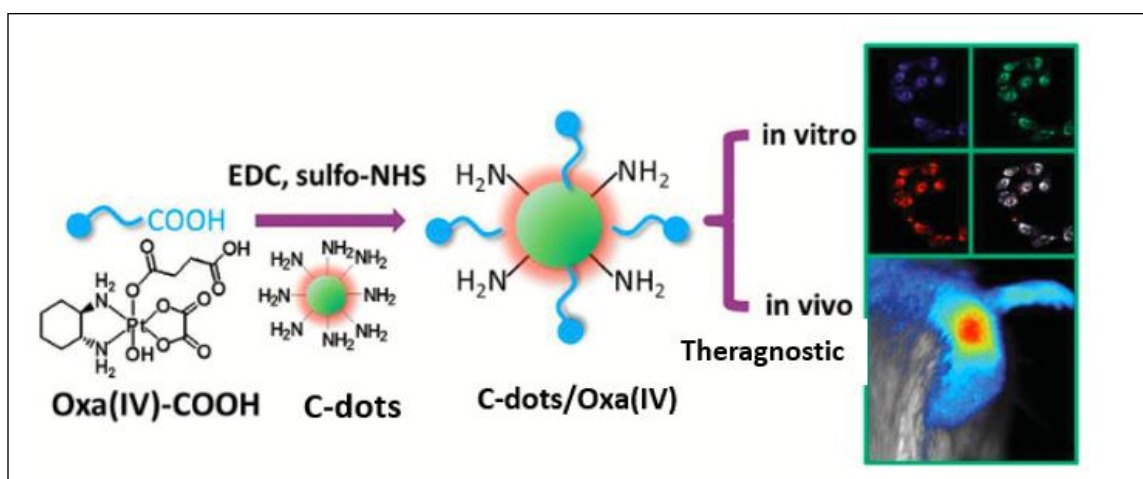


Figure 58: Synthetic scheme for C-dots/Oxa(IV) and its applications in bioimaging and theragnostic (135).

The cancer theragnostic studies were done by using Kunming male mice with liver cancer (H22), they shaved the area of the tumor in the mice to avoid the autofluorescence, then the mice were injected twice (with 24 h and 20 minutes time difference) with 20 μL of 0.72 mg/mL C-dots/Oxa(IV) intralesional injection directly in the center of the tumor. Then the mice were imaged at various times 0-time, 2 min, 6 h, 24 h, 24 h and 20 minutes (time for the second

injection), 48 h, and 72h (135). Figure 59 shows the fluorescence images of the mice at the timeslots have been mentioned earlier with $\lambda_{ex} = 445-490$ nm. At 0-time, the images were taken under wight light where the red circle marks the location of the tumor, ate earlier time the fluorecence by the C-dots/Oxa(IV) is very bright with high intensity (Figure 59 b), after that the fluorecence start to spread around the injection site resulting gradient intensity distribution which is centered at the tumor (Figure 59 c). at later time, the gradient intensity distribution that formed remains but with lower intensity (Figure 59 d) which indicates the digestion of the C- dots/Oxa(IV) by the body. Since the fluorecence signal had weakened after 24 hours, the mice were injected with the second injection at 24 h and 20 minutes time, which resulting an immediate increase in the fluorecence intensity (Figure 59 e). after 48 h of the first injection, the fluorecence signal had faded gradually with weak intensity which indicates that some of the C-dots/Oxa(IV) still remain in the tumor (Figure 59 f). The fluorecence has faded almost completely after 72 h of the first injection (Figure 59 g). Furthermore, Figure 59 i-m show an optical image of the rat with the tumor after immediately after the injection, in which shows an obvious protuberance at the tumor site. After a period of time and with the injections, the tumor site becomes flatter until the protuberance disappeared after 72 h of treatment with two injections of C-dots/Oxa(IV), the tumor size chart shown in Figure 59 n. As a result, the drug has been delivered inside the tumor cells and caused necrotic of the tumor tissue (135).

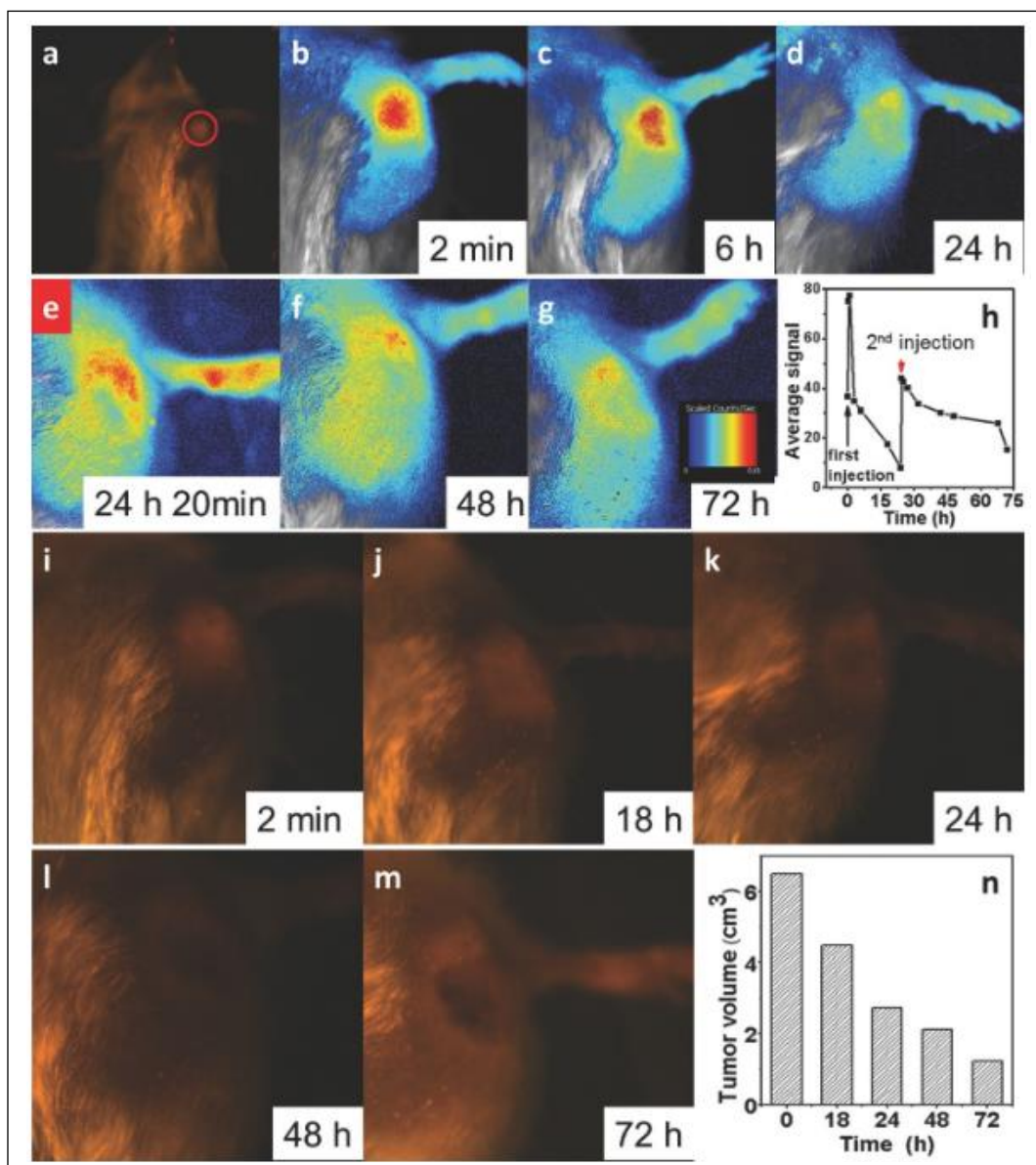


Figure 59: in vivo fluorescence images of mouse bearing H22 liver cancer after the first intralesional injection of C-dots/Oxa(IV); a) 0 minutes (taken under white light, b) 2 minutes, c) 6 h, d) 24 h, e) 24 h 20 minutes (the second injection), f) 48 h, and g) 72 h. All taken under blue light unless otherwise stated (a). Semiquantitative fluorescence intensities of the tumor area are determined at different times. The red arrow indicates the 2nd injection. i–m) Photographs of the tumor area after intralesional injection of C-dots/Oxa after i) 2 minutes, j) 18 h, k) 24 h, l) 48 h, and m) 72 h. n) Tumor sizes of H22 xenograft model as a function of time (135).

1.5 Peptides, proteins, and polymers overview

1.5.1 Peptides:

Peptides are organic substances which are formed of amino acids, attached together by a covalent bond between the carboxylic acid side of an amino acid and the amine side of the other amino acid either in form of a chine or branches, resulting in an amide bond which is commonly known for this purpose a peptide bond as shown in Figure 60 (137).

The smallest peptides can be formed by two amino acids, and they can be classified according to the physical structure and the size and the number of amino acids units into; I) oligopeptides which are composed of a short chain of few amino acids 10-20 units, II) polypeptides which are composed of many amino acids, more than 40 units and less than 100 amino acids, as stated by the International Union of Pure and Applied Chemistry (IUPAC) (138).

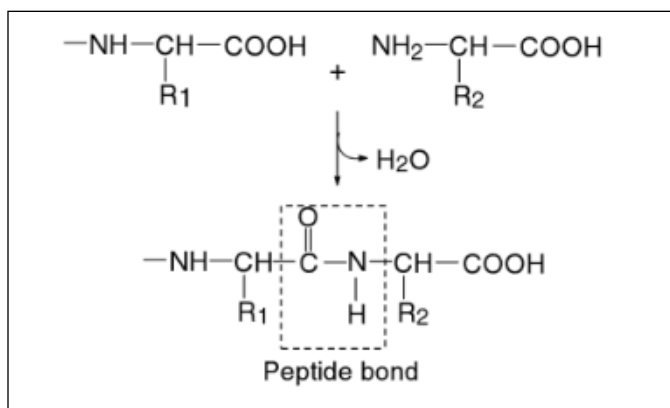


Figure 60: Mechanism of reaction of the formation of the peptide bond (139).

To understand the structure of the peptides, we need to investigate the structure of the amino acids as they are the building units of the peptides. The amino acids structures are composed of a chiral carbon which is attached to a hydrogen atom, an amino functional group, and a carboxyl functional group via covalent bond, in addition to a side chain which is the R group (could be any chemical structure and unique in each amino acid), as shown in Figure 61 (139).

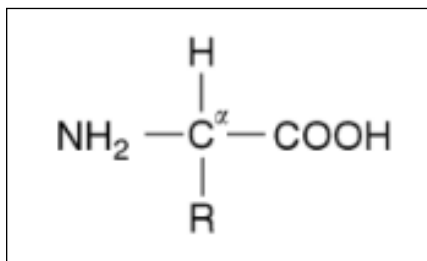


Figure 61: Genal chemical structure of amino acids, in which the R is different from amino acid to another (139).

The amino acid can be classified in different ways based on the polarity (polar and non-polar amino acids, and the solubility in water (hydrophilic and hydrophobic) depending on the chemical structure of the R group (140). Furthermore, the R group of the amino acid determine the physicochemical properties of the amino acid such as; the solubility, the net charge, the chemical reactivity, and the potential of the hydrogen bonding. Therefore, the reactivity, and the physicochemical properties of a peptide depends on the number of the amino acids that forms the peptide, in addition to the nature of the amino acids. In the bonding of the amino acids to form a peptide, the peptide will have N-terminal which by definition represented by the α amino group, and a C-terminal which represented by the α -COOH group, in which the N-terminal is the beginning of the peptide, and the C-terminal is the end of the peptide (139).

1.5.1.1 Cell penetrating peptides.

It has been well known that the membrane of the animal cells has a semipermeable nature, and it is more challenging for the macromolecules to penetrate through them, as they cannot achieve that by endocytosis due to the size, the charge, or the chemical properties (141). Therefore, in order to facilitate cell permeability a use of a biocompatible carrier that has the ability to penetrate the cells is needed, in which a desirable peptide especially that can penetrate cells via different mechanisms especially cell penetrating peptides (CPPs), that have those properties and are often used as drug carriers (142).

The CPPs mechanisms to penetrate the cell membrane vary and can be classified according to the energy loss into two main routes which are; 1) membrane translocation and 2) endocytosis as shown in Figure 62 (143). The membrane translocation is an energy independent route which can be called as passive or direct uptake, while the endocytosis is an energy dependent route which can be called active uptake (143).

1.5.1.1.1 Membrane translocation uptake

As mentioned above, this energy independent route requires no energy yet an interaction between the positively charged CPPs and the negatively charged components of the cell membrane such as the phospholipids bilayer is essential for the CPP to be uptake by the cell, might require permanent or temporary destabilization of the cell membrane (144). Furthermore, this route can take place at high concentration of CPPs especially for amphipathic CPPs (145). The membrane transport route includes;

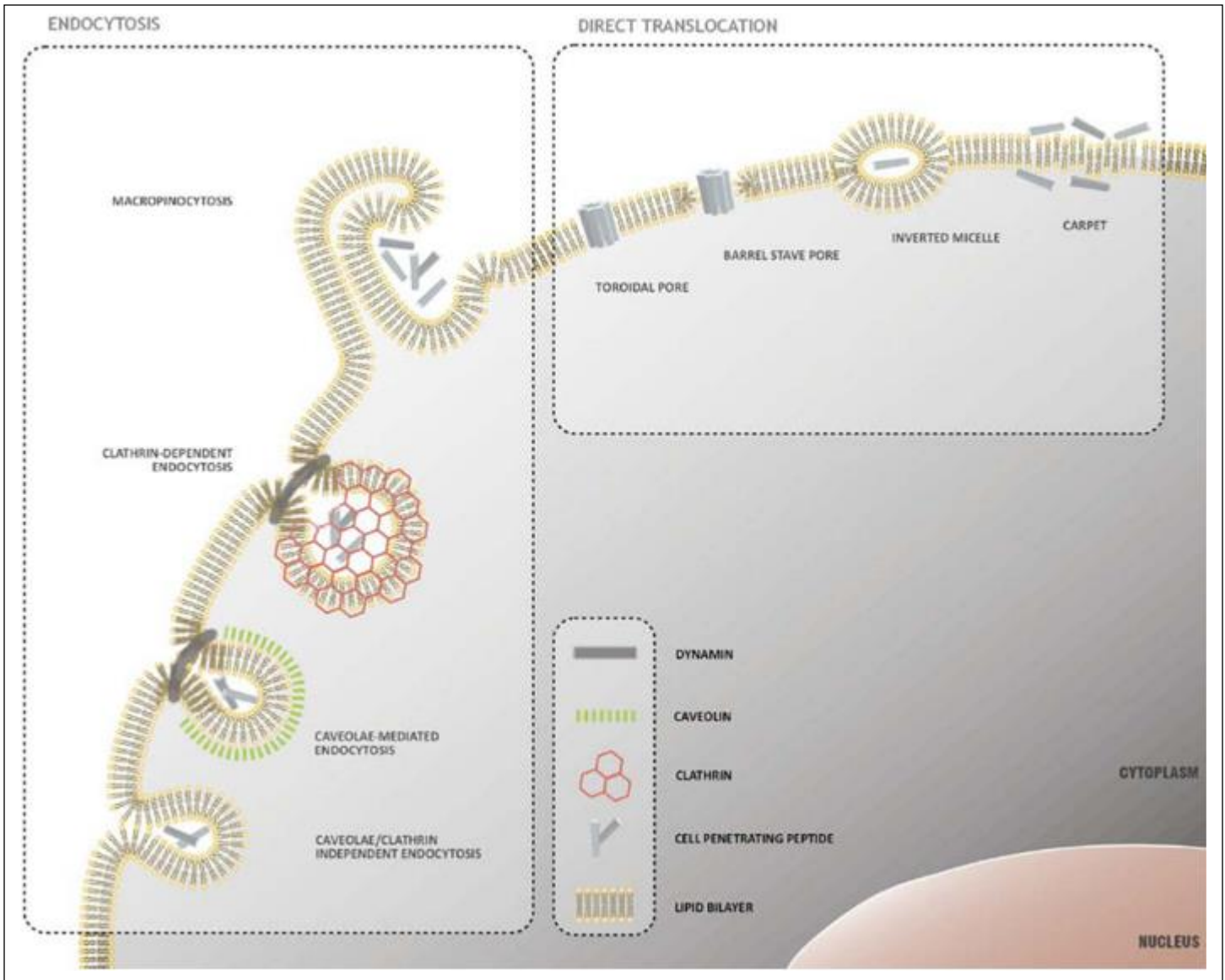


Figure 62: Mechanisms of CPPs uptake, direct translocation through the cellular membrane, which requires no energy, and endocytosis, an energy-dependent process (146).

1.5.1.1.1 Carpet model

This mechanism was first reported by Pouny et al., which is based on lying the positively charged peptide covering the cell membrane (like a carpet) parallel to the cell membrane and forming a hydrogen bond with the acidic phospholipids on the surface, as shown in Figure 62

(143), (147). The hydrophobic sites of the CPP will be embedded in the lipid region of the lipid bilayer of the membrane, and the hydrophilic sites orient in the hydrophilic region, in which resulting reorganization of the CPP. Moreover, the electrostatic interactions are considered as an important factor for the binding between the CPP and the cell membrane, and indirectly contribute to increased concentration of CPP on the cell membrane (148).

1.5.1.1.1.2 Inverted micelle

This mechanism is based on electrostatic interaction between the CPP and the cell membrane, affecting the organization of the lipid bilayer, resulting a change in the membrane curvature, as shown in Figure 62 (149). The change in the membrane curvature promotes the formation of inverted micelles that entrap the CPP, creating a hydrophilic core that allows the accumulation of the CPP which is favourable for transporting into the cells compounds conjugated to the CPP carriers. In the cytoplasm, the inverted micelle will be destabilized resulting the CPP-cargo complex to be released into the cytoplasm (143).

1.5.1.1.1.3 Pore formation

The pore formation mechanism depends on the membrane perturbation a way that have similarity to the inverted micelle (yet, not the same), which drive the cell uptake process (143). The pore formation mechanism can be classified into two models which are; the barrel stave model and the toroidal model, depending on the way of the pore formation, and the type of CPP.

The barrel stave model is mainly formed by the amphipathic α -helical peptides, in which the peptides interact with the cell membrane to form a bundle with channels at the centres. The formed pore is facing the hydrophilic surface of the lipid membrane inwardly, and an

interaction with the hydrophobic residue of the lipid membrane outwardly, as shown in Figure 62 (150).

While the toroidal model is mainly formed by the peptides with ability to form an α -helices when they interact with the cellular membrane, in which the positively charged side of the peptide interact with the phosphate groups of the lipid membrane resulting accumulation of the peptide on the outer side of the membrane as shown in Figure 62. Then the peptides create a bend in the lipid layer to the interior resulting a hydrophilic gap within the membrane, where phospholipids and peptides present (151).

1.5.1.1.2 Endocytosis

As mentioned earlier, this is an active route for cell uptake includes energy consumption and the use of vesicles vacuoles that were pinched off the cell membrane, in which can be done via two steps are; the endocytic uptake step followed by an endosomal escape step (152).

The endocytosis is a complicated process compose of many steps with different mechanisms, in which can be generally divided into two classes are; phagocytosis and pinocytosis. The phagocytosis is restricted to specialized cells such as macrophages, neutrophils, and monocytes, in which based on the uptake of large particles, as shown in Figure 63 (153).

The pinocytosis can be done by all cells, and it is based on the cellular uptake of fluids and solutes (smaller particles) (153). Figures 62 and 63 show the different mechanisms for the pinocytosis which includes;

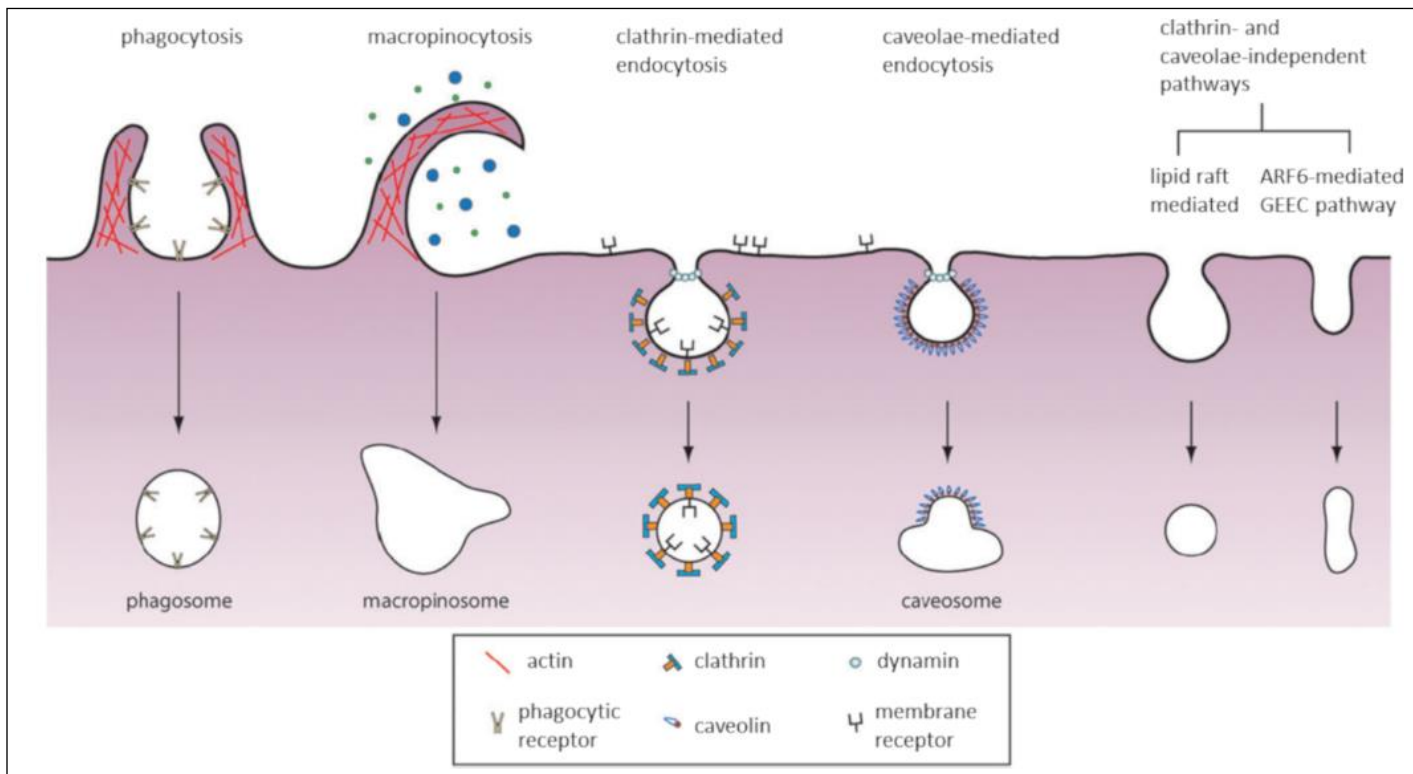


Figure 63: Mechanisms of endocytic entry into the cell including both classes phagocytosis and pinocytosis (154).

1.5.1.1.2.1 Micropinocytosis

Micropinocytosis is considered as a lipid raft dependant and receptor independent mechanism which requires a stimulation by growth factor or a cellular signal to process the membrane ruffling (155). This mechanism includes the formation membrane protrusion which initialized by the actin protein in which cause an increase in fluid uptake, then the protrusions collapse onto and fuse with the cell membrane resulting large endocytic vessel known as macropinosomes, as shown in Figures 62, and 63 (153). It has been reported that this mechanism is widely used for drug delivery as well as pathway used by arginine rich CPPs (143).

1.5.1.1.2.2 Clathrin mediated endocytosis.

This mechanism is considered to be the most understood and best characterised mechanism, it is a receptor dependant clathrin mediated and dynamin required mechanism (dynamin is a GTPase, enzyme that catalysis the hydrolysis of phosphate in which is one of the main components of the cell membrane) (156), in which take place in all mammalian cells enhance the uptake of bulky essential nutrients such as; LDL particles (a lipoprotein bind to LDL receptor and carry cholesterol to cells), and iron loaded transferrin Tfn (binds to the Tfn receptor) (153). Furthermore, the importance of this mechanism comes from driving the uptake of transmembrane receptors and transporters, in order to initiate the plasma membrane composition remodelling as a reaction to the environmental changes in addition to regulating cell surface signalling process (143). This mechanism can be described as a process that involves a strong binding of a ligand to a specific receptor on the cell membrane, to form clathrins in a polyhedral lattice on the cytosolic surface of the cell membrane. Then the clathrin coated membrane on the surface invaginated towards the cytoplasm to form a coated hole that have the same shape of the spherical membrane structure with a diameter of 100-150 nm (143). A progressive invagination will turn the shallow holes into a dome like shape, in which are connected with the plasma membrane via a funnel like rim, as shown in Figures 62, and 63 (157). With more invagination, the dome like vesicle shape will turn into a spherical bud, while the rim develops into an hourglass like membrane neck, and finally the neck get fission into the cytoplasm, this step requires dynamin (157).

1.5.1.1.2.3 Caveolae mediated endocytosis.

This mechanism was reported for the first time at early 50s by Palade, in which the structure of the caveolae mediated endocytosis has been described as a flask like shape invaginations in the cell membrane (as shown in Figures 62, and 63, with a diameter of 50-100 nm and occur in many cell types (158). For many years it has been assumed that the caveolae is mediators in the transportation of serum protein into the tissue across the endothelium cells of the blood

vessels. Recently it has been reported that the caveolae have the ability to encircle cholesterol, and the sphingolipid domains of the plasma membrane, where an accumulation of signalling molecules located (153). Due to the highly hydrophobic nature of the caveolae as well as the content that is rich in cholesterol and sphingolipids, they can be called lipid rafts (159), and they exhibit many functions enabling them to have an important role in cell signalling, lipid regulation and endocytosis (160).

1.5.1.1.2.4 Clathrin and caveolae independent endocytosis

This pathway is considered as a mixture of both caveolae and clathrin mediated endocytosis (as shown in Figures 62, and 63), in which mainly takes place in cells with lack of caveolae, or when a lipid-fluid moiety needed to be delivered into the cell (161). It has been demonstrated that the lipid-protein interaction is very important in many cell functions and in functional compartmentalization of the plasma membrane into microdomains (in which can be called lipid rafts) (143). The lipid rafts formed by interaction of sterols and sphingolipids with a diameter of 40-50 nm with ability to diffuse freely on the cell surface. Some macromolecules can be partitioning into lipid rafts, which makes it easier for them to be uptake by cells via clathrin- and caveolae independent endocytosis pathway (143).

Although the caveolae can be characterised as a lipid raft subtype, it is well proven that the endocytosis can take place even in cells without caveolae which explain the fast kinetics of the independent pathway knowing that the caveolae-mediated endocytosis is considered a slow process (143). Furthermore, this mechanism can be dynamin dependant or dynamin independent. As an example, the fluid phase uptake can be done in the presence of dynamin mutant form, in which blocks the endocytosis (153). This process is good for the uptake of glycosylphosphatidylinositol anchored proteins, viruses and for cytokine receptors on the lymphocytes (153), (161), (143).

1.5.1.2 Solid phase peptide synthesis

Solid phase peptide synthesis is considered as modern approach that is used in peptide synthesis (162). The multistep peptide synthesis process is achieved by using one reaction vessel for the entire synthesis, there is no need for unnecessary transfer of the materials (this contributes to high yield of the peptide) (163). Furthermore, the solid phase peptide synthesis producing a product with less impurities due to the simple filtration and washing steps after the use of high concentrated reagents each step, due to the reality that the formed peptide is in a solid form (164). This method includes the use of a solid support (resin) as a starting unit to build up the peptide on, the principle of the solid phase peptide synthesis reaction is shown in Figure 64, where the N-protected C-terminal amino acid moiety is anchored by the carboxyl group into a hydroxyl, chloro, or amino resin resulting an amide or ester linked peptide, in which producing a C-terminal amide or C-terminal acid peptide. When the lading of the first amino acid loading completed, the goal peptide chain will be sequenced in a linear fashion starting in a reverse order way with C-terminal to the N-terminal, which mean the final unit of the peptide at the C-terminal and the first unit of the peptide at the N-terminal, in which called the C→N strategy, following repetitive reactions including N^α deprotection and amino acid coupling (164). The side chains functional groups of each amino acid should be always attached to permanent protective groups (P), in which are stable throughout the reactions regardless the conditions of the reactions of the peptide synthesis to prevent side chains of the amino acid from reacting. On the other hand, the α-amino group is protected via a temporary protecting group (T, mostly a urethane derivative), in which removed upon the need for the α-amino to react with the next amino acid (164). The temporary protecting group can be easily removed via mild reaction conditions, which can remove the protecting group without affecting the integrity of the peptide and avoid the epimerization, which might happen by 5(4H)-oxazolone formation during the coupling of the activated amino acid, as shown in steps 2 and 3 of Figure 65 (164). Furthermore, the epimerization can be prevented by the urethanes, and this is how the predominant C→N strategy can be achieved. When the coupling of the new amino acid step is completed, a washing is required in order to remove all the unreacted chemicals, the biproducts, and any of the unwanted reagents, following by removing the temporary N-

terminal protecting group to allow the coupling with the new added N-urethane protected amino acid residue via its α -carboxylic acid side after the activation of the α -carboxylic acid (164). The process of deprotection followed by coupling is repeated at each addition of an amino acid until the desired peptide sequence is obtained, in which is attached to the permanent side chains protecting groups as well as the resin, which are removed all of them in one cleaving reaction (164).

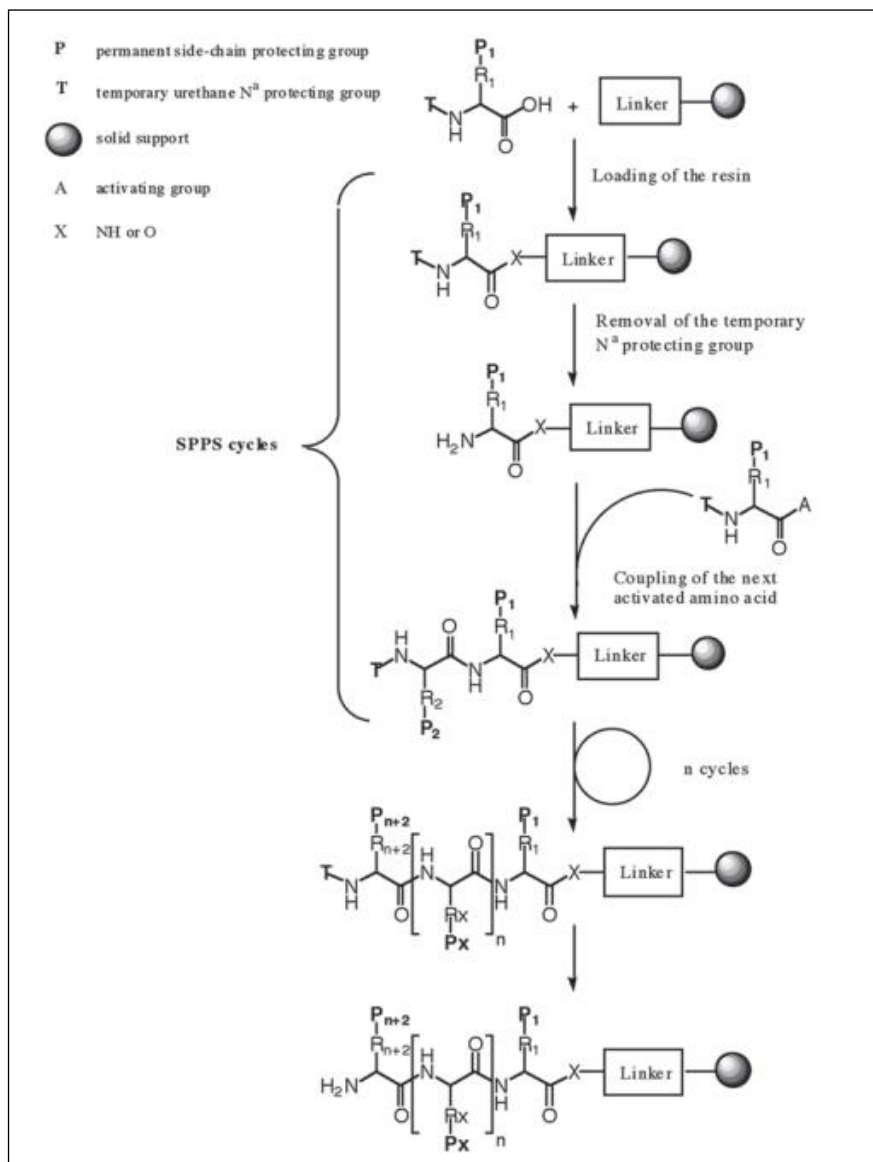


Figure 64: Principle of solid phase peptide synthesis, (P) is the permanent side chain protecting group, (T) is the temporary urethane N^α protecting group, (A) activating group, (X) NH or O, (SPPS) solid phase peptide synthesis (164).

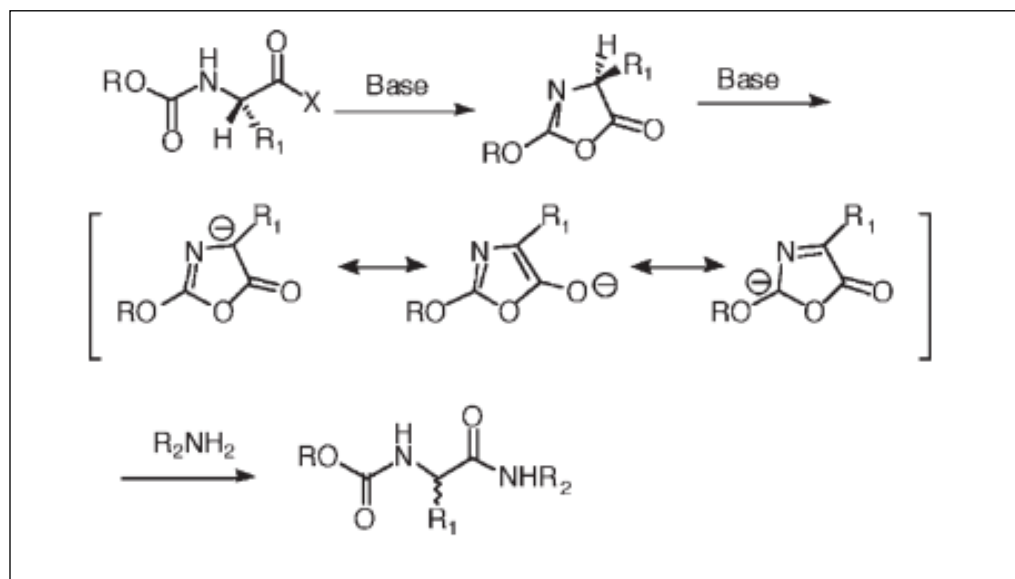


Figure 65: Epimerization by oxazolone formation (164).

1.5.1.3 Fmoc and Boc of solid phases peptide synthesis

As mentioned before, it is essential to have certain active functional groups at the amino acid protected in order to drive the reaction towards a desirable peptide sequence. In order to achieve that, there are two known strategies of protection which are by using tert-Butyloxycarbonyl (Boc) as a protection group or Fluorenylmethoxycarbonyl (Fmoc) (164).

After the formation of the desired peptide, the Boc can be removed using neat trifluoroacetic acid, or trifluoroacetic acid in dichloromethane which resulting the cleaving of the resin as well. Alternatively, strong acid such as hydrofluoric acid anhydrous can be used, yet it is more efficient for large peptide chains and small proteins. Furthermore, the toxicity of the hydrofluoric acid anhydrous and the need to use special polytetrafluoroethylene-lined apparatus, limit this method in addition to the fact that strong acid can affect the integrity of the peptide sequence, especially if the peptide contains fragile segments (164).

On the other hand, the Fmoc is based on protecting the amino acid functional group using orthogonal protecting group, in which uses the base labile N-Fmoc to protect the α -amino functional group, while using an acid labile linker protecting group to protect the C-terminal of the amino acid (165). The advantages of the Fmoc strategy is that the temporary protection, the permanent protection, and the resin can be removed via different mechanisms, in which allows the use of milder acidic reaction conditions to achieve the cleaving of the resin and the final deprotection (164). Therefore, the Fmoc strategy considered the most using strategy recently for the solid phase peptide synthesis.

1.5.1.4 Solid support (resin)

The solid support is known as the resin in the solid phase peptide synthesis, refers to the system of the matrix polymer and the linker that used to support the peptide synthesis (166). The resin should have the ability to be swollen in a solution of dimethylformamide and dichloromethane as the first step of the solid phase peptide synthesis, in which drive the diffusion of the reacting chemicals into the polymer matrix and enhance the accessibility of linker sites to be buried into the bead (167). The resins generally can be classified into two classes: hydrophobic supports resins such as crosslinked polystyrene (PS), and hydrophilic support resins such as Crosslinked polyamide-based resins (PA) and composite PS-Polyethylene glycol (PEG)-based (168).

1.5.1.5 Conjugation of CPPs

Since the CPPs have the ability to penetrate the cells via various mechanisms, the CPPs can be used as cargo to initiate intracellular delivery without affecting the cell membrane integrity (169). Moreover, the CPPs are also used for targeted delivery to subcellular organelles such as nucleus, mitochondria, lysosome, and cytoplasm (170). It has been reported that CPPs are

successfully delivering small molecules, peptides, proteins, nucleic acids, quantum dots, polysaccharides, liposomes, and nanoparticles (171).

Although, it is well known that CPPs are both biocompatible and can act effectively as a cargo, they exhibit some undesirable characteristics including being nonspecific to certain targeted cells, in which the peptides can enter any cell they are in contact resulting drug induce toxic effect in healthy cells (172). Another undesirable characteristic is limited stability in the body fluids, due to the naturally structure disintegration by the plasma lysis enzymes before they reach the target site (173). Therefore, it is required to be protected against lysis process until they penetrate the target site. To protect the CPPs a shielding strategy was reported to be successful, in which includes the immobilization of the CPPs on the surface of ligand (i.e., any of the particles have been mentioned earlier with ability to conjugate to CPPs) following two methods either by electrostatic interaction between the positively charged CPPs and the negatively charged ligand (174), or the attaching to long polymers chains such as polyethylene glycol via covalent bond (175).

1.5.1.5.1 Non-covalent attachment of CPPs to nanoparticles

This attachment strategy is considered the simplest surface modification strategies, which is based on the self-assembly of biomolecules and materials each carrying an opposite surface charge to each other (176). Furthermore, this strategy depends on the ionic strength of both materials as well as the pH values, which resulting less control of the number of molecules attached and less control on the orientation on the attached molecule, in addition to the possibility of the ligand exchange in the presence of other higher charged biomolecule in a comparison to the covalent attachment (177). The strategy of releasing the drug in the active site depends on the disintegration of the biomolecule, in which the slow disintegration gives an advantage because it gives enough time for the conjugate to reach the active site and release the drug (176).

Furthermore, this strategy is simple and can be achieved by synthesis with no modification of CPPs structure is needed (176). On the other hand, the disadvantage of this strategy is that it is a pH sensitive in addition to low control over the number and the orientation of the attached CPPs as mentioned above (176). Figure 66 shows the advantages and disadvantages of the non-covalent attachment of CPPs to nanoparticles, as well as a comparison with the covalent attachment of CPPs to nanoparticles.

1.5.1.5.2 Covalent attachment of CPPs to nanoparticles

This strategy can be considered one of the most important methods to surface modifications of the nanoparticles. This is due to the providing of selectivity of the binding site, and the high stability of the binding in which resulting a preservation of the CPPs against the disintegration by lysis enzymes, as well as preserving the functions and the properties (176). This method might require a structural modification for CPPs in which to avoid the formation of steric hindrance on the surface of the nanoparticles via using a molecule as a spacer such as polyethylene glycol. This method can be done following the carbodiimide based coupling strategy in which includes the formation of an amide bond between the free amines and carboxylic acid groups in the presence of carbodiimides, such as 1-ethyl-3-(3-dimethylaminopropyl) carbodiimide (EDC), and preferably in an aqueous environment (176). Due to the chemical structure of the CPPs, they can provide the amine group as well as the carboxylic acid groups, in which makes the carbodiimide reactions versatile with high synthesis accessibility and flexibility in binding to different nanoparticles (176).

On the other hand, the large number of active sites in the structure of the CPPs that have a chance to form a covalent bond with the nanoparticles can also create an unspecific binding in which resulting alteration of the molecular function of the CPPs (176). Therefore, investigating and selecting a less functionalities for the binding of CPPs and nanoparticles is required. For an example, the free thiol in CPPs can react with maleimide residues to form a stable covalent bond of carbon-sulphur (178). Furthermore, nanoparticles with metallic surface can linked with

the sulphur in the sulfhydryl containing CPPs due to the high affinity of the noble metals to the sulphur in which derives from the soft acid soft base interaction (179).

In addition to the advantages and disadvantages of this strategy that have been mentioned above, this strategy can sometimes produce an unfavourable reaction's conditions (176). Figure 66 shows the advantages and disadvantages of the non-covalent attachment of CPPs to nanoparticles, as well as a comparison with the covalent attachment of CPPs to nanoparticles.

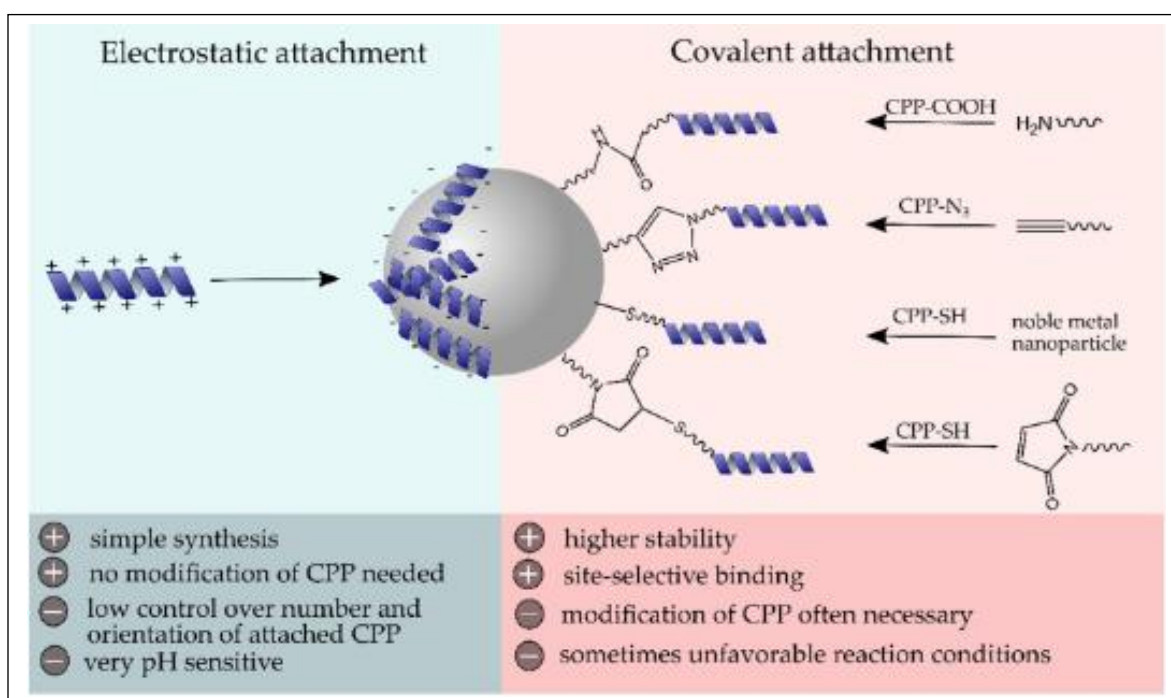


Figure 66: Schematic surface modification of nanoparticles with CPPs using electrostatic or covalent coupling strategies and their major advantages and disadvantages (176).

1.5.1.6 Applications of peptides conjugated C-dots

1.5.1.6.1 Cancer targeting

The conventional chemotherapeutic medications share a very common property which is the lack of selectivity. This means that cytotoxic chemotherapy has the ability to penetrate healthy cells as well as cancer cells resulting serious side effects (176). Therefore, it is very important to create some specific combination of the chemotherapeutic drugs and cancer cells targeting ligands. This process can be done by combining the peptide-C-dots system with cancer cells targeting moiety, which is usually a moiety that has the ability to recognize a receptor on the surface of the cancer cells (176). Furthermore, the same principle can be followed to enable the CPPs-C-dots system to cross the blood brain barrier (180).

On the other hand, there are some peptides with specificity to certain cells, in which can be recognized by specific receptors on some cell membranes such as Arg-Gly-Asp (RGD), this small peptide is recognized by α_v integrin receptor in which is overexpressed on the cell membrane of cancer cells (181). This approach does not require biomarkers or specific ligands to specifically deliver the peptide-C-dots system into certain cells (176).

Yang et al. synthesised a peptide functionalised C-dots for the purpose of targeting cancer cells, to synthesize C-dots they followed the hydrothermal synthesis process by using PEG-2000 and CA as the source of carbon, in which were dissolved in deionized water and stirred for 2 h at room temperature then transferred into an autoclave and heated at 160 °C for 8 h (182). The synthesised C-dots exhibit an average diameter of 6 nm with strong blue λ_{em} at $\lambda_{ex} = 365$ nm and QY = 75.8%. The synthesised C-dots were functionalised by nuclear localization signal peptide (NLS) via using standard EDC/NHC coupling method (the EDC: 1-ethyl-3-(3-dimethylaminopropyl) carbodiimide hydrochloride, and the NHC: N-hydroxysuccinimide), they dissolve the peptide (NLS) in PBS solution of pH 7.4, then added 1:1 mM of EDC and NHS, in which the solution were stirred at room temperature for 2 h to activate the carboxylic group of the peptide. Then the C-dots were added into the solution and the reaction was done at room temperature for 48 h in the darkness (182). Then the peptide functionalised C-dots were loaded

with doxorubicin (DOX) for cancer targeting studies, in which the DOX will be released from the system after the system was uptake by the cancer cells due to the pH dependant nature of the DOX, as shown in Figure 67. The cellular uptake of peptide functionalised C-dots loaded with DOX was tested in a comparison to the cellular uptake of the DOX by itself using the flow cytometry profile of adenocarcinoma human alveolar basal epithelial cells A549) (183). The flow cytometry results show an increase in the cellular uptake of the conjugation system in a comparison to the DOX by 1.7 folds after treatment of 4 hours, this is due to the cellular uptake strategy of the complex which can be done following the caveolae and clathrin mediated endocytosis as well as the passive diffusion, while the cellular uptake of DOX is done by passive diffusion only (184).

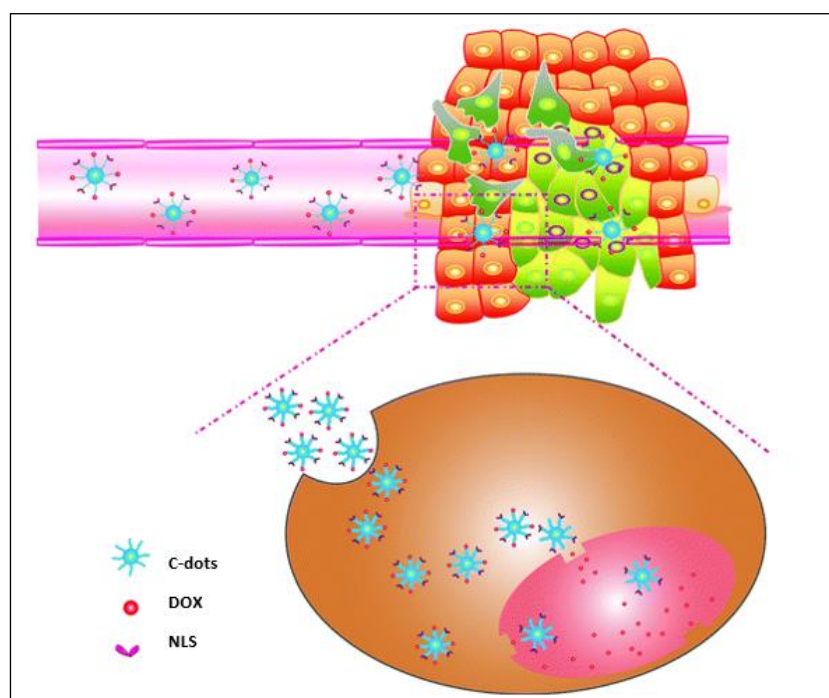


Figure 67: Schematic illustration of the DOX-C-dots-NLS accumulating at the tumor site and releasing DOX into the cell nucleus (183).

1.5.1.6.2 Cancer imaging

As mentioned earlier the C-dots exhibit remarkable PL properties and very low cytotoxicity levels, therefore after certain modifications they can be good candidates to be used for the specific bioimaging applications (i.e., high efficiency diagnostic tool) (176).

Song et al. synthesized C-dots then functionalised them with TAT CPPs, for cancer cells imaging, they synthesised the C-dots following the hydrothermal synthesis by using tryptophane (a free amino acids) as the source of carbon in which has been dissolved in water then formic acid was added, and the mixture was transferred into an autoclave which was heated at 200 °C for 10 h (185). The synthesised C-dots exhibit an average diameter 1.7 nm with blue λ_{em} at $\lambda_{ex} = 360$ nm and a QY = 58.4%. Then the C-dots were functionalised by TAT peptide (which is a CPP capable of carrying large molecules into the cells) by mixing the C-dots with Benzotriazol-1-yl-oxytripyrrolidinophosphonium, hexafluorophosphate (PyBOP) and 1-hydroxybenzotriazole hydrate (HOBt) then mixed with DMF solution which were stirred for 2 h at room temperature to activate the carboxylic acid group on the surface of the C-dots. After the 2 hours, the TAT peptides on beads with unprotected free amino groups on N-terminal were added (TAT attached to the resin and cleaving is required), then the whole mixture was shaken at room temperature for 48 hours, followed by a cleaving step resulting TAT-C-dots conjugate (185).

For the cell imaging study mouse melanoma cells (B16-F10) were used, grown in cell culture dishes specific for confocal microscope with a density of 2×10^5 cells/ mL, the cells were incubated for 4 h at 37 °C and 5% CO₂. Then the dishes were classified into three groups, the first group had been treated with C-dots, the second group had been treated with TAT-C-dots, and the third group had been treated with propidium iodide stain (PI) (to allocate the cell nuclear) and incubated following the same incubation conditions for 24 h (185). The cells were tested using confocal microscope under bright light, 405, 488, and 543 nm excitation, and the λ_{em} in the range of 425–475, 500–530, and 560–660 nm respectively. The cells images are shown in Figure 68, in which the top row is for the cells treated with C-dots, the middle row is for the cells treated with TAT-C-dots, and the bottom row is for cells treated with PI stain. In Figure 68 the bright field images show proper concave and convex surface which indicate the

morphology of the B16-F10 cells Figures 68 a, f, and k. the fluorescence images show that the cells emitted bright blue light at 405 nm excitation, green light at 488 nm excitation, and red light at 543 nm excitation. Furthermore, the cells treated with PI show λ_{em} only at 543 nm excitation, which is expected. The cells treated with C-dots only show λ_{em} within the cytoplasm only which indicate the cellular uptake of the C-dots yet, the C-dots did not penetrate the cell nucleus as shown in Figures 68 b, c, d, and e. on the other hand, the cells treated with TAT-C-dots show an emission by the nuclei as well, which indicate that the TAT-C-dots not only achieved cellular uptake, it also managed to enter cell nuclei as shown in Figures 68 g, h, i, and j. therefore, the TAT-C-dots have a potential for use in cancer imaging applications as a fluorescence probe in in nuclear targeting cellular imaging (185).

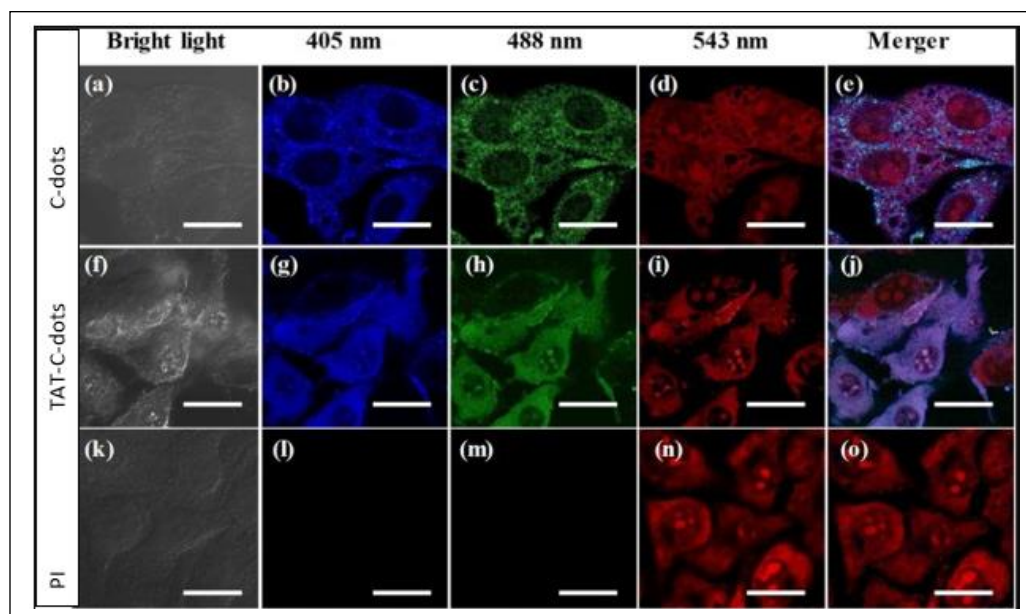


Figure 68: One-photon cell imaging of mouse melanoma B16-F10 cancer cells under (a) bright field, λ_{ex} = (b) 405 nm, (c) 488 nm, (d) 543 nm and (e) merger image of (b), (c) and (d) with C-dots. One-photon cell imaging of mouse melanoma B16-F10 cancer cells under (f) bright field, λ_{ex} = (g) 405 nm, (h) 488 nm, (i) 543 nm and (j) merger of (g), (h) and (i) with TAT-C-dots. One-photon cell imaging of mouse melanoma B16-F10 cancer cells under (k) bright field, λ_{ex} = (l) 405 nm, (m) 488 nm, (n) 543 nm and (o) merger of (l), (m) and (n) stained with PI (185).

1.5.1.6.3 Cancer therapy

The modification of C-dots with peptides has proven to be a successful multimolecular combination to be used in cancer targeting applications as well as in cancer imaging applications. Therefore, by combining the peptide modified C-dots to anticancer agents seems to be promising in the cancer therapy applications, due to the urgent demand to administer the appropriate drugs to patients and selectively deliver them to cancer cells (186).

Shen et al. synthesised functionalised supra-C-dots with mitochondrial targeting peptide (MLS) and the CPP RGD to be used for cancer treatment following the NIR photothermal therapy (PTT) (187). They synthesised the C-dots following the hydrothermal method by using CA as the source of the carbon in which was mixed with dicyandiamide and the mixture were dissolved in water then the solution was transferred into an autoclave to be heated at 180 °C for 3 h to obtain C-dots with pH 11 (188). The synthesised C-dots then were modified into the supra-C-dots by regulating the pH to 5.0 resulting precipitate which was filtered out, leaving the supernatant to be heated at 37 °C for 12 h resulting the supra-C-dots. The supra-C-dots exhibit an average diameter of 10 nm with red λ_{em} when excited at a range of 500-800 nm and QY = 2.3% (187), (188). The supra-C-dots were functionalised with MLS and RGD by using a solution of equal molar ratio of EDC and NHC with the supra-C-dots to activate the carboxyl group, then the mixture was added into the MLS and the RGD, in which be4en stirred for 12 h at room temperature resulting factionalized supra-C-dots with MLS and RGD (187), as shown in Figure 69.

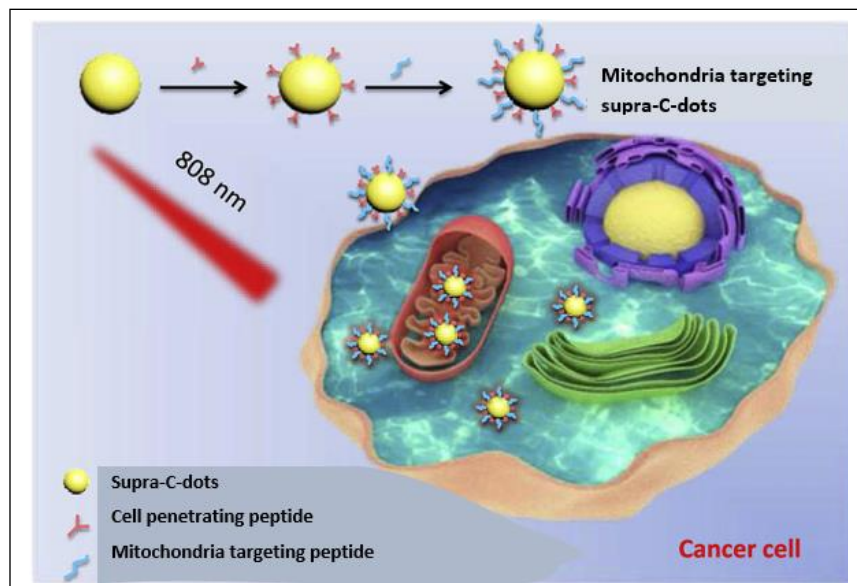


Figure 69: Schematic illustration of the synthesis of functionalized supra-C-dots with MLS and RGD, and the use of the complex in the cancer treatment following the PTT rout (187).

For the mitochondrial targeting study, they used HepG2 (human hepatocellular carcinoma) and L02 cells (human liver cell line), in which they were incubated at 37 °C and 5% CO₂ for 24 hours. Then the functionalised supra-C-dots were added and incubated for 24 h and images using confocal microscope have been taken at $\lambda_{ex} = 488$ nm resulting green emission. Some of the treated cells were stained with MitoTracker Red CMXRos (a stain used for labelling the mitochondria) as shown in Figure 70.

Figures 70 A₁, shows the mitochondria of the HepG2 stained with MitoTracker Red CMXRos stain to allocate the mitochondria (as a control), A₂ shows the mitochondria of HepG2 treated with the functionalised supra-C-dots under $\lambda_{ex} = 488$ nm, and A₃ is a merged image of A₁ and A₂.

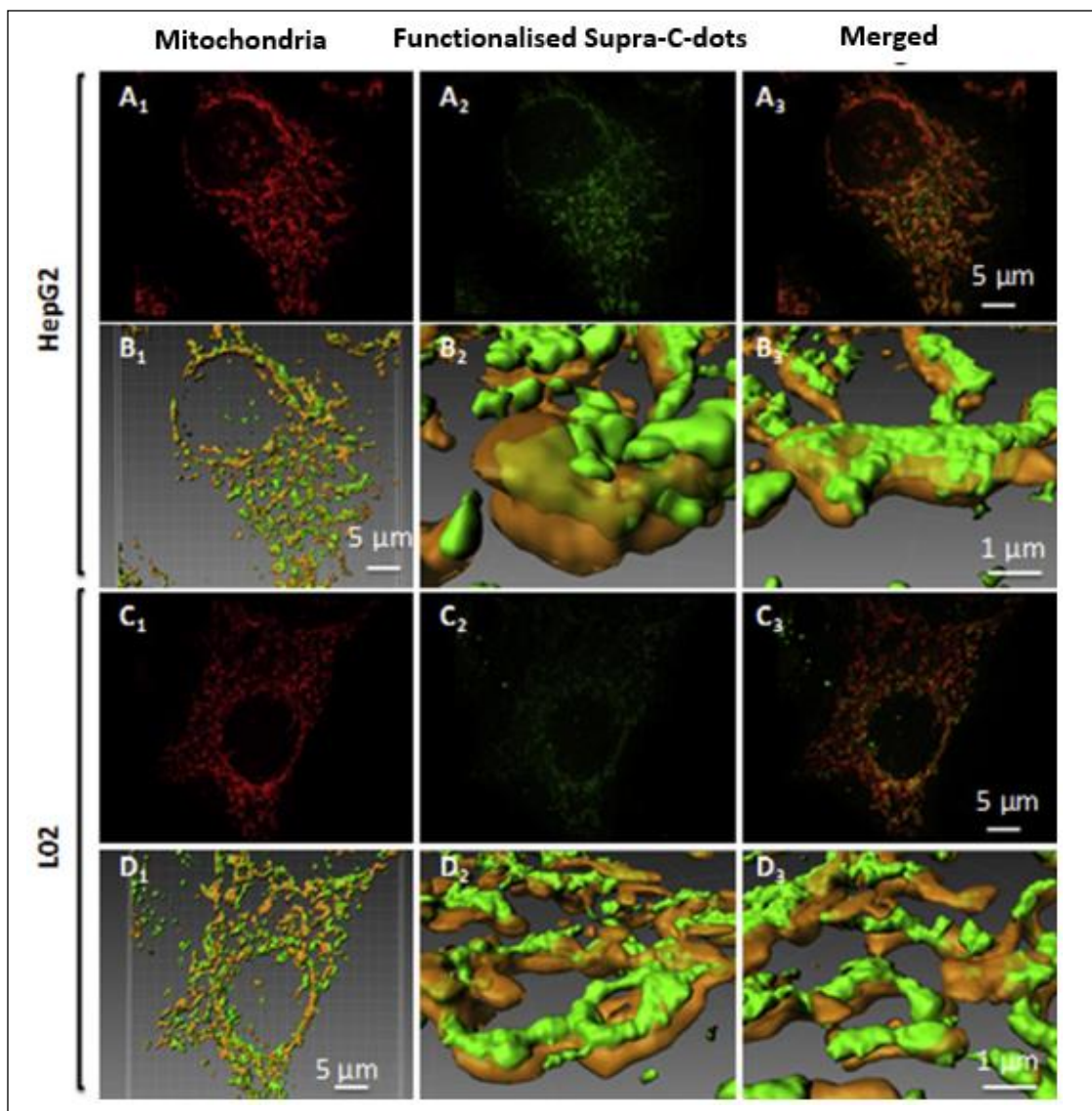


Figure 70: (A1-A3 and C1-C3) Super-resolution fluorescence images of HepG2 cells and L02 cells treated with functionalized supra-C-dots (green), while the mitochondria were stained in red. B1 and D1 of the panorama simulation images of A3 and C3. B2, B3 and D2, D3 show the enlarged regions from B1 and D1 (187).

Figure B₁ is a panorama simulation of A₃, B₂ and B₃ show the enlargement regions from B₁.

Figure 70 C₁ shows the mitochondria of L02 stained with MitoTracker Red CMXRos stain, C₂ shows the mitochondria of L02 treated with functionalised supra-C-dots under $\lambda_{ex} = 488 \text{ nm}$, and C₃ is a merged image of C₁ and C₂. Finally, Figure D₁ is a panorama simulation of C₃, D₂ and

D₃ show the enlargement regions from D₁. Figure 70 indicates that the functionalising the supra-C-dots enabled them not to just penetrate the cells, but to enter the mitochondria as well (187).

For the PTT treatment, the HepG2 and L02 cells were incubated for 24 h at 37 °C and 5% CO₂, then the cells were treated with the functionalised supra-C-dots then incubated for 24. After that, the cells were treated with irradiation under 808 nm laser with power density of 4.0 W/cm² at different times (3, 7, and 10 minutes), then the cells were imaged using confocal microscope as shown in Figure 71.

Figure 71 A shows the HepG2 cells treated with the functionalised supra-C-dots (the top row), L02 cells treated with functionalised supra-C-dots (the middle row), and the HepG2 cells treated with the supra-C-dots (bottom row) with green λ_{em} under 488 nm excitation. As we can observe, the L02 cells remained alive even after irradiation for 10 minutes. On the other hand, the HepG2 cells treated with the functionalised supra-C-dots after 3 minutes of exposure to irradiation, the shape of the cells become round yet, they are still alive. Further irradiation for 7 minutes shows red dots in which indicate the death of cells induced due to the hyperthermia created by the functionalised supra-C-dots (187). Furthermore, after 10 minutes of irradiation the cell death increased, which indicate that the functionalised supra-C-dots has high tumour specificity as compared to the specificity toward normal cells, as well as lower side effect for normal cells (187).

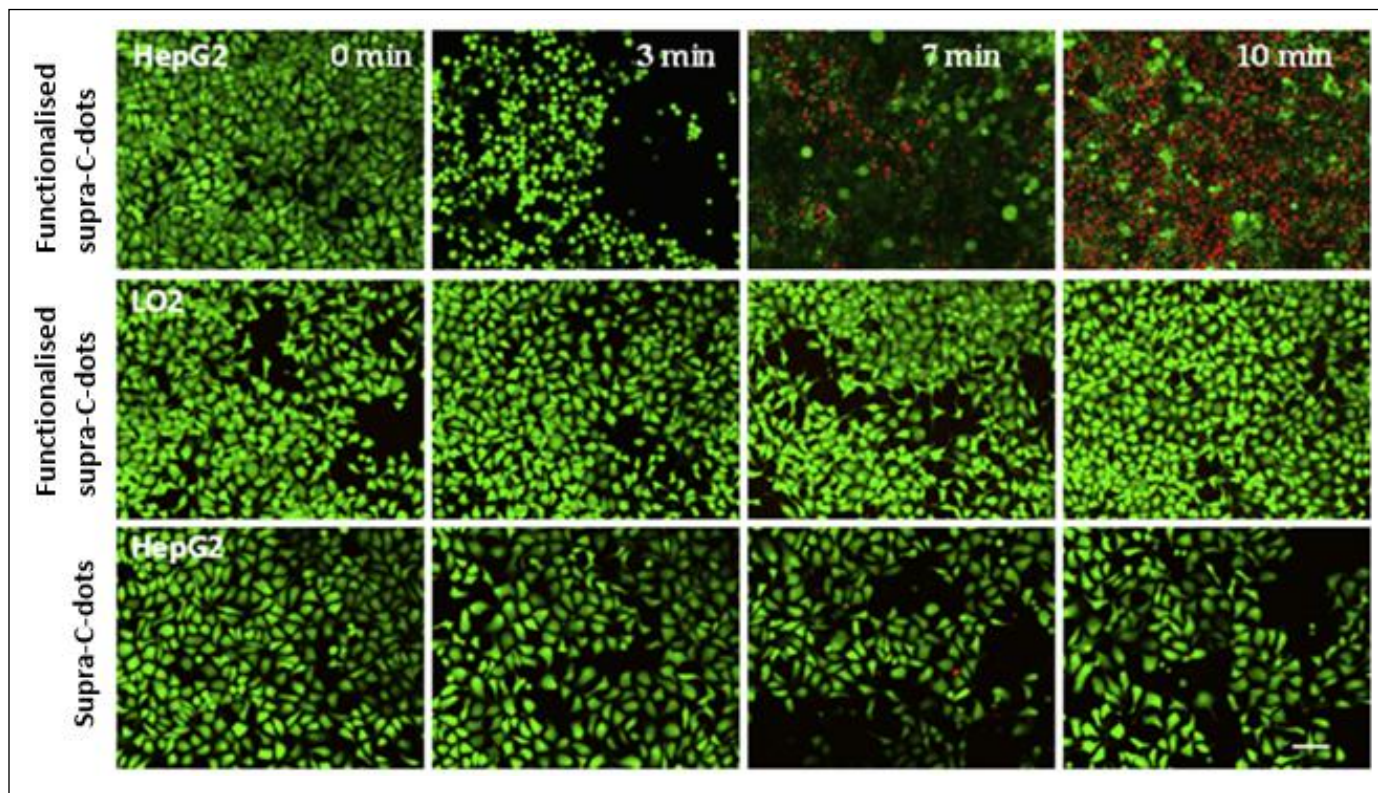


Figure 71: Images of HepG2 treated with functionalized supra-C-dots (top row), L02 cells treated with functionalized supra-C-dots (middle row), and HepG2 treated with supra-C-dots followed by irradiation for 3, 7, and 10 mins. The viable cells were stained as green, while the dead cells were stained as red. The scale bar is 50 μm (187).

Furthermore, the HepG2 cells treated with the supra-C-dots shows that very high population remained alive even after 10 minutes of irradiation, which indicate the lack of specificity of the non-functionalised supra-C-dots in comparison to the cells treated with the functionalised supra-C-dots, which proves that the targeted cells used have been successful in targeting the cancer cells.

In addition to that, a quantification evaluation of cell death was done via the WST-1 cell viability assay, which shown in Figure 72. Figure 72 shows that the functionalised supra-C-dots did not induce cell death for L02 cell line, on the contrary the cell viability increased with irradiation

which indicates that exhibiting that light irradiation has no photodamage effect on the normal cell line. On the other hand, the HepG2 treated with functionalised supra-C-dots its viability significantly decreased proportionally with the irradiation time, with 43% cell viability after 10 minutes of exposure to irradiation. Furthermore, after 10 minutes of exposure to irradiation the cell viability difference between the HepG2 and the L02 is 70%.

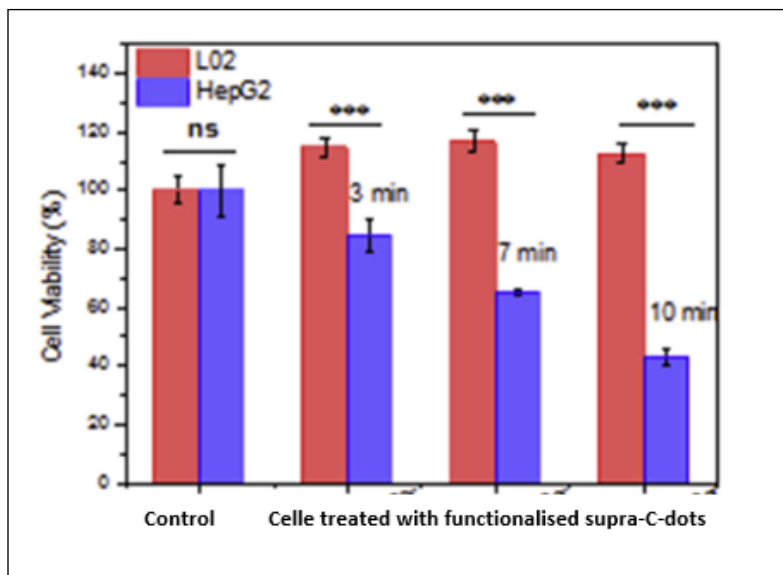


Figure 72: Cell viabilities of L02 cells and HepG2 cells treated with functionalized supra-C-dots using WST-1 cell viability assay (187).

1.5.1.5 Peptides as antimicrobial agents

As it has been mentioned in section 1.4.7.3, the antibiotic resistance is a concerning issue that has risen in the last few years, therefore there is an urgent need for alternative antimicrobials that do not cause antibiotic resistance (189).

Gough et al., demonstrated two cationic peptides MBI-27 composes of KWKLFFKIGIGAVLKVLTTGLPALIS, and MBI-28 composes of KWKLFFKIGIGAVLKVLTTGLPALKLTK, with antibacterial activity *in vitro* and *in vivo* using animal modes (190). The MBI-27 and MBI-28 have the ability to bind to the Lipopolysaccharides (LPS) with an affinity that is equivalent

to the affinity of Polymyxin B. Simultaneously, when the MBI-27 and MBI-28 incubated with RAW 264.7 murine macrophage cell line, the peptides stop the LPS from stimulate cells to induce the endotoxic shock mediator (TNF) , even after 60 minutes of the stimulation of the TNF, which are equivalent to Polymyxin B (190). Furthermore, Gough et al., reported that MBI-28 provided protection for the galactosamine-sensitized mouse model from the lethal endotoxic shock, which associated with the ability of the MBI-28 to reduce LPS-induced circulating TNF by nearly 90%. In addition, the MBI-27, and the MBI-28 peptides reported to have antibacterial activity against gram negative bacterial in both the *in vitro* and the *in vivo* studies against *Pseudomonas aeruginosa* infections in neutropenic mice (190).

Singh et al., developed a new class of Host Defence Peptides (HDPs) that is lipidated α/α -AA heterogeneous peptides that has remarkable antimicrobial activity against Gram positive and Gram-negative bacteria. The mechanism of action of the is lipidated α/α -AA heterogeneous peptides is to cause bacterial membrane disruption, which is considered to be the main reason to reduce the ability of bacteria to develop antibacterial resistance (191). Furthermore, they demonstrated that the is lipidated α/α -AA heterogeneous peptides rapidly caused bacterial death, which make them promising antibacterial agents with the ability to stop the formation of antibiotic resistance (191).

1.5.1.6 K7 peptide as CPP for cancer therapy

The K7 peptide is a short chain hydrophilic CPP composed of 7 lysine amino acid units, in which have a helical structure with positive charge (192). The hydrophilic nature of the K7 in addition to the rgd being cationic peptide, enable it to be a CPP with a sequence of 7 lysine molecules KKKKKKK (193). Due to the properties of the K7 as a CPP, it can interact with the cell membrane via the difference in the electrostatic charges of the positive K7 and the negative charge of the phospholipid cell membrane, in which enable the K7 to be cargo for certain molecules, in order to be used in drug delivery, cell targeting, or bioimaging applications (194). The K7 firstly was

derived from the gram-positive bacteria *Lactobacillus gasseri*, they have an antibacterial activity against many bacteria such as *Helicobacter pylori* (195).

It has been demonstrated that cancer patients suffer from reduction in the immune system especially elderly people, this is due to either the effect of the prognosis of the cancer or to the side effect of the anticancer (196). Therefore, the K7 can be used as a drug carrier because it is a CPP at the same time act as an antibacterial agent due to the antibacterial properties.

Walther et al. modified quantum dots (QD) for the purpose of delivering negatively charged molecules such as RNA into the cells using the K7 peptide as a cargo (197). They used amine functionalised QD with green λ_{em} and red λ_{em} , in which were equivalently coupled with the K7 on the surface of the QD. They mixed the QD with sulfosuccinimidyl 4-(N-maleimidomethyl) cyclohexane-1-carboxylate (sulfo-SMCC) to activate the QDs, as shown in Figure 73. Then the activated QDs were mixed with the K7, in which formed a covalent bond conjugating the QDs with the K7.

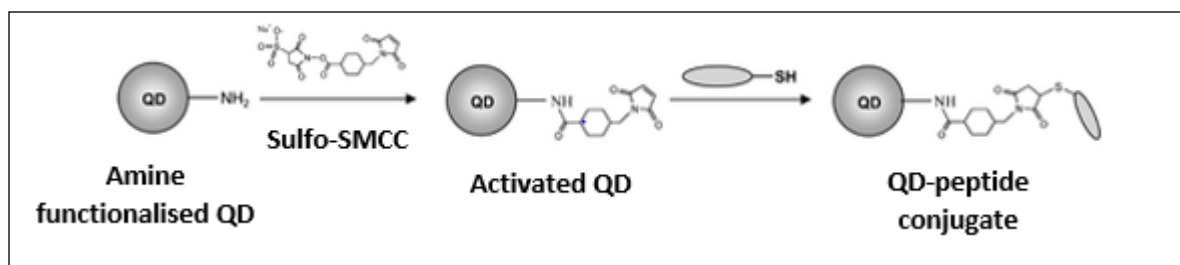


Figure 73: Amine-functionalized QDs were activated with sulfo-SMCC, subsequently followed by reaction with the thiol group of the peptide (197).

They used the peptide conjugated QDs were used as cargo for 83 base RNA, in which the RNA was diluted with RNase and heated at 70 °C for 5 minutes, to enable the RNA to form a hydrogen bond with the peptide conjugated QDs. Then the peptide conjugated QDs were added after the RNA solution was slowly cooled down at room temperature, then the mixture was stirred for 1 hour at 37 °C. The RNA was delivered to two cell lines; HEK293 (epithelial cells

isolated from the kidney of a human embryo) and HeLa cell. The cells were incubated at 37 °C and 5% CO₂ for 24 hours, then a solution of the RNA loaded QDs conjugated peptide and incubated at 37 °C and 5% CO₂ for 1 and 6 hours. The fluorescence microscope images are shown in Figure 74, the top row is for HeLa cells and the bottom row is for the HEK293 cells. The images after 1.5 h show that the RNA-K7-QD system have been successfully uptake by both cell lines and accumulated inside the cytoplasm. The green dots refer to the QD, the red dots refer to the RNA and the cell nuclei were stained blue. After 6 h incubation there was no significant change, indicates that the cellular uptake happened as fast as 1.5 hour (197).

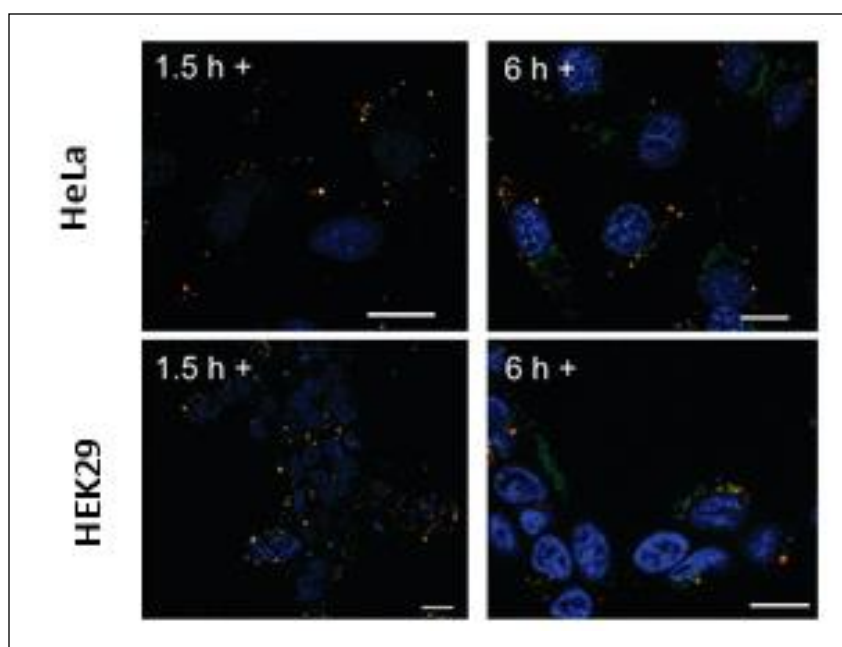


Figure 74: RNA delivery mediated by the QD-k7 conjugate. Delivery of the 83 base long RNA in HeLa (top row), and HEK 293 cells (bottom row). RNA in red, QD-K7 green, and the nucleus was stained with blue. Both cell lines were incubated for 1.5 h, and 6 h (197).

1.5.1.7 RGD peptide

RGD is a short peptide with a sequence of Arginine-Glycine-Aspartic acid as shown in Figure 75 (198). The RGD is a specific peptide with ability to target $\alpha_v\beta_3$ integrin receptors (ABIR) (199). The ABIR are receptors on the cell membrane, the overexpress of the ABIR indicates angiogenesis (the process of forming new blood vessels from existing vessels for abnormal growth of cells i.e., in case of tumour (200). Therefore, the RGD peptide is considered a good candidate for targeting, bioimaging, and cargo for cancer therapy.

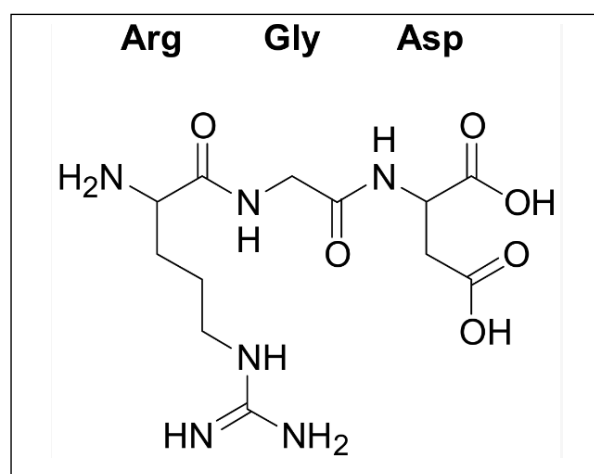


Figure 75: Chemical structure of the RGD peptide (198).

Wang et al. modified GQDs by conjugating them with RGD peptide for chemo photothermal therapy, in which they used aminated GQDs and functionalised them with the thiolated RGD peptide following the thiolation reaction (201). This reaction requires the use of a crosslinker, in which PEGylated N-succinimidyl 3-(2-pyridyldithio)-propionate (PEG12-SPDP) were used to enable the formation of a covalent bond between the thiol of the RGD and the amine of the GQD. They mixed the PEG12-SPDP with the GQDs in a solution that was heated at 25 °C for 4 h in the darkness, then a solution of the RGD was added to the mixture, and the mixture was left for 24 h to complete the reaction under the same conditions, as shown in Figure 76 (step one) (201).

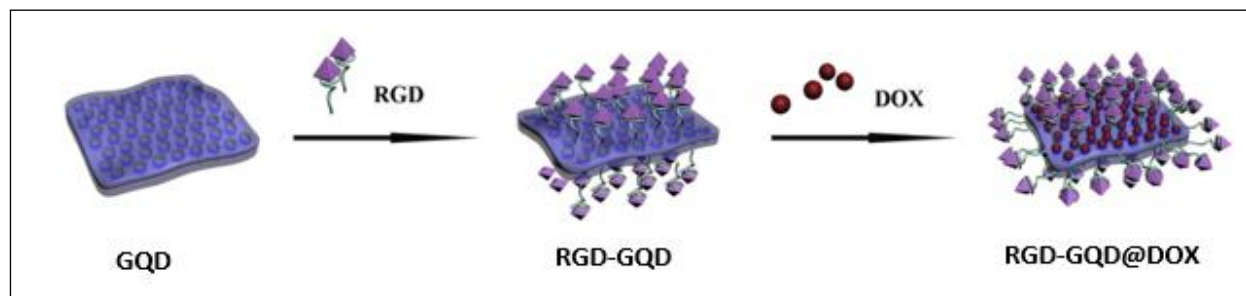


Figure 76: Schematic illustration of the modification of the GQD with RGD and loading the system with DOX (201).

Then they loaded the peptide conjugated GQDs with the DOX, in which they mixed a solution of the RGD-GQD and DOX, then heated them at 25 °C for 24 h in the darkness, resulting RGD-GQD@DOX as shown in Figure 76 (step two) (201).

For cell uptake studies they used two cell lines, a H460 (non-small lung cancer cell line), and the SK-mel-5 (melanoma cell line). They incubated the cells for 24 h at 37 °C and 5% CO₂, then the RGD-GQD@DOX was added to both cell lines and the H460, and the SK-mel-5 were incubated for 2 hours, and 1 hour respectively. Furthermore, both cell lines were treated with a solution of DOX, a solution of GQDs, and a solution of GQD-DOX for a comparison in addition to the use of Hoechst as a control (which is a DNA stain with blue colour), the treated cells were excited at 488 nm using confocal microscope (201).

Figure 77 shows the images of the H460 cell line and Figure 78 shows the images of the SK-mel-5 cell line, in which the strong red fluorescence under $\lambda_{ex} = 488$ nm refers to the RGD-GQD@DOX indicating the high cellular uptake of the loaded system by both cell lines. On the other hand, the cells treated with GQDs@DOX in both cell lines were not clearly show proper emission indicating the absence of the RGD did not enhance the cellular uptake, as none of the components of the GQDs@DOX combination has the ability to target the cells, the RGD can target the cells (201).

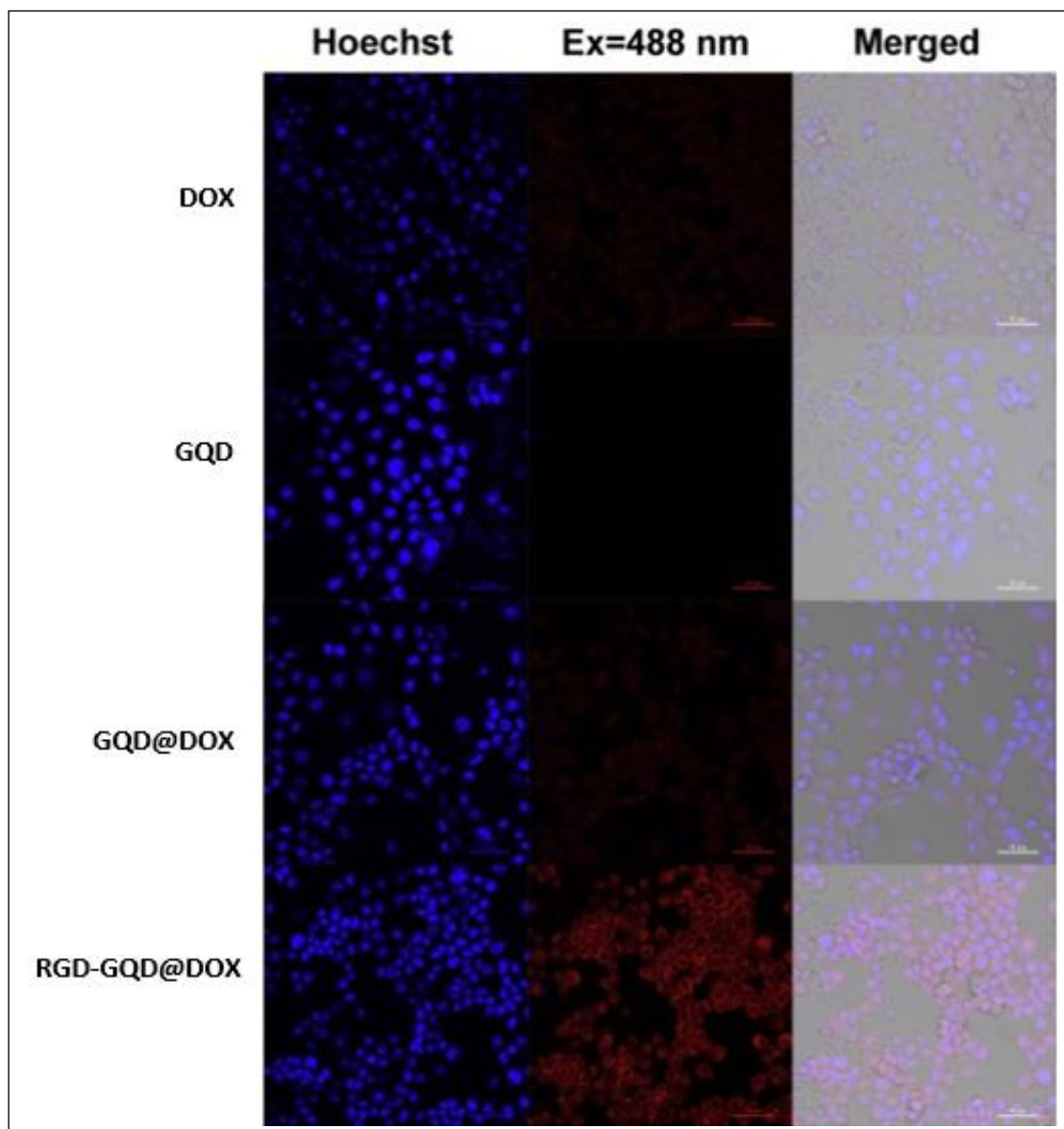


Figure 77: Confocal microscope images for the intracellular uptake and localization of DOX, GQD, GQD@DOX, and RGD-GQD@DOX in H460 cells with incubation for 2 h (scale bar: 50 μm) (201).

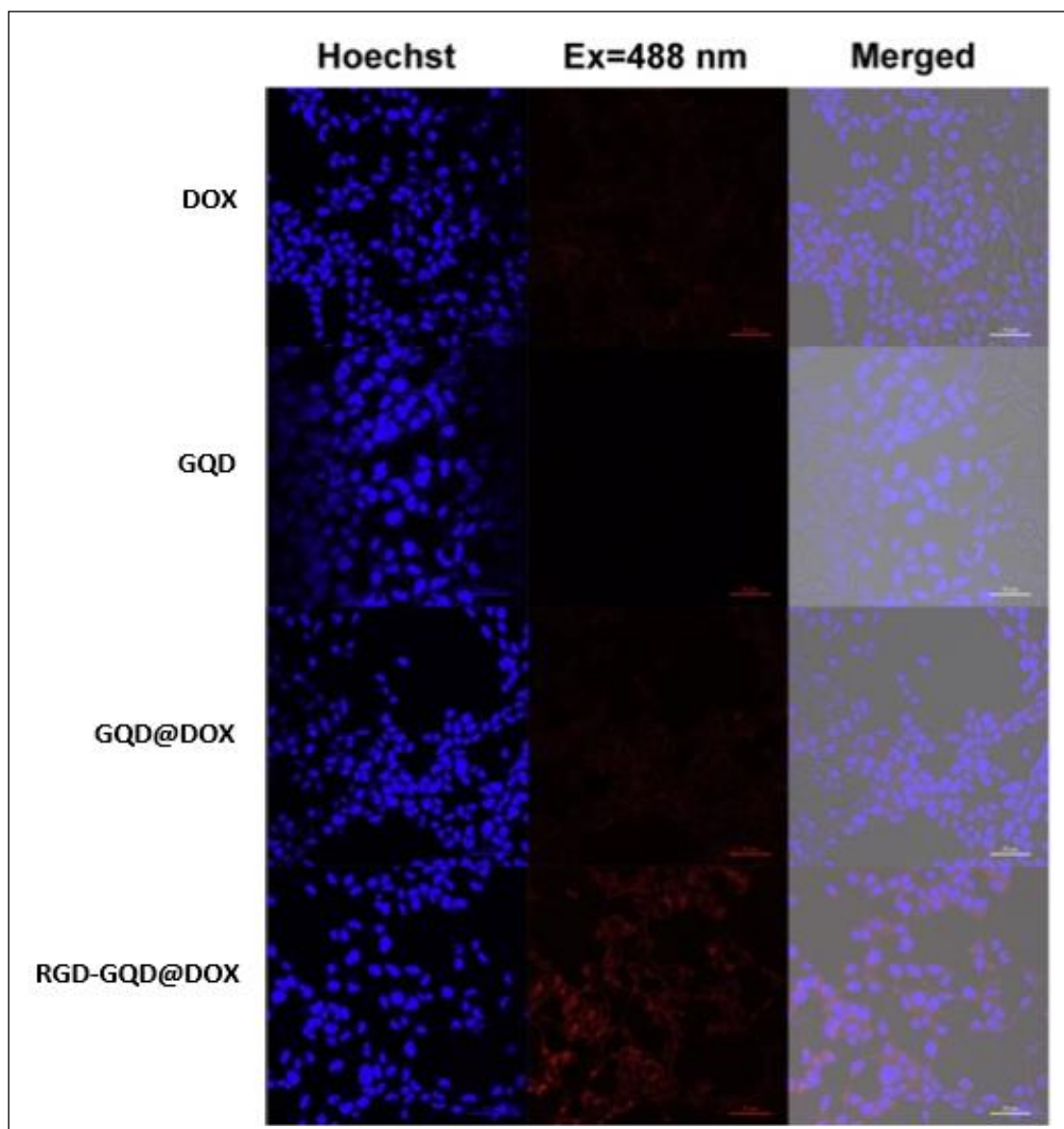


Figure 78: confocal microscope images for the intracellular uptake and localization of DOX, GQD, GQD@DOX, and RGD-GQD@DOX in SK-mel-5 cells with incubation for 1 h (scale bar: 50 μm) (201).

1.5.2 Proteins

The proteins are a class of macromolecules that naturally synthesised in the body with nitrogen containing substances and are formed by amino acids (202). The quality and the properties of the protein are determined by the chemical composition, the properties, and the bioavailability of the essential amino acids that building the protein (203). The proteins have many roles in the body, they produce enzymes, cell receptors, hormones, and haemoglobin which are essential for the metabolism reactions as well as all the body daily activities (202). In addition, the proteins have an important role in building up muscles as it has been demonstrated that the cells size enhances when the cells have with high protein intake (204). Furthermore, the proteins can be used as a good source of energy, yet this cannot be considered as the primary source of energy due to the need for the proteins to be metabolised into their amino acids building blocks (202).

Since the proteins are naturally made inside the body, they can be used as drug carriers especially transferrin proteins (a class of proteins) for targeting certain cells via transferrin receptor mediator (205). On the other hand, it has been demonstrated that the C-dots have the ability to suppress protein fibrillation (protein fibrillation can cause serious brain diseases such as Alzheimer's disease) (206). Li et al. conjugated C-dots to transferrin protein covalently, in order to use the transferrin as a drug carrier to cross the blood brain barrier and target the central nervous system, using zebrafish as a model organism (207). They tested C-dots alone and a conjugate of C-dots and transferrin by injecting each one of them into the heart of the zebrafish, to be circulated in the blood, then the central nervous system area was imaged using the confocal microscope. The observation of the *in vivo* studies showed that the conjugated C-dots have been delivered into the central nervous system, unlike the C-dots (207).

1.5.3 Polymers

The polymers have existed naturally since the beginning of the life, such as DNA, RNA, proteins, and polysaccharides, which are essential elements in plant and animal life (208). On the other hand, man has been using some natural polymers in clothing, shelter, decoration, tools, and writing materials. Yet, the real discovery of the polymers did not happen until the nineteenth century when Thomas Hancock in 1820 added some additives to the natural rubber resulting in easier moulding and masticated material due to the change in the physical properties and become more liquid (208). Later on in 1839, Charles Goodyear discovered that the addition of sulphur with heating the natural rubber resulting change in the physical properties in form of thickness elimination and harder, establishing the vulcanization process. Few years later, in 1851 Charles's brother Nelson did vulcanization with addition of large amount of sulphur to produce a quite hard material in which commonly known as hard rubber, ebonite, or vulcanite (208). Followed by many other modifications leading to many discoveries in the polymers field.

Therefore, a polymer can be defined as: a substance that is composed of certain molecules in long sequences of one or more than one species of atoms or group of atoms, which are linked with each other by mostly covalent bond (208). The skeletal structure of polymers can be different based on the layout and the number of the sequence(s) that form the polymer. They can be either linear such as branched and network or they can be cyclic as shown in Figure 79 (208).

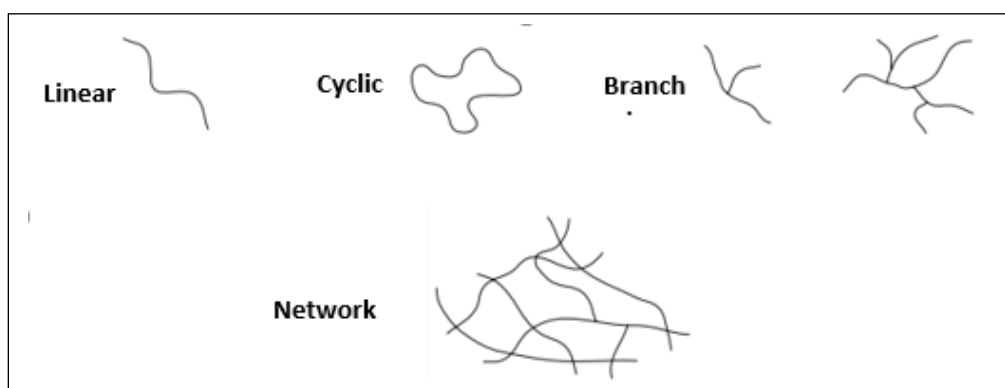


Figure 79: Skeletal structures representative of polymers (208).

Due to the lack of chain ends in the cyclic polymers, they acquire properties different to the linear counterparts. On the other hand, the branched polymers have branched or chains of linear polymers of significant length in which connected to the main chain at certain points can be called the junction points that characterised depending on the number and the size of the branches. While the network polymers are with three-dimensional structure, where each chain is connected to other chains within the same polymer by a sequence of junction points resulting crosslinking. Furthermore, the network polymers characterised by the crosslink density or as known as the degree of crosslinking in which is depending on the number of the junction points per unit volume. The formation of branched and network polymers can be done by polymerization process, alternatively they can be linked together by crosslinking with pre-existing chains (208).

The differences in the skeletal structure results in big differences in the polymers properties, e.g., the linear polymers acquire a melting point higher than the branched polymers. On the other hand, the network polymers do not melt under heating and cannot be dissolved. They can swell in compatible solvents due to the presence of high-density crosslinking. The crosslinking can be increased by the vulcanization process, therefore polymers with less sulphur resulting flexible elastomer, and more rigid with high crosslink density (208).

In addition to the traditional skeletal structures that have been explained, there has been a rising interest in skeletal forms of macromolecular polymers, are the dendrimers, and the hyperbranched polymers, as shown in Figure 80. The dendrimers are a class of highly branched polymer with a well-defined structure and molar mass. While the hyperbranched polymers are similar in the skeletal to the dendrimers but with much less well-defined structure and molar mass. The structure of these two classes of polymers resulting unusual properties to the previous skeletal structural of polymers, such as: they have voids and channels within the molecular structure, despite the fact they are crowded, due to the high level of branches. In addition to large number of end functional groups, as well as the periphery in which can be highly functionalised with ligands, drug, and targeting molecules, resulting good cargo molecule which can be good candidate for drug delivery applications (208).

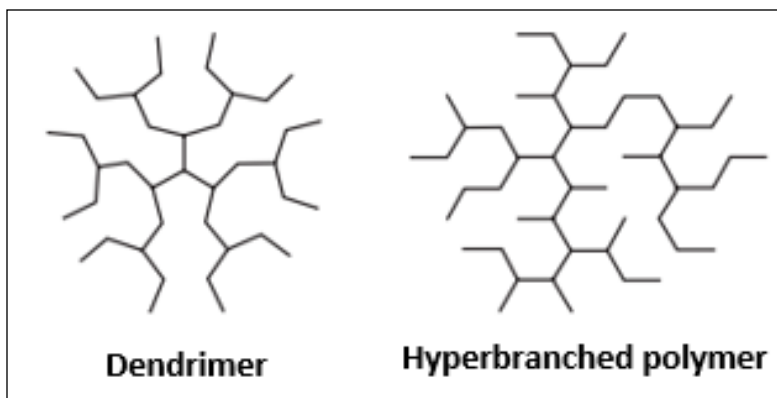


Figure 80: Skeletal structures representative of dendrimers and hyperbranched polymers (208).

Depending on the type(s) of segments that forms the polymer, they can be divided into two groups: the homopolymers and the copolymers.

The homopolymers are polymers composed of one species of monomer, by the definition of the homopolymer word, it can also mean that the polymer is composed of repetitions of the same type of a unit as shown in Figure 81. The homopolymer can be written using one letter in which refers to the unit or the monomer and repeated times n in between brackets like such as; $\sim A-A-A-A-A-A-A \sim$, in which A refers to the monomer or the unit which repeated n times to form the homopolymers (208).

The copolymers are polymers composed of two or more than one species of monomers, by the definition of the word copolymer, it can also mean that the copolymer is a polymer that composed of more than one type of repeat unit (two or more) as shown in Figure 79. The repetitions of the units in the copolymers can be either organized resulting alternately arranged copolymer such as $\sim A-B-A-B-A-B-A-B-A-B \sim$, or it can be randomly repeated resulting random copolymer such as $\sim BBBA \text{ --- --- } BBA-B A-A \sim$ (208).

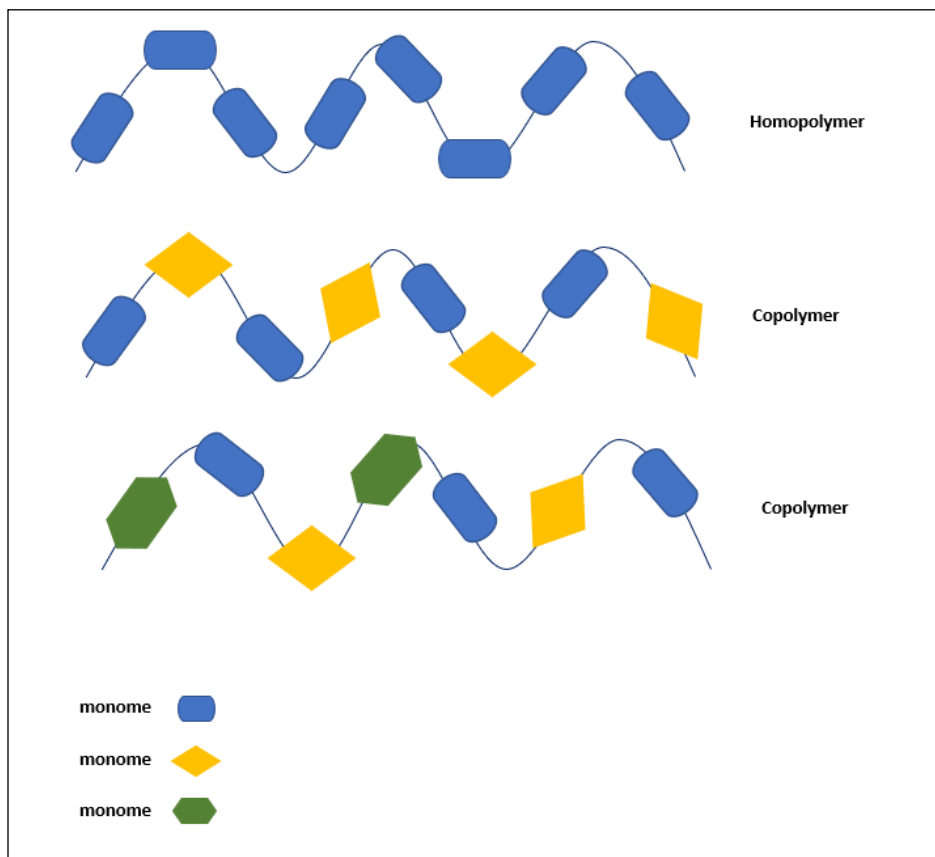


Figure 81: Composition of the homopolymers and copolymers.

1.5.3.1 Classification of polymers

Polymers can be classified based on the underlying molecular structure into thermoplastic, elastomers, and thermosets, where the thermoplastic can be subclassified into crystalline and amorphous, as shown in Figure 82 (208).

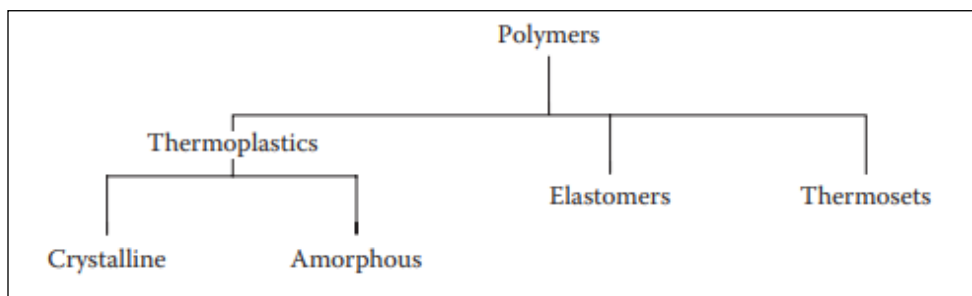


Figure 82: Classification of polymers (208).

The thermoplastics are known as the plastic and they can be either linear or branched polymers, in which can be turned into liquid when the heat applied. They can also be moulded remoulded to any shape following different techniques such as extrusion, and injection moulding. The thermoplastic is considered the largest class in terms of the population of the polymers that involves in the commercial manufacturing. After the thermoplastics liquidised due to heating, it is very hard to recrystallise with cooling, this is because the crystallising process requires significant ordering of the highly coiled and crosslinked macromolecules in the liquid state. Even if they do crystalline, the crystallization is not perfect, in which can be called semi-crystalline because they will be forming crystalline structure with amorphous regional. On the other hand, the amorphous polymers are completely amorphous and incapable of forming crystalline structure even by annealing. The amorphous polymers as well as the semi-crystalline polymers, can be characterised by their glass transition temperature T_g (in which the temperature the material immediately transform from glassy state (i.e., hard) into the rubbery state (i.e., soft)). The transition of the polymers corresponds to the sudden change of the chain motion, where below the T_g the polymer chains are frozen and unable to move. The increase in the T_g and the T_m (the melting temperature) resulting increase in the chain stiffness as well as the force of the intermolecular attraction (208).

Elastomers are crosslinked rubbery polymers, mainly networks, in which are fixable and can be stretched up to 10 folds the original dimensions, that can restore the original dimensions once the stress applied was released. The most significant property of the elastomer is the low crosslinking in the structure, and this is the reason of the flexibility, in which can also be called

the rubbery polymer. Yet, the low level of crosslinking enables them to restore the original dimension and to prevent the permanent flow, after the stress was released (208).

Finally, the thermosets are rigid polymers and are mainly formed of network polymers, in which the chain motion is very restricted by the crosslinking due to the high degree of crosslinking degree. The elastomers have good level of stability once they were formed, and they are intractable and not easy to degrade even under heat. They can also become fluids under the application of heat. Therefore, to be used in artefacts they need to go through processes such as compression moulding, in which require minimum amounts of flow (208).

1.5.3.2 Polymerization process

The polymerization is the process of creating polymers, it can be defined as a multi steps chemical reaction in which including linking monomers to produce a chain or multichine crosslinked compound called the polymer (209). The polymerization process can be divided into five approaches which are: polymerization by condensation, chain-reaction polymerization, step growth polymerization, and ring opening polymerization.

The polymerization by condensation is the strategy in which two different symmetric bifunctional monomers (i.e., XaaX and YbbY) react to produce a polymer with aabb repeating sequence (210). It is based on the condensation chemical reaction between two molecules (monomers) resulting a polymer and a small by-product molecule such as water or ethanol (211). An example of the condensation polymerization is the poly esterification of a hydroxy acid, in which includes intermolecular esterification reaction between two monomers resulting a dimer as shone in the chemical equation:



The reaction can stop here, or it can be followed by another step in which the produced dimer can react with a monomer by the condensation reaction resulting trimer and a water or ethanol

as by-product. Alternatively, the produced dimer can react with another dimer by condensation reaction to produce a tetramer and water or ethanol as a by-product (211).

The chain reaction polymerization is based on the addition of monomer(s) into an activated (initiated) form of the monomer, in which including change in the bonds from an sp^2 to an sp^3 bond (212). The chain reaction polymerization is a three steps reaction that it needs to be initiated or catalysed to start the reaction, as it cannot be a spontaneous reaction making the first step as the initiation step followed by the propagation step which can be called the growth step, and finally ends with the termination step (212). The initiator molecule can be either cation, anion, or a free radical, and the mechanism of the chain reaction polymerization described in Figure 83.

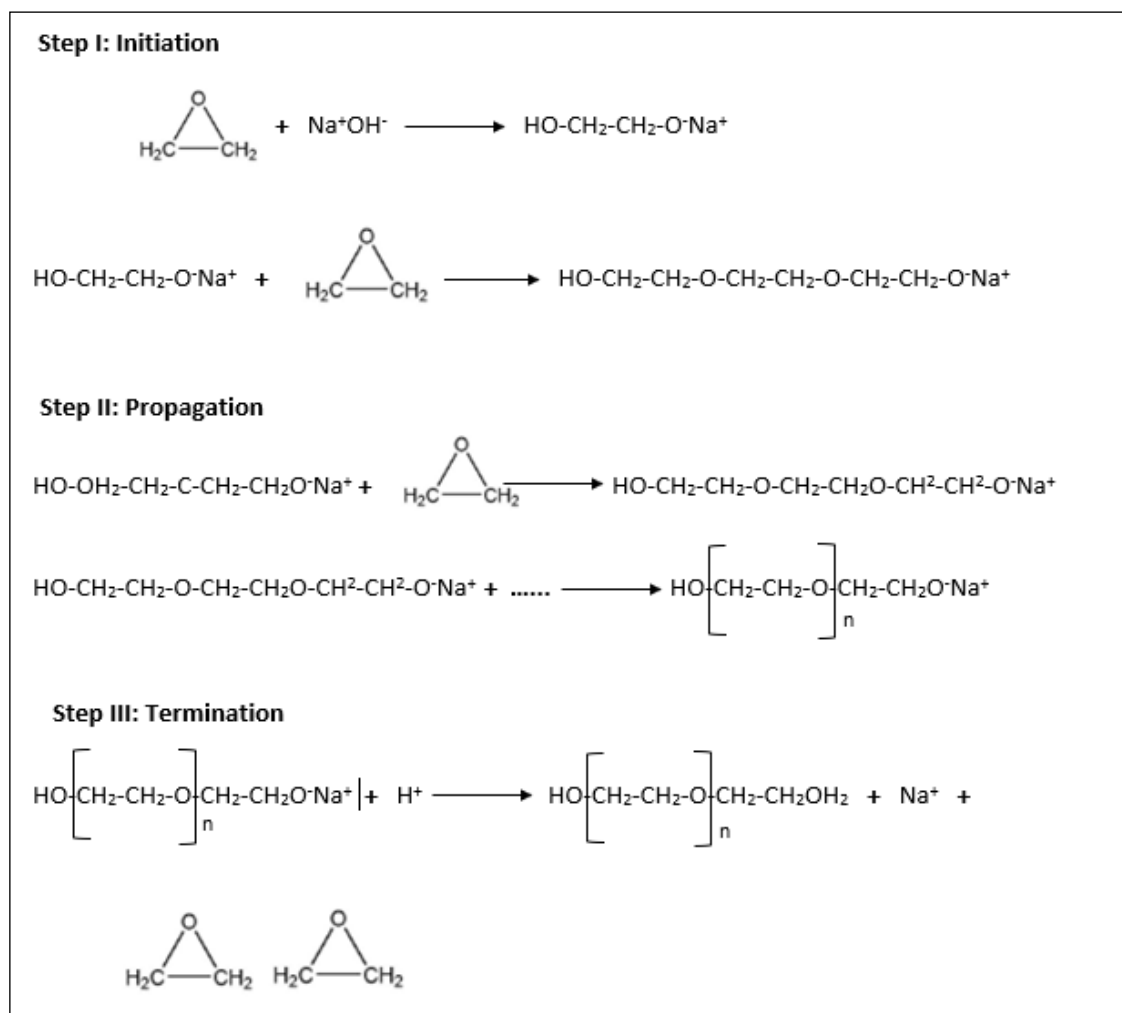


Figure 83: Illustration of the mechanism of action of the chain reaction polymerization of polyetylenglykol.

In the initiation step the free radical was formed to initialise the reaction as shown in Figure 83 step I, then an addition of monomer process starts in the propagation step resulting a longer chain with a free radical in which can call the active site, as shown in Figure 83 step II. The addition of monomers stops at certain time, then tow chains with free radicals ends attached to each other in the terminal step creating the polymer of choice as shown in Figure 83 step III (212).

Step growth polymerization is an approach in which does not require an initiation and it is a slow process of building up the polymer chain, in which might include building up chains then crosslinking them at the same time (212). The step growth polymerization requires difunctional monomers or different classes of difunctional monomers to form either linear high molecular weight polymer or crosslinked high molecular weight polymer, therefore it depends on the functional groups of the monomers. A monomer can react with another monomer via the functional groups to form a dimer, and the resulting dimer can react with another monomer or dimer to form a trimer or tetramer respectively, in which each functional group can react at the same time to produce a high molecular wight polymer over long period of time, as shown in Figure 84.

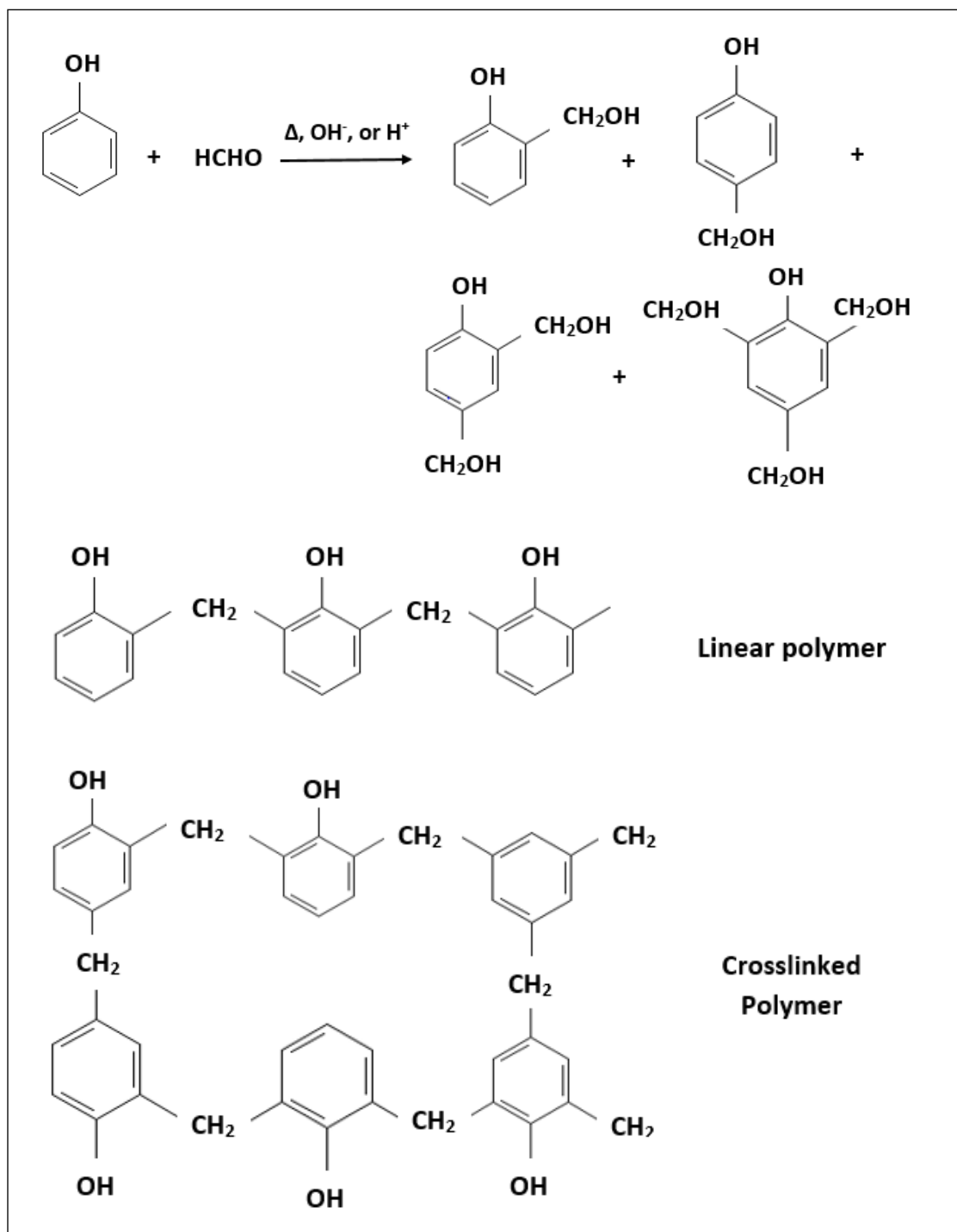


Figure 84: Illustration of the step growth polymerization strategy with the possible products.

Figure 84 shows the polymerization following the step growth approach, in which shows the different monomers that can be connected to each other by the functional groups to build up different products possibilities i.e., linear polymer or crosslinked polymer (212).

Ring opening polymerization is based on the presence of cyclic monomer(s), as it considers opening the cyclic monomer(s) to create a non-cyclic polymer either, linear or branched polymer as shown in Figure 85 (213).

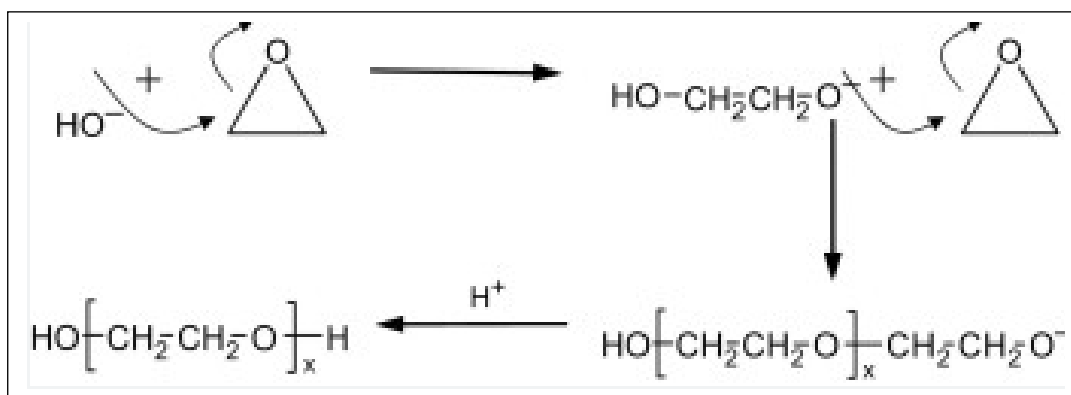


Figure 85: Illustration of polymerization of polyethylene oxide following the ring opening approach (214).

The ring opening polymerization can be simple addition monomer(s) into a growing polymer chain, and it can be more complicated including the use of activated monomers (215). The importance of the ring opening polymerization comes from the use of it in the synthesis of very specific polymers with controlled properties, the production of synthetic polymers in which are variants to some naturally occurring polymers, and synthesis of biodegradable polymers in which can be used in the medicinal, pharmaceutical, and agricultural applications (215). The ring opening polymerization has several characteristic features including the capability of introducing some functional groups into the polymer main chain such as ester, ether, amide, or carbonate in order to form polymers can be used in many industrial applications such as; polyethylene oxide, and polypropylene oxide (213).

1.5.3.3 Applications of polymers conjugated C-dots

Sun et al. functionalised C-dots with polymers to improve the PL properties of the synthesised C-dots. They followed the laser ablation method using a mixture of graphite and cement in the presence of water vapour and argon gas as the carrier (22). The synthesised C-dots exhibit an average diameter of 5 nm, with QY = 4% and λ_{ex} dependant emission PL properties. They used diamine-terminated oligomeric poly (ethylene glycol) $\text{H}_2\text{NCH}_2(\text{CH}_2\text{CH}_2\text{O})_n\text{CH}_2\text{CH}_2\text{CH}_2\text{NH}_2$ (average $n \sim 35$, PEG_{1500N}) as a surface passivating agent in which they mixed the PEG_{1500N} with C-dots were treated with an acid and heated the mixture to 120 °C for 72 h (22).

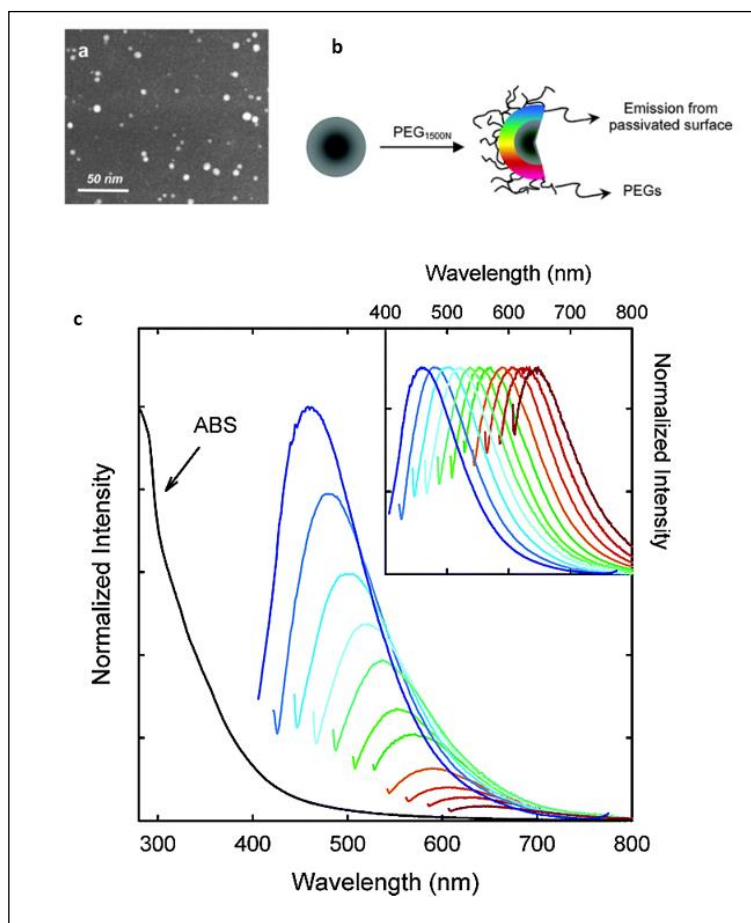


Figure 86: C-dots synthesized by Sun et al.: a) TEM images, b) the passivated C-dots with PEG_{1500N} exhibit better photoluminescence properties, and c) absorption of photoluminescence spectra of the passivated C-dots under different wavelength starting with 400 nm and increment of 20 nm (22).

It has been observed that the passivated C-dots have not had a significant size increase due to the conjugation with polymer as shown in Figure 86 a. Yet, the PL properties have been improved as shown in Figure 86 b, as the passivated C-dots covers an emission of a broader wave lengths reaches into the near infrared region when excited at 400 nm with 20 nm increment as shown in Figure 86 c. Furthermore, the QY Has been increased up to 10% (22).

Kuo et al. synthesised N-doped C-dots and functionalised them with polymers for the purpose of cancer cell targeting and bioimaging, they followed the oxidation method using graphite as the source of carbon, in which they mixed the graphite with sodium nitrate and dispersed the mixture in sulfuric acid, then the mixture was heated at 35 °C for 30 minutes (216). The synthesised C-dots exhibit an average size of 7 nm, with QY = 0.6% and λ_{ex} dependant emission (217). Then the synthesised C-dots have been conjugated with polyethylene amine (PEI), by forming a covalent bond between the carboxylic group on the surface of the C-dots and the nitrogen of the PEI (217). The conjugated C-dots did not show any difference in the size of the C-dots. Yet, the QY was nearly increased by 10 folds, as the conjugated C-dots exhibit a QY = 6.2% (217). For cancer cell targeting they used epidermoid carcinoma cell line (skin cancer cells, A431), in which the cells exhibit an over expression of anti-epidermal growth factor receptor (Ab_{EGFR}) (217). Therefore, the conjugated C-dots were attached to Ab_{EGFR} antibody for labelling to increase the specificity. The cells were grown and treated with the conjugated C-dots that are attached to the Ab_{EGFR} antibody and incubated at 37 °C and 5% of CO_2 , then two photon luminescence microscope (TPL) was used for the bioimaging, and the images are shone in Figure 87.

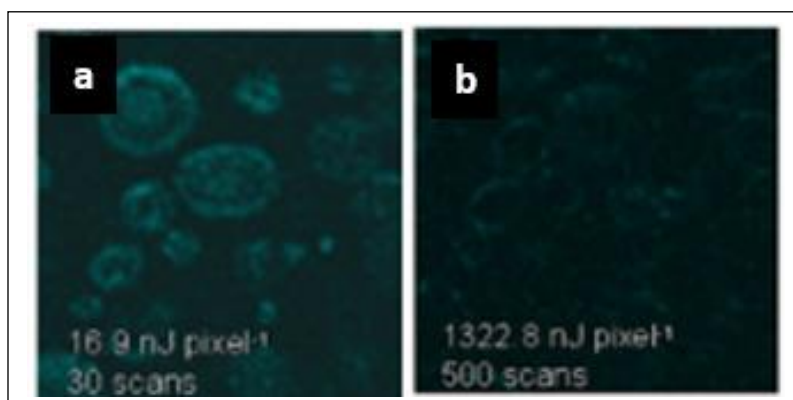


Figure 87: TPL images of A431 cells: a) were treated with conjugated C-dots attached to Ab_{EGFR} antibody, and b) cells treated with the conjugated C-dots (217).

In Figure 87 a, the cells were treated with the conjugated C-dots an attached to Ab_{EGFR} antibody shows better cellular uptake due with more accumulation of the materials. On the other hand, the Figure 87 b shows that the cells which were treated with the conjugated C-dots have shown successful uptake of the system, yet the intensity is not that high which indicates that the uptake is not as good as the cells treated with the conjugated C-dots an attached to Ab_{EGFR} antibody (217).

1.5.3.4 PEI/QAS

The PEI/QAS is a conjugate compound with bactericidal and fungicidal activity, which is composed of a quaternary ammonium salt conjugated with Polyethyleneimine (PEI) via a covalent bound (218). Refer to Figure 88 for the chemical structure of the PEI/QAS.

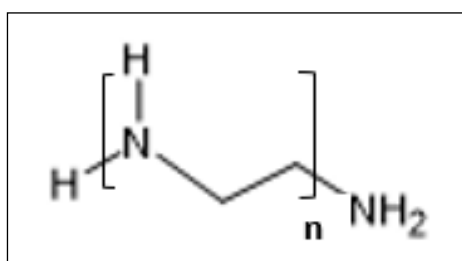


Figure 88: Illustration of the chemical structure of the quaternary ammonium salt conjugated with Polyethyleneimine PEI/QAS.

Lin et al. modified cotton and wool for the purpose of creating clothes with bactericidal activity in order to be used as beds sheets and gowns in the hospitals to prevent and/or reduce the transition of bacterial infections (219). They simply washed a 5X5 cm cotton cloth very well in distilled water, then dried it and soaked it in a solution of 5 mL of 4-bromobutyrylchloride in 95 mL of dry chloroform to acylate the cloth, in which was stirred at room temperature for 5 h as shown in Figure 89 step 1 (220). After the cloth was acylated, it has been washed with chloroform in order to remove any remaining of the unreacted 4-bromobutyrylchloride, in which then was sacked in a mixture of 10 g of PEI, 0.1 g of potassium hydroxide, and 90 mL of tert-amyl alcohol, as shown in Figure 89 step 2 (219). The cloth was stirred in the mixture at 75 °C for 9 h, then the PEI-cloth was washed with methanol to remove the unreacted PEI as well as the other chemicals, followed by drying naturally in the air (221). The PEI-cloth then was soaked in a solution of 0.1 g of potassium hydroxide, 10 mL of bromhexine, and 90 mL of tert-amyl alcohol, in which was stirred overnight at 75 °C (221). Then the PEI-cloth was washed with methanol, and finally was methylated using a solution of 10 mL of iodomethane in 90 mL of tert-amyl alcohol, in which was heated at 40 °C for 5 h in a sealed container, as shown in Figure 89 step 3 (222). Finally, the cloth was washed by methanol, then distilled water, and was soaked overnight with 1% liquid soap at 55 °C (219).

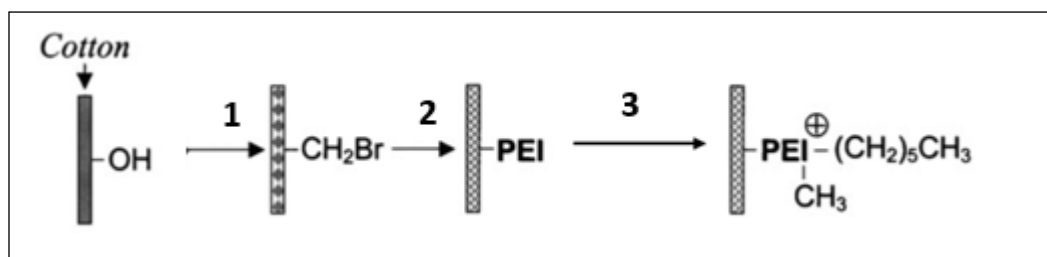


Figure 89: Schematic representation of the synthesis of methylated PEI-cloth. Step 1: the acylation of the cloth with 4-bromobutyrylchloride, step 2: the attachment of PEI, step 3: the methylation of the PEI-cloth using iodomethane (219).

The antibacterial activity of the methylated PEI-cloth was tested against the gram-positive bacterium *S. aureus*, using different PEI molecular weight of 750 kDa, 25 kDa, 2 kDa, and 0.8 kDa as shown in Figure 90.

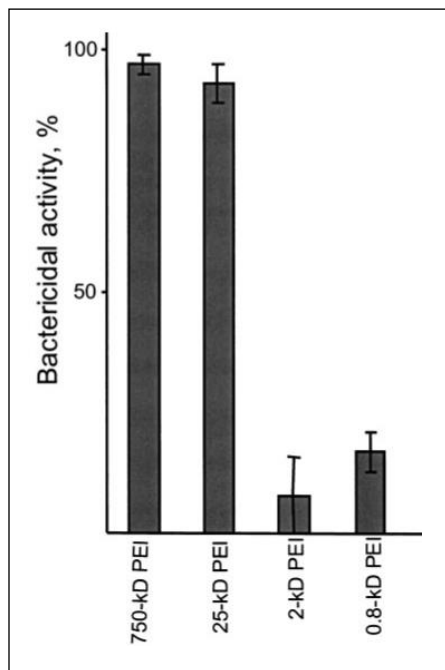


Figure 90: Bactericidal activities against air borne *S. aureus*, using PEI-cloths of different PEI molecular weights (219).

Figure 90 shows that the 750 kDa and the 25 kDa PEI exhibit very high levels of bactericidal activity, while the 2 kDa and the 0.8 kDa show very low levels of bactericidal activity, proving that the bactericidal activity is molecular weight dependent (219).

1.5.3.5 Jeffamine D-230

Jeffamine D-230 is a polymer from the polyamine family composed of repeating oxypropylene units as the backbone with two coordination sites of a primary amine on both ends of the chemical structure (223), (224). The molecular weight of the Jeffamine D-230 is around 2000 gm/mole, and the chemical structure is shown in Figure 91 (223).

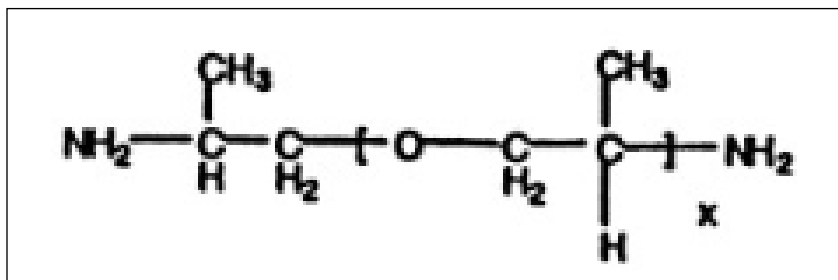


Figure 91: Illustration of the chemical structure of the Jeffamine D-230. $x = 33$ (223).

Jeffamine D-2000 has been used due to the presence of the primary amine groups, as the amine groups can covalently bonded to the carboxyl groups on the surface of the C-dots.

Due to the poly-ether backbone of Jeffamine D-230, it exhibits interesting curing properties in which make them good candidates as curing agents, in addition to many other properties such as: fixable backbone, low viscosity, safe to be used due to the very low toxicity, and biocompatible (225), (226).

Due to the flexibility of the Jeffamine as well as the biocompatibility properties, they can be used in synthesis of hydrogels. Yu et al. synthesised an antibacterial hydrogel using Jeffamine, in which have been improved the properties of the hydrogel in terms of the molar mass, as the Jeffamine increased the molar mass of the hydrogel (226). Furthermore, the Jeffamine significantly affect the three-dimensional architectural structure of the hydrogel, in which increased the pore size of the hydrogel, due to the reality of the role of the Jeffamine as a linker in the hydrogel network. Moreover, the use of Jeffamine resulting a hydrogel with regular pores distribution, in which is required in the biomedical applications such as drug delivery and wound healing gels (226).

Hydrogels are soft materials that are widely used as a base in many biological systems due to their structural functionality (227). The structure of the of the hydrogels is made of physically or covalently crosslinking of an amorphous polymer network, that can be achieved either during

the polymerization process using a multifunctional monomer as a crosslinker (227). Alternatively, it can be achieved via chemical post modification reaction of a produced polymers. The properties of the hydrogels depend on the materials that build them up, and the properties of the interactions between materials in the network structure system (228).

Krakovsky et al. prepared a hydrogel network using Jeffamine ED-2003 of 2000 gm/mol molecular mass, and polyoxypropylene bis(glycidyl ether) about 90 wt. % with 640 gm/mole molecular mass. They mixed the starting materials and stirred them at 100 °C for 15 min, then transferred the mixture into a Teflon mould (229). Then a curing reaction have been done by heating the materials at 120 °C for 48 h. The produced network has been purified by triple extraction using toluene solvent, then the network has been derided firstly naturally in the open air followed by drying using vacuum oven at 40 °C for 48 h, producing transparent hydrogel (229).

Chapter 2: Experimental section

2.1 Materials

Citric acid monohydrate 99% (CA) (Alfa Aesar), ethanolamine $\geq 99\%$ (EA) (Alfa Aesar), nitric acid (Alfa Aesar), distilled water (Sigma-Aldrich), snakeskins dialysis bags with 3.5 K MWCO 22 mm (Thermo Fisher scientific), dialysis tubing benzoylated 1.5 K MWCO 10 mm (Sigma-Aldrich), 1-methyl-2-Pyrrolidone (NMP) (Sigma-Aldrich), piperidine (Alfa Aesar), N,N-dimethylformamide (DMF) (Sigma-Aldrich), Dichloromethane (DMC) (Alfa Aesar), Wang resin (Sigma-Aldrich), Lysine (Alfa Aesar), 2-(1H-benzotriazol-1-yl)-1,1,3,3-tetramethyluronium hexafluorophosphate (HBTU) (Alfa Aesar), N-EthylDiisopropyleamine (DIEA) (Alfa Aesar), Trifluoroacetic acid (Sigma-Aldrich), Triisopropylsilane (Alfa Aesar), Tert-Butyl methyl ether (Alfa Aesar), Acetonitrile (Alfa Aesar), pure water for HPLC gradient (Alfa Aesar), Polyethyleneimine (Alfa Aesar), Sodium bicarbonate (Alfa Aesar), Anhydrous methanol (Sigma-Aldrich), Iodomethane (Alfa Aesar), N-hydroxysuccinimide (NHC) (Alfa Aesar), N-(3-dimethylaminopropyl)-N'-ethylcarbodiimide hydrochloride (Alfa Aesar), RGD peptide (Sigma-Aldrich), 2,5-(Bis(5-tert-butyl-2-benzo-oxazol-2-yl)thiophene (Thermo Fisher scientific), Isopropyl Alcohol 70% (Sigma-Aldrich), Dulbecco's Modified Eagle Medium (Thermo Fisher scientific), Fetal Bovine Serum (Sigma-Aldrich), L-Glutamine (Thermo Fisher scientific), Phosphate Buffered Saline (made in the lab), Trypan Blue (Sigma-Aldrich), virkon (Sigma-Aldrich), 3-[4,5-di-methylthiazol-2yl]-2,5-diphenyl-tetrazolium bromide (MTT) (Sigma-Aldrich), PrestoBlue (PB) (Sigma-Aldrich), Pluronic P123 (Sigma -Aldrich), Ibuprofen (Sigma-Aldrich), Temozolomide (Sigma-Aldrich), HeLa cells (Sigma-Aldrich), U87 cells (Sigma-Aldrich), T98G cells (Sigma-Aldrich), GC-1 SPG cells (Thermo Fisher scientific), *Escherichia coli* (K12), *Staphylococcus aureus* (ATCC 25923) (Thermos Fisher scientific), nutrient broth (breckland Scientific), $\frac{1}{4}$ strength Ringer's solution (Thermo Fisher scientific).

2.2 Synthesis and purification section

2.2.1 Synthesis and purification of C-dots

The synthesis of C-dots was done by following the hydrothermal approach, as was reported by Krysmann et al. (7). The synthesis involves using 30 g of CA monohydrate and 28 g of EA with a molar ratio of 1:3 (CA to ethanolamine), in which they were mixed in a round bottom flask as shown in Figure 93 a. The mixture was heated in a graphite bath at 180 °C for 30 minutes under water reflux and continuous stirring as shown in Figure 93 b to form the precursor of the C-dots (the chemical equation is shown in Figure 92 A). The precursor is a yellow sticky material as shown in Figure 93 c.

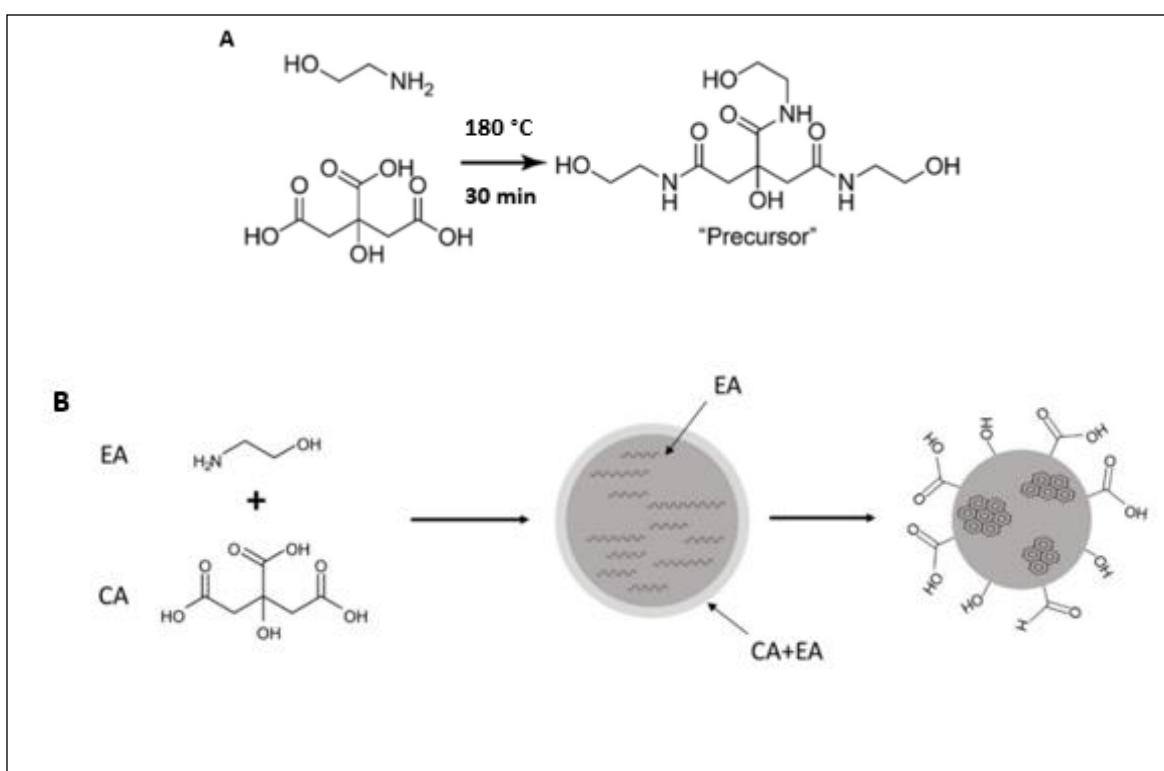


Figure 92: Illustration of the chemical reaction for the synthesis of C-dots, A) the generation of the precursor (230), and B) the full synthesis of the C-dots (231).

Then the precursor was heated in a graphite bath at 230 °C for 30 minutes with continuous stirring and without reflux as shown in Figure 93 d to form C-dots230, in which the colour turns into dark brown material. After the formation of the C-dots230, they were transferred into a porcelain crucible as shown in Figure 93 e. The C-dots230 have a narrow size distribution with an average diameter of 19 nm as shown in Figure 94 a (7).

The C-dots320 then were heated using furnace at 300 °C for one hour with a heating rate of 3 °C /minutes to form the C-dots. The synthesised C-dots are black solid material as shown in Figure 93 f, in which have been left to cool down naturally resulting the C-dots with an average diameter of 8 nm as shown in Figure 94 b (7). An illustration of the chemical reaction of the C-dots is shown in Figure 93 b.

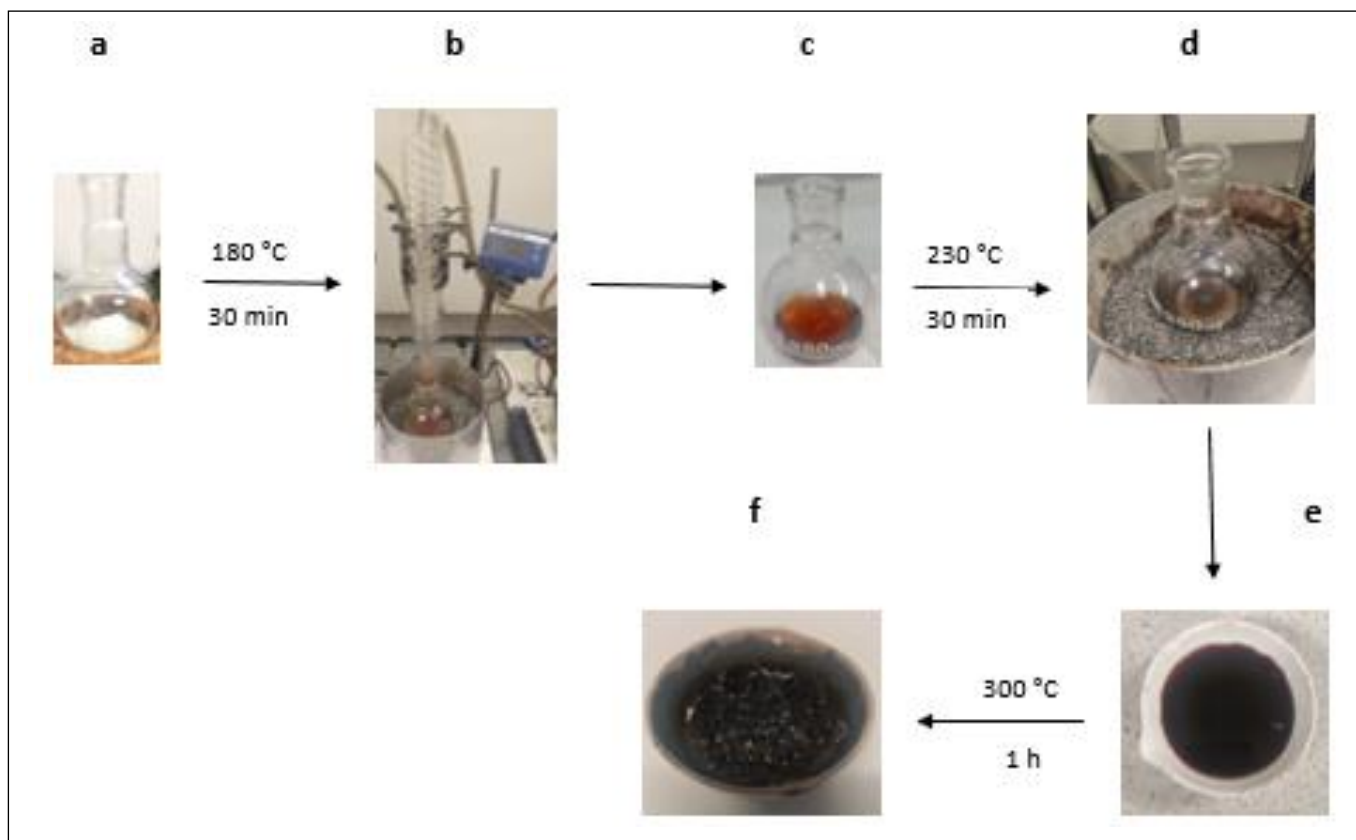


Figure 93: Illustration of the hydrothermal synthesis of C-dots. a) the mixture of the starting materials b) the generation of the precursor under reflux c) the precursor material, d) the generation of the C-dots230, e) the C-dots230 material, f) the generation of the C-dots.

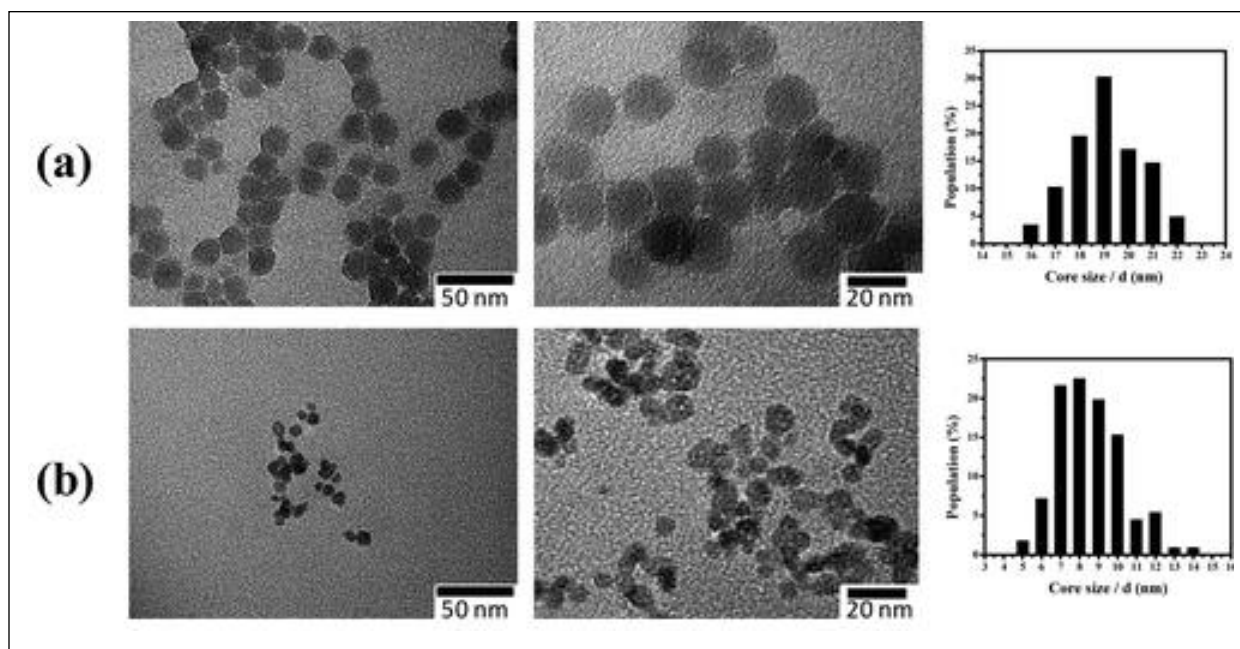


Figure 94: TEM images and size histograms of (a) C-dots230 and (b) the C-dots (7).

After the C-dots had cooled down, they were transferred into a mortar and pestle in which were grinded and crushed very fine into powder. The powder then was transferred into a round bottom flask to be oxidated in which were dispersed in a 200 mL solution of 3 molar nitric acid and heated in a graphite bath at 100 °C for 16 h under water reflux and continuous stirring as shown in Figure 95 to passivate the surface of the C-dots with hydroxyl group. After the oxidation a dark brown solution formed and left to cool down naturally (the chemical equation shown in Figure 92 B).



Figure 95: Passivation of the C-dots using nitric acid with reflux.

The purification of the C-dots, the oxidated solution was double filtered to get rid of the large nonreacted particles using vacuum filtration with filter paper, then using Buchner funnel and filtration membrane with 40 μm pore size. To get rid of the small particles, the collected solution was dialysed using snakeskins dialysis bags with 3.5K MWCO, 22 mm against deionised water as shown in Figure 96 a. The dialysis water turned dark at the beginning of the dialysis process due to the impurities as shown in Figure 96 b, in which the water has been changed few times until the dialysis water is clear, which indicates no impurities as shown in Figure 96 c. Then the pure C-dots solution was transferred into vials to be frozen and dried using the freeze dryer, producing sponge like dark brown material.

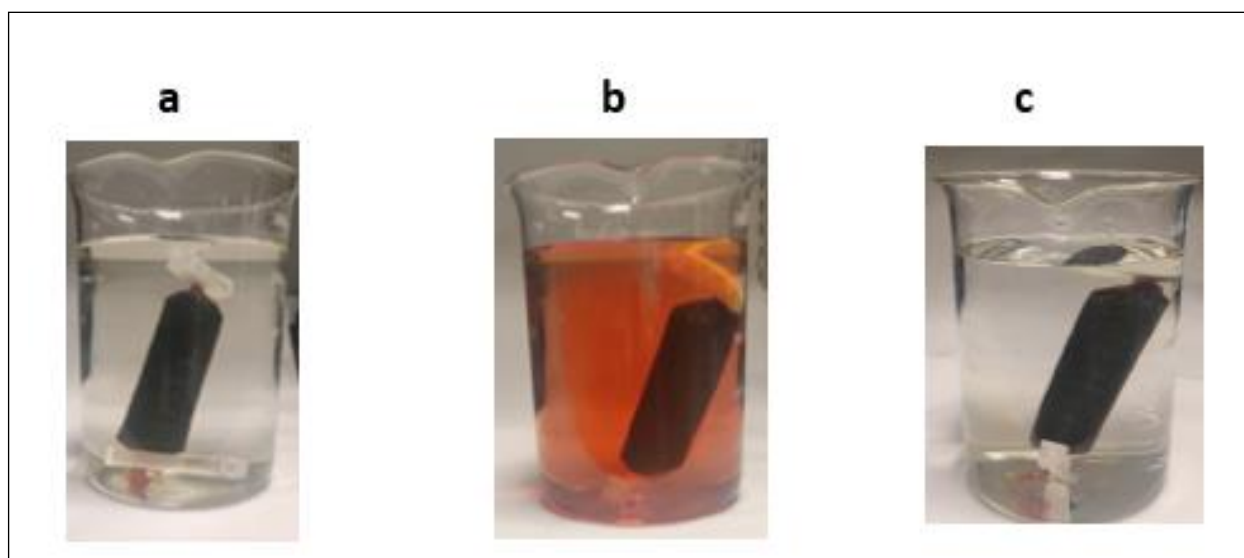


Figure 96: Purification of the C-dots using dialysis a) at zero-time, b) after a 3 h of the dialysis, c) completely purified C-dots.

2.2.2 Synthesis and purification of K7

The synthesis of K7 was done following the solid phase peptide synthesis approach, in which a Biotage Initiator and SP wave Semi automated peptide synthesiser were used. Different solutions were used for the different steps of the synthesis in which has been explained previously in ('Solid phase peptide synthesis' in chapter one) such as swelling, coupling, deprotection, and washing. The solutions systems have been used are: Solution 1 is NMP,

Solution 2 is 25% piperidine solution in DMF, Solution 3 is DMC, and Solution 4 is DMF. The synthesis of K7 were done following few steps:

- The resin used is Wang resin that has lysine attached to it protected with Fmoc group (as the temporary protection) and Boc group (as the permanent protection) as shown in Figure 97 and explained in the solid phase peptide synthesis.

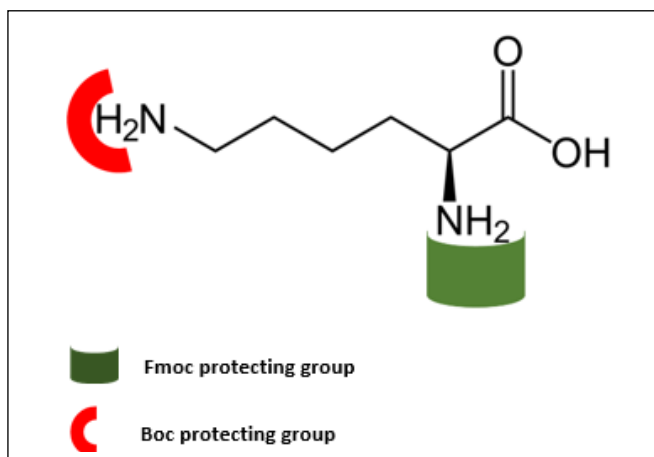


Figure 97: Chemical structure of the protected Lysine used for the synthesis of K7. The Fmoc is the temporary protecting group that protects the terminal NH_2 of the Lysine. The Boc is the permanent protecting group that protects the NH_2 of the R group of the Lysine.

- 0.2 g of the resin was put in 10 mL reacting chamber, to initialise the swelling process.
- The swelling process followed by a deprotection step to remove the Fmoc and make the lysine ready to be attached to the next added lysine as shown in Figure 98.

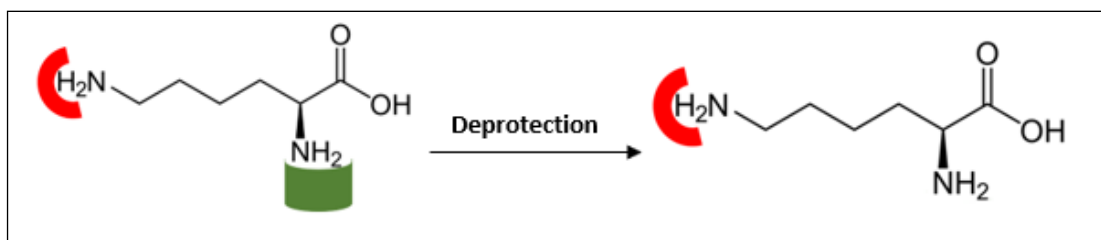


Figure 98: Deprotection of the Lysine using the peptide synthesizer, removing the Fmoc that makes the Lysine ready to be attached to the next Lysine via peptide bond as shown in Figure 60.

- A lysine moiety was added 6 times individually to produce the 7 lysine K7, as the first lysine attached to the resin.
- To make the lysine ready to be attached, it should be mixed with 0.14 g HBTU.
- The lysine was dissolved in 1.5 mL of 1-methyl-2-Pyrrolidone (NMP) and mixed with a 0.11 g of 2-(1H-benzotriazol-1-yl)-1,1,3,3-tetramethyluronium hexafluorophosphate (HBTU) dissolved in 1.425 mL of NMP.
- Then 285 μ L of a solution of N-EthylDiisopropyleamine (DIEA) in NMP was added to activate the lysine to enable it to be attached to the activated lysine in the reacting chamber in the peptide synthesiser, only 5 minutes before the addition to the reaction chamber.
- Once the activated lysine was added into the reaction chamber, it will be attached to the previously added lysine then deprotected (both processes have been done by the peptide synthesiser).
- Each attachment process and each deprotection process must be followed by a washing step using 0.75 mL of DMF to wash off and discard the unreacted chemicals.
- By the end of the addition of the 6th lysine, the result is a peptide with 7 lysine moieties attached covalently to the resin.
- Following the solid phase peptide synthesis, a cleaving process has been done to detach the peptide from the resin and to remove the remaining Boc side protecting groups from the peptide chain.
- The cleaving process done by transferring the peptide into a glass vial, and 20 mL of a scavenger solution was added into the peptide.
- The scavenger is made of 95:2.5:2.5 volume ratio of trifluoroacetic acid, water and triisopropylsilane respectively.
- The peptide and the scavenger were incubated at room temperature for 3 h in a shaker incubator. During the incubation, the resin beds were detached from the peptide.
- After the incubation, they were filtered using disposable glass pipettes with cotton wool inside as a filter in order to trap all the resin beds inside the pipette as shown in Figure 99.

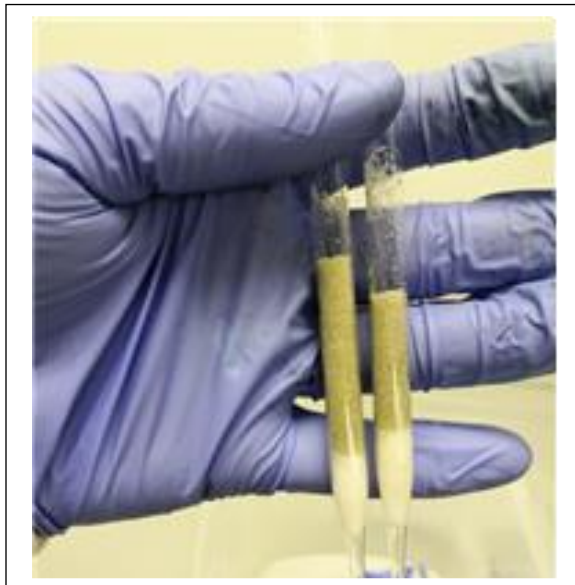


Figure 99: Filtration of the K7 after the resin was cleaved, showing the beds of the resin.

- The filtrated peptide solution was transferred into a round bottom flask to concentrate the peptide solution using rotary evaporator at 21 C°.
- The concentrated peptide solution then was transferred into a falcon tube and was cooled down using an ice bath.
- Then the peptide was precipitated using a spray of cold tert-Butyl methyl ether strongly, in which a white precipitation/ thick suspension of peptide formed.
- The precipitation/ thick suspension was placed in the fridge overnight for further precipitation.
- The supernatant was sucked up using a pipette leaving the peptide precipitation, in which were dissolved in distilled water in order to make it ready for the purification process.

The purification of the peptide was done using Agilent Technologies 1220 Infinity LC HPLC, with autosampler and a Luna Omega 5 μm PS C18 100 Å, LC column 250 x 10 mm semi-prep column,

following the method in table 1. An OPenLAB CDS software used for the analysis of the HPLC results, further information about the HPLC process will be discussed in section 2.4.10.

Table 1: The HPLC method for separation the K7, A: water with 0.1% trifluoroacetic acid, B: Acetonitrile with 0.1% trifluoroacetic acid, with a flow rate is 3 mL/ minutes.

Time (min)	A%	B%
0	98	2
24	5	95
24.1	98	2
35	98	2

A 100 μ L of the peptide solution was injected into the HPLC, and the HPLC run was monitored in order to collect the outcome solution of the column as soon as the peak of interest starts showing on the graph, which will be the pure peptide in a solution of water. The peptide solution then was frozen, and the frozen peptide was dried using the freeze dryer. The solid peptide is a white candy cotton like material.

2.2.3 Synthesis and purification of PEI/QAS

The synthesis of PEI/QAS was achieved by mixing 1g of polyethyleneimine, 4.26 of iodomethane, and 20 mL of anhydrous methanol, in which they were heated in a graphite bath at 150 °C for 4 h under water reflux and stirring. Then 3.15 g of sodium bicarbonate were added, and the heating was continued for another 24 hours, the chemical reaction shown in Figure 100. Two layers were formed, a gooey yellow material at the bottom and a pale-yellow solution on the top, in which was discarded, and the gooey material was collected to be purified. The purification process has been done by mixing the gooey material with tert-Butyl methyl ether and stirred gently using glass rod for 10 minutes where the gooey material started

to solidify, and more liquid was produced. The liquid was discarded, and more tert-Butyl methyl ether was added following the same procedure for 4 times. The collected solid material was further dried using vacuum oven, producing a sticky light brown solid material. Figure 100 shows the chemical reaction for the formation of the PEI/QAS.

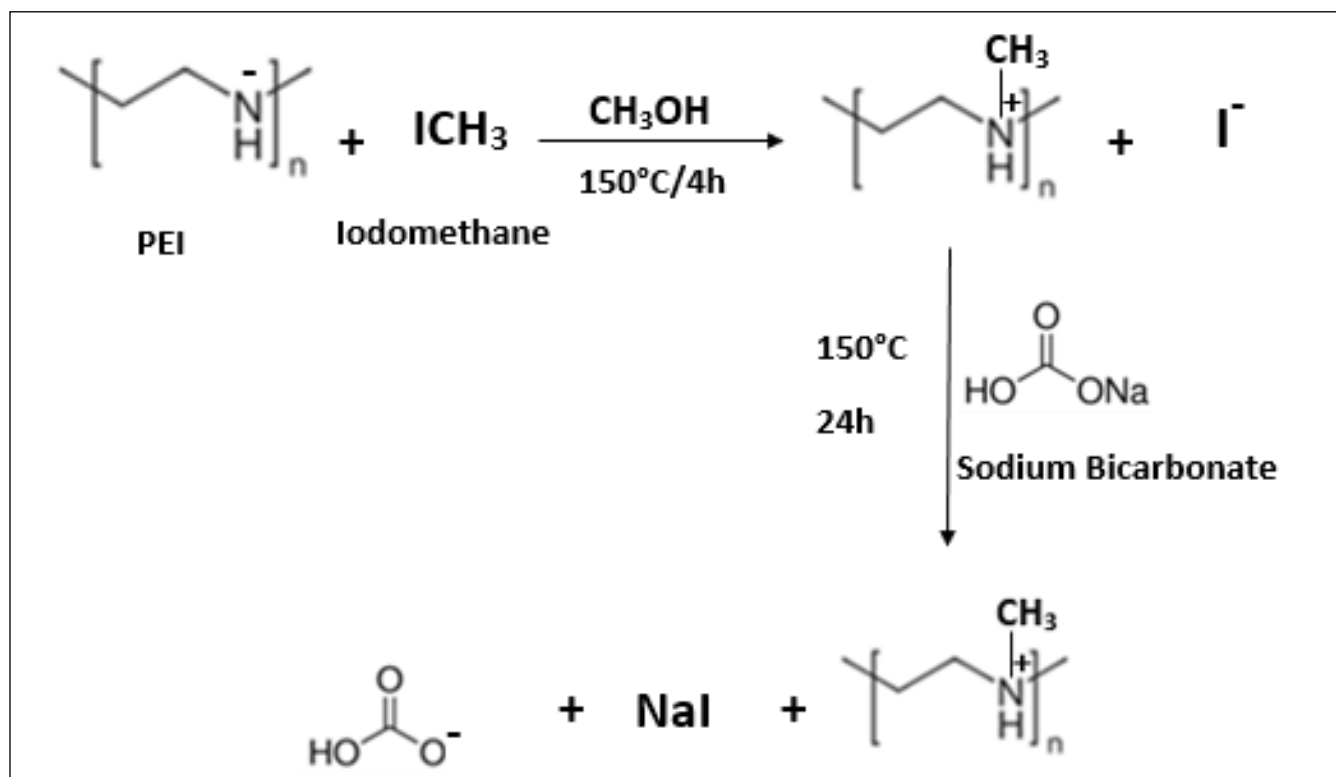


Figure 100: Illustration of the chemical reaction for the synthesis of PEI/QAS.

2.3 Conjugation section

2.3.1 Conjugation of C-dots with K7

For functionalizing C-dots with K7 peptide, a 1:1 molar ratio of N-hydroxysuccinimide (NHC) and N-(3-dimethylaminopropyl)-N'-ethylcarbodiimide hydrochloride (EDC) respectively as an activator for the formation of the amide bond between the COO^- on the surface of the C-dots and the terminal NH^+ of the K7. The molar ratio of the activators to the K7 is 1:1:1, and a 1:4 mass ratio of C-dots and K7 respectively were used, in which 0.214 g of N-hydroxysuccinimide and 0.365 g of N-(3-dimethylaminopropyl)-N'-ethylcarbodiimide were dissolved in 10 mL of distilled water and stirred for 20 min. Then a 1.7 g of K7 was mixed with 0.425 g of C-dots and dissolved in 10 mL of distilled water in which was stirred at room temperature for an hour. After that, both solutions were mixed and the whole solution was stirred at room temperature for 24 hours, Figure 101 shows the conjugation reaction of C-dots and K7.

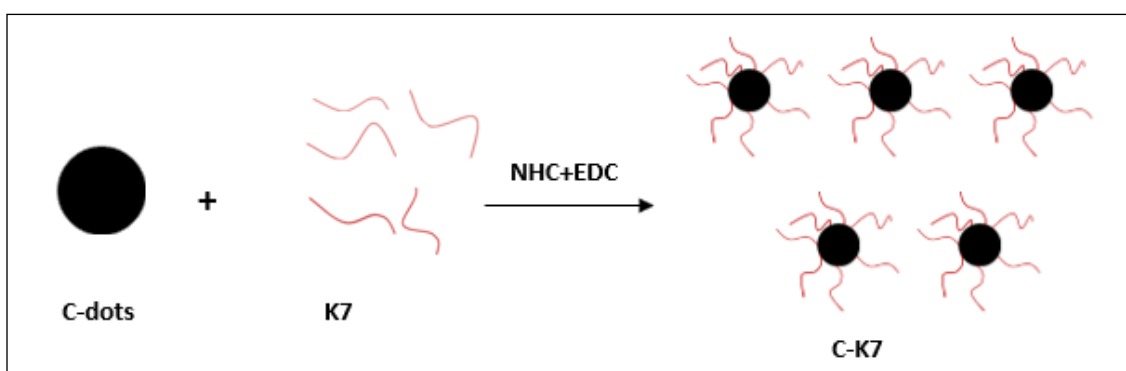


Figure 101: Illustration of the conjugation reaction of C-dots with K7.

The solution obtained was purified by using a dialysis tubing of 1.5 kda against deionised water for 5 days with regular change of the dialysis water. Then the solution was transferred into falcon tubes, and frozen. Then they were dried using the freeze dryer, resulting a light brown solid material resembles the C-dots, but fluffier.

2.3.2 Conjugation of C-dots with RGD

In this project the C-dots have been functionalised with the cell targeting peptide RGD, in which called RGD in this project.

The C-dots were conjugated with RGD by forming an amide bond between the hydroxyl groups of the C-dots and the amine groups of the RGD, following the same process of conjugating C-dots to K7. A 1:1:1 molar ratio of NHC, EDC, and RGD respectively, and the RGD:C-dots mass ratio is 4:1. A 0.214 g of hydroxysuccinimide, a 0.365 g of N-(3-dimethylaminopropyl)-N'-ethylcarbodiimide, a 0.65 g of RGD, and a 0.16 g of C-dots were used following the same C-dots conjugation to K7 process, Figure 102 shows the conjugation reaction of C-dots and RGD.

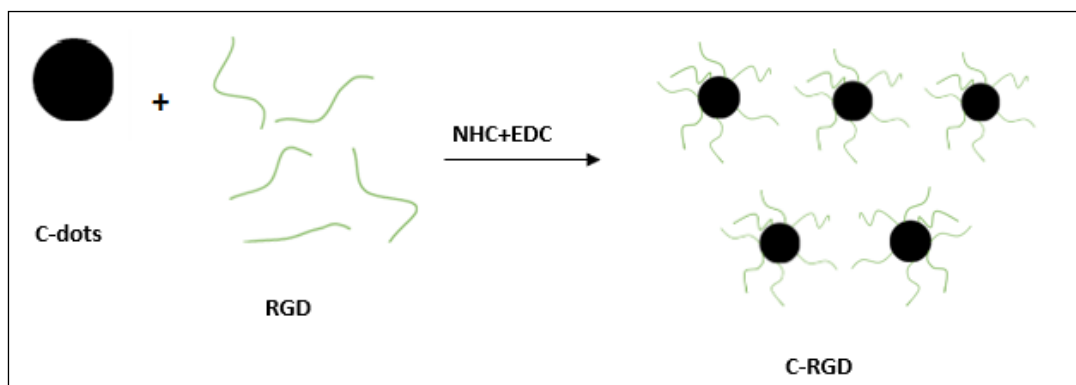


Figure 102: Illustration of the conjugation reaction of C-dots with RGD.

Furthermore, the purification process has been done following the dialysis process in which a 1500 kda from Sigma-Aldrich Dialysis tubing were used against deionized water for 5 days, and the water have been changed regularly. The solution was transferred into falcon tubes and frozen then dried using freeze drier, resulting a dark brown solid spongy like material.

2.3.3 Conjugation of C-dots with PEI/QAS

The C-dots were conjugated (as a form of functionalization of the C-dots) with the functionalised polyethyleneimine with iodomethane (PEI/QAS) by the formation of ionic bond between the negatively charged carboxyl or hydroxyl groups on the surface of the C-dots and the positively charged nitrogen in the PEI/QAS as shown in Figure 103. The conjugation reaction took place at room temperature by dissolving 0.75 g of PEI/QAS in 20 ml of water, and 0.25 g of C-dots were dissolved in 20 ml of water. Then both solutions were mixed and left for 24 hours on stirring at room temperature.

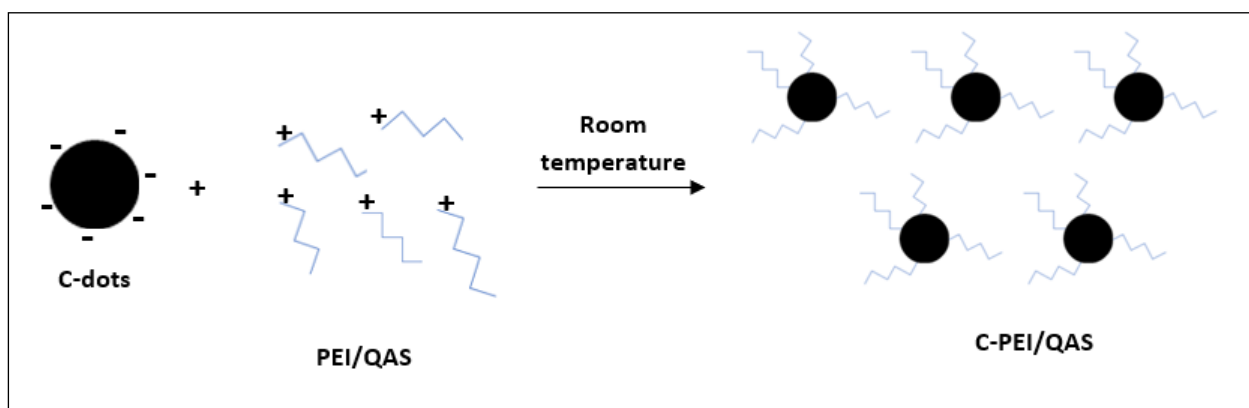


Figure 103: Illustration of the conjugation reaction of C-dots with PEI/QAS.

2.3.4 Conjugation of C-dots with Jeffamine

The C-dots were conjugated with Jeffamine following the same conjugation process that was used for the K7, the RGD, and the PEI/QAS, as well as the molar ratios and the purification process, Figure 104 shows the conjugation reaction of C-dots and Jeffamine.

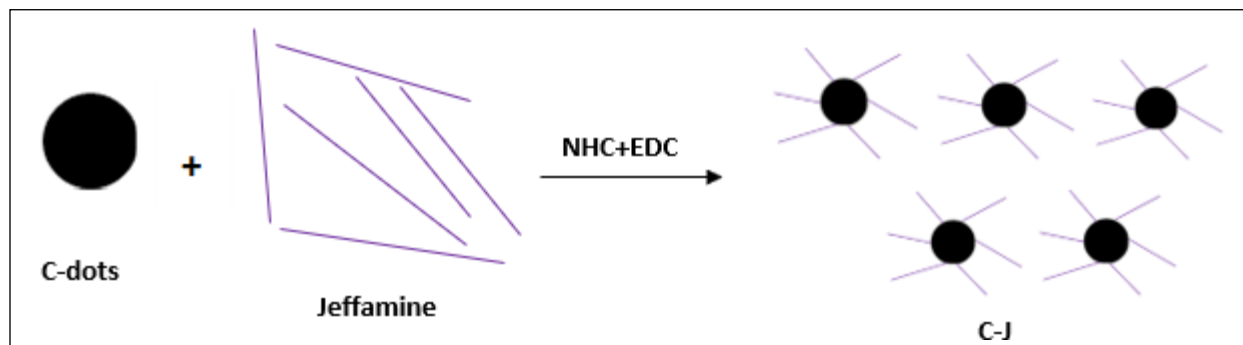


Figure 104: Illustration of the conjugation reaction of C-dots with Jeffamine.

2.4 Characterization of K7

2.4.1 High-performance liquid chromatography (HPLC)

The HPLC has been used for two purposes, the first one is for the analysis purpose using Agilent Technologies 1220 Infinity LC HPLC with autosampler and a bioZen 3 μm Peptide PS-C18, LC Column 150 x 4.6 mm with a flow rate of 0.7 mL/minutes to analyse the K7. The nature of the K7 peptide is hydrophilic, therefore it was expected to have the peak of interest in the hydrophilic region. Furthermore, due to the high molecular mass of the K7 of a 915.23 g/mole, it is expected that the peak of interest will not appear immediately.

For optimising the K7 analysis method, three potential methods were suggested by Agilent Technologies, the three methods have been tried are listed in table 2.

Table 2: The three methods that were suggested by Agilent technologies for the separation of the K7.

Mobile phase	A) 0.1% trifluoroacetic acid in H ₂ O B) 0.1% trifluoroacetic acid in acetonitrile		
Flow rate	3 mL/ minutes		
Method 1	Time (min)	%A	%B

	0	98	2
	24	5	95
	24.1	98	2
	26	98	2
Method 2	Time (min)	%A	%B
	0	97	3
	1	97	3
	31	40	60
	33	5	95
	34	5	95
	34.1	97	3
	36	97	3
Method 3	Time (min)	%A	%B
	0	97	3
	1	97	3
	51	40	60
	55	5	95
	55.1	5	95
	57	97	3

Method one was used first, it successfully separated the K7, yet we had an issue with the separation, as the first run went well but the second run was disturbed showing peaks at the beginning of the run. This indicates that the first run was not enough to separate all the materials that were injected to the column, therefore the stocked materials left the column at the beginning of the second run resulting disruptions in the peak's times. Therefore, we tried the second method as it has longer run time with higher percentage of the aqueous mobile phase compared to the oily mobile phase. The second method had similar issues the first method had, however less distributions were recognised. We tried the third method, in which separated the K7 as well as all the materials (i.e., impurities, by products, and the unreacted chemicals). Yet, a flat line was observed with no peaks towards the end of the run, indicates that all injected materials were cleared out of the column. The issue with this method is that it is time and mobile phase consuming.

Finally, the second method was modified in order to separate the K7 as well as clean the column and let all the injected materials to leave the column in one run, so as not to affect the

following run. A longer time with higher percentage of the aqueous mobile phase compared to the oily mobile phase, which is called the cleaning phase of the run. The modified run is shown in table 1 with a flow rate of 3 mL/min. As soon as the peak was separated (i.e. shows in the diagram), the materials leaving the column were collected for further analysis.

The second purpose of the HPLC, is for purification of the K7 (as mentioned in section 2.2.2), in which an Agilent Technologies 1220 Infinity LC HPLC with autosampler and a Luna Omega 5 μm PS C18 100 Å, LC column 250 x 10 mm have been used, following the modified method in table 1, with a flow rate of 3 mL/min.

For the analysis purpose a low concentration of the non-pure K7 was used and injected, to allocate the peak. While for the purification process a concentrated solution of the non-pure K7 was injected, due to the reality that the peak time is known. The K7 peak resulting from the purification process has a flat top instead of the normal pointy top, indicating the overlading of the sample due to the concentrated solution was used.

2.4.2 Liquid chromatography–mass spectrometry (LC-MS)

The LC-MS used is LCQ Advantage MAX from Thermo Electron corporation, and the signals have been detected and analysed using Xcalibur (Roadmap) software for the characterisation of the K7. The sample was approached using the HPLC by simply collecting the sample as soon as the peak starts. Then the obtained sample was simply injected into the LC-MS and the materials have been analysed.

2.5 Characterization of C-dots and their conjugates

2.5.1 Transmission electron microscopy (TEM)

The transmission electron microscopy is technique that provides morphological structural information in form of very high-resolution images for a nano-scaled size materials and considered as one of the most used techniques in samples' characterisation (232). The concept of the TEM is based on the interaction of electrons with the sample, using a beam of electrons passing through a specimen (the sample) to generate a highly magnified up to 2 million times image (233). As shown in Figure 105 (which demonstrate an image of the compartments of the TEM), the TEM has a source of electrons at the top of it that emits electrons which travel inside a column in the presence of vacuum. Then the electrons pass through electromagnetic lenses to focuses the electrons into a very thin beam, then the thin electrons beam passes through the sample. Some electrons will be scattered, and others will not in which the un-scattered electrons then collected on a detector to create a bright filed image of the components of the sample (233).

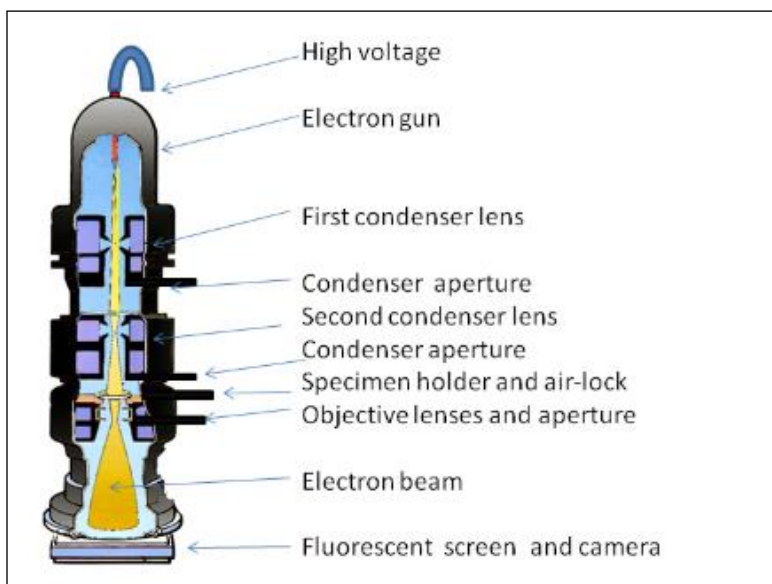


Figure 105: A diagram of a transmission electron microscope (233).

The sample of interest should be a very thin layer allowing the electrons beam to pass through, therefore preparation the sample is an important process and have an impact on the detected image. There are three main methods for sample preparation which are: 1) Drying, 2) staining, and 3) cryo-TEM (232).

The drying method is the most used method for characterising samples using TEM, it is based on using a sample in form of a solution in which a drop (2-3 μl) of the sample placed on a carbon coated or polymer coated grid. Then the sample left for a period of time (few minutes to hours, depending on the nature of the solvent) to dry out before the imaging process (234). The drying method is good for highly stable samples.

The staining method is based on using a sample in a solution state (the same as the drying method), then including staining the sample in either 1) positive stain, or 2) negative stain (233). The positive staining is based on applying iodine, ruthenium, or osmium tetra oxide on the sample in which the stain acts as a scattering agent that adhere to the areas of the sample (235). The negative staining is based on coating the surface and the surrounding of the sample (does not penetrate the sample at all), showing all the sample's details (236) .

The cryo-TEM is based on vitrification of the sample in a thin layer of solvent, which should be imaged at a very low temperature in order to preserve the sample's medium from changing or being evaporated under the high vacuum (237). The thin layer of the sample is made by subsequently adding a drop of the sample via blotting the drops on a lacy or wholly carbon coated grid. the vitrification of the water is done by rapid cooling using liquid ethane, cooled to its melting point. The vitrification process is carried out very quickly so resulting the sample is physically fixed in its current state (237).

The C-dots and all the C-dots conjugates have been characterised using the TEM in a cooperation with DR. Özge Çavuşlar/ Sabanci University nanotechnology research and application centre (Turkey).

2.5.2 Fourier transform infrared spectroscopy (FTIR)

The Fourier transform infrared spectroscopy is an analytical technique that measures the absorption of the electromagnetic radiation of a sample with wavelengths within the mid-infrared region ($4000\text{--}400\text{ cm}^{-1}$) (238). The FTIR is used to investigate the surface and the interfacial phenomena of a sample by identifying the vibrational absorption bands (238).

The FTIR technique is based on interference waves that interact with a sample, in contrast to a dispersive instrument. As the interacting energy assumes a well-defined wavelength range, the interference wave is presented by an interferometer as shown in Figure 106 (239). An FTIR instrument is composed of a source of energy, a fixed mirror, a moving mirror, a beam splitter as a support that is made of KBr or CsI and coated with a thin germanium layer, an ADC analog digital converter, and a computer to present the signals, as shown in Figure 106.

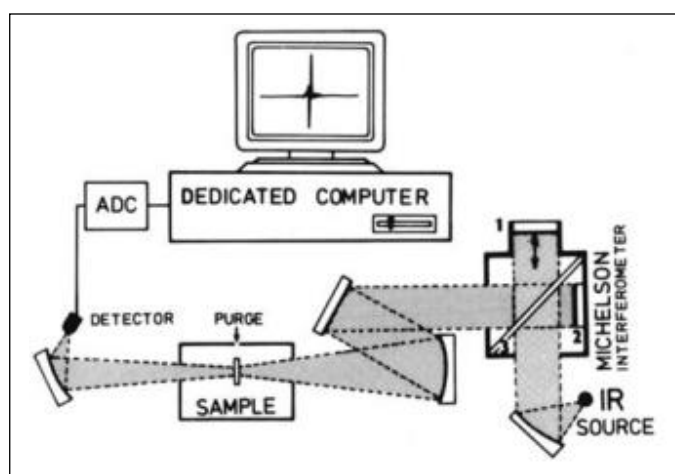


Figure 106: Schematic diagram of the FTIR instrument, (1) moving mirror, (2) fixed mirror, (3) beam splitter, and ADC analog digital converter (239).

All samples were analysed in a solid form including the C-dots and all the conjugations of the C-dots, as well as K7, RGD, and PEI/QAS, except the Jeffamine (as it was presented in a liquid form) that has been analysed in a liquid form. The mass of samples used are unknown as

the solid materials were used just enough to cover the crystal (moving mirror). An Agilent Technologies Cary 630 FTIR was used with a MicroLab PC software to analyse the signals.

2.5.3 Elemental analysis

Elemental analysis is a technique that is used for the characterisation of a material of interest by providing a qualitative and quantitative analysis of the organic components of the material, in which mainly detect oxygen, carbon, hydrogen, and nitrogen are detected (240). The concept of the elemental analysis technique is based on the oxidative decomposition of the organic substances of the material of interest, followed by the reduction of nitrogen and sulphur oxides resulting carbon dioxide, water, elemental nitrogen, and sulphur oxide (240).

The C-dots, the K7, the PEI/QAS, and all the C-dots conjugates were tested by the elemental analysis technique using Flash 2000 CHNS Analyzer and Eager Xperience software was used for analysing the results. Before testing the samples, the machine was calibrated by a bypass (which is non measurable pan), then a standard has been analysed 3 times (in which 2,5-(Bis(5-tert-butyl-2-benzo-oxazol-2-yl) thiophene known as BBOT used as the standard). All the samples have been weight then placed individually in aluminium pans (CE INSTRUMENTS, UK) in order to be analysed.

2.5.4 Thermogravimetric analysis (TGA)

The thermogravimetric analysis is a technique that used for the characterisation and the analysis of the components of a sample. The thermogravimetric is based on temperature controlled thermal analysis and combustion behaviour of materials, that measured by the loss in the mass of the sample (241). The TGA is done by heating a known mass of a sample in a closed system with a controlled heating rate in the presence of a nitrogen gas, the heating resulting vaporization and combustion of some sample components, that leads to reduction in

the mass of the sample. The reduction of the mass over time can show as signals detected by the TGA and show in the software in a form of a graph that shows the time and temperature that the signal takes place in (242).

All samples were analysed using TGA Q500 instrument and the signals were detected and analysed using TA Instrument Explorer software. The analysed samples include the C-dots, the C-dots conjugations, and the K7. Each sample was placed in a TA Tzero Pan in order to be thermally pyrolyzed using the TGA.

2.6 Photophysical analysis

2.6.1 Ultraviolet-visible spectroscopy (UV-vis)

The UV-vis spectroscopy is a characterisation technique considered as a qualitative analysis investigates the absorption radiation of the materials in a sample in the range of ultraviolet to visible region (190-800 nm), where the ultraviolet region is between (190-390 nm) and the visible region is between (390-800 nm) (243).

In more detail, the theory of UV-vis spectroscopy is based on electron transition, that is, any electron transition defined by its energy and probability, which are called the oscillator strength, resulting a signal (an individual absorption band) (244). The position and the area of the resulting signal band is determined by the transition of the material(s), therefore, it can be used as a fundamental characteristic method to estimate transitioned material(s) (244).

All samples were analysed using a UV-3600 shimadzu (UV-Vis-NIR spectrophotometer). The signals were detected and analysed using UVProb – [Kinetics] software. The samples analysed includes the C-dots and their conjugations in addition to the K7, RGD, PEI/QAS, and the Jeffamine to show the effect of the conjugated materials on the C-dots. The samples were tested in a solution form with a concentration of 0.1 mg/mL placed in a quartz cuvette.

2.6.2 Fluorescence spectroscopy

Fluorescence spectroscopy analysis technique is a sensitive optical technique used to characterise certain materials with polyatomic fluorescent molecules. This technique is based on measuring the λ_{em} of that is created by an electron (245). When an electron(s) absorbs UV or visible radiations, transition of the electron(s) from singlet ground state to a singlet excited state result, which is an unstable state. Due to the instability of the of the singlet excited state, the electron(s) will return to the singlet ground state emitting the absorbed energy in form of UV or visible radiation. i.e., the emission occurs during the relaxation of electron(s) from an electronic excited states to an allowable vibrational level in the electronic ground states (246). The fluorescence excitation and emission spectra are considered as the reflection of the vibrational level structures in the ground electronic state and the excited electronic state respectively (245). The process of excitation of the electron(s) and the emission of the UV/ visible radiations can be concluded using what is known as Jablonski diagram shown in Figure 107.

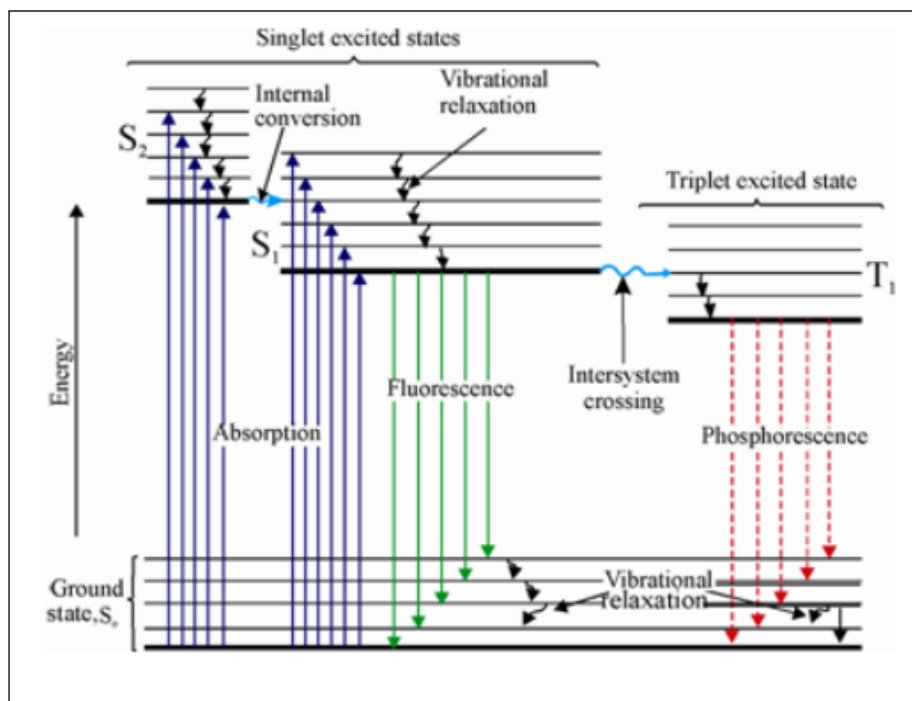


Figure 107: Illustration of the Jablonski diagram (245).

All samples were analysed using FluoroMax-4 Spectrofluorometer from HORIBA JOBIN YVON. The signals were detected and analysed using FluorEssence V3.5 software, using different excitations starts with 320 nm up to 600 nm with increasement of 20 nm. The samples analysed includes the C-dots and their conjugations in addition to the K7, RGD, PEI/QAS, and the Jeffamine to show the effect of the conjugated materials on the C-dots. The samples have been tested in a solution form of 0.085 mg/mL using a quartz fully transparent walls cuvette.

2.6.3 Quantum yield (QY)

The QY is a technique that is used to refer to the efficiency of the emitted fluorescence, in which the higher the QY the stronger the emitted fluorescence (247). In more details, the QY can be defined as the ratio of the number of the emitted photons to the number of absorbed photons (248), as shown in equation (1):

$$\Phi_F = \frac{\text{Number of photons emitted through fluorescence}}{\text{Number of photons absorbed}} \quad (1)$$

Where Φ_F is the QY (249).

The QY demonstrates how efficiently the fluorophore converts the excitation energy (light) into fluorescence, even at low concentration and the higher the value of the QY, the higher the sample's ability to emit a bright λ_{em} (247), (248).

There are two methods for measuring the QY of a material which are 1) the absolute method, and 2) the relative method (249). The concept of the absolute method is based on the ratio of the corrected intensity of the sample to be tested to the intensity of the excitation of the sample to be tested (250). While the concept of the relative method (which was used in this project) is based on the comparison of the fluorescence of the sample to be tested to highly

fluorescent dyes, which act as a group of reference standards with well-known QY (249). The relative QY can be measured by equation (2):

$$Q_s = Q_r \left(\frac{A_r}{A_s} \right) \left(\frac{E_s}{E_r} \right) \left(\frac{n_s}{n_r} \right)^2 \quad (2)$$

Where the Q is the fluorescence quantum yield, the A is the absorbance of the solution, E is the integrated fluorescence intensity of the emitted light, n is the refractive index of the solvent, and the subscripts 'r' and 's' refers to the reference and the sample to be tested respectively (249).

In which the previous equation can be simplified by combining the E_r and the A_r in equation (3):

$$Q_s = Q_r \left(\frac{m_s}{m_r} \right) \left(\frac{n_s}{n_r} \right)^2 \quad (3)$$

Where m is the gradient of the plot of integrated fluorescence intensity against absorbance (249).

The most reported QY values of the C-dots is around 10%, in which can be increased by surface passivation up to more than 30% (247), (251).

The QY of the C-dots and all the conjugations of C-dots been done using FluoroMax-4 Spectrofluorometer from HORIBA JOBIN YVON, and the signals were detected and analysed using FluorEssence V3.5 software.

2.6.4 Fluorescence lifetime

The fluorescence lifetime is a sensitive analysis technique of fluorescent materials, and it is used in the catechisation of a sample (252). The fluorescence lifetime is based on measuring the time elapsed between the excitation of the electron(s) and the emission of the photons from the excited electron(s) (253). During the excited state lifetime of the electron(s) (while the electron(s) in the singlet excited state) some conformational changes occur to the fluorophore, due to the interaction with other molecules, the rotation, and diffusion through the local environment (254). When a fluorophore containing sample excited using UV or visible radiation, an initial population of fluorophores (n_0) created in the singlet excited state, with time this population will decays as a result of the fluorescence emission, that is described in the differential equation (4):

$$\frac{dn(t)}{dt} = - (k_r + k_{nr})n(t) \quad (4)$$

Where $n(t)$ is the number of molecules in the excited state at time (t) following the excitation. k_r is the radiative constant and k_{nr} is the non-radiative constant. This results in an exponential decay of the singlet excited state giving by equation (5):

$$n(t) = n_0 \exp(-t/\tau) \quad (5)$$

Where T is the fluorescence lifetime of the molecule expressed as the reciprocal of the total decay rate as shown equation (6):

$$\tau = (k_r + k_{nr})^{-1} \quad (6)$$

The natural or radiative lifetime of the fluorophore is defined as $\tau_0 = k_r^{-1}$, the fluorescence decay following pulsed excitation of a sample is schematically shown in Figure 108 (254).

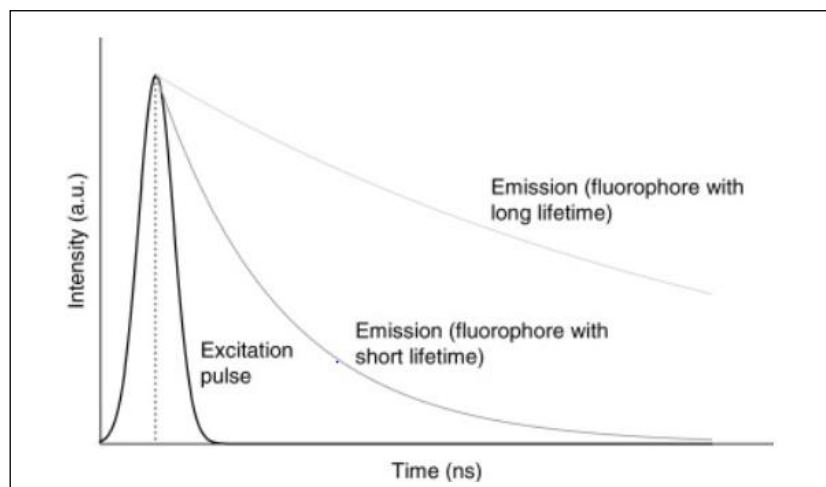


Figure 108: A schematic illustration of the fluorescence decays after pulsed excitation (254).

All samples were analysed using LifeSpec II from EDINBURGH INSTRUMENTS. The signals were detected and analysed using F980 software, using two different laser beams a 375 nm, and a 450 nm. The samples analysed includes the C-dots and their conjugations. The samples have been tested in a solution form of 0.085 mg/mL using a quartz fully transparent walls cuvette.

2.7 The biological analysis

2.7.1 Cytotoxicity

As has been demonstrated earlier in chapter one sections 1.4.5.1 and 1.4.5.2, that the C-dots have a very low level of toxicity and high biocompatibility. Therefore, in this project all the synthesised samples alongside the C-dots conjugated samples have been assessed in terms of toxicity using two different assays: 1) MTT assay (that will be explained in in section 2.8.2), and 2) PrestoBlue assay (that will be explained in section 2.9). The samples have been assessed using four different cell lines, which are: 1) HeLa, 2) U87, 3) T98G, and 4) GC-1 SPG.

2.7.1.1 HeLa cells

The HeLa cells are cancer cells that were isolated from the aggressive glandular cervical cancer of a young woman and considered to be the first continuous cancer cell line that have been used in the *in vivo* studies. The HeLa cells have been used for so many years, and almost all the information about the processes that take place inside the human body have been proved using the HeLa cells (255). The HeLa cells are considered to be one of the easier cell lines to be synchronised by many methods, this is the reason that they are used as a good model system for studying many cell activities (256).

2.7.1.2 U87 cells

The U87 are cancer cells that were isolated from malignant glioma (that is the primary brain tumour) tumour, which is the glioblastoma of a male patient, that are widely used in neuroscience and immune oncological research (257). The U87 have an epithelial cells morphology and considered one of the most aggressive glioblastoma cell lines (258).

2.7.1.3 T98G cells

The T98G cells are a type of glioblastoma cancer cells, which is considered one of the most deadly brain tumours due to the poor prognosis of the disease (259). The T98G cells have a fibroblast like cells structure, that were isolated from a male patient (259).

2.7.1.4 GC-1 SPG

The GC-1 SPG cells are a type of spermatogonia isolated from an adult mouse testis (260). The GC-1 SPG cells are demonstrated to be the cells most similar to spermatocytes (a male germ cell-type). Therefore, they can be used as a human model in the *in vivo* research (260).

2.7.2 Cell culture processes

All the experiments including cell culture and tissue culture have been carried out under sterile conditions (261). The aseptic techniques are important for a successful cell culture process, and they are based on keeping the air, the floor, and the surfaces of the working stage free of contamination (including dust and germs). Therefore, all the work must be performed inside a laminar flow cabinet (261). The laminar flow sterile cabinet should be switched on for at least 15 minutes before even the beginning of the experiment, this is due to allowing enough time for the machine to flow enough sterile air and get the atmosphere ready for the sterilisation process of the surfaces and the floor. Then the inside of laminar flow sterile cabinets should be sprayed with plenty of isopropyl alcohol 70% then wiped completely. After that, the laminar flow sterile cabinet is ready for experiments. To maintain successful aseptic techniques, all samples and any material involved in any of the cell culture processes that required to be inside the laminar flow sterile cabinet should be sterile by autoclaving and be sprayed with plenty of isopropyl alcohol 70% before entering the laminar fume hood. The laminar flow sterile cabinet keeps flowing air horizontally from the back of the cabinet towards the front to maintain a sterile atmosphere during the experiment (261).

2.7.3 Media preparation

The process of growing cells and tissues must be carried out in a medium that provides enough nutrients, proteins, and antibacterial agents to make sure that the cell proliferation is being performed properly and the cells have the required elements for growth. In this project the media used was Dulbecco's modified eagle medium (DMEM) which compose of Sterile filtered DMEM, (-)L-leucine, (-)L-methionine, 4.5g/L glucose, 4.0mM L-glutamine, sodium pyruvate, and phenol red, therefore it is considered as a good source of energy (262). The DMEM media is capable to some extent of mimicking the body plasma and the whole blood. However, the DMEM can be contaminated with microorganisms (262). To overcome the possible contamination, we added penicillin-streptomycin antibiotic (1%), and to enhance the DMEM

even more, we added fetal bovine serum (FBS) (10%), and L-Glutamine (1%). The media is ready for use in any of the cell culture processes.

2.7.4 Thawing cells

All the cells were placed in a 1.5 mL cryogenic vial and have been frozen in a -70 °C (using liquid nitrogen freezers) so they remain preserved. To use the cells, they are defrosted in a process called thawing cells, in which the cryogenic vial has been immersed in warm water (37 °C) for one minute. Caution is important in this stage, as the cryogenic vial should be wiped before placing in the warm water to avoid the hazard of explosion if any nitrogen particles stuck on the cryogenic vial. Then inside the laminar flow sterile cabinet, the cells were transferred into a universal tube with 10 mL of media, then the cells and the media were centrifuged at 800 rpm for 5 minutes. Then, the supernatant was discarded, and the pellet (the cells) was resuspended in a 10 mL of media. The centrifugation step was repeated once, and the purpose of the centrifugation is to get rid of the dimethyl sulfoxide (DMSO) (this explained in section 2.7.1.13). After the second resuspending of the pellet in 10 mL of media resulting a cell suspension, the cells are ready for the counting cell viability.

2.7.5 Counting cell viability

Counting cell viability is important to determine the number of viable cells in the flasks, and to know the amount of cell suspension required for subculturing the cells as well as calculating the amount of the cell suspension needed for doing any tests. For counting cells there are two methods: 1) Use of haemocytometer and coverslip, and 2) Using the cell countess machine.

2.7.6 Haematocytometer

The haematocytometer and the coverslip should be cleaned with alcohol and completely dried before use, then the coverslip was moist with PBS and placed on the haematocytometer chambers (affix well). In a sterile Eppendorf tube 100 μL of the cell suspension were added and a 400 μL of Trypan Blue (the final concentration is 0.32%) to stain the cells and mix gently. 10 μL of the Trypan Blue-treated cell suspension were taken using a pipette, and gently place the pipette tip on one of the haematocytometer chambers where it meets the coverslip and release the cell suspension. The cell suspension will load the whole chamber evenly by capillary action, then the other chamber was loaded following the same process. Then the cells were counted using the light microscope with 10X objective. The haematocytometer contains a square with 9 grids as shown in Figure 109, each grid is composed of 16 squares with a 1 mm side, and the capacity of each grid is 10^{-4} mL. The living cells were counted in grids A, B, C, and D individually, taking in consideration that the cells were only counted if they are inside the grid or lay on the square's right or bottom sides. Then the number of viable cells was calculated by taking the average of the cells counts from grid A, B, C, and D, then the number was multiplied by 10^4 to find out the number of cells in 1 mL of cell suspension. And finally, the number was multiplied by 5, to correct for the 1:5 dilution from the dilution with Trypan Blue, resulting the total number of living cells in a 1 mL of the cell suspension.

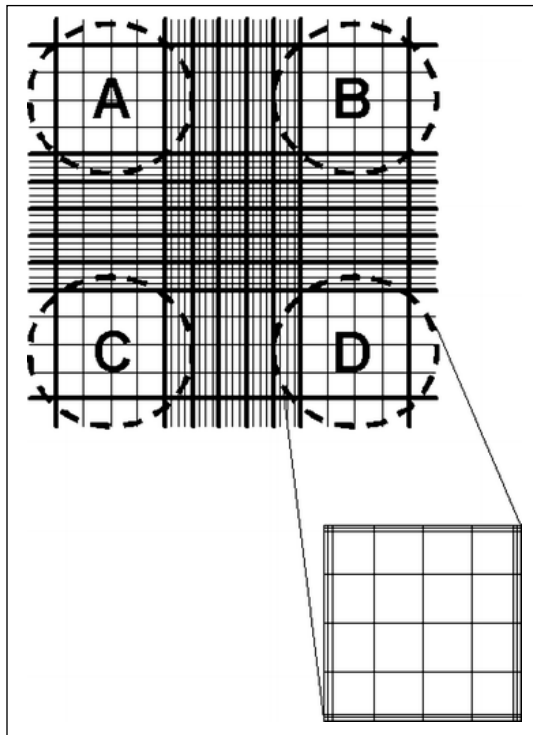


Figure 109: Grids of one chamber on the haemocytometer under the microscope (263).

2.7.7 Cell countess

The cell countess method includes the use of an automated counter, and a disposable special slide with two chambers (compatible with the cell countess) to count the viable cells. In a sterile Eppendorf tube 100 μL of the cell suspension were added and a 400 μL of Trypan Blue (the final concentration is 0.32%) to stain the cells and mix gently. 10 μL of the Trypan Blue-treated cell suspension were taken using a pipette and injected into one of the chambers of the slide as shown in Figure 110. Then the slide was placed in a special input in the cell countess and the cells were counted automatically in less than a minute. The countess is capable of counting the living cells as well as the dead cells providing a viability percentage.

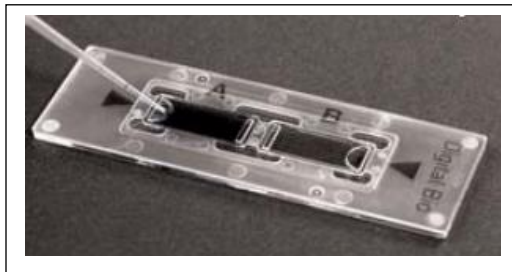


Figure 110: Process of loading the slide with the cell suspension using the cell countess method.

2.7.8 Growing cells

The cells should be grown in the lab mimicking the human body conditions (as mentioned previously in section 2.5.1.1). After counting the cells in a cell suspension, 10000 cells were transferred into a T-75 flask and topped up to 7 mL of the medium, then the flask was incubated in the incubator that provided a 5% CO₂, and 37 °C conditions. The contents of the medium alongside the conditions of the incubator, provided a good environment that is similar to the blood. At the first couple of h of transferring the cells into the flask, they will be moving freely in the media, later, the cells start adhering onto the flask surface and grow.

The cells were checked under the microscope every 24 hours, to make sure that the cells are growing successfully. The cells were checked after 24 h and showed 20% confluency as shown in Figure 111 A, which were kept in the incubator for another 24 h to grow more. After another 24 h the cells were checked and they were 70% confluent as shown in Figure 111 B, in which were returned to the incubator as they need to grow more. Then after 24 hours, the cells were checked, and they were 85% confluent as shown in Figure 111 C, in which the cells are ready for splitting. The splitting is required to prevent the overgrowth of the cells, and when there is now enough space on the surface of the flask the cells will start growing on the top of each other causing asphyxia and cell death.

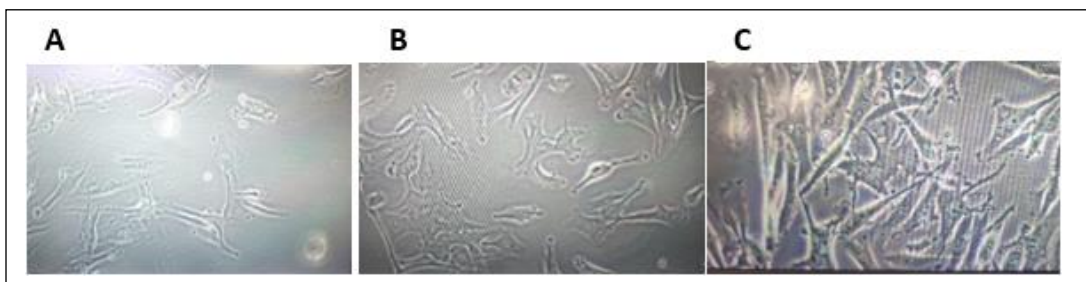


Figure 111: HeLa cells under the microscope, A) 20% confluent, B) 70% confluent, and C) 85% confluent.

2.7.9 Splitting cells

When the cells confluency reaches 85% or more, they are recommended to be split, and the process of splitting the cells is called trypsinisation (264). The laminar flow sterile cabinet was prepared as demonstrated in section 2.5.1, and all the materials, equipments and the T-75 flask were placed inside the laminar flow sterile cabinet following the aseptic techniques. The culture medium was removed from the flask using a sterile pipette and discarded into a waist contained with virkon (a disinfectant that used for the destruction of pathogens (265)). Then 3 mL of 1X trypsin-EDTA were added into the T-75 flask. The trypsin-EDTA is serine protease enzyme has the ability to breakdown the peptide bonds that adhere the cells into the walls of the flask as well as splitting the cells from each other's (266). Then the flask was gently shaken and rocked forward and back for few seconds, to make sure that the trypsin-EDTA had accessed into all the areas of the flask. After that, the trypsin-EDTA treated cells were incubated in an incubator with 5% CO₂ at 37 °C for 3-5 minutes, the time is critical due to the possibility of breaking down the cells membranes if the cells kept for longer time. Then the flask was taking out of the incubator, and 6 mL of fresh media were added into the flask (inside the laminar flow sterile cabinet) then swirled gently to make sure that the trypsin-EDTA effect was neutralised. resulting a cell suspension that is ready for regrowing, plating, freezing, and any other cell culture experiments.

2.7.10 Freezing cells

The process of freezing cells is important to preserve cells when cells are not in use. To freeze cells, they should be as a cell suspension form, in which the cell suspension was centrifuged at 800 rpm for 5 min. Then the supernatant was discarded into virkon, and the pellet was resuspended in a 1 mL of freezing media and transferred into a 1.5 mL cryogenic vial, then kept in the -70 °C freezer for future work.

The freezing media was made by adding 70 mL of the media for culturing (the media that were enhanced (as demonstrated in section 2.5.1.1), 20 mL of fresh media (media that never been enhanced), and 10 mL of DMSO. The freezing media has the ability to keep the cells in good conditions until they needed to be used in the future.

2.8 MTT assay

The 3-[4,5-di-methylthiazol-2yl]-2,5-diphenyl-tetrazolium bromide (MTT) is a reagent that is used to determine the cell viability via a colorimetric assay (267). The MTT assay was first described by Mosmann, in which they demonstrated that the concept of the MTT assay is based on measuring the reduction of tetrazolium salt by the mitochondrial succinic dehydrogenase in the viable cells (268). The reduction of the tetrazolium salt produces formazan crystals which are purple in colour and not soluble in the aqueous solution.

2.8.1 Plating the cells

In this project the MTT assay was used to assess the toxicity of the synthesised materials, using HeLa cells, U87, T96G, and GC-1 SPG in a 96-well plate. This process required growing the cells in each well of the 96-well plate, which has a very small area. In addition, to obtain a fair result, each well should have the same population of cells.

In order to plate the cells, the cells should be in a cell suspension with media and cell counting process should be performed prior to the plating process (refer to section 2.5.1.3 for cell counting).

Each well should contain a volume of 50 μL of the cell suspension with 0.5×10^5 cell/ mL. Once the number of the viable cells has been determined per mL of the cell suspension, we calculate the amount of media that should be added to the cell suspension (as the cell suspension is usually very concentrated) to dilute it. As each well should contain a 50 μL of the cell suspension, a 96-well plate needs 4.8 mL of the cell suspension, in this project we made 5 mL of the cell suspension with 0.5×10^5 cell/ mL to make sure we have enough cells for each well (as lose can occur due to human errors).

2.8.2 MTT procedure

The procedure of the MTT assay starts with plating the cells in a 96-well plate. As mentioned in section 2.5.2.1, we added 50 μL with 0.5×10^5 cell/mL of cell suspension in each well except column 1, instead we added 50 μL of media only, then the 96-well plate was incubated in the incubator with 5% CO_2 at 37 °C for 24 h in order to give the cells enough time to adhere onto the well surface and to recover from the trypsinisation process. Then 10 different concentrations of the synthesised samples were pre-prepared and autoclaved for the purpose of the cell viability assay. The concentrations were prepared for each sample are: 10, 20, 30, 40, 50, 60, 70, 80, 90, and 100 $\mu\text{g}/\text{mL}$, each sample was tested in triplicate. A positive and a negative control were used the positive control is the cells suspension with none of the samples added to it, and the negative control is the media with no cells in them. They layout of the 96-well plate is shown in Figure 112.

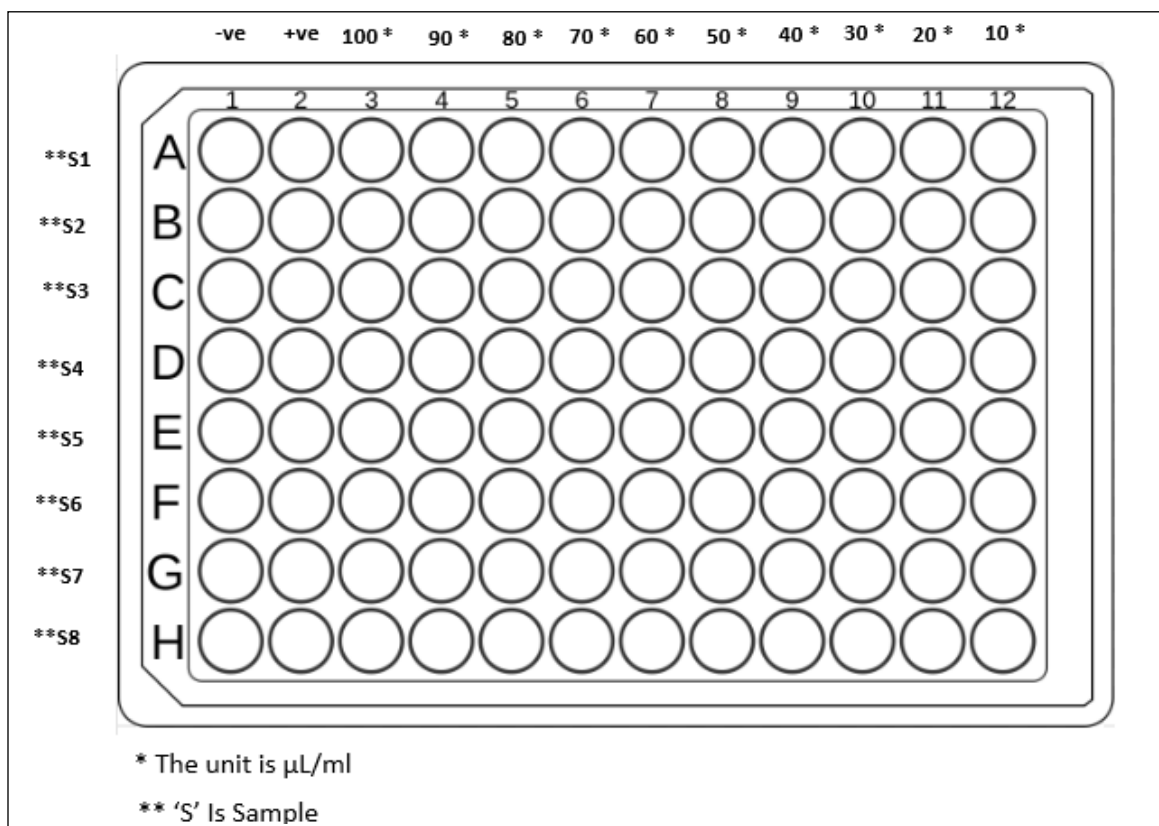


Figure 112: Layout of the 96-well plate.

Then the 96-well plate was incubated in the incubator with 5% CO_2 at 37 °C for 24 hours. After that, 10 μL of the MTT reagent were added in each well (including the wells with samples-treated cells, the wells with the +ve control, and the wells with the -ve control) in the darkness. Then incubated in the incubator with 5% CO_2 at 37 °C for 2-4 hours. During the incubation, the living cells start the reduction of the tetrazolium salt producing formazan crystals, while the dead cells cannot. After that, the suspensions in the wells turned into purple colour (some darker than the others), indicating the reduction of the tetrazolium salt producing formazan crystals in the living cells only. As the formazan crystals are insoluble in an aqueous solution, we used MTT reagent (which is an acidified solubilizing solution) to solubilise the crystals in order to be measured using the plate reader. A 100 μL of the MTT detergent were added into each one of the 96 wells in the darkness, then the plate was covered (or left in the darkness) for 2-4

h (no need for incubation). Finally, the 96-well plate was placed in the plate reader to measure the absorbance of the living cells using a filter with wavelength range of 550-600 nm. In this project we use TECAN Labtech.com infinite F200PRO plate reader, and Omega – Data Analysis software to display the collected data.

2.9 PrestoBlue assay

PrestoBlue is a resazurin based reagent used for determining the cell viability via fluorometrically assay (267). The PrestoBlue is a quick cell-mediated cytotoxicity assay that is used to assess the viability of the cells by changing into its reduced form resorufin via aerobic respiration of metabolically active cells (269). The reduction of PrestoBlue results a red colour thus indicating that cells are viable. As only metabolically active cells will be able to convert PrestoBlue to its red form. The main benefit of PrestoBlue is its ability to significant signals within 10 minutes which is shorter than other cell viability assays that usually require 1-4 h of incubation.

The PrestoBlue assay requires plating exactly as the MTT (refer to 2.5.2.1 plating cells section). After incubating the 96-well plate in an incubator with 5% CO₂ at 37 °C for 24 hours, the samples were added in the same manner as the samples were added in the MTT assay, as shown in Figure 105. After the addition of the samples, the 96-well plate was incubated for 24 h in an incubator with 5% CO₂ at 37 °C. Then 10 µL of the PrestoBlue reagent were added to each well (including the samples-treated cells, the +ve control, and the -ve control). Then the 96-well plate was incubated in an incubator with 5% CO₂ at 37 °C for 10 minutes, in which the PrestoBlue being reduced by the viable cells and the colour was changed from blue to pink (some wells darker than others depending on the viable cells). Finally, the 96-well plate was placed in the plate reader and the absorption of the living cells was measured using a filter with wavelength range of 535-560 nm. In this project we used the same plate reader that used for the MTT assay as well as the same software to display the collected data.

2.10 Haemolysis assay

The Haemolysis assay is a test of some biological activity that can be caused by certain material, the haemolysis test is based on measuring the lysis of the erythrocytes that results by interacting with certain material that has the ability to penetrate the cell membrane (270). In addition, the haemolysis assay gives an indication of the toxicity of a material. In this project all the synthesised samples were tested using Columbia Blood Agar Settle plates (Sigma Aldrich).

The haemolysis assay was done by creating a hole with 8 mm diameter in the blood agar using the bottom of a 1 mL sterile pipette tip, then the hole was filled with a 100 µg/mL of the sample of interest. After that, the plate was incubated in an incubator with 5% CO₂ at 37 °C for 24 hours. Finally, any lysis of the erythrocytes was measured.

2.11 Fluorescence microscopy on HeLa cells

The fluorescence microscopy technique is an advanced tool of microscopy that can provide a unique and effective approach to study cells, this is due to the specificity, versatility, and the high sensitivity of the fluorescence microscope (271). The concept of the fluorescence microscopy is based on directing a laser beam into a specimen, which absorbs the energy then emits the energy into a detector which collects the emitted light in form of an image (272). The fluorescence microscope is composed of a source of energy which directs the light source into a filter (to filter in only the wavelength of interest) (271). Then the filtered light moves into a condenser to create a condensed beam, and the beam passes through the objective lens into the specimen (271). When the light hits the specimen, some of it will scatter and the rest will be emitted into the detector, in which will show the emitted light in form of an image demonstrating details of the specimen. An illustration of the fluorescence microscope is demonstrated in Figure 113.

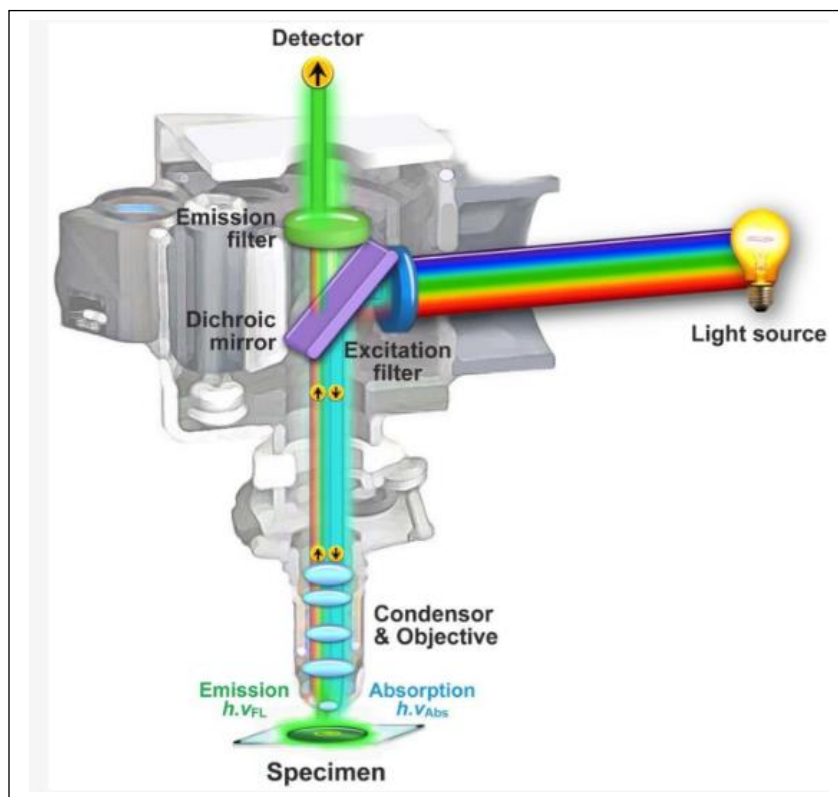


Figure 113: Illustration of the fluorescence microscope (271).

The samples were tested against HeLa cells at three different concentrations 10, 30, and 100 $\mu\text{g}/\text{mL}$. Furthermore, each sample was tested at five different incubation time intervals 2, 4, 6, 8, and 24 h with 100 $\mu\text{g}/\text{mL}$ concentration.

The slide preparation process was done by plating the cells in a 24 well plate with a 0.5×10^5 cell/mL (0.3 mL per well), with a 9 mm diameter a coverslip placed in each well (to allow the cells to adhere onto the coverslip). The plate was incubated for 24 h in an incubator with 5% CO_2 at 37 °C. Then a 0.3 mL of 100 $\mu\text{g}/\text{mL}$ of the sample of interest was added and then the plate was incubated in an incubator with 5% CO_2 at 37 °C for the period of time required (as mentioned in the previous paragraph). After that, the coverslips were taken out of the well using a sterile forceps and each one placed on a glass slide upside-down, then histomount was added around the coverslip to fix it on the slide, and to seal the small gap between the slide and

the coverslip. The slides then were tested under the fluorescence microscope using ZEISS AXIO Scope.A1 microscope, and ZEN software was used to detect the results in form of mages.

2.12 Antimicrobial study

The antimicrobial studies include testing the activity of the samples of interest against bacteria to assess the antimicrobial activity of the samples. Therefore, this process requires to be done in sterile conditions and the materials/equipments should be all autoclaved prior to any experiment, similar to the tissue/cell culture work. Refer to section 2.7.1.5.

In this project two bacteria species were used: *Escherichia coli* and *Staphylococcus aureus*.

2.12.1 *Escherichia coli* K12

The *Escherichia coli* (*E. coli*) is a facultatively anaerobe Gram negative bacterium, that is considered as predominant facultative of the human colonic normal flora, start colonizing the gastrointestinal tract of infants within hours of life, which the *E. coli* and the human derive mutual benefit (273). However, the *E. coli* can be harmful and cause broad spectrum of diseases for human, that are usually infected the mucosal surfaces, or it can spread throughout the body (274). Furthermore, the *E. coli* can cause three main infections: 1) urinary tract infection, 2) sepsis or meningitis, and 3) enteric or diarrheal disease (274).

2.12.2 *Staphylococcus aureus* ATCC 25923

The *Staphylococcus aureus* (*S. aureus*) is a facultatively anaerobic gram positive bacterium, that colonise the skin and gastrointestinal tract of the human body, which is considered as an invasive pathogen that causes highly contagious diseases such as skin infections and soft tissue infections (275). The main pathological effect of the *S. aureus* is the formation of lesions with

purulent abscess around the pathogen's nidus mainly via the infiltration of neutrophils (276). The infections caused by *S. aureus* do not develop protective immune responses, therefore chronic persistent and recurrent infections are very common (277).

2.12.3 Antimicrobial process

In this project the antibacterial activity was carried out in cooperation with Dr. Ella Nicole Gibbons.

The testing was carried out in liquid media, first by adding 9 mL of nutrient broth into a 30 mL universal bottle, then inoculating the nutrient broth with a single loop of bacteria and incubating for 24 h overnight in a SciQuip Incu-Shake MIDI orbital shaker set to 200 rpm and 37 °C.

After 24 h, the overnight cultures were transferred into 50 mL falcon tubes and centrifuged at 4000 rpm for 10 minutes in a Thermo Scientific SL 8R. The supernatant was discarded and 9 mL of ¼ strength Ringer's solution was added, then the falcon tubes were vortexed. The centrifugation process was repeated, and the pellet was re-suspended in 2 mL of ¼ strength Ringer's solution. Using a Biochrom WPA S800 visible spectrophotometer set to 600 nm, the resuspended culture was diluted in ¼ strength Ringer's solution to obtain an absorbance reading equivalent to a 0.5 MacFarlane standard, which corresponds to 1.5×10^8 CFU/mL.

For the control and test samples, 2 mL Eppendorf tubes had their standard flip tops removed and replaced with lids of aluminium foil. The Eppendorf tubes with foil lids were then sterilised using an autoclave. 800 µL of nutrient broth was added into each Eppendorf tube as well as 100 µL ¼ strength Ringer's for the control samples, or 100 µL of the compound in ¼ strength Ringer's solution for the test samples. 100 µL of the washed and resuspended bacterial culture was then added to each Eppendorf tube. Then, the Eppendorf tubes were grown for 24 h in a shaking incubator set to 200 rpm and 37 °C. The control and test samples were then plated onto nutrient agar using the drop plate method.

The drop plate method was carried out by performing serial dilutions via aliquoting 100 μL of sample into 900 μL $\frac{1}{4}$ strength Ringer's solution. This process was repeated a total of 7 times. Agar plates were split into 4 sections, with each section representing a different dilution factor, for a total of 4 dilution factors per plate. 3 $10 \mu\text{L}$ drops of sample at the respective dilutions were deposited onto each section, and each plate was done in triplicate. The plates were then incubated for 20 h at 37 °C in a static incubator, then counted for colonies. Dilutions with 3 - 30 colonies were recorded, alongside the respective dilution factor. Averages were calculated from these values, and percentage decrease compared to the control was calculated for each test sample using the formula:

$$\frac{\text{Control} - \text{Test}}{\text{Control}} * 100$$

2.13 Drug delivery study

In the past few years, the nanoparticles have been demonstrated to be good candidates to be used as drug carriers, this is due to many reasons such as: the ability of the nanoparticles to penetrate the cells, the specificity of the nanoparticles to certain sites of the body, and the controlled release of the drug from the system into the body (278). The concept of drug delivery studies is to create a system including the nanoparticles that are loaded with a drug of interest, followed by injecting the system into a solution that mimics the body fluids in order to monitor the release of the drug of interest (279). There are many methods for studying the drug release including: 1) sample and separate method (SS), 2) continuous flow method (CF), and 3) dialysis method (DM) (280).

The SS method is based on introducing the nanoparticles drug carried system into a vessel containing the releasing media (determine by the solubility and the stability of the drug), in which the temperature of the media is constantly maintained. Then, the drug release is

assessed over time, by sampling of the media and analysing it using a suitable tool depending on the drug of interest (281).

The CF method (or the dissolution method) is based on placing the nanoparticles drug carried system inside a column in a USP IV dissolution apparatus, in which the buffer (the release medium) is constantly circulate through the column (which the nanoparticles drug carried system is immobilised inside it) (282). Then the drug release is analysed by sampling the buffer over periods of time using a suitable tool depending on the drug of interest.

The DM method is considered to be one of the most popular methods for the assessment of the drug release using a nano-sized drug delivery system (280). The DM method is based on the physical separation of the dosage form that placed inside a dialysis membrane in a medium (283). Then the drug release is analysed by sampling the medium surrounding the dialysis membrane over periods of time using a suitable tool depending on the drug of interest.

In this project, a drug delivery system was created to assess the release of two drugs, Ibuprofen (as a model), and Temozolomide. The drug delivery system was made by creating a gel system using Pluronic P123 32.5% in PBS, in which 16.25 g of P123 were dissolved in 33.75 g of PBS. Simultaneously, 25 mg of the drug was mixed with 100 mg of the C-dots, then suspended in 0.265 g of PBS (to maintain the 32.5% of solids in PBS). One system for each drug was made and assessed using the four conjugates of the C-dots as well as the C-dots themselves, in order to be compared to the gel without any C-dots, or any C-dots conjugates.

In this project, the dialysis method was used with a dissolution enhancer cell 0.5 cm², 1 cm (Agilent Technologies) as shown in Figure 114, to assess the drug release of each system at room temperature (25±1 °C). For each experiment, 1.8 gm of the drug delivery system of interest was placed inside the dissolution enhancer cell (1 cm depth), then a circular piece of dialysis membrane 3.5K MWKO pre-soaked in PBS was placed to cover the drug delivery system. Then, the cell was covered with the washer and the retaining ring and placed in a beaker with 500 mL of PBS (the releasing media) with a continuous stirring. Then a sample of 1.5 mL of the releasing media so the releasing of the drug analysed using UV-6300PC Double

Beam Spectrophotometer, and the data were collected and analysed using UV-Vis Analyst software. The releasing media samples were taken at zero time of the dialysis, then after 0.5, 1, 1.5, 2, 2.5, 3, 4, 5, 6, 7, 8, 24, 48, 72, and 96 h of the beginning of the dialysis.

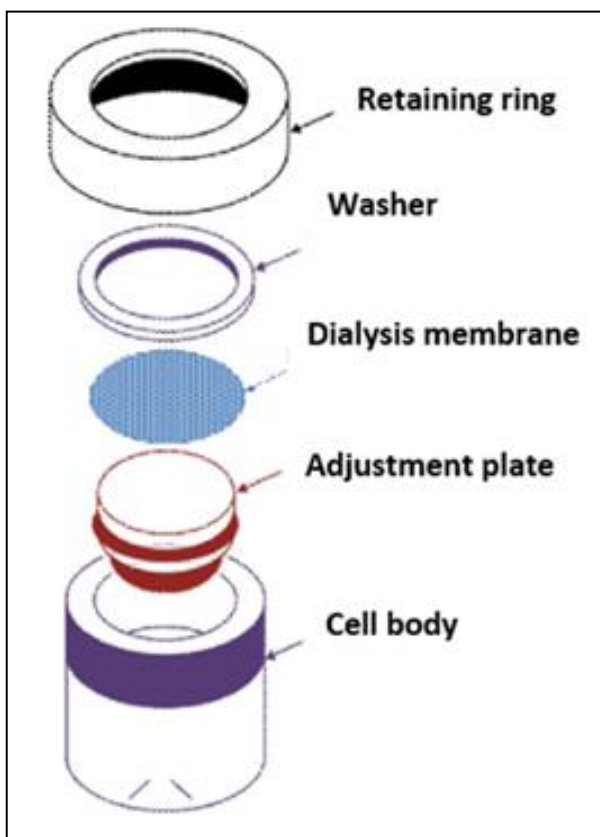


Figure 114: Illustration of the dissolution enhancer cell (284).

Chapter 3: Results and discussion

3.1 Characterization of materials

3.1.2 Purification and characterisation of K7

The HPLC was used for the characterisation and separation of the K7 peptide (as mentioned in section 4.2.1).

When the cleaved K7 was injected into the HPLC, it mixed with the mobile phase then ran through the stationary phase (the column). The injected materials then separated at different rates according to the polarity and the hydrophilicity nature of the materials. This is due to the different rate of interacting with the stationary phase and the mobile phase (285).

The K7 was separated in the higher percentage hydrophilic stationary phase (around 14 min-18 minutes of the injection of the sample) as shown in Figure 115, this is expected due to the hydrophilic nature of the Lysine amino acid (286). Two peaks very close to each other were separated, and they were both collected separately. The two peaks were then injected separately to the LC-MS to identify the molecular masses of the material(s).

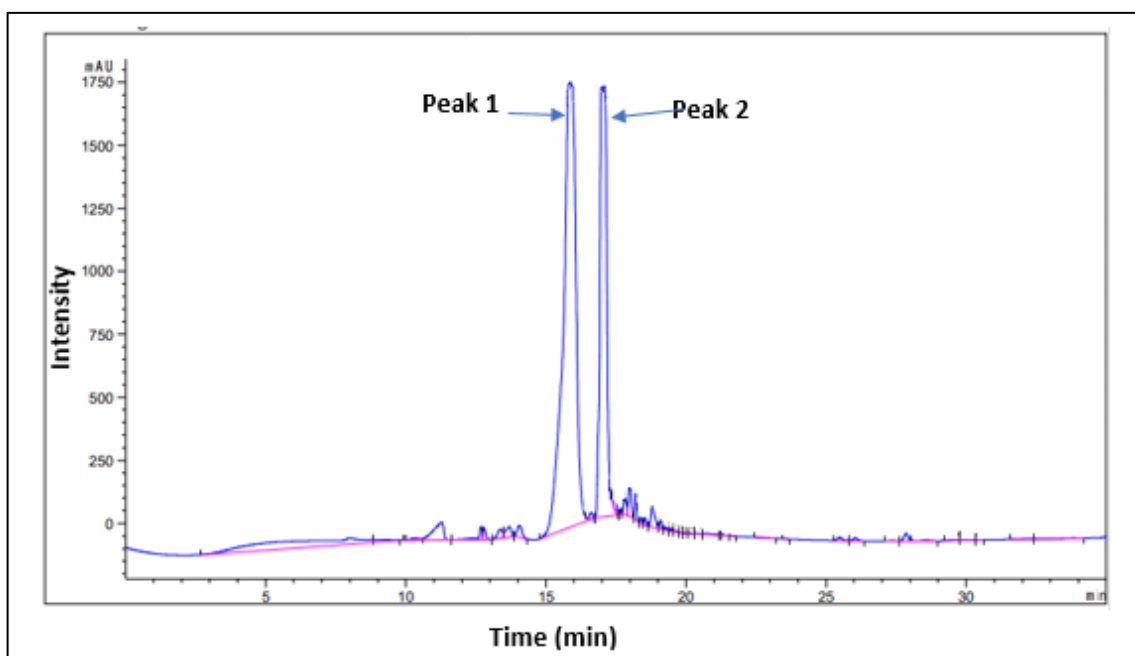


Figure 115: HPLC chromatogram of the K7 right after the cleaving of the resin showing the two separated peaks.

The first LC-MS spectrum of peak 1 demonstrates the presence of structure with molar masses of 915 (m/z) which represent the molecular mass of the K7 peptide. The LC-MS spectrum also shows structures with molar masses of 771, 628, 572 and 514 as shown in Figure 117. These molecular masses suggest that fragmentations of the K7 peptide occurred during the analysis, due to the protonation of the side chains amine groups in the structure of the K7, Figure 116 shows the structure of the K7 peptide presenting the locations around the carbonyl bonds where the fragmentation occurred (287). The protonation of the amine groups explains the presence of the two peaks in the HPLC chromatogram. On the other hand, the chromatogram of peak 2 in the LC-MS shows two structures with molar masses of 626 and 578, that both of them related to the fragmentation of the K7, and the molar masses shifted slightly due to the protonation occurred, as shown in Figure 118.

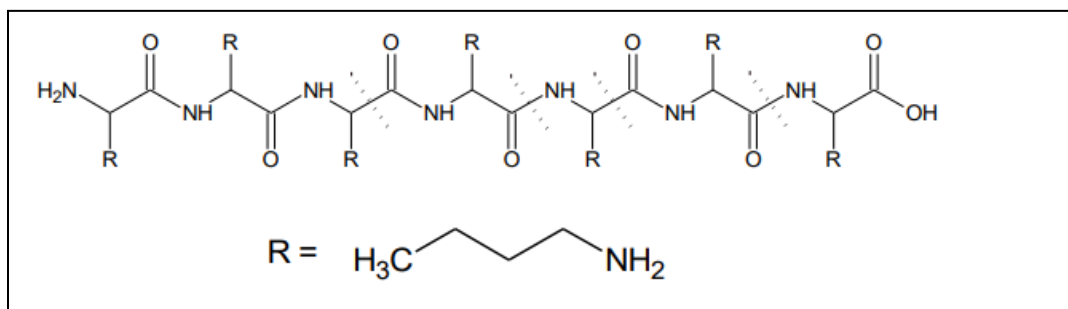


Figure 116: Molecular structure of K7 showing the locations around the carbonyl bonds where fragments occur. The R group represents the side groups (288).

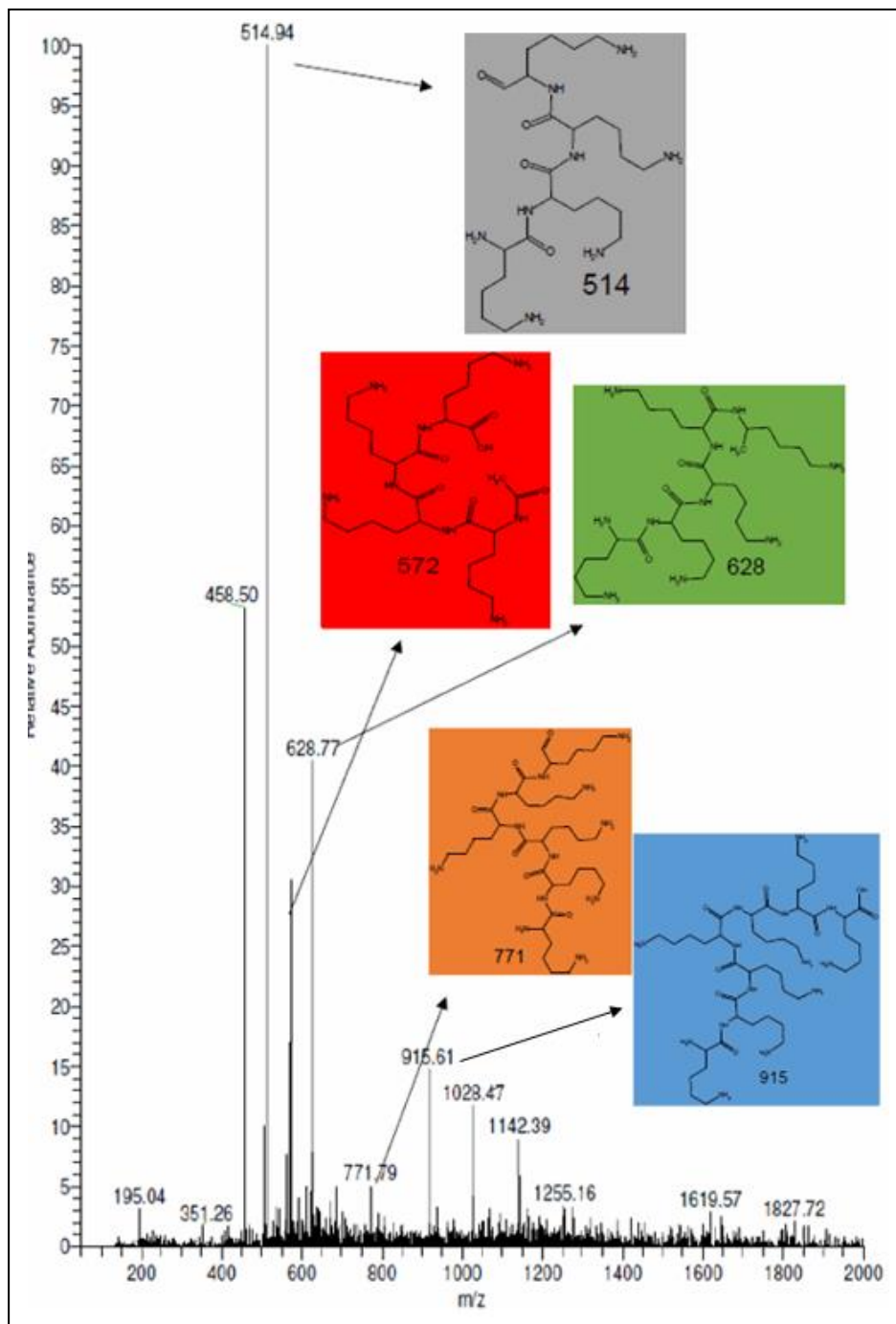


Figure 117: Mass spectrum for Peak 1 of K7 as shown in Figure 115.

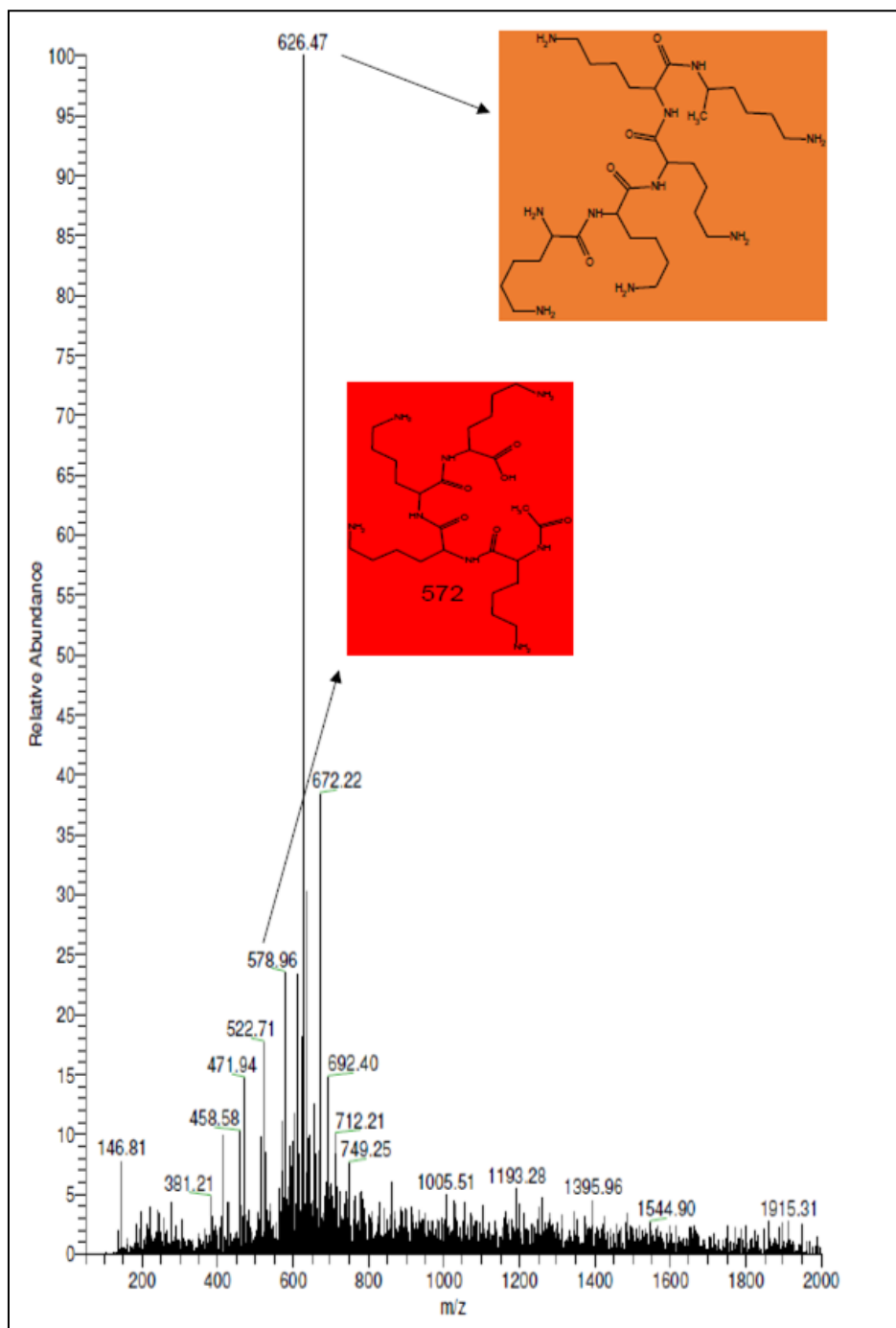


Figure 118: Mass spectrum for Peak 2 of K7 as shown in Figure 115.

3.1.3 TEM of C-dots, the C-K7, the C-RGD, and the C-PEI/QAS

The TEM images of the C-dots, C-K7, the C-RGD, the C-PEI/QAS TEM images indicates that they have an average size of 11 ± 2 nm as shown in Figure 119. This size is comparable to that reported in a previous publication which synthesised C-dots following the same method were used in this project (7).

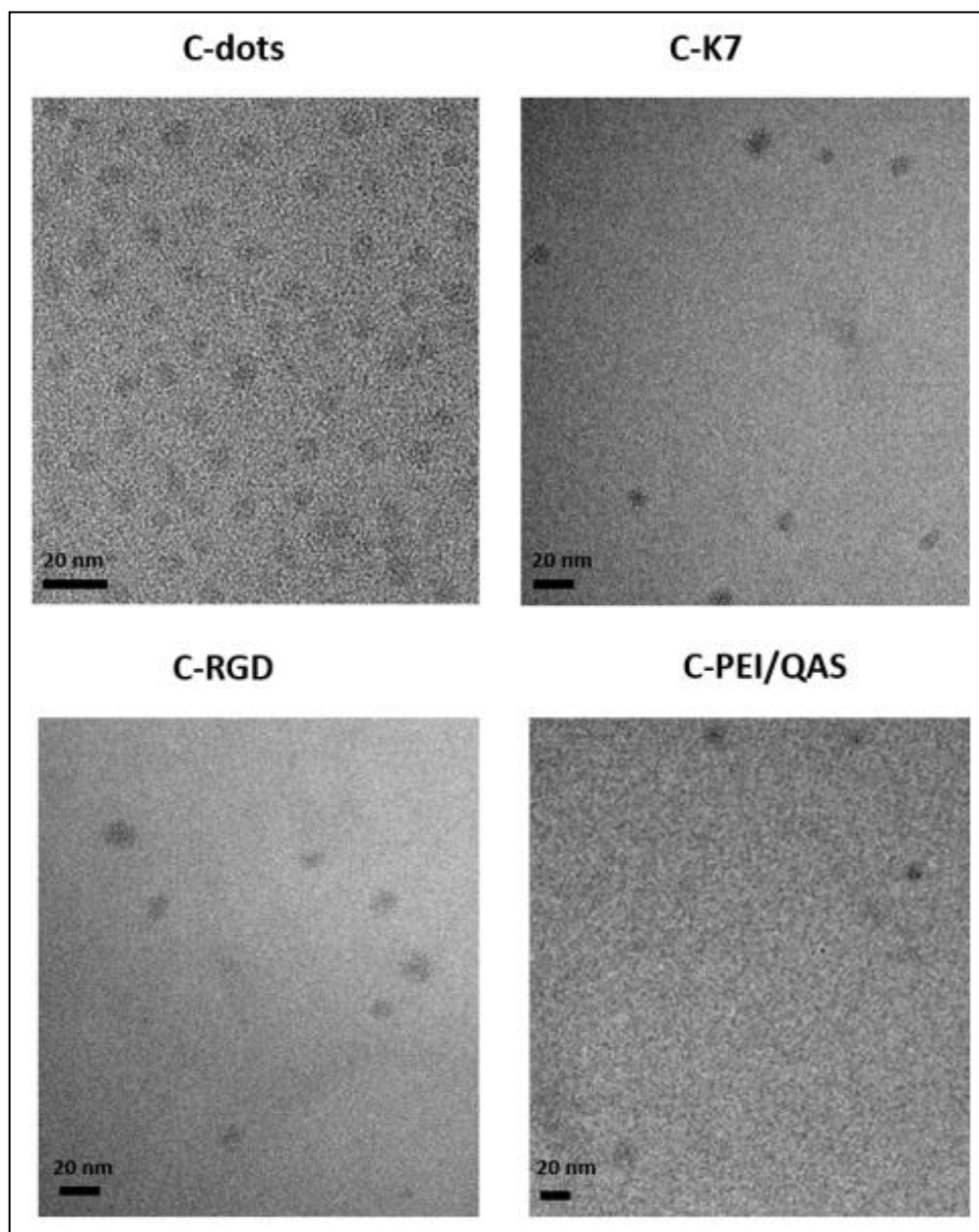


Figure 119: TEM images of: C-dots, C-K7, C-RGD, and C-PEI/QAS.

3.1.4 FTIR spectroscopy

The C-dots FTIR shows the presence of (O-H) broad region at 3418 cm^{-1} , which represents the presence of the COOH group on the surface of the C-dots. Supporting the presence of COOH, an O-H stretch shown at 1383 cm^{-1} as shown in Figure 120 a (289). Furthermore, the C-dots shows presence of amide bond by the stretching C=O at 1625 cm^{-1} , supported by an N-H bending at 1590 cm^{-1} , and an N-H stretching centred at 3100 cm^{-1} , due to the formation of the amide-containing fluorophores (289). The FTIR also shows signal related to the sp^2 vibration which represents aromatic rings at 3120 cm^{-1} (290). Supporting the FTIR of the C-dots, the elemental analysis results show the presence of C, N, O, and H with 49.98%, 12.41%, 32.56%, and 5.05% respectively that reflects the functional groups in the FTIR (289), as shown in table 3.

The FTIR analysis of the K7 demonstrates the formation of amide bond, due to the presence of stretching C=O centered at 1640 cm^{-1} , in addition to an N-H bending at 1590 cm^{-1} , and an N-H stretching centred at 3100 cm^{-1} (291). Furthermore, an O-H broad region centred at 3420 cm^{-1} , a C-N stretch centred at 1153 cm^{-1} , and an sp^2 vibration centred at 2953 cm^{-1} , as shown in Figure 120 b.

The FTIR analysis of the C-K7 demonstrates that the conjugation was successful, this is due the presence of signals in the C-K7 are similar to the signals in C-dots and K7. The conjugate exhibits an amide as shown in the signal at 1625 cm^{-1} represents to the C=O stretching, a signal centred at 1590 cm^{-1} represents the N-H bending, and an N-H stretching centred at 3100 cm^{-1} . Furthermore, the C-K7 shows a signal at 1383 cm^{-1} represent the O-H bending stretch in addition to the O-H broad at 3418 cm^{-1} , which they represent the COOH on the surface of the C-dots, as shown in Figure 120 c. Figure 120 c also shows the presence of C-N around 2000 cm^{-1} which indicates the formation of the covalent bond between the C-dots and K7.

The FTIR results supported by the elemental analysis results, as the elemental analysis of the C-K7 shows that it is composed of 48.73% of C, 33.77% of O, 12.42% of N, and 5.89% of H.

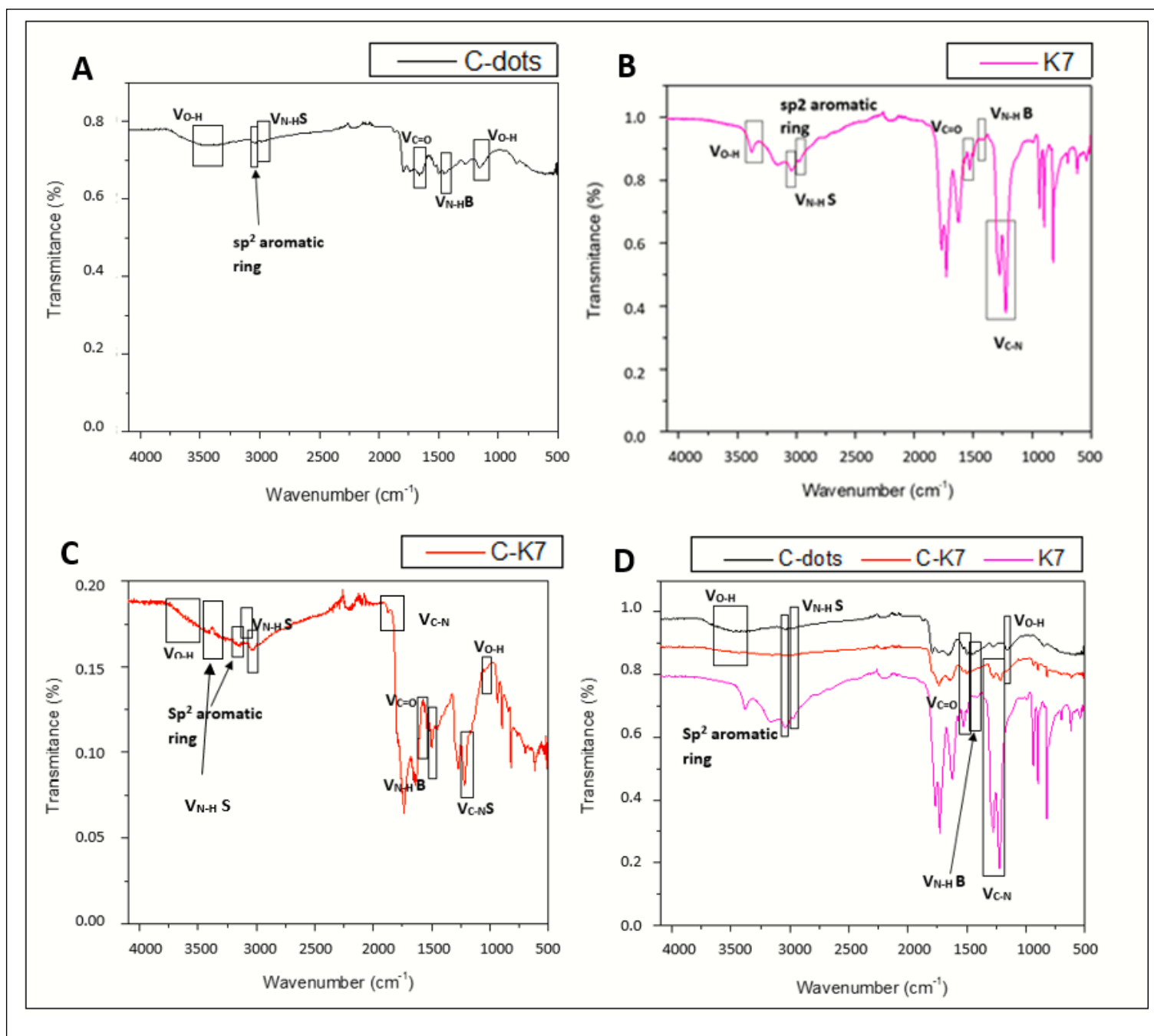


Figure 120: FTIR spectra of: A) C-dots, B) K7, C) C-K7, and D) a comparison of A, B, and C. All the samples were tested in solid state.

The FTIR of the RGD peptide shows that the RGD it has a strong signal at 1655 cm^{-1} which represents the primary amide, and a strong signal at 1500 cm^{-1} which represents the secondary amide (292). Furthermore, the FTIR of the RGD shows that it exhibits an N-H band at 1590 cm^{-1} , and C-N stretch at 1153 cm^{-1} , in addition to a stretching of C=O centred at 1625 cm^{-1} , and a broad region of O-H centred at 3412 cm^{-1} (292). Refer to Figure 121 b.

The FTIR analysis of the C-RGD demonstrate that the conjugation was successful, this is due to the presence of a signal around 2000 cm^{-1} that demonstrates the formation of N-C between the C-dots and the RGD as shown in Figure 121 C. Furthermore, the signals in the C-K7 are similar to the signals in C-dots and the RGD. The conjugate shows signals of I amide centred at 1655 cm^{-1} and II amide centred at 1500 cm^{-1} similar to the FTIR of the RGD, as shown in Figure 121 c. Furthermore, the conjugate exhibits an (O-H) broad region at 3418 cm^{-1} as well as an O-H bending stretch centred at 1383 cm^{-1} , that determine the presence of COOH, which is similar to the signals that appeared in the FTIR analysis of the C-dots as shown in Figure 121 A. The conjugate also shows signals centered at 1153 cm^{-1} that represents the C-N stretch, and 1625 cm^{-1} that represents the C=O, in which both signals are shown in the FTIR analysis of the C-dots and the RGD as shown in Figure 121 D.

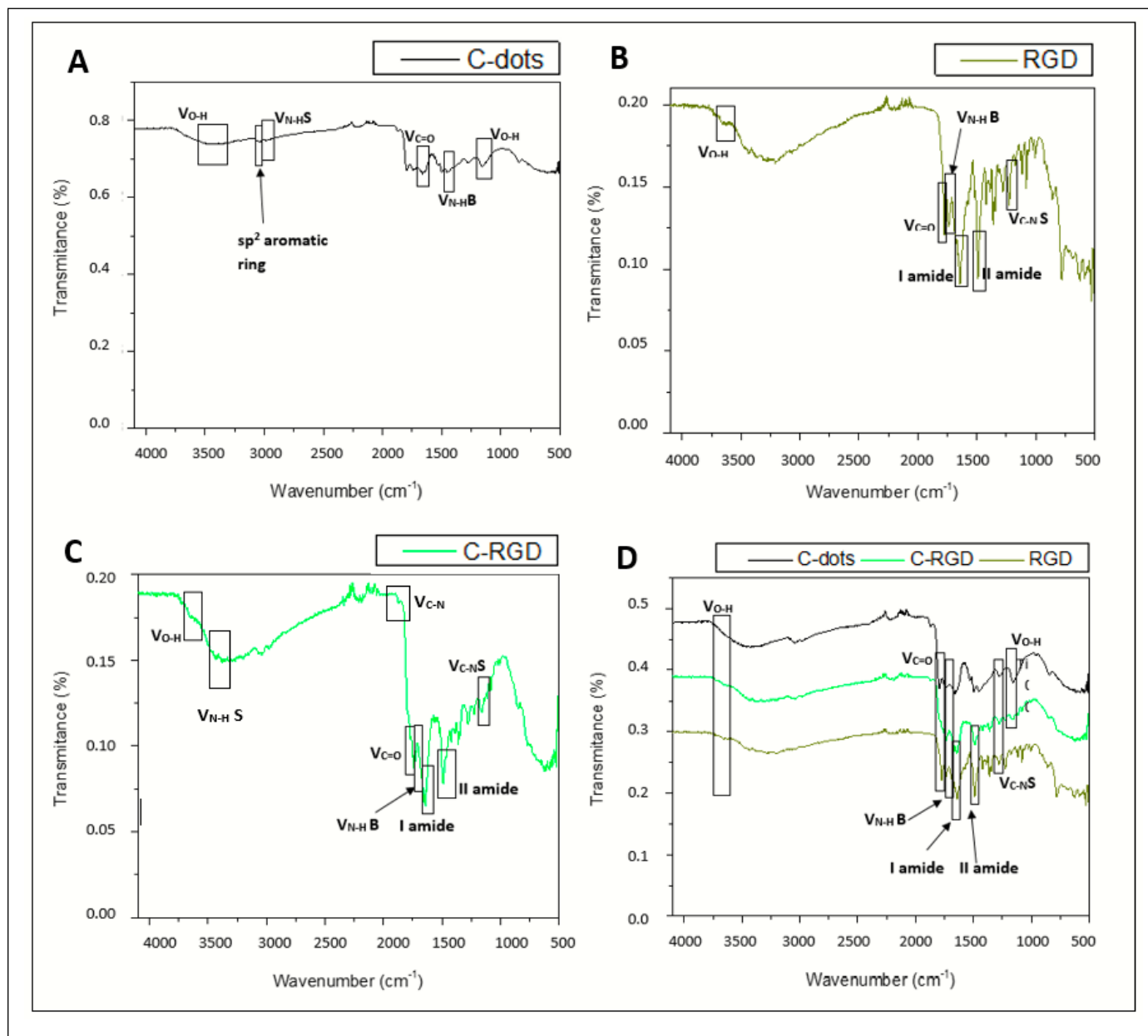


Figure 121: FTIR spectra of: A) C-dots, B) RGD, C) C-RGD, and D) a comparison of A, B, and C. All the samples were tested in solid state.

The FTIR analysis of the PEI/QAS shows that it has a C-H stretching band of the alkylammonium cations centred at 3020 cm^{-1} , as shown in Figure 122 b (293). In addition to a strong C-H band centred at 2856 cm^{-1} represents the CH_2 groups of the quaternary ammonium salt, as shown in Figure 122 b (294). Furthermore, the FTIR analysis also shows a vibration of C-H bending centred at 1487 cm^{-1} that represents the $(\text{CH}_3)_4\text{-N}^+$, and a C=O stretching band centred at 1640 cm^{-1} as shown in Figure 122 b (294).

The FTIR analysis of the C-PEI/QAS demonstrates that the conjugation of the C-dots and the PEI/QAS was successful, due to the similarity of the FTIR signals of the C-PEI/QAS to the signals of the C-dots and the signals of the PEI/QAS. The conjugate shows that a C-H stretching band of the alkylammonium cations centred at 3020 cm^{-1} still exists after the conjugation, as well as the C-H band centred at 2856 cm^{-1} which is related to the C-H_2 of the quaternary ammonium salt, as shown in Figure 122 c. In addition to the O-H broad region at 3418 cm^{-1} which exists in the PEI/QAS as well as the C-dots, that is related to the COOH on the surface of the C-dots, supported by the O-H bending stretch centred at 1383 cm^{-1} , as shown in Figure 122 c. Furthermore, the conjugate shows a signal of C-H bending at 1487 cm^{-1} that represents the $(\text{CH}_3)_4\text{-N}^+$ of the quaternary ammonium salt, and signal of a C=O stretching band centred at 1640 cm^{-1} which exists in the C-dots as well as the PEI/QAS, as shown in Figure 122 c. The elemental analysis results support the FTIR analysis of the C-PEI/QAS as it demonstrates that it is composed of 21.10% of C, 48.31% of O, 5.03% of N, and 3.88% of H, as shown in table 3.

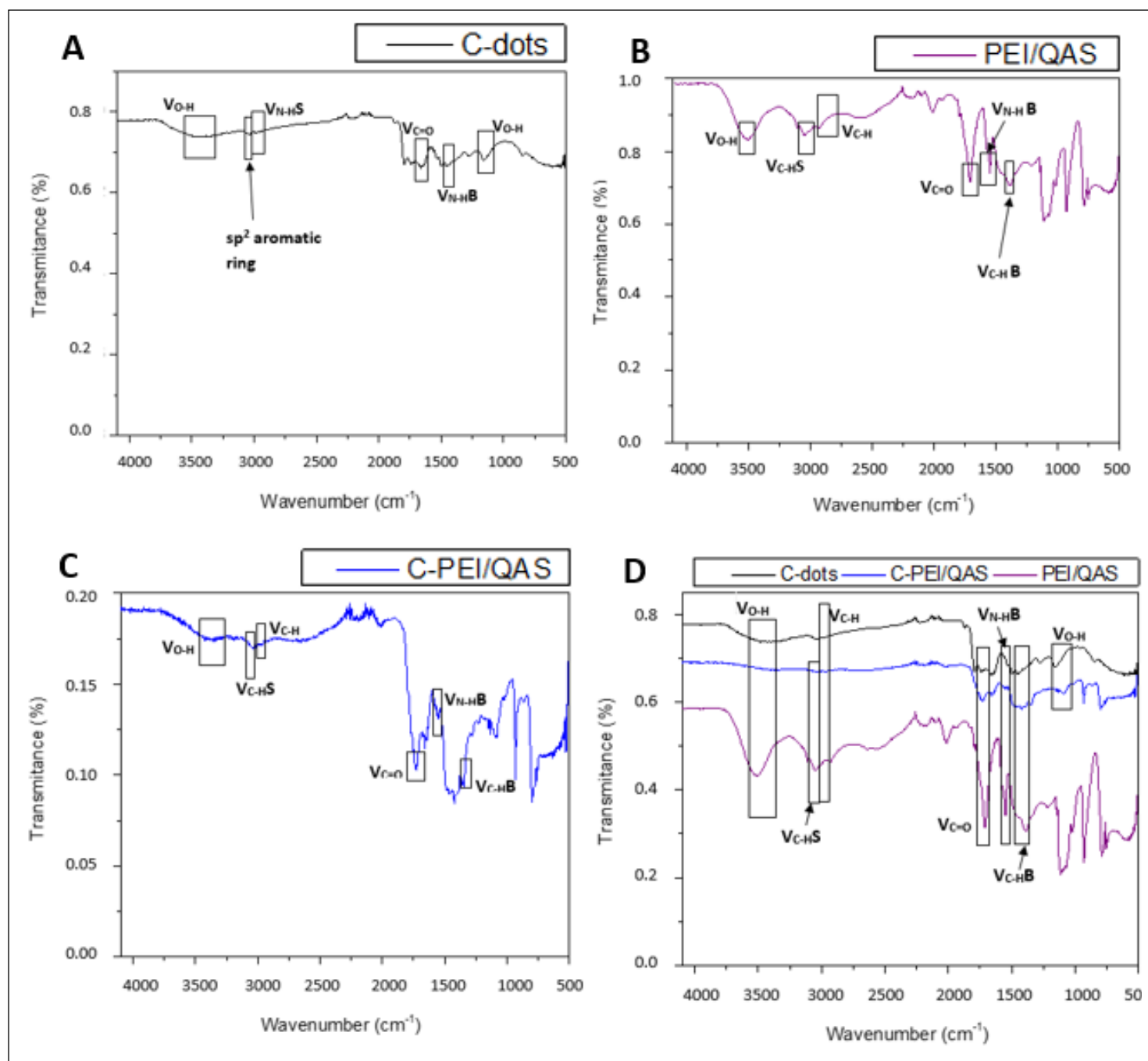


Figure 122: FTIR spectra of: A) C-dots, B) PEI/QAS, C) C-PEI/QAS, and D) a comparison of A, B, and C. All the samples were tested in solid state.

The FTIR analysis of the Jeff shows a C-O stretching at 1108 cm^{-1} that represents the C-O-C of the ethylene glycol group, and a signal for the C-N stretching centred at 1228 cm^{-1} which represents the C-N-C of the III amine, as shown in Figure 123 b (295). Furthermore, the FTIR analysis of Jeff shows a C-H bending centred at 1463 cm^{-1} , and a C-H stretching at 2850 cm^{-1} , as shown in Figure 123 b (295). In addition to an O-H stretching at 1353 cm^{-1} as shown in Figure 123 b.

The FTIR analysis of the C-J demonstrates that the conjugation of the C-dots and the Jeff was successful, this is due to the presence of common signals in the C-J and the C-dots, as well as the Jeff. The FTIR of the C-J shows a signal at 3418 cm^{-1} that represents the O-H broad region of the COOH on the surface of the C-dots, in addition to the vibration of the sp^2 which is centred at 3120 cm^{-1} , and a C=O stretching at 1652 cm^{-1} as shown in Figure 123 c. Furthermore, the FTIR of the C-J shows a signal of C-H stretching at 2850 cm^{-1} , as well as a C-H bending at 1463 cm^{-1} , which are present in the Jeff FTIR analysis as shown in Figure 123c. The FTIR analysis of the C-J also shows a signal centred at 1353 cm^{-1} related to the O-H stretching, which is common in the FTIR of the Jeffamine, as shown in Figure 123 c. The elemental analysis of the C-J supports the FTIR analysis, as it shows that the C-J composes of 37.75% of C, 48.86% of O, 8.85% of N, and 4.45% of H, as shown in table 3.

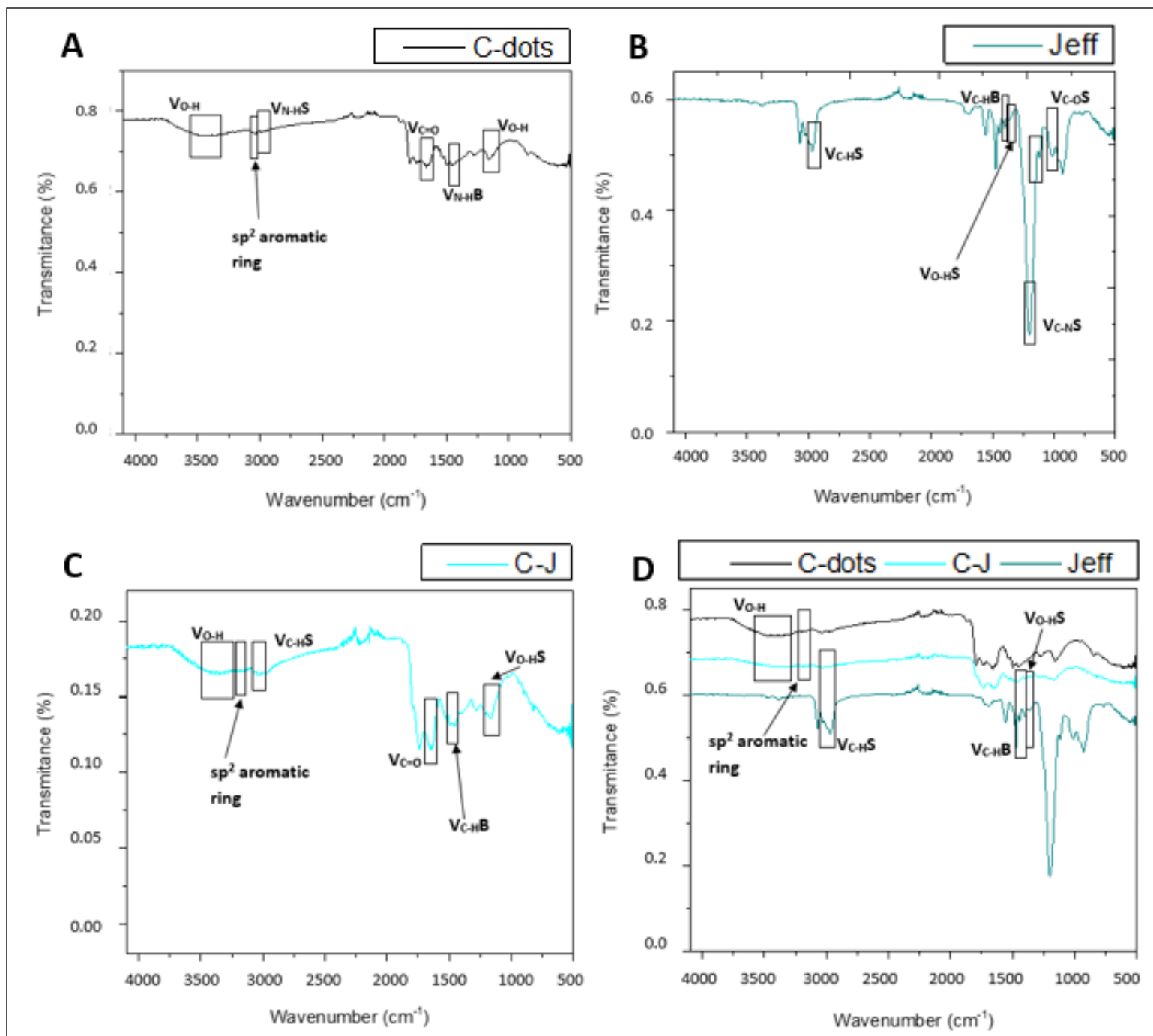


Figure 123: FTIR spectra of: A) C-dots, B) PEI/QAS, C) C-PEI/QAS, and D) a comparison of A, B, and C. All the samples were tested in solid state, except Jeff where it was tested in a liquid state (as approached by the provider).

3.1.5 Elemental analysis

The elemental analysis results of the C-dots, the C-K7, the C-RGD, the C-PEI/QAS, the C-J, the K7, and the PEI/QAS demonstrate the percentages of the C, O, N, and the H in each of the synthesised samples, and are presented in the table below.

Table 3: Elemental analysis for C-dots, C-K7, C-RGD, C-PEI/QAS, and C-J.

Material	C	N	O	H
C-dots	49.98%	12.41%	32.56%	5.05%
C-K7	48.73%	12.42%	33.77%	5.89%
C-RGD	49.35%	12.13%	33.03%	5.49%
C-PEI/QAS	41.72%	13.16%	36.82%	8.30%
C-J	37.75%	8.85%	48.86%	4.54%

3.1.6 TGA

The TGA analysis of the C-dots shows that there is a gradual weight loss starting at 30°C until the temperature reaches 100°C, with a percentage weight loss of 9.15% of the sample. This loss is due to the moisture in the sample (296). Then the sample remains relatively stable until the temperature reaches 270°C followed by gradual loss of the weight, until the temperature reaches 500°C with a percentage weight loss of 35.9% that is related to the decomposition of the C-dots, as shown in figure 124 (296).

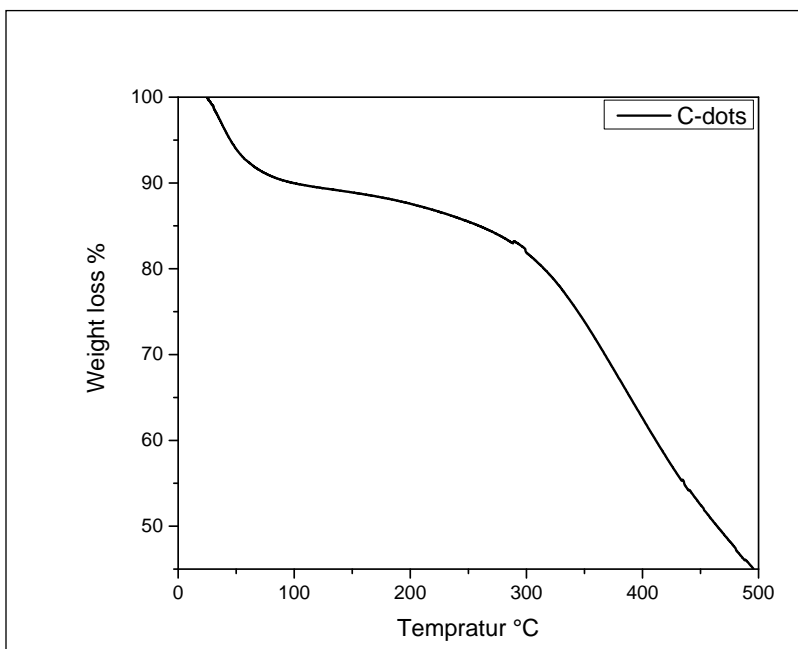


Figure 124: TGA curve of C-dots.

The TGA analysis of the K7 shows that there is a slow weight loss starting at 55°C until the temperature reaches 99°C, this is due to the loss of moist of the sample with a percentage weight loss of 2.5% (297). Then the sample relatively stabilises until the temperature reaches 180°C, followed by a dramatic weight loss (phase one) continues until the temperature reaches 240°C with 35% weight loss of the sample, that is related to the loss of the organic content of the peptide (297). After that, followed by a (phase two) gradual weight loss starts at 250°C until the temperature reaches 500°C with a percentage weight loss of 51% related to the further decomposition of the organic content of the peptide, as shown in Figure 125.

The TGA analysis of the C-K7 shows that there is a gradual weight loss starting at 30°C until the temperature reaches 68°C, then the loss become slow until the temperature reaches 104°C with 7.15% weight loss, due to the moist in the sample. Then the sample is relatively stabilising and start gradually losing weight at 151°C until the temperature reaches 290°C with a percentage of 12% weight loss, in which is behaving in a similar way to the K7 as shown in Figure 125 B, and this demonstrate that the conjugation of the C-dots, and the K7 was successful. In addition, the C-K7 start losing weight dramatically at 311°C until the temperature

reaches 500°C with a percentage of weight loss of 31%. In which shows similarity to the C-dots, as shown in Figure 125.

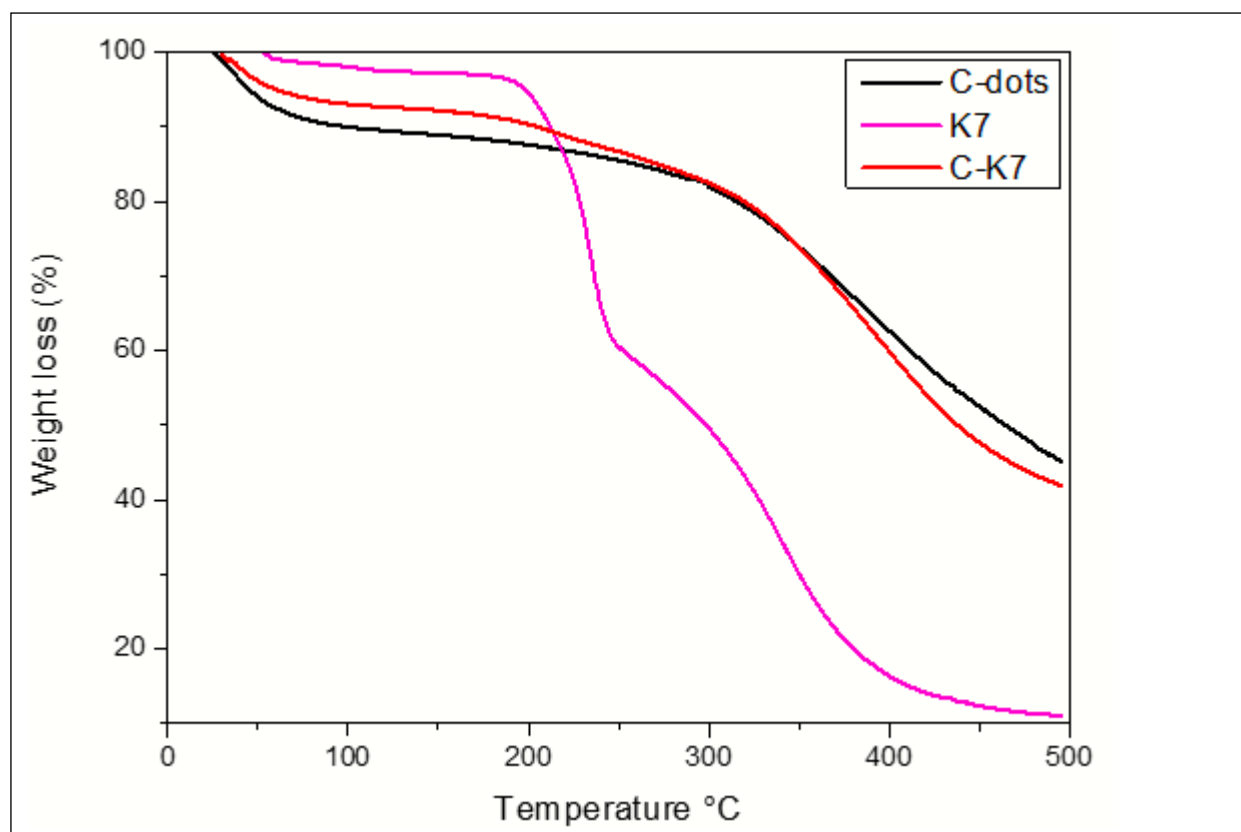


Figure 125: TGA curves of C-dots, K7, and C-K7.

Figure 125 also demonstrates that the conjugation of the C-dots had increased the organic content of the C-dots, yet not significantly, hence the increase is 3.5% as shown in table 4.

The TGA analysis of the RGD peptide demonstrates that there is a dramatic weight loss starting at 50 °C until the temperature reaches 70°C with 10% loss due to the loss of the moist content. The RGD decompose between 280°C and 300°C (298) as shown in Figure 126.

The TGA analysis of the C-RGD shows that there is a gradual weight loss starting at 25°C until the temperature reaches 100°C with a percentage of weight loss of 9%, this is due to the loss of the moisture in the sample (298). Then the sample relatively stabilises until the temperature

reaches 104°C and the sample starts losing weight gradually until the temperature reaches 500°C with 50% weight loss this is due to the decomposition of the organic content of the RGD peptide as well as the C-dots (298), as shown in Figure 126.

The functionalisation of the C-dots with RGD increased the organic content of the C-dots by 6.23% as shown in Figure 126 and table 4.

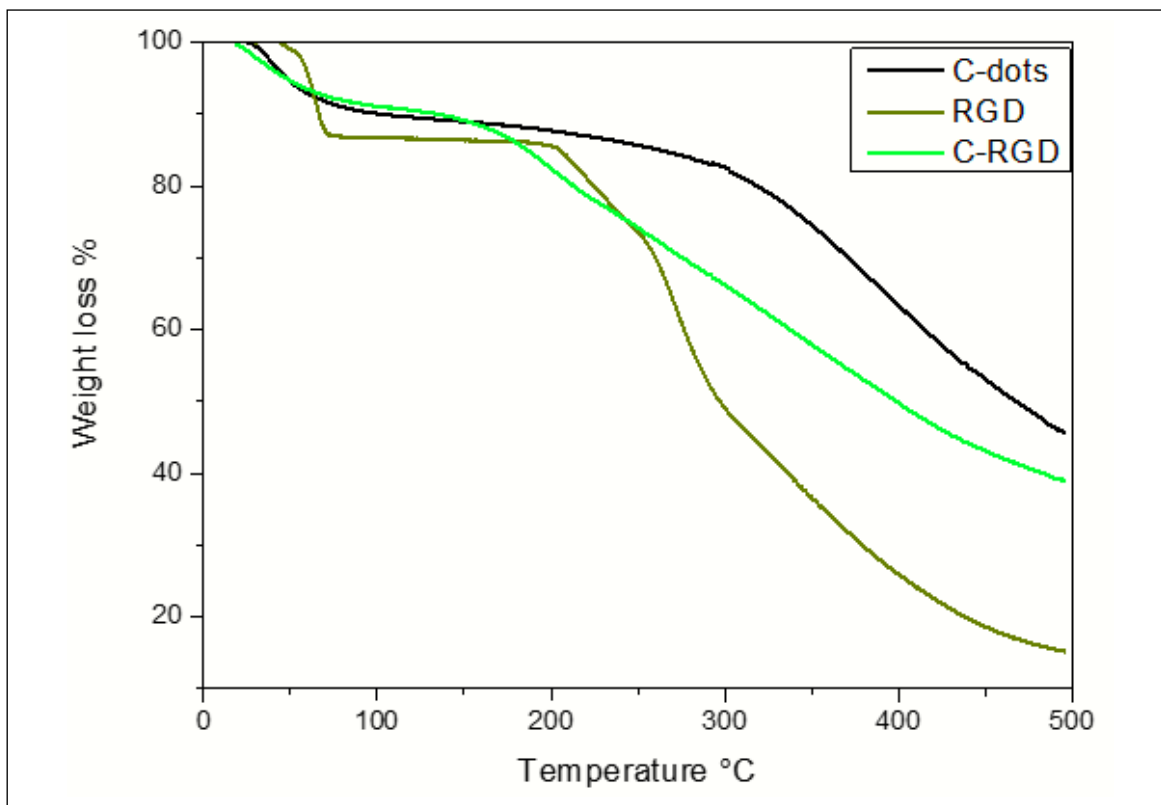


Figure 126: TGA curve of C-dots, RGD, and C-RGD.

The TGA analysis of the PEI/QAS shows that there is slow weight loss starts at 40°C and continues until the temperature reaches 85°C then the weight loss started getting faster until the temperature reaches 119°C with percentage of weight loss of 6.5%, this is due to the loss of the moist in the sample (299). Then the temperature relatively stabilises until 171°C followed by a dramatic loss of the weight until the temperature reaches 307°C with a percentage of weight loss of 43.5% which is related to the decomposition of the organic content of the PEI/QAS (299). Followed by slow loss of weight until the temperature reaches 500°C in which

related to further decomposition of the organic content with a percentage loss of 2.5%, as shown in Figure 127.

The TGA analysis of the C-PEI/QAS shows that there is a gradual weight loss starts at 115 °C until the temperature reaches 146 °C with 6.15% of weight loss, this is due to the loss of the moist in the sample. Then followed by a dramatic weight loss starts until the temperature reaches 274 °C with a percentage of weight loss of 45.6% due to the decomposition of the organic content of the PEI/QAS, as shown in Figure 127, which supports the prove of the conjugation of the C-dots and the PEI/QAS. After that, more weight loss continues until the temperature reaches 500 °C, due to the decomposition of the organic content of the C-dots as shown in Figure 127.

Figure 127 also shows that the conjugation of the C-dots with PEI/QAS increased the organic content by 8.28%.

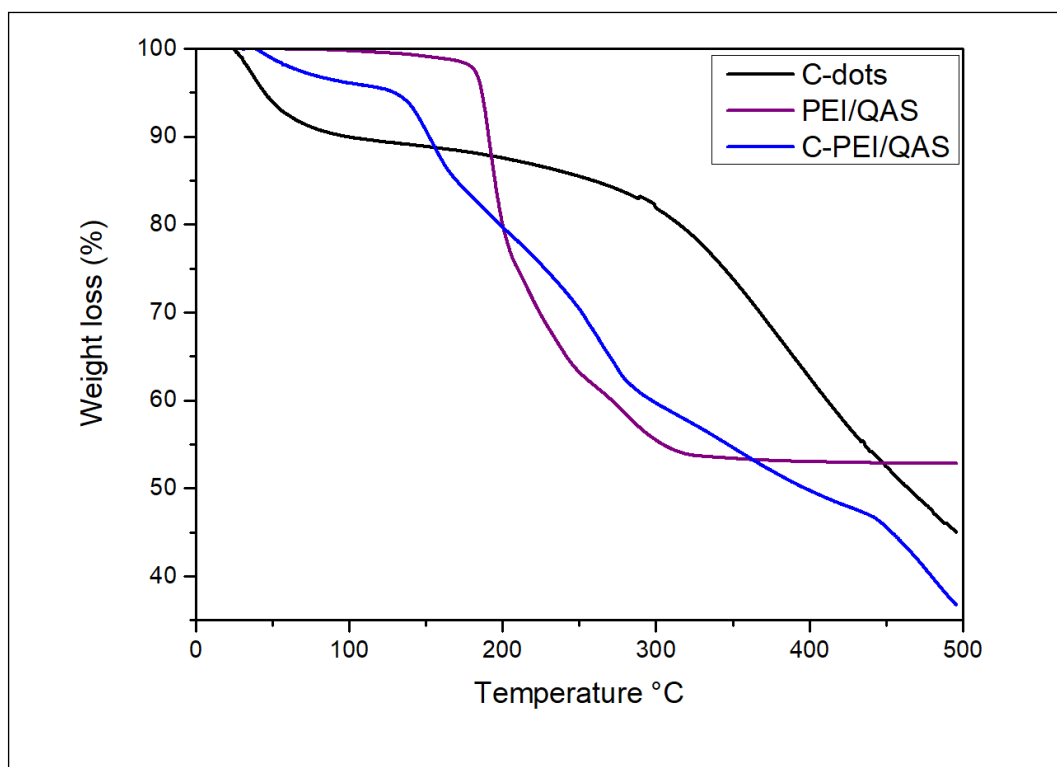


Figure 127: TGA curves of C-dots, PEI/QAS, and C-PEI/QAS.

Table 4: the percentage of weight loss of the samples using the TGA analysis.

Sample	Weight loss (0°C-100°C)	Total weight loss (0°C-500°C)	Δ C-dots of the conjugates
C-dots	10.3%	54.96%	
K7	2.13%	89.03%	
C-K7	7.04%	58.46%	3.5%
RGD	13.37%	84.98%	
C-RGD	8.92%	61.19%	6.23%
PEI/QAS	0.24%	47.14%	
C-PEI/QAS	4%	63.7%	8.74%

3.2 Photophysical properties

3.2.1 UV-vis

The UV-vis spectrum of aqueous dispersion of C-dots is dominated by the peak centered at 341 nm that is attributed to the $n-\pi^*$ transition state of the C=O bond (301), (302) as shown in Figure 128. Conjugation of C-dots with K7, RGD, and Jeffamine does not have any major impact on the UV- spectra, however C-PEI/QAS shows significantly reduced the intensity, an effect that might be attributes to the bulky nature of the surface functional groups.

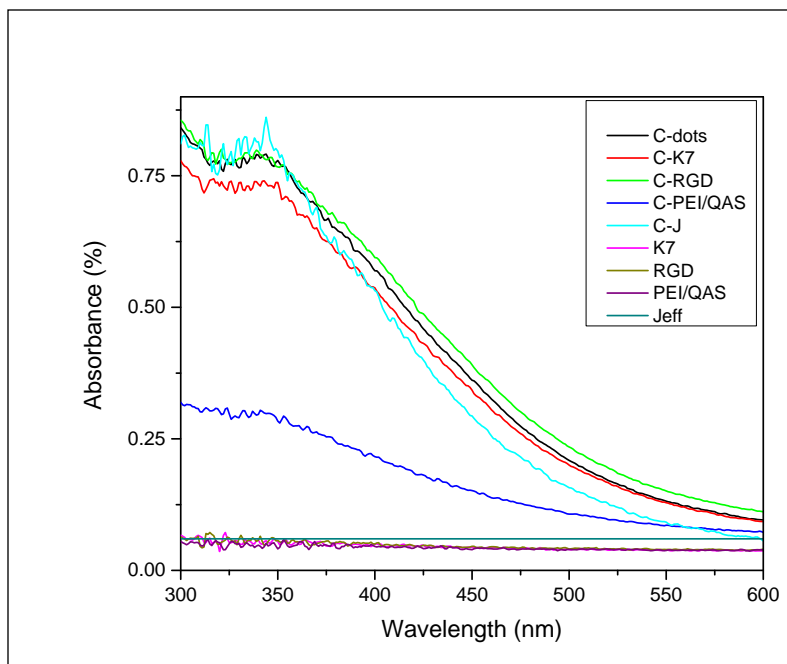


Figure 128: UV-vis spectra of 0.1 mg/mL aqueous solutions of C-dots, C-K7, C-RGD, C-PEI/QAS, C-J, K7, RGD, PEI/QAS, and Jeffamine.

3.2.2 Photoluminescence

It has been demonstrated that C-dots derived from a mixture of CA with an amine-based precursor (such as EA or ammonia) show a dual emissive mode due to the λ_{ex} -dependent emission of the carbogenic cores and the λ_{ex} -independent emission of organic fluorophores (303), (304). It is now well-understood that this λ_{ex} -independent contribution can be traced back to the early studies of Behrmann et al. and Sell et al. who in 1884 and 1894 demonstrated the formation of the fluorophore citrazinic acid as a result of the hydrothermal decomposition of CA and urea or ammonia (305), (306).

As shown in Figure 129 C-dots demonstrate an λ_{ex} -dependent emission stemming from the presence of carbogenic cores, along with an λ_{ex} -independent emission (that is dominant at

low λ_{ex}) arising from the presence of organic fluorophores (303), (304). Figure 129 shows that the higher λ_{em} intensity is at 480 nm excitation, and the intensity reduces as the wavelength increases.

The PL spectra of the C-K7, C-RGD, C-PEI/QAS and C-J (shown in Figures 130, 131, 132, and 133, respectively) are dominated by λ_{ex} -dependent emissions, indicating a suppressed PL mode of the organic fluorophores units. The PL spectra of conjugates show pronounced blue shifts compared to C-dots.

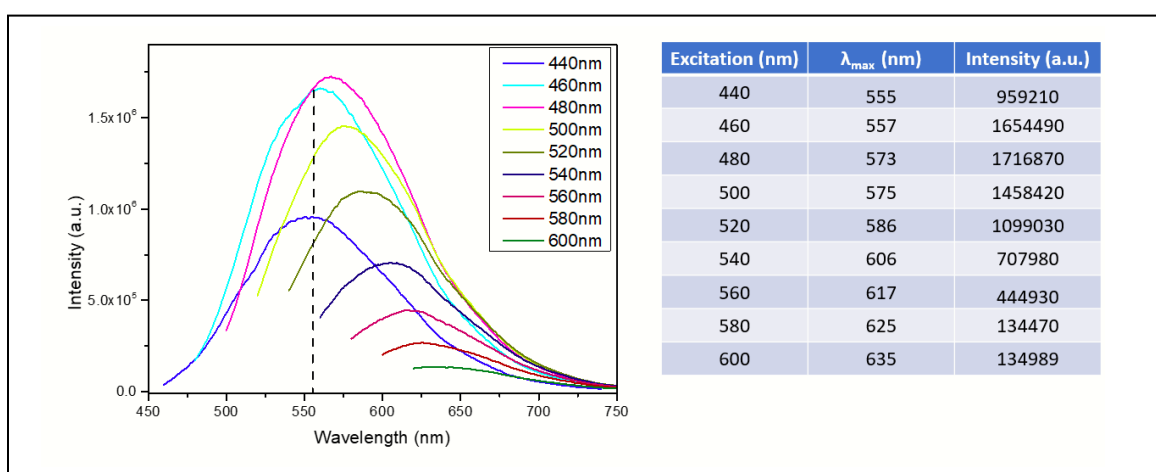


Figure 129: PL spectra of 0.085 mg/mL aqueous solution of C-dots λ_{ex} range of 440-600 nm with 20 nm increment. The dashed line indicates the λ_{ex} -independent emission that is apparent at low λ_{ex} .

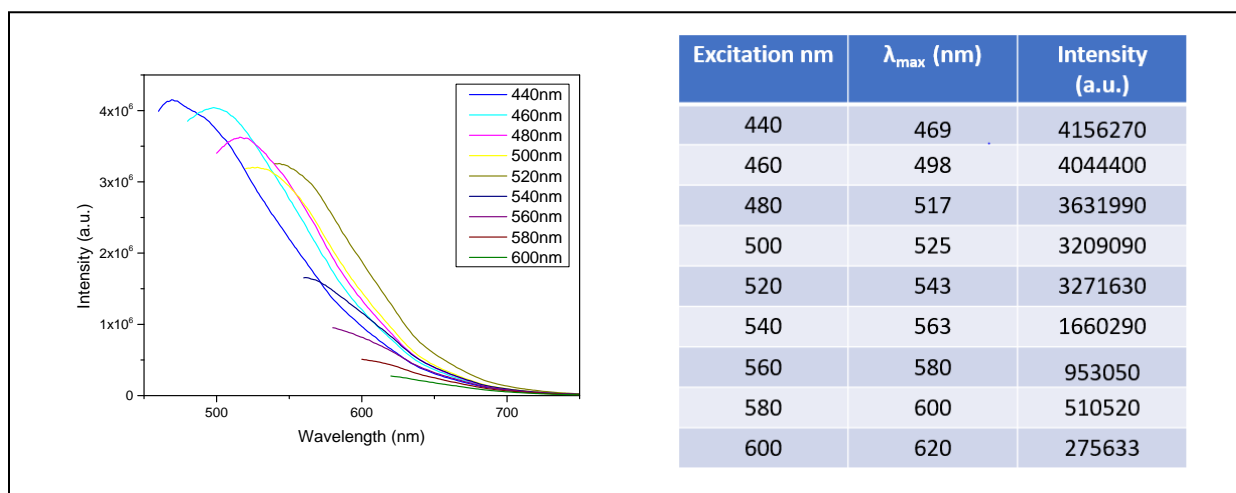


Figure 130: PL spectra of 0.085 mg/mL aqueous solution of C-K7 λ_{ex} range of 440-600 nm with 20 nm increment.

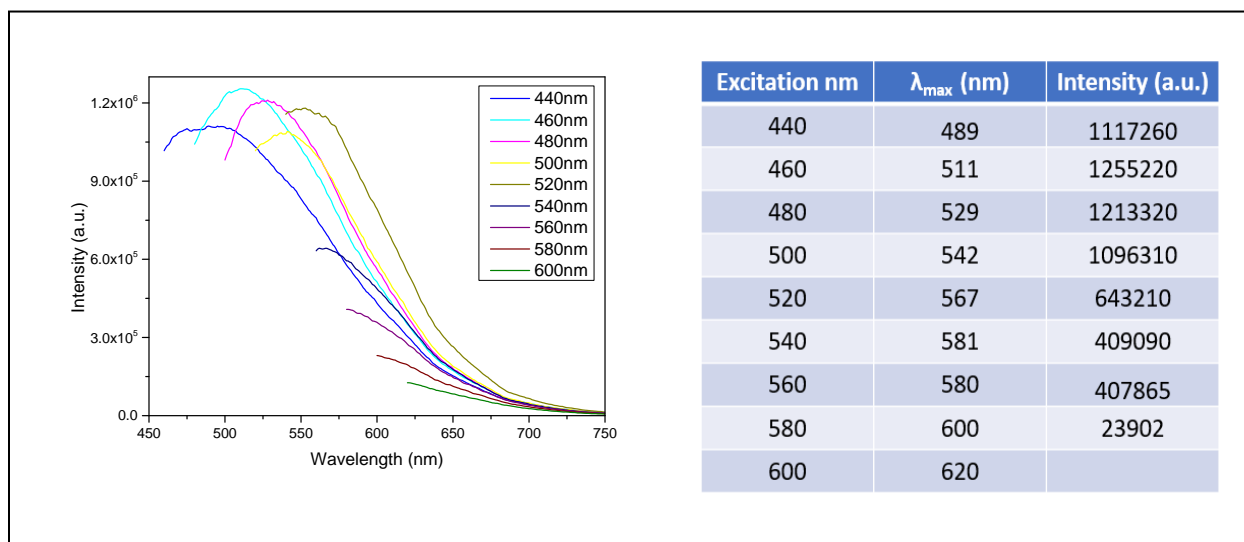


Figure 131: PL spectra of 0.085 mg/mL aqueous solution of C-RGD λ_{ex} range of 440-600 nm with 20 nm increment.

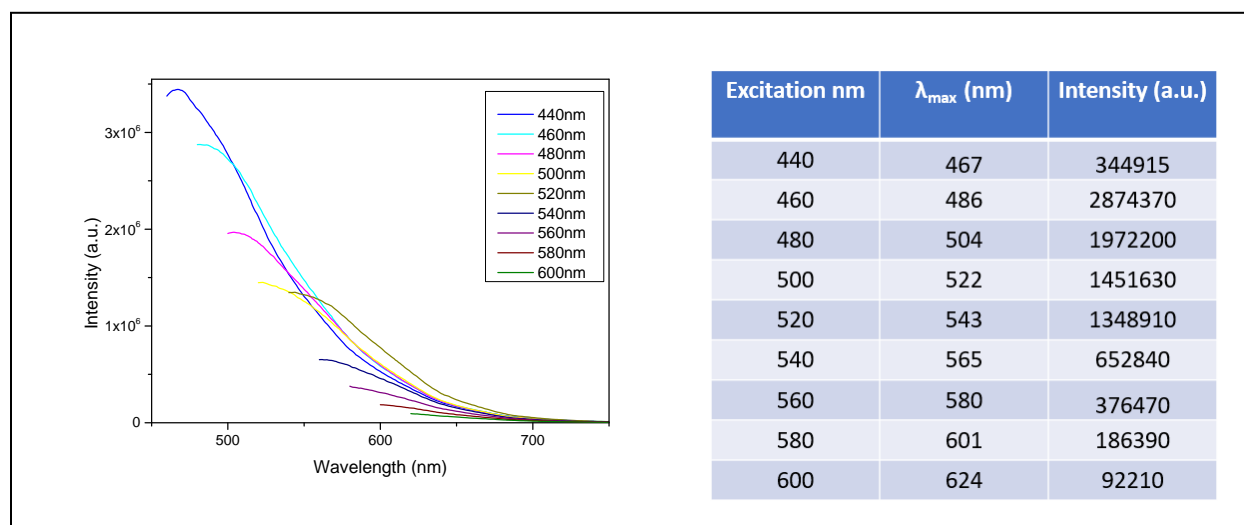


Figure 132: PL spectra of 0.085 mg/mL aqueous solution of C-PEI/QAS λ_{ex} range of 440-600 nm with 20 nm increment.

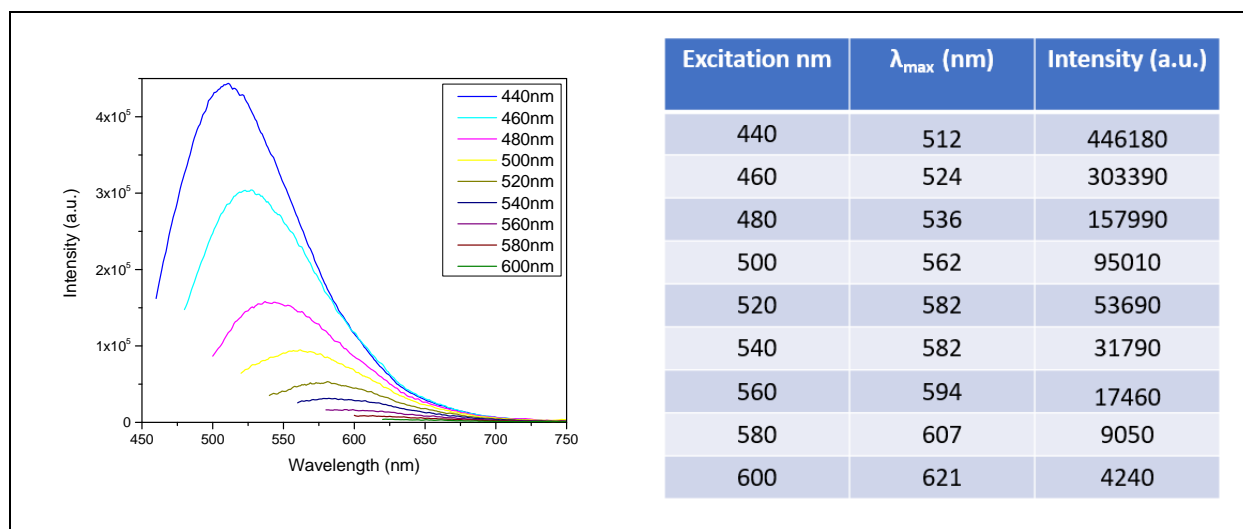


Figure 133: PL spectra of 0.085 mg/mL aqueous solution of C- λ_{ex} range of 440-600 nm with 20 nm increment.

3.2.3 Quantum yield

The QY values of the C-dots as well as all the conjugations that were synthesised in this project were calculated in regard to a reference dye, in which DAPI was used with λ_{ex} of 345 nm and QY of 92%. The results are shown in table 5.

Table 5: QY values of the C-dots, the C-K7, the C-RGD, the C-PEI/QAS, and the C-J, in an aqueous solution $\lambda_{\text{ex}} = 345$ in correspondence to DAPI dye.

Sample	QY%
C-dots	4.2
C-K7	5.4

C-RGD	7.4
C-PEI/QAS	7.3
C-J	5.1

Table 6: UV-vis and PL measurements used to calculate the QY of the nanoparticles.

Sample	Concentration (mg/mL)	Absorbance (a.u.)	PL (a.u.)
C-dots	0.1	0.044	1.21E8
	0.09	0.039	1.09E8
	0.083	0.034	1.01E8
	0.076	0.030	9.04E7
C-K7	0.058	0.042	1.27E8
	0.055	0.030	1.22E8
	0.052	0.025	1.04E8
	0.05	0.024	1.19E8
C-RGD	0.058	0.070	1.64E8
	0.055	0.063	1.70E8
	0.052	0.056	1.73E8
	0.05	0.051	1.34E8
C-PEI/QAS	0.25	0.027	1.45E8
	0.33	0.033	1.79E8
	0.5	0.074	2.01E8
	0.4	0.058	1.75E8
C-J	0.1	0.042	1.10E8
	0.14	0.037	1.65E8
	0.125	0.032	1.39E8
	0.11	0.092	1.20E8

As shown in table 5, the C-dots exhibit a value of 4.2% which is similar to other reports for C-dots were synthesised using hydrothermal treatment of CA (7) (307). On the other hand, all the conjugated C-dots exhibit a higher QY in comparison to the C-dots, which is expected as the passivation of the C-dots increase the QY value (308), refer to table 5.

Table 6 shows the data collected for each sample showing different maximum intensity under different λ_{ex} .

3.2.4 Lifetime

For further photophysical properties investigation, the fluorescence lifetime of the C-dots, and all of the C-dots conjugate samples were tested with $\lambda_{ex} = 375$ and 450 nm. the decay fitting results are listed in table 7, and the curves are shown in Figures: 134 and 135.

The decay of the C-dots at $\lambda_{ex} = 375$ nm shows a τ_{avg} of 8.2 ns, which is expected for the CA C-dots (309), as shown in table 7 and Figure 134 A. The decay of the C-K7, the C-RGD, the C-PEI/QAS and the C-J shows τ_{avg} values of 7.70 ns, 7.97 ns, 7.99 ns, and 5.13 ns respectively. This reduction of the τ_{avg} in the conjugate is due to the change in the molecular state of C-dots via the formation of C=N (310). The full decay curves of the C-K7, the C-RGD, the C-PEI/QAS and the C-J are shown in Figure 134.

Table 7: τ_{avg} values of the C-dots, C-K7, C-RGD, C-PEI/QAS, and C-J. All the samples were tested in an aqueous solution of 0.085 mg/mL.

Excitation Wavelength (nm)	Sample	τ_{avg} (ns)
375	C-dots	8.20
	C-K7	7.70
	C-RGD	7.97
	C-PEI/QAS	7.99

450	C-J	5.31
	C-dots	5.82
	C-K7	5.43
	C-RGD	5.24
	C-PEI/QAS	5.35
	C-J	4.35

The decay of the C-dots at $\lambda_{\text{ex}} = 450$ nm shows a τ_{avg} of 5.82 ns, which is expected for the CA C-dots at this wavelength (311), as shown in table 7 and Figure 136 A. The decay of the C-K7, the C-RGD, the C-PEI/QAS and the C-J shows τ_{avg} values of 5.43 ns, 5.24 ns, 5.35 ns, and 4.35 ns respectively. We can see a reduction in the τ_{avg} values of the conjugates, as was seen in the τ_{avg} values at 375 excitation, due to the same reason of the formation of C=N, resulting a change in the molecular state of C-dots (310). The full decay curves of the C-K7, the C-RGD, the C-PEI/QAS and the C-J are shown in Figure 136.

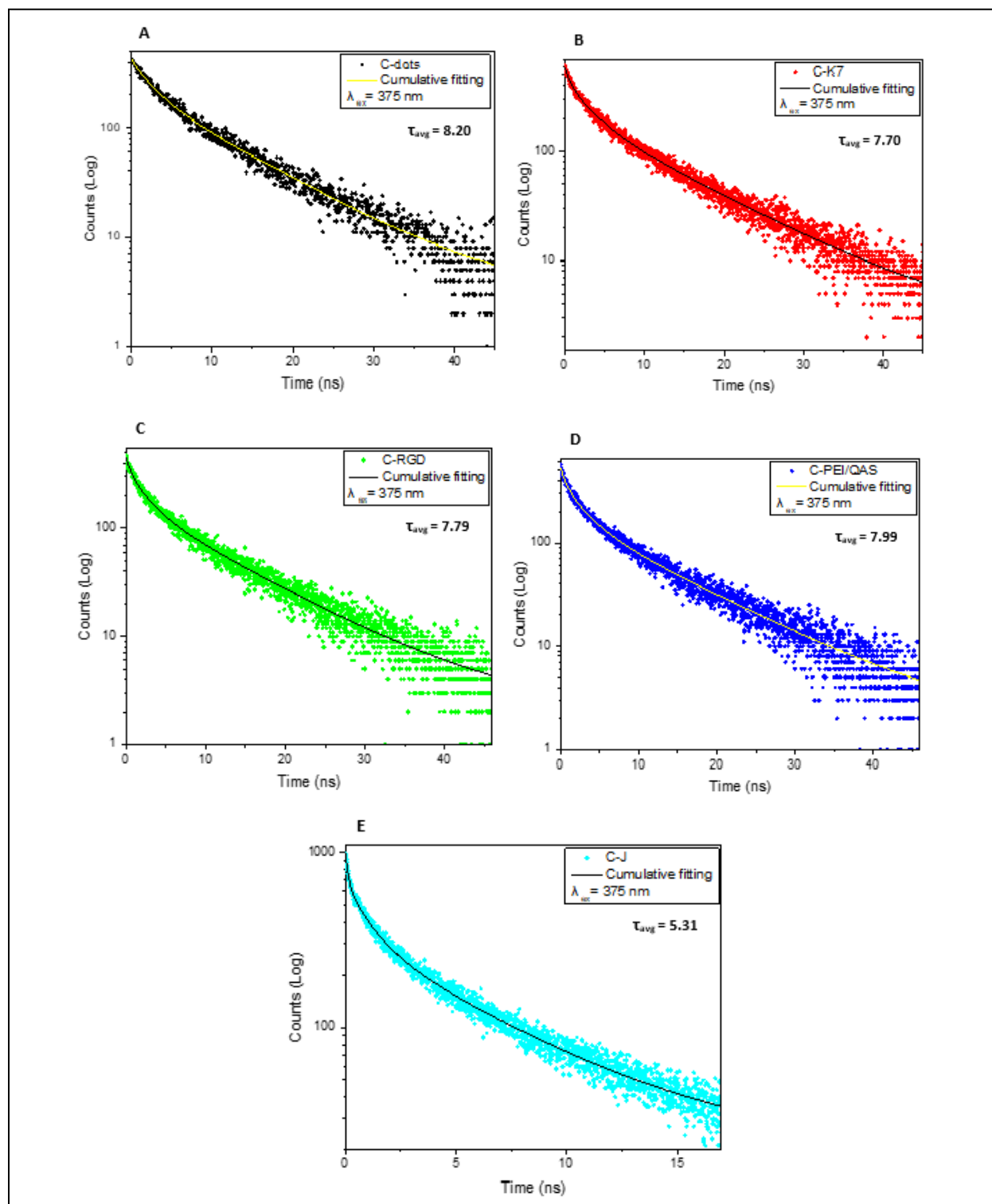


Figure 134: Fluorescence lifetime decay at $\lambda_{ex} = 375$ nm of 0.085 mg/mL aqueous solution of: A) C-Dots, B) C-K7, C) C-RGD, D) C-PEI/QAS, and E) C-J. The points represent the experimental data, and the lines correspond to the cumulative fitting curves.

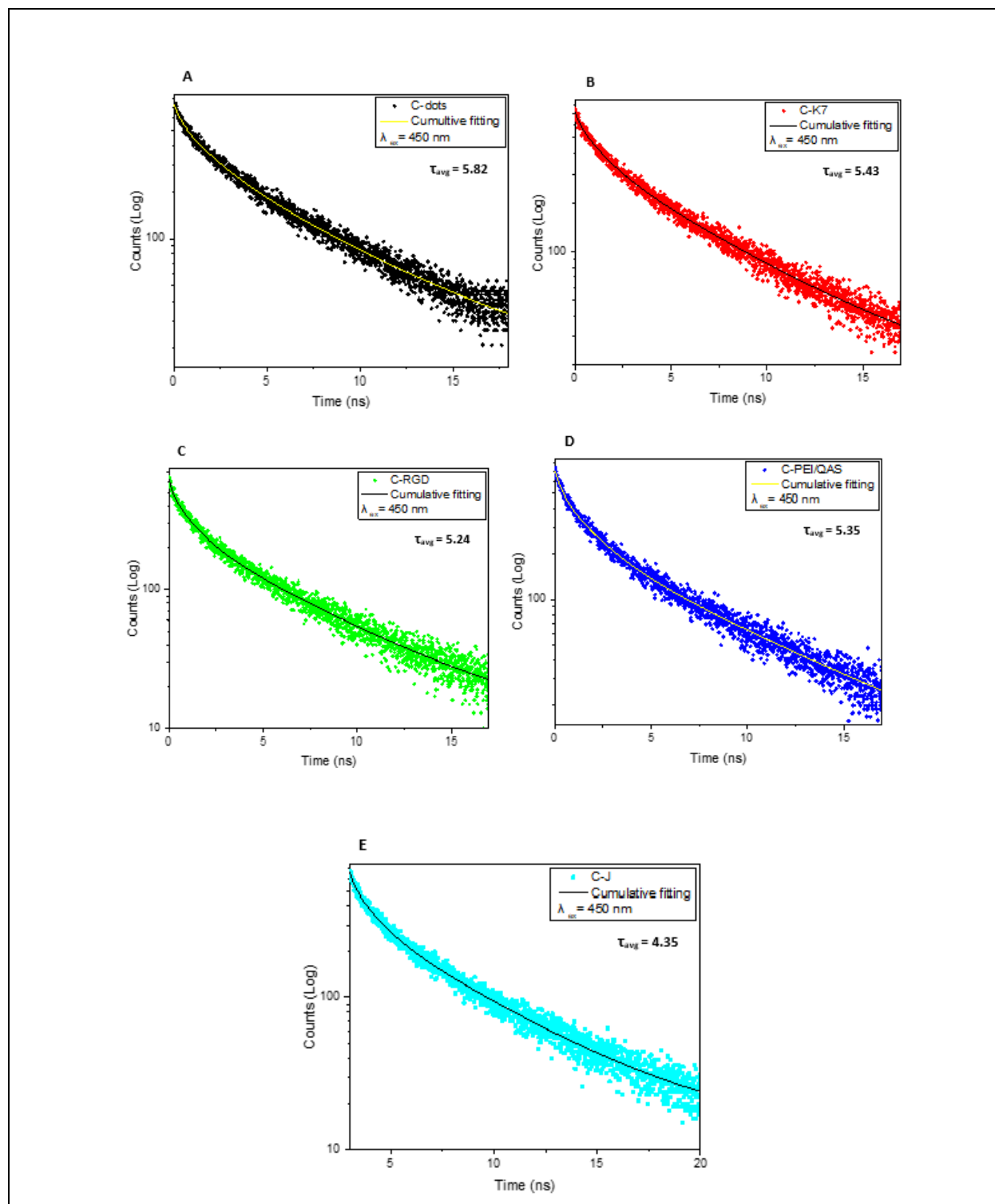


Figure 135: Fluorescence lifetime decay at λ_{ex} =450 nm of 0.085 mg/mL aqueous solutions of: A) C-Dots, B) C-K7, C) C-RGD, D) C-PEI/QAS, and E) C-J. The points represent the experimental data, and the lines correspond to the cumulative fitting curves.

3.3 Biological analysis

In this project various biological analysis were done in order to assess and prove the suitability of the C-dots and their conjugation as well as the K7 and the PEI/QAS (i.e., all the samples were synthesised) for the biomedical applications. Furthermore, to demonstrate the impact of the conjugated molecules on the C-dots. Therefore, two different toxicity assays were done: a) MTT assay, and b) PrestoBlue assay. In addition to Haemolysis assay.

Furthermore, C-dots and their conjugation were assessed as bioimaging materials, and as antibacterial agents.

3.3.1 MTT results

The C-dots has been reported to be materials with very low toxicity, that can be considered to be promising for the biomedical application (90). The Cell viability for HeLa cells incubated with C-dots for 24 h remains close to 100% for 10 $\mu\text{g}/\text{mL}$ C-dots, and gradually decreases upon increasing the C-dot loading, thus approaching 86% for HeLa in the presence of 100 $\mu\text{g}/\text{mL}$ C-dots, as shown in Figure 136. Furthermore, the cell viability of U87 cells incubated with C-dots for 24 h is at high level with 99% for 10 $\mu\text{g}/\text{mL}$ loading of C-dots, and the cell viability gradually decreases as the loading of the C-dots increases resulting 84% cell viability for U87 cells with 100 $\mu\text{g}/\text{mL}$ C-dots, as shown in Figure 136. The cell viability of T98G incubated with C-dots for 24 h shows cell viability remains close to 100% for 10 $\mu\text{g}/\text{mL}$ loading C-dots, and the cell viability gradually decreases as the loading of C-dots increased resulting 85% cell viability with 100 $\mu\text{g}/\text{mL}$ C-dots, as shown in Figure 136. The cell viability of GC-1 SPG incubated with C-dots for 24 h shows high cell viability of 98% with 10 $\mu\text{g}/\text{mL}$ loading of C-dots, and the cell viability gradually decreases as the loading with C-dots increases resulting 84% cell viability with 100 $\mu\text{g}/\text{mL}$ of C-dots loading, as shown in Figure 136.

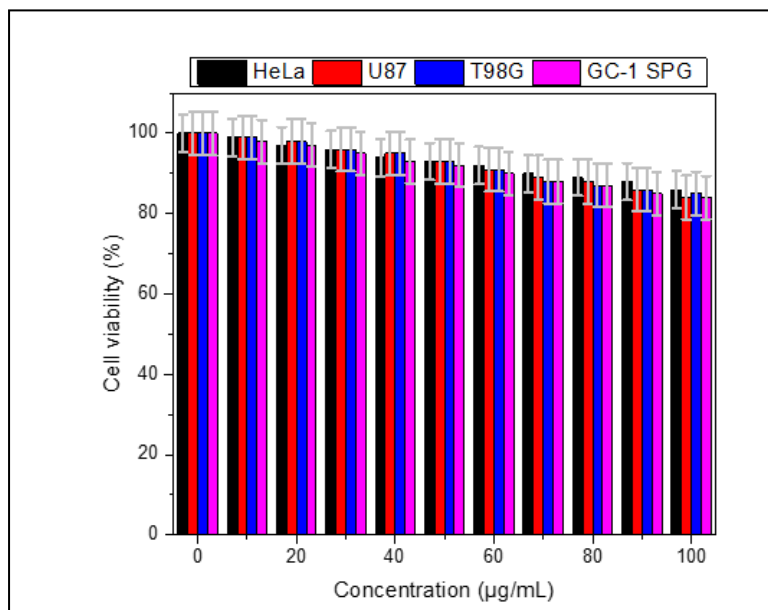


Figure 136128: Viability of HeLa, U87, T98G and GC-1SPG cells following incubation with C-dots for 24h, using MTT assay.

The cell viability results for HeLa, U87, T98G, and Gc-1SPG cells incubated for 24 h with C-K7, RGD, C-PEI/QAS, C-J, K7, and PEI/QAS separately are shown in Figures 137, 138, 139, 140, 141, and 142, respectively. The results show that the cell viability for the samples at 10 µg /mL concentration are very high, between 100% and 97%. And the cell viability decreases as the concentration of the samples increase with a range of 86% to 83% at 100 µg /mL concentration.

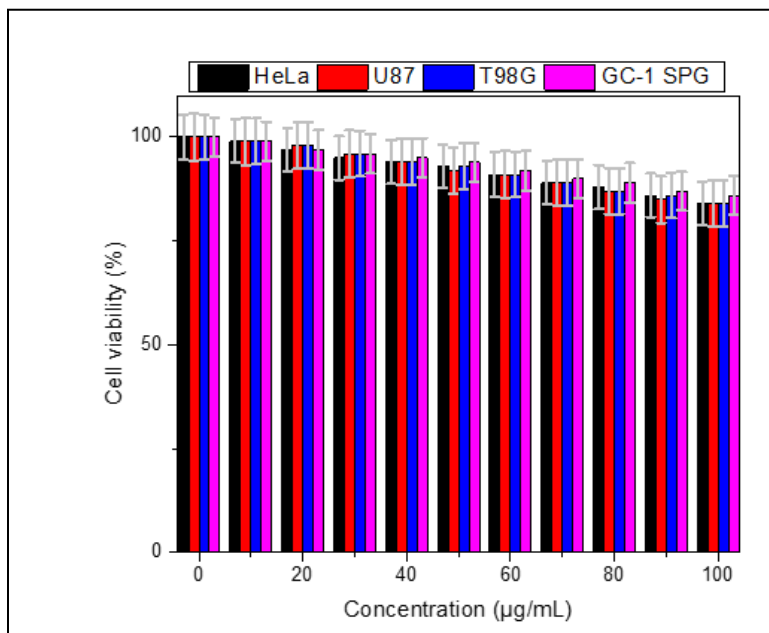


Figure 137: Viability of HeLa, U87, T98G and GC-1SPG cells following incubation with C-K7 for 24h, using MTT assay.

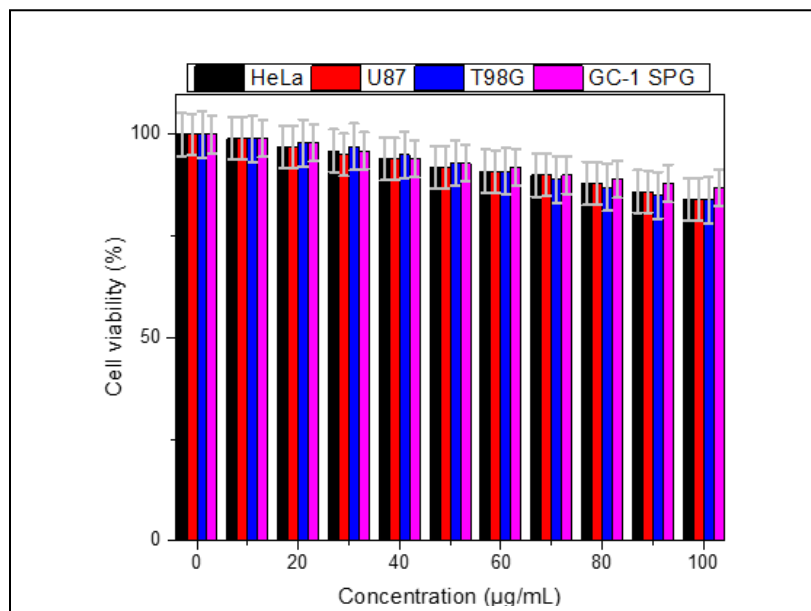


Figure 138: Viability of HeLa, U87, T98G and GC-1SPG cells following incubation with C-RGD for 24h, using MTT assay.

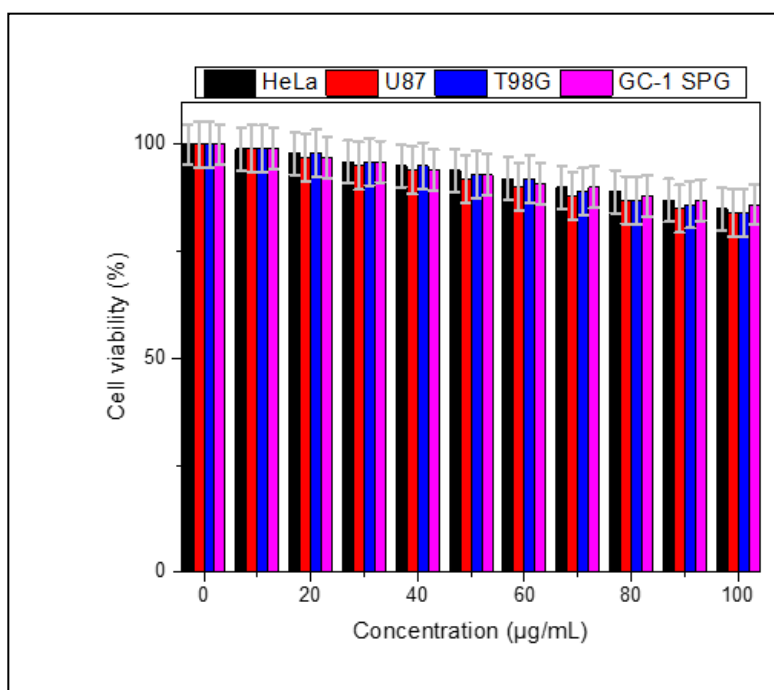


Figure 139: Viability of HeLa, U87, T98G and GC-1SPG cells following incubation with C-PEI/QAS for 24h, using MTT assay.

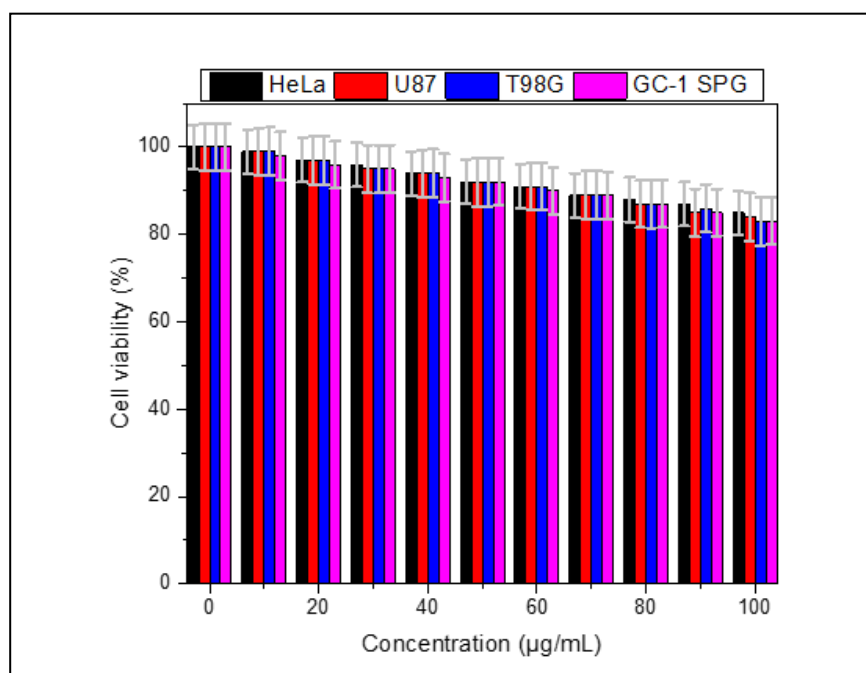


Figure 140: Viability of HeLa, U87, T98G and GC-1SPG cells following incubation with C-J for 24h, using MTT assay.

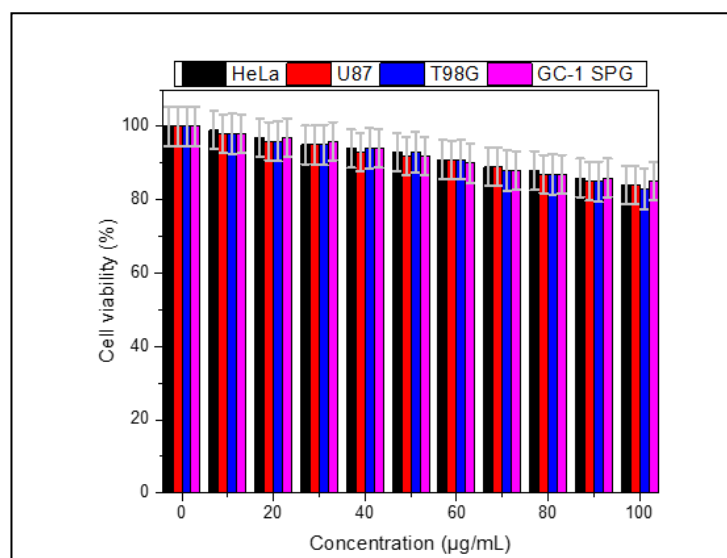


Figure 141: Viability of HeLa, U87, T98G and GC-1SPG cells following incubation with K7 for 24h, using MTT assay.

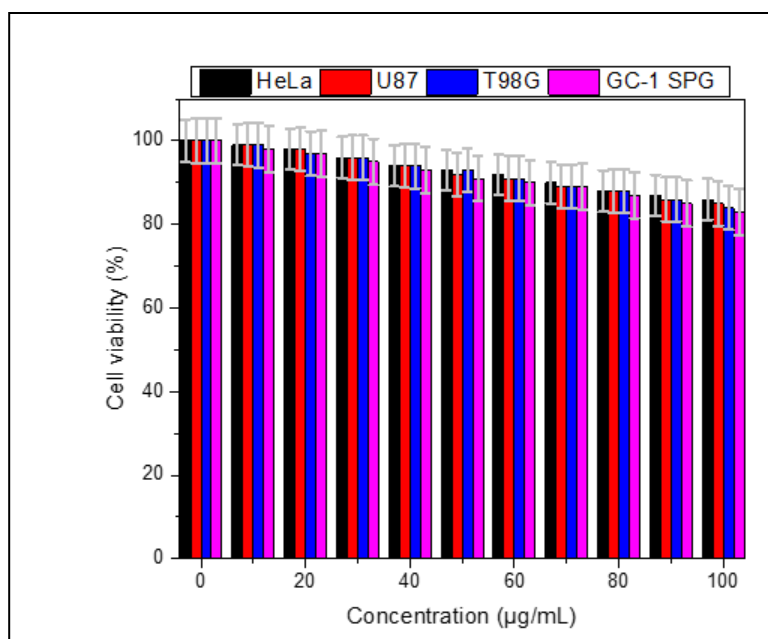


Figure 142: Viability of HeLa, U87, T98G and GC-1SPG cells following incubation with PEI/QAS for 24h, using MTT assay.

3.3.2 PrestoBlue assay

The toxicity of the samples was synthesised in this project assessed against PrestoBlue assay, including the C-dots, the conjugations of the C-dots, the K7 peptide and the PEI/QAS.

The Cell viability for HeLa cells incubated with C-dots for 24 h is 97% for 10 $\mu\text{g}/\text{mL}$ C-dots, and gradually decreases upon increasing the C-dots loading, thus approaching 83% for HeLa in the presence of 100 $\mu\text{g}/\text{mL}$ C-dots, as shown in Figure 143. Furthermore, the cell viability of U87 cells incubated with C-dots for 24 h is at high level with 98% for 10 $\mu\text{g}/\text{mL}$ loading of C-dots, and the cell viability gradually decreases as the loading of the C-dots increases resulting 82% cell viability for loading with 100 $\mu\text{g}/\text{mL}$ C-dots, as shown in Figure 143. The cell viability of T98G incubated with C-dots for 24 h shows cell viability of 98% for 10 $\mu\text{g}/\text{mL}$ loading C-dots, and the cell viability gradually decreases as the loading of C-dots increased resulting 83% cell viability with 100 $\mu\text{g}/\text{mL}$ C-dots, as shown in Figure 143. The cell viability of GC-1 SPG incubated with C-dots for 24 h shows high cell viability of 98% with 10 $\mu\text{g}/\text{mL}$ loading of C-dots, and the cell viability gradually decreases as the loading with C-dots increases resulting 85% cell viability with 100 $\mu\text{g}/\text{mL}$ C-dots loading, as shown in Figure 143.

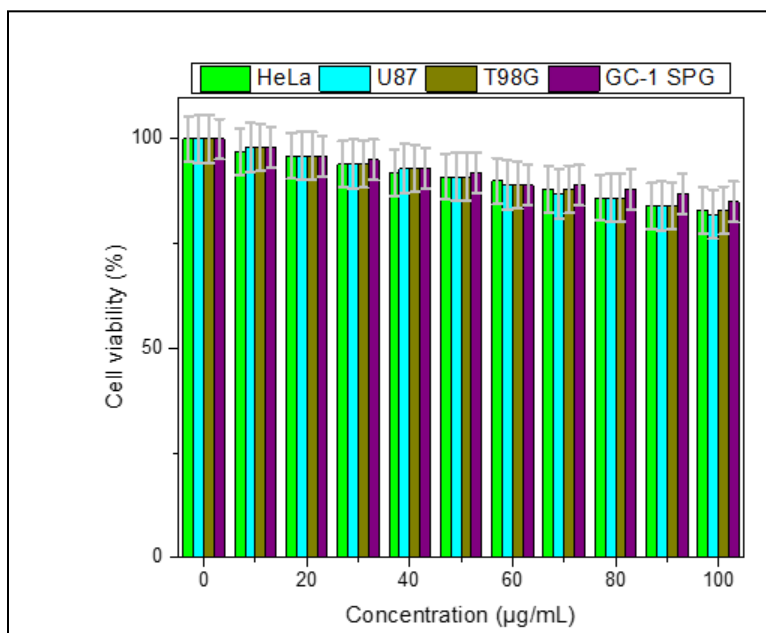


Figure 143: Viability of HeLa, U87, T98G and GC-1SPG cells following incubation with C-dots for 24h, using PrestoBlue assay.

The cell viability assay results for HeLa, U87, T98G, and GC-1SPG incubated for 24 h with C-K7, C-RGD, C-PEI/QAS, C-J, K7, and PEI/QAS are presented in Figures 144, 145, 146, 147, 148, and 149. The results demonstrate very high cell viability between 99-97% with 10 µg /mL, and the cell viability decrease as the concentrations of the samples increase, with a range of cell viability between 86-83% at 100 µg /mL.

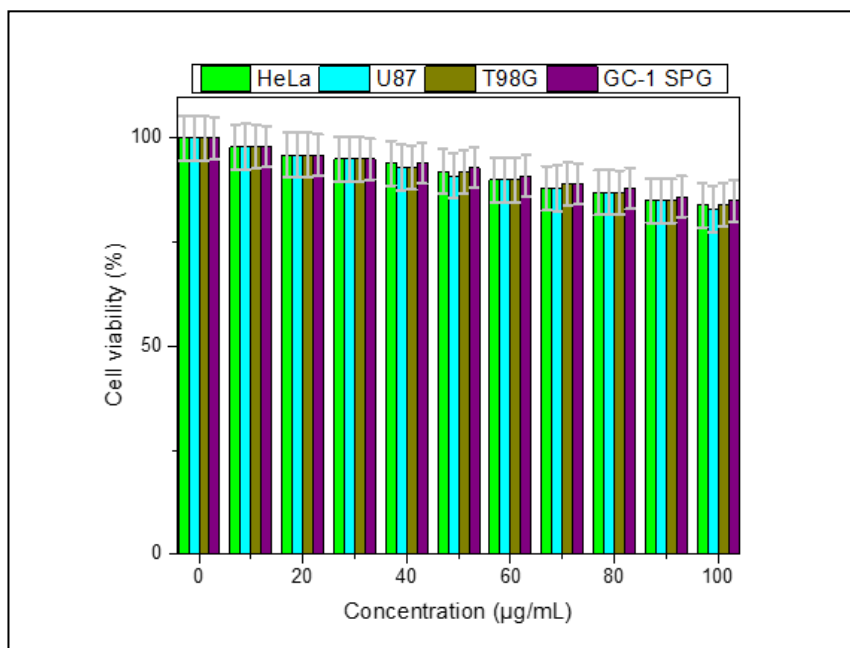


Figure 144129: Viability of HeLa, U87, T98G and GC-1SPG cells following incubation with C-K7 for 24h, using PrestoBlue assay.

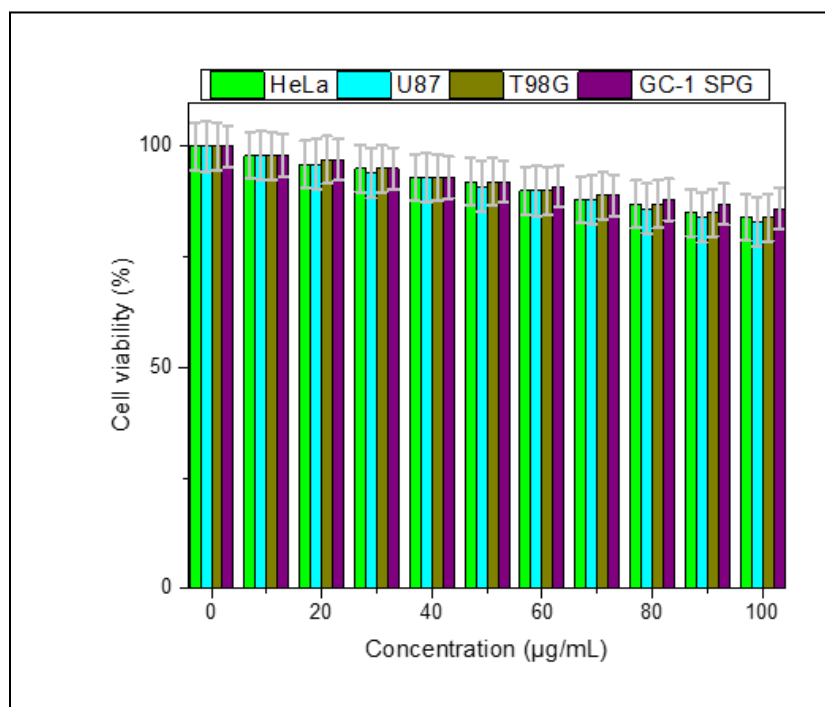


Figure 145: Viability of HeLa, U87, T98G and GC-1SPG cells following incubation with C-RGD for 24h, using PrestoBlue assay.

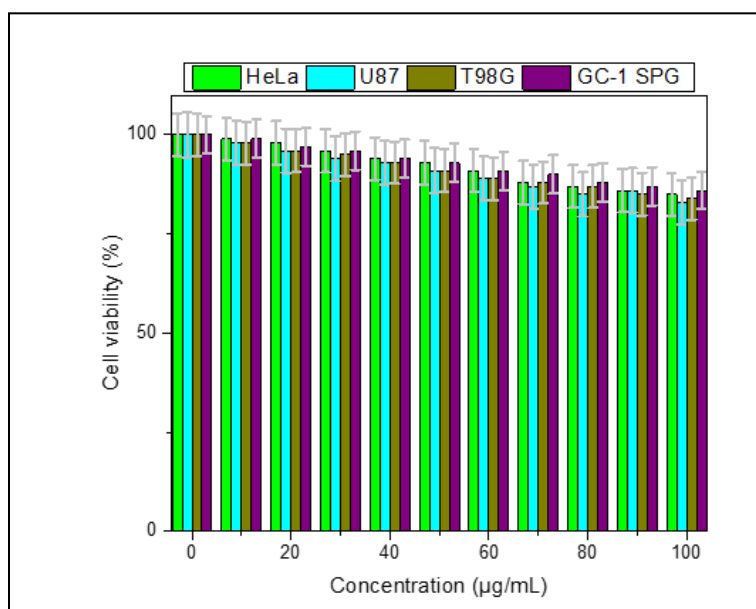


Figure 146: Viability of HeLa, U87, T98G and GC-1SPG cells following incubation with C-PEI/QAS for 24h, using PrestoBlue assay.

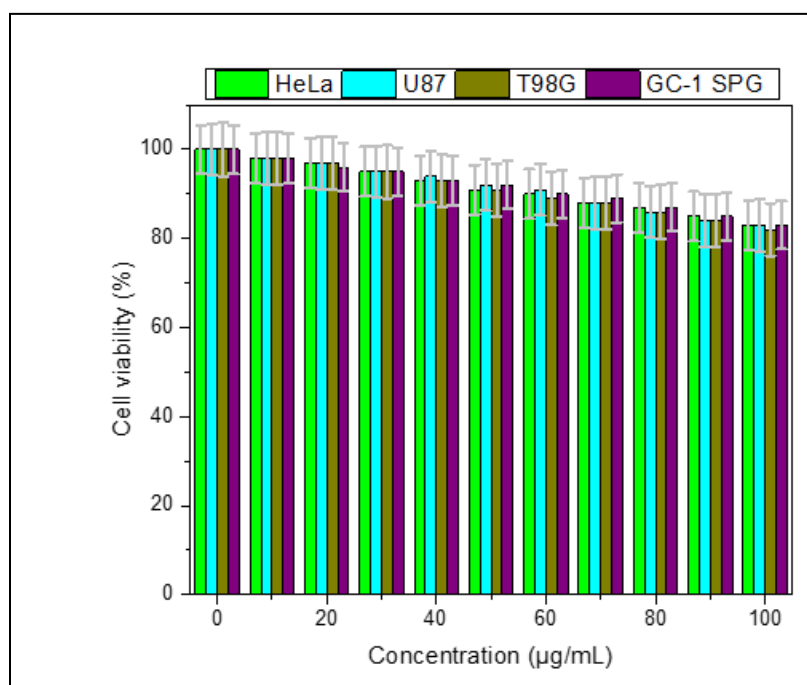


Figure 147: Viability of HeLa, U87, T98G and GC-1SPG cells following incubation with C-J for 24h, using PrestoBlue assay.

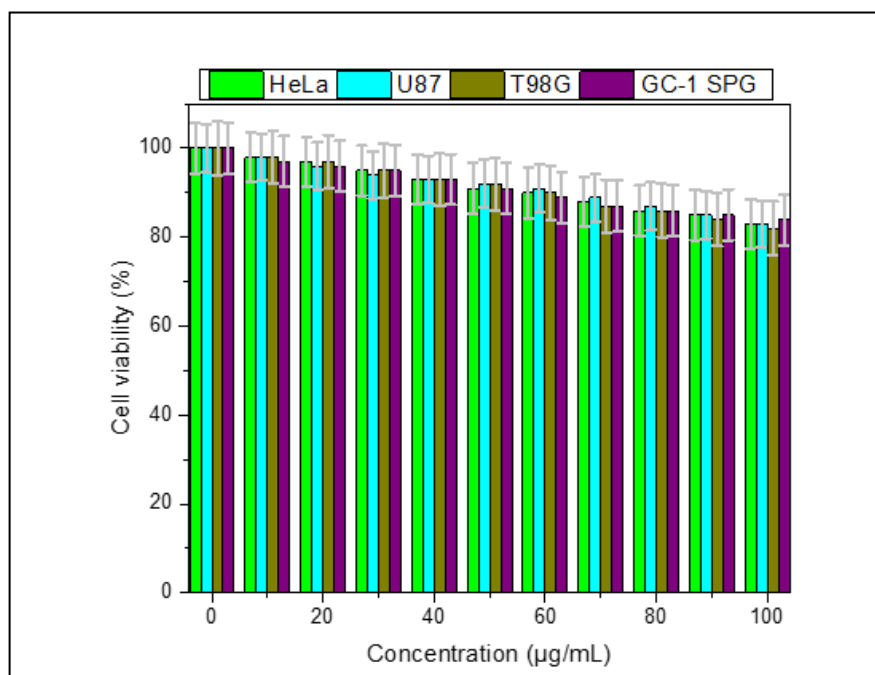


Figure 148: Viability of HeLa, U87, T98G and GC-1SPG cells following incubation with K7 for 24h, using PrestoBlue assay.

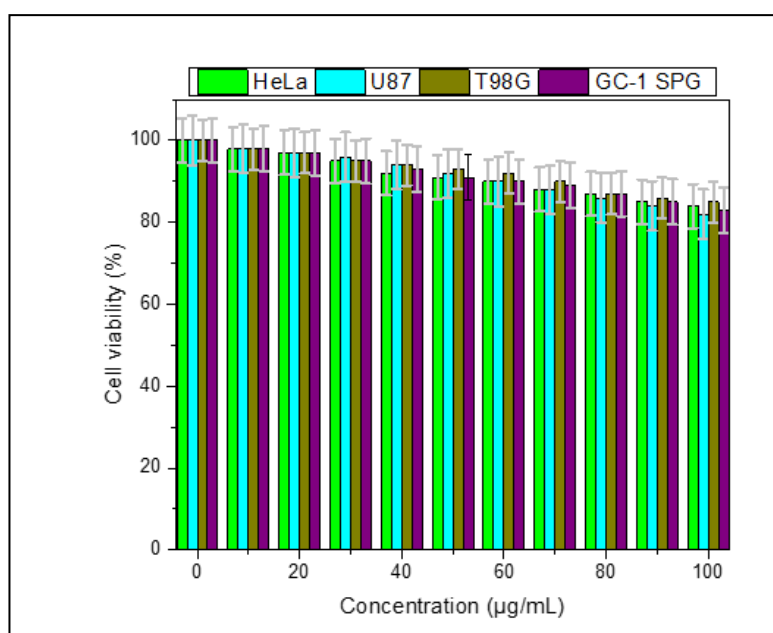


Figure 149: Viability of HeLa, U87, T98G and GC-1SPG cells following incubation with PEI/QAS for 24h, using PrestoBlue assay.

We can conclude from the results of the MTT assay and the PrestoBlue assay, that the synthesised samples in this project shows a low level of toxicity, and can be good candidates in the biomedical applications.

3.3.3 Haemolysis

The haemolysis assay completed for the C-dots, and all the conjugates of C-dots, to determine whether they can cause any red blood cells destruction. Figure 150 shows the positive control, which is 1% triton-x, and the negative control, which is $\frac{1}{4}$ strength Ringer's, which were used as references for the assays.



Figure 150130: Positive control (to the left), 1% triton-x, and negative control (to the right) $\frac{1}{4}$ strength Ringer's of the haemolysis assay.

Figure 151 shows the results of the Haemolysis assay in form of images of the blood agars were used. By comparing of the results of the samples to the positive control and the negative

control in Figure 150, we can determine that the samples are similar to the negative control, which means that there is no red blood cells destruction. In addition, the C-dots, the C-K7, the C-RGD, and the C-J show diffusion in form of dark colour around the hole of the sample, which mean the samples had diffused through the blood agar without causing any damage, and that the dark colour is related to the dark colour of the samples. On the other hand, the C-PEI/QAS is the only conjugate that did not show darker ring, this is due to the content of the materials, as the molecular size of the PEI/QAS is bigger when compared to the C-dots (refer to section 3.1.6.).

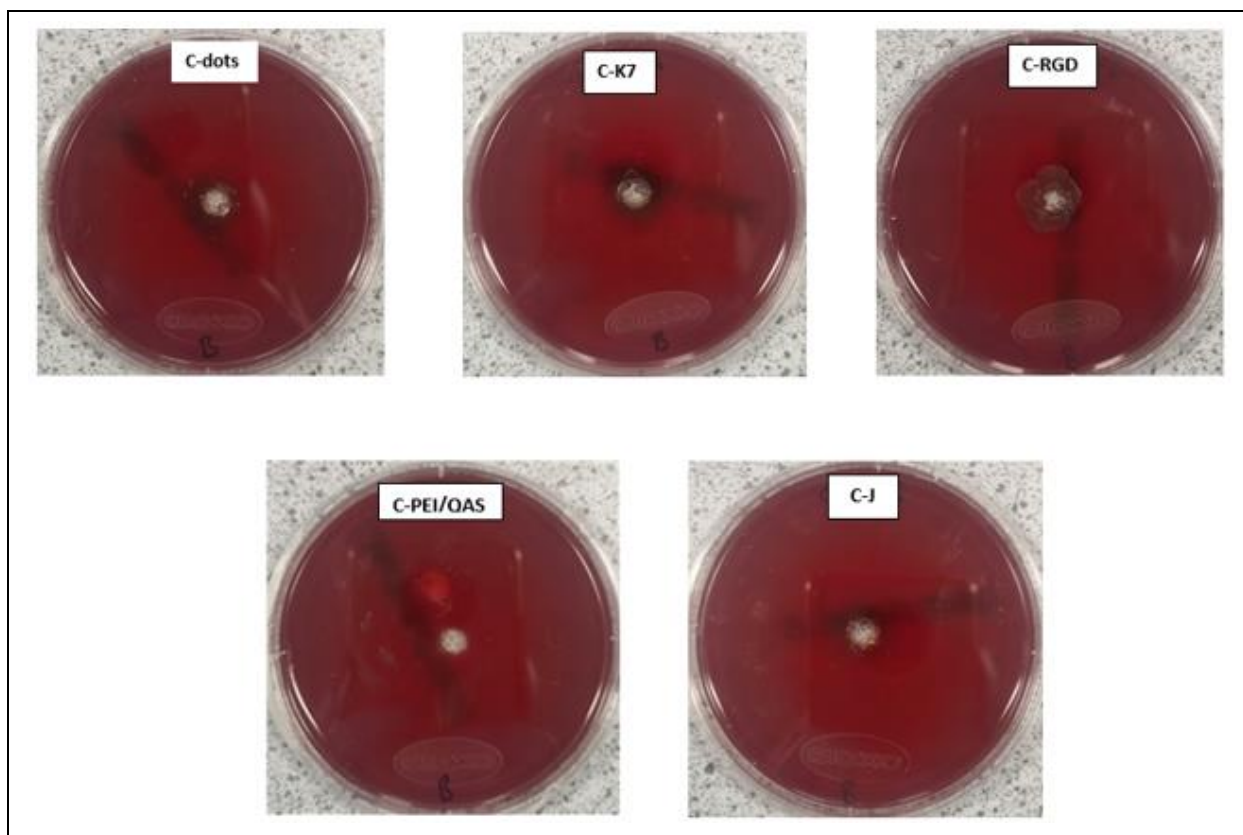


Figure 151131: Haemolysis test of 100 µg/mL aqueous solution of: C-dots, C-K7, C-RGD, C-PEI/QAS, and C-J. All the samples were incubated for 24 h in a pre-made hole in blood agar.

3.4 Fluorescence microscopy on HeLa cells

The images of HeLa cells incubated with 10 $\mu\text{g}/\text{mL}$ of the synthesised nanoparticles for 24 h demonstrate that the C-K7 managed to penetrate the cells with good signal as shown in Figure 152. While the C-dots, the C-RGD, the C-PWI/QAS, and the C-J images did not demonstrate any cell penetration with 10 $\mu\text{g}/\text{mL}$ incubation against HeLa cells for 24 h as shown in Figure 152.

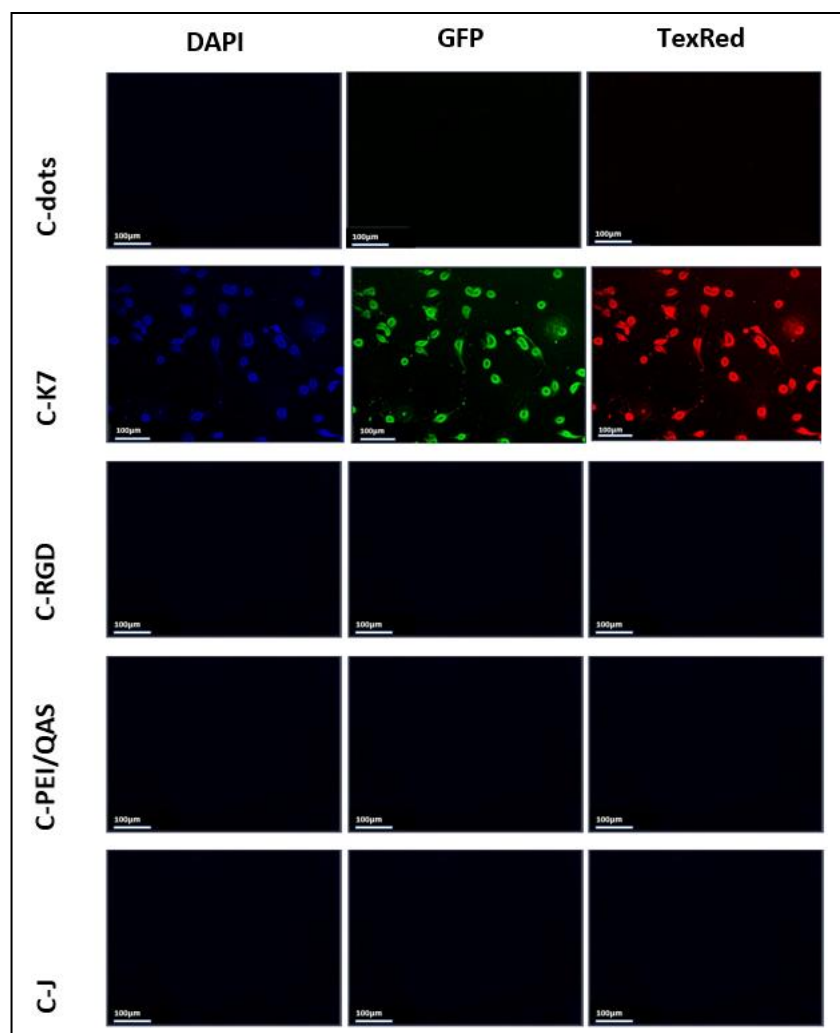


Figure 152132: Fluorescence microscope images of HeLa cells incubated with 10 $\mu\text{g}/\text{mL}$ of C-dots, C-K7, C-RGD, C-PEI/QAS, and C-J for 24 hours, under UV, blue, green λ_{ex} . Scale bar 100 μm .

The HeLa cells incubated with 30 $\mu\text{g}/\text{mL}$ of the synthesised nanoparticles for 24 h demonstrate that all the nanoparticles managed to penetrate the HeLa cells as shown in Figure 153. Moreover, the C-K7 and the C-RGD show more penetrated cells than the other nanoparticles as shown in Figure 153.

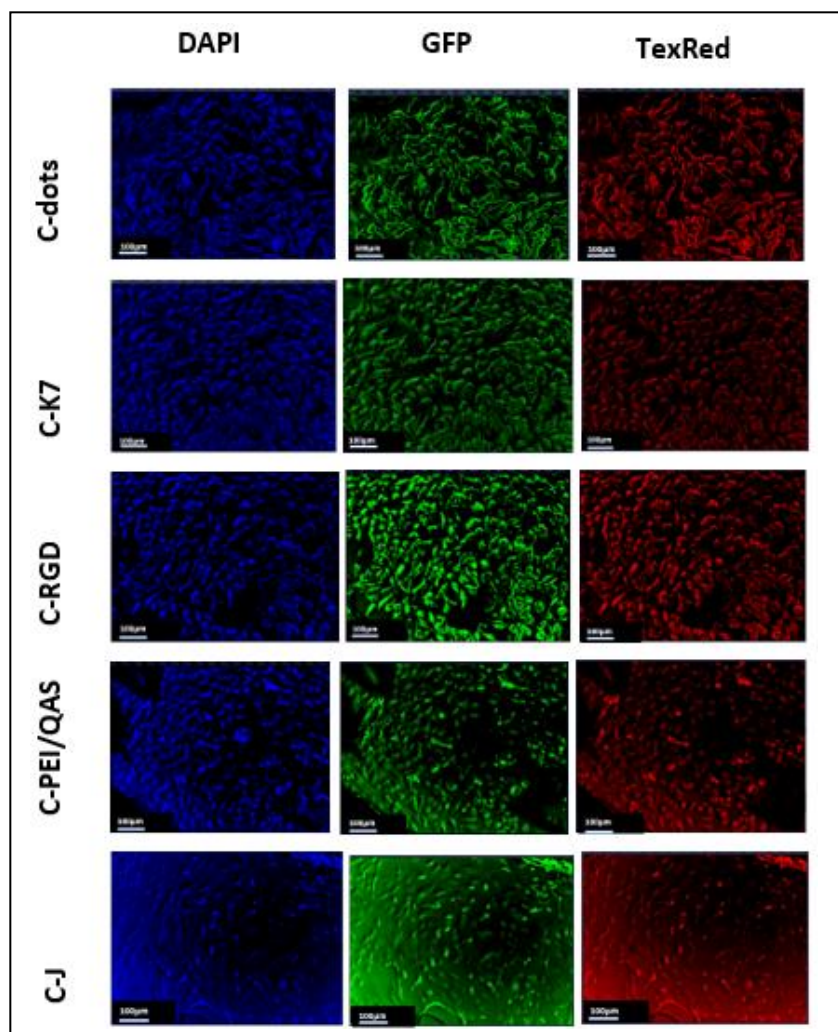


Figure 153: HeLa cells images under the fluorescence microscope after incubation with 30 $\mu\text{g}/\text{mL}$ of C-dots, C-K7, C-RGD, C-PEI/QAS, and C-J for 24 hours, under UV, blue, green λ_{ex} . Scale bar 100 μm .

The HeLa cells incubated with 100 $\mu\text{g}/\text{mL}$ of the synthesised nanoparticles for 2 h demonstrate that all the nanoparticles did not penetrate the HeLa cells as shown in Figure 154.

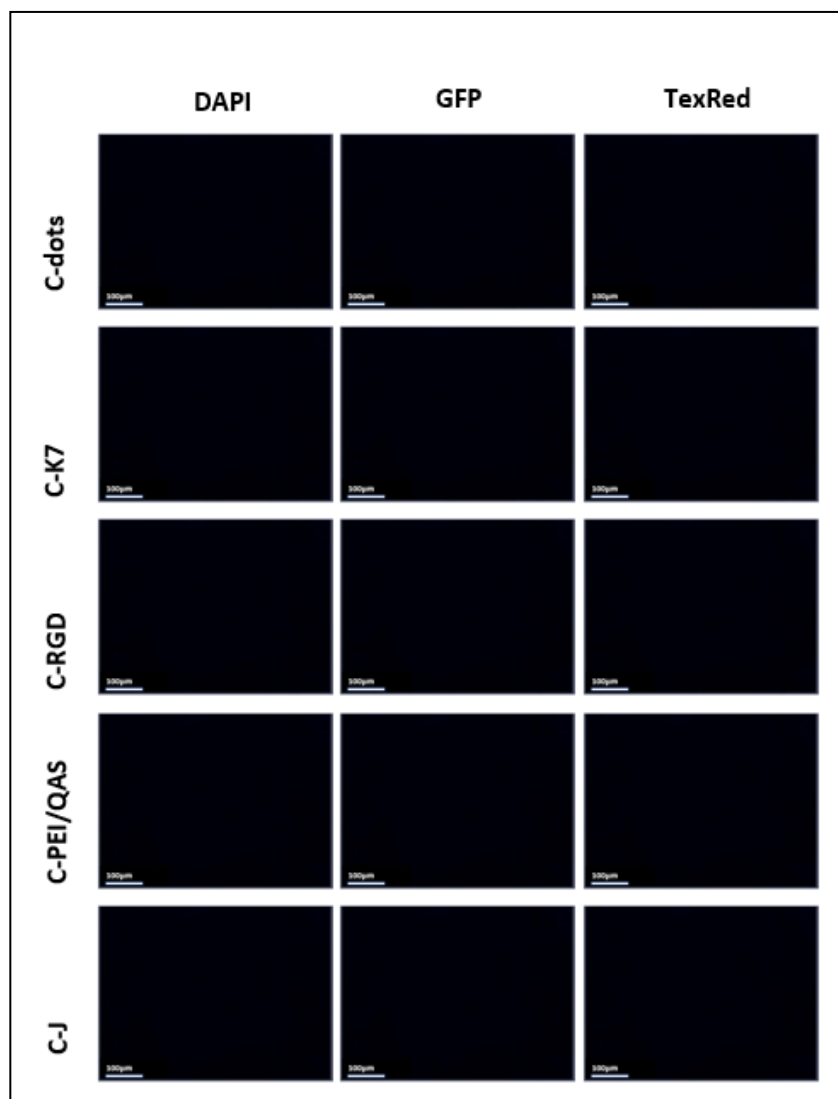


Figure 154: HeLa cells images under the fluorescence microscope after incubation with 100 $\mu\text{g}/\text{mL}$ of C-dots, C-K7, C-RGD, C-PEI/QAS, and C-J for 2 hours, under UV, blue, green λ_{ex} . Scale bar 100 μm .

The HeLa cells incubated with 100 $\mu\text{g}/\text{mL}$ of the synthesised nanoparticles for 4 h demonstrate that all the nanoparticles managed to penetrate the HeLa cells. Moreover, the C-K7 show more penetrated cells than the other nanoparticles, following by C-RGD as shown in Figure 155. On the other hand, the C-PEI/QAS and the C-J demonstrate better penetration than the C-dots, yet less than the C-K7 and the RGD, as shown in Figure 155.

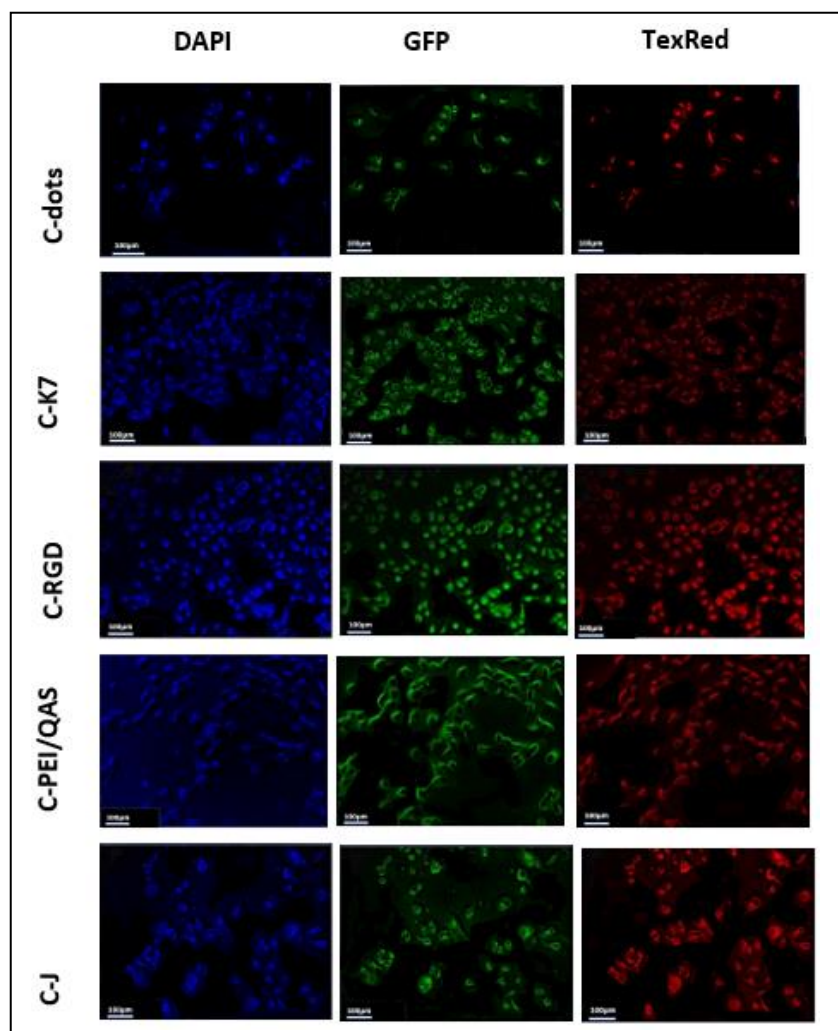


Figure 155: HeLa cells images under the fluorescence microscope after incubation with 100 $\mu\text{g}/\text{mL}$ of C-dots, C-K7, C-RGD, C-PEI/QAS, and C-J for 4 hours, under UV, blue, green λ_{ex} . Scale bar 100 μm .

The HeLa cells incubated with 100 $\mu\text{g}/\text{mL}$ of the synthesised nanoparticles for 6 h demonstrate that the cell penetration improved in comparison to the HeLa cells incubated for 4 h in Figure 155. Moreover, the C-K7 show more penetrated cells than the other nanoparticles as shown in Figure 156.

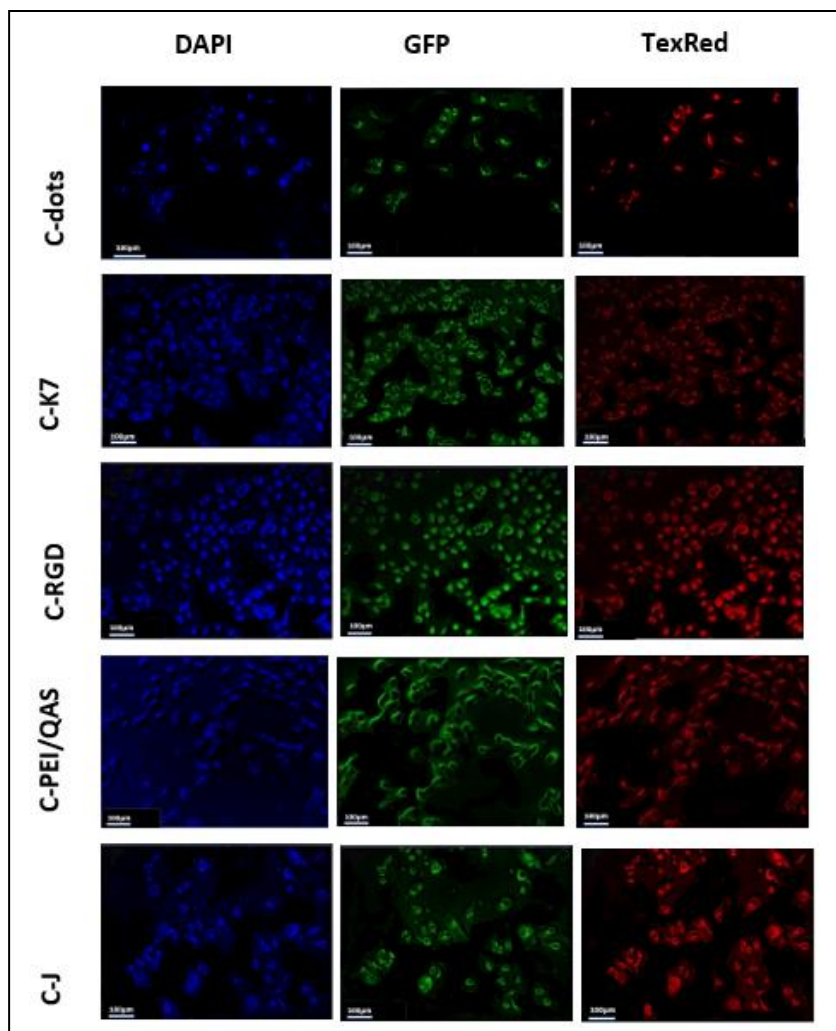


Figure 156: HeLa cells images under the fluorescence microscope after incubation with 100 $\mu\text{g}/\text{mL}$ of C-dots, C-K7, C-RGD, C-PEI/QAS, and C-J for 6 hours, under UV, blue, green λ_{ex} . Scale bar 100 μm .

The HeLa cells incubated with 100 $\mu\text{g}/\text{mL}$ of the synthesised nanoparticles for 8 h demonstrate that the cell penetration improved even more in a comparison to the HeLa cells incubated for 6 h in Figure 156. Moreover, the C-K7 show more penetrated cells than the other nanoparticles as shown in Figure 157. Then after 24 h of incubation, the HeLa cells penetration improved even more, with better penetration is shown in the images of the HeLa cells incubated with C-K7, as shown in Figure 158.

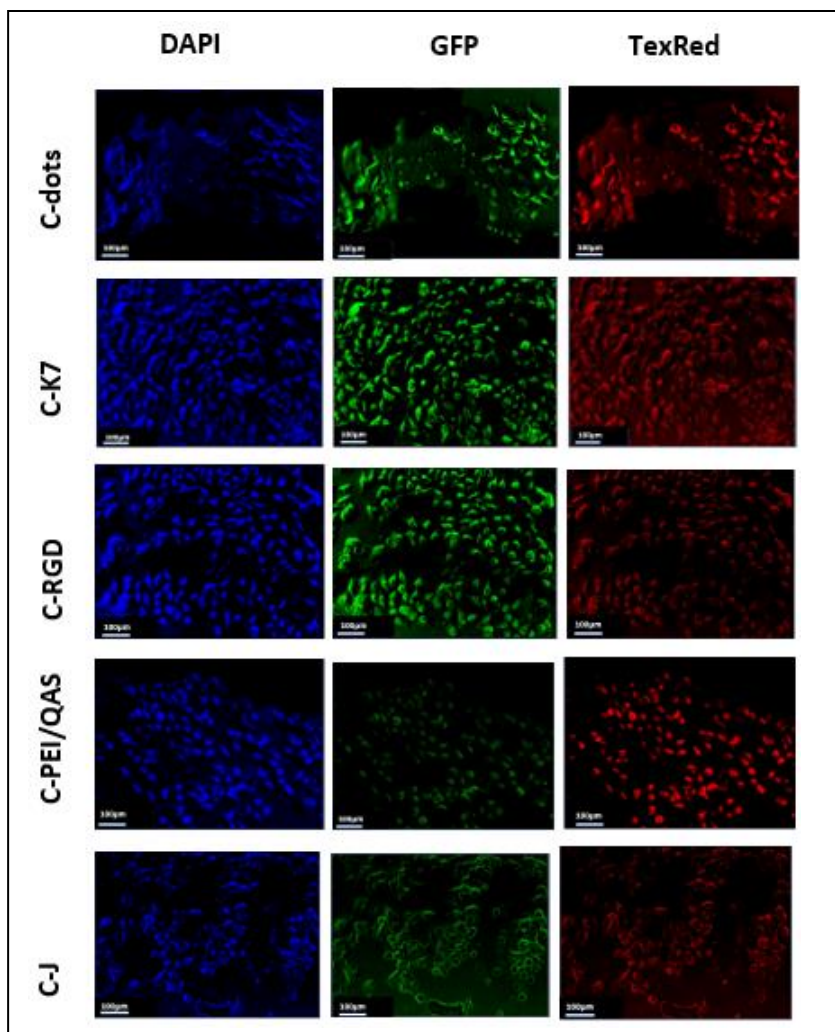


Figure 157: HeLa cells images under the fluorescence microscope after incubation with 100 $\mu\text{g}/\text{mL}$ of C-dots, C-K7, C-RGD, C-PEI/QAS, and C-J for 8 hours, under UV, blue, green λ_{ex} . Scale bar 100 μm .

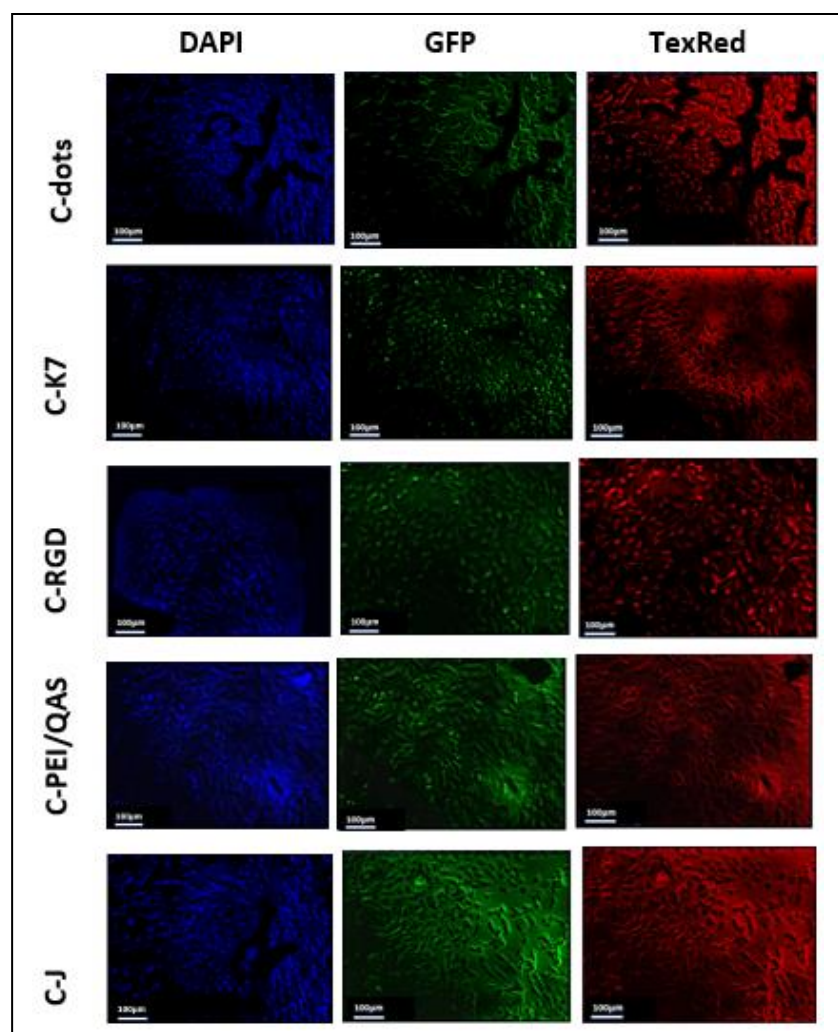


Figure 158: HeLa cells images under the fluorescence microscope after incubation with 100 µg/mL of C-dots, C-K7, C-RGD, C-PEI/QAS, and C-J for 24 hours, under UV, blue, green λ_{ex} . Scale bar 100 µm.

3.5 Microbiology

The C-dots demonstrate good antibacterial activity with 94.4% reduction in the colonies of the *E. coli*, and 96.7% reduction of the colonies of the *S. aureus* as shown in Figure 159. The conjugation of the C-dots with PEI/QAS improved the antibacterial activity by 99.9% reduction in the colonies of the *E. coli*, and 99.96% reduction in the colonies of the *S. aureus* as shown in Figure 159. The conjugation of the C-dots with K7 improved the antibacterial activity against *E. coli* with 95.3% reduction in the colonies, while the antimicrobial activity against the *S. aureus* reduced with 86% reduction in the colonies as shown in Figure 159.

On the other hand, the conjugation of the C-dots with C-PEI/QAS reduced the antibacterial activity of the C-dots with 66.9% reduction in the colonies of the *E. coli*, and 86% reduction in the colonies of the *S. aureus* as shown in Figure 159. Simultaneously, the conjugation of C-dots with Jeffamine reduced the antibacterial activity of the C-dots with 91.8% reduction in the colonies of the *E. coli*, and 94% reduction in the colonies of the *S. aureus* as shown in Figure 159.

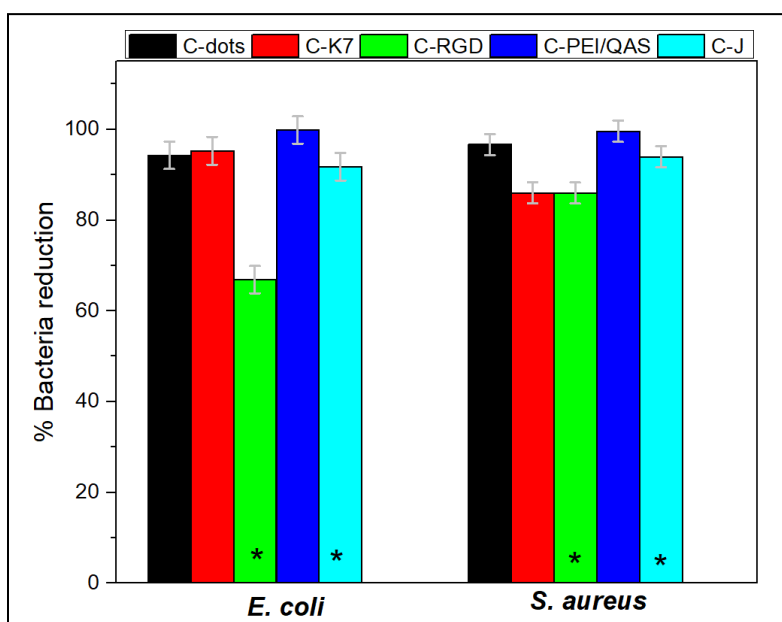


Figure 159: Average percentage reduction in colony formation units of *E. coli*, and *S. aureus* incubated for 20 h with: C-dots, C-K7, C-RGD, C-PEI/QAS, and C-J. *: these data obtained at 0.5mg/mL, while the rest at 5mg/mL.

3.6 Drug release

The drug release study of Ibuprofen shows that the Ibu-C-dots system (P123 C-dots based gel with Ibuprofen loaded to the system) has faster release rate of the drug at the first 10 h in a comparison to the Ibuprofen (Ibuprofen loaded P123 gel), then there is not much difference in the release after the 10 h as shown in Figure 160. The Ibu-C-K7 (P123 C-K7 based gel with Ibuprofen loaded to the system) shows a faster release rate than the Ibuprofen and the Ibu-C-dots, and even faster release rate of the drug in the Ibu-C-RGD (P123 C-RGD based gel with Ibuprofen loaded to the system) and the Ibu-C-J (P123 C-J based gel with Ibuprofen loaded to the system), which both of them (Ibu-C-RGD and Ibu-C-J) have no much difference in the release rate, except that the drug release in the Ibu-C-J plateaued after 72 hours, as shown in Figure 160. The Ibu-C-PEI/QAS (P123 C-PEI/QAS based gel with Ibuprofen loaded to the system) shows the fastest release rate of the drug at all times, and the release rate plateaued after 48 hours, as shown in Figure 160. From the data we can conclude that the introduction of C-RGD can facilitate an almost linear ibuprofen release as a function of time for 100 h, an effect that is highly desirable for controlled and sustained drug release applications.

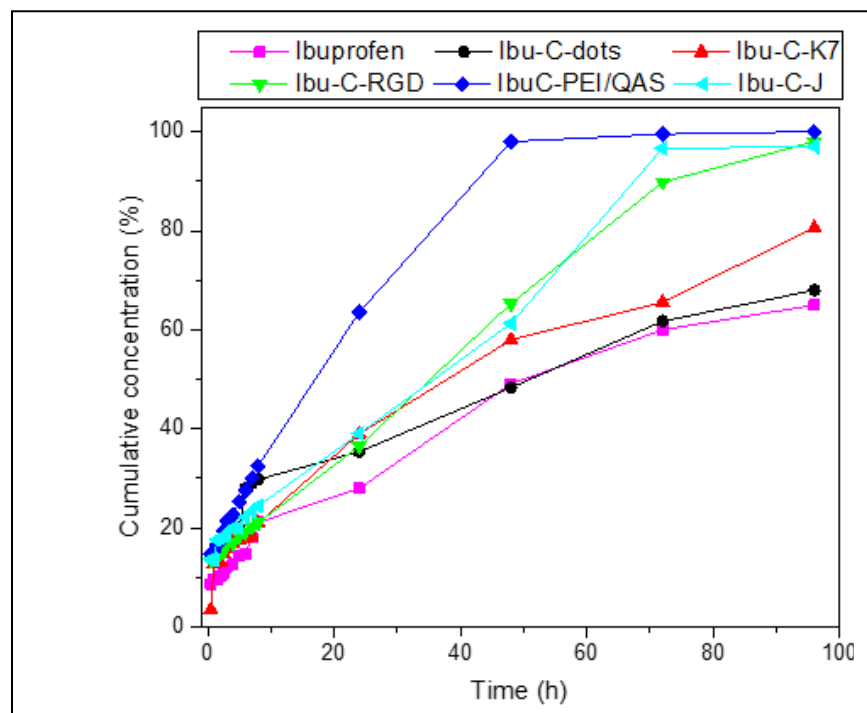


Figure 160: Drug release profile of the Ibuprofen against PBS at 25 ± 1 °C initially loaded in: ■ P123 gel system, ● P123 and C-dots system, ▲ P123 and C-K7 system, ▼ P123 and C-RGD system, ◆ P123 and C-PEI/QAS system, and ◀ P123 and C-J system.

The drug release study of the Temozolomide shows that the Temo-C-dots system (P123 C-dots based gel with Temozolomide loaded to the system), the Temo-C-K7 (P123 C-K7 based gel with Temozolomide loaded to the system), the Temo-C-RGD (P123 C-RGD based gel with Temozolomide loaded to the system), the Temo-C-PEI/QAS (P123 C-PEI/QAS based gel with Temozolomide loaded to the system), and the Temo-C-J (P123 C-J based gel with Temozolomide) loaded to the system have faster release rate of the drug in a comparison to the Temozolomide (Temozolomide drug loaded P123 gel). Furthermore, all the systems slightly plateaued after 24 h as shown in Figure 161. On the other hand, the Temo-C-dots shows slower release in the first 10 h in a comparison to the C-dots conjugates systems as shown in Figure 161.

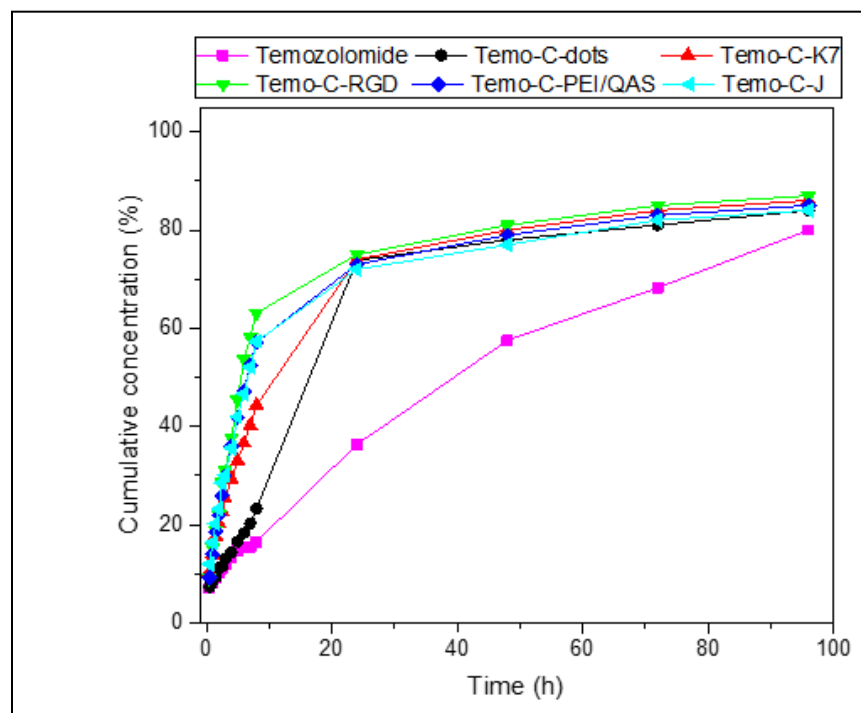


Figure 161: Drug release profile of the Temozolomide against PBS at 25 ± 1 °C initially loaded: ■ P123 gel system, ● P123 and C-dots system, ▲ P123 and C-K7 system, ▼ P123 and C-RGD system, ◆ P123 and C-PEI/QAS system, and ◄ P123 and C-J system.

In conclusion, the conjugation of the nanoparticles system based, demonstrate a better drug release for nearly 100 h, with maximum of 96% release of the drug, which indicates a good releasing capacity.

Conclusion

In this project we focus on the synthesis and characterization of a series of peptide/C-dots and polymer/C-dots conjugates, denoted as C-K7, C-RGD, C-PEI/QAS and C-J, respectively. It was observed that conjugation of C-dots with K7, RGD, PEI/QAS and Jeffamine does not adversely affect the QY, although the fluorescence spectra of conjugates show pronounced blue shifts, while demonstrating the characteristic excitation-wavelength dependent emission.

The cytotoxicity MTT and PrestoBlue assays indicated that the viability of HeLa, U87, T96G, and GC-1 SPG cells remains at high levels in the presence of 100 $\mu\text{g}/\text{mL}$ conjugate, approaching 100% in the presence of 10 $\mu\text{g}/\text{mL}$ conjugate. Furthermore, it was observed that the conjugates do not cause the breaking down of blood cells. The fluorescence microscope images showed that all types of conjugates considered here are able to penetrate the HeLa cells, an important performance characteristic that make them ideal candidates for bioimaging applications. The C-K7 appears to be the best performing conjugate for *in vivo* bioimaging, given that it provides strong fluorescent signal at concentrations as low as 10 $\mu\text{g}/\text{mL}$, while the other conjugates fail to do so at this concentration level.

While all conjugates show significant antimicrobial behavior, C-PEI/QAS show more than 3 orders of magnitude reduction in the population of *E. coli* and *S. aureus*. The incorporation of conjugates to micellar hydrogels accelerates the release of temozolomide compared to the nanoparticle-free counterparts. Introduction of C-RGD to hydrogels results in an almost linear release profile of Ibuprofen as a function of time for 100 h, a behavior rarely seen in similar systems.

The study paves the way for the development of a new generation of multifunctional materials that are promising for applications related to bioimaging, antimicrobial agents and drug carriers.

References

- (1) Wang Y, Anilkumar P, Cao L, Liu J, Luo PG, Tackett KN, et al. Carbon dots of different composition and surface functionalization: cytotoxicity issues relevant to fluorescence cell imaging. *Exp Biol Med* 2011;236(11):1231-1238.
- (2) Tummala S, Kumar MS, Pindiprolu SK. Improved anti-tumor activity of oxaliplatin by encapsulating in anti-DR5 targeted gold nanoparticles. *Drug Deliv* 2016;23(9):3505-3519.
- (3) Tong G, Wang J, Wang R, Guo X, He L, Qiu F, et al. Amorphous carbon dots with high two-photon fluorescence for cellular imaging passivated by hyperbranched poly (amino amine). *Journal of Materials Chemistry B* 2015;3(4):700-706.
- (4) Pandey A, Devkota A, Yadegari Z, Dumenyo K, Taheri A. Antibacterial properties of citric acid/ β -alanine carbon dots against gram-negative bacteria. *Nanomaterials* 2021;11(8):2012.
- (5) Boschi F, De Sanctis F. Overview of the optical properties of fluorescent nanoparticles for optical imaging. *European journal of histochemistry: EJH* 2017;61(3).
- (6) Krysmann MJ, Kellarakis A, Giannelis EP. Photoluminescent carbogenic nanoparticles directly derived from crude biomass. *Green Chem* 2012;14(11):3141-3145.
- (7) Krysmann MJ, Kellarakis A, Dallas P, Giannelis EP. Formation mechanism of carbogenic nanoparticles with dual photoluminescence emission. *J Am Chem Soc* 2011;134(2):747-750.
- (8) Mourdikoudis S, Pallares RM, Thanh NT. Characterization techniques for nanoparticles: comparison and complementarity upon studying nanoparticle properties. *Nanoscale* 2018;10(27):12871-12934.
- (9) Sciortino A, Cannizzo A, Messina F. Carbon nanodots: a review—from the current understanding of the fundamental photophysics to the full control of the optical response. *C* 2018;4(4):67.
- (10) Wolfbeis OS. An overview of nanoparticles commonly used in fluorescent bioimaging. *Chem Soc Rev* 2015;44(14):4743-4768.
- (11) Tao S, Zhu S, Feng T, Xia C, Song Y, Yang B. The polymeric characteristics and photoluminescence mechanism in polymer carbon dots: A review. *Materials today chemistry* 2017;6:13-25.

- (12) Qu S, Wang X, Lu Q, Liu X, Wang L. A biocompatible fluorescent ink based on water-soluble luminescent carbon nanodots. *Angewandte Chemie international edition* 2012;51(49):12215-12218.
- (13) Park Y, Yoo J, Lim B, Kwon W, Rhee S. Improving the functionality of carbon nanodots: doping and surface functionalization. *Journal of Materials Chemistry A* 2016;4(30):11582-11603.
- (14) Kelarakis A. From highly graphitic to amorphous carbon dots: A critical review. *MRS Energy & Sustainability* 2014;1.
- (15) Ponomarenko LA, Schedin F, Katsnelson MI, Yang R, Hill EW, Novoselov KS, et al. Chaotic Dirac billiard in graphene quantum dots. *Science* 2008.
- (16) Dong Y, Pang H, Ren S, Chen C, Chi Y, Yu T. Etching single-wall carbon nanotubes into green and yellow single-layer graphene quantum dots. *Carbon* 2013;64:245-251.
- (17) Gokus T, Nair RR, Bonetti A, Bohmler M, Lombardo A, Novoselov KS, et al. Making graphene luminescent by oxygen plasma treatment. *ACS nano* 2009;3(12):3963-3968.
- (18) Lu J, Yeo PSE, Gan CK, Wu P, Loh KP. Transforming C60 molecules into graphene quantum dots. *Nature nanotechnology* 2011;6(4):247-252.
- (19) Yan X, Cui X, Li L. Synthesis of large, stable colloidal graphene quantum dots with tunable size. *J Am Chem Soc* 2010;132(17):5944-5945.
- (20) Yan X, Cui X, Li B, Li L. Large, solution-processable graphene quantum dots as light absorbers for photovoltaics. *Nano letters* 2010;10(5):1869-1873.
- (21) Sadhanala HK, Khatei J, Nanda KK. Facile hydrothermal synthesis of carbon nanoparticles and possible application as white light phosphors and catalysts for the reduction of nitrophenol. *RSC Advances* 2014;4(22):11481-11485.
- (22) Sun Y, Zhou B, Lin Y, Wang W, Fernando KS, Pathak P, et al. Quantum-sized carbon dots for bright and colorful photoluminescence. *J Am Chem Soc* 2006;128(24):7756-7757.
- (23) Zhou J, Booker C, Li R, Zhou X, Sham T, Sun X, et al. An electrochemical avenue to blue luminescent nanocrystals from multiwalled carbon nanotubes (MWCNTs). *J Am Chem Soc* 2007;129(4):744-745.
- (24) Zheng L, Chi Y, Dong Y, Lin J, Wang B. Electrochemiluminescence of water-soluble carbon nanocrystals released electrochemically from graphite. *J Am Chem Soc* 2009;131(13):4564-4565.

- (25) Lu J, Yang J, Wang J, Lim A, Wang S, Loh KP. One-pot synthesis of fluorescent carbon nanoribbons, nanoparticles, and graphene by the exfoliation of graphite in ionic liquids. *ACS nano* 2009;3(8):2367-2375.
- (26) Li Y, Hu Y, Zhao Y, Shi G, Deng L, Hou Y, et al. An electrochemical avenue to green-luminescent graphene quantum dots as potential electron-acceptors for photovoltaics. *Adv Mater* 2011;23(6):776-780.
- (27) Niyogi S, Bekyarova E, Itkis ME, Zhang H, Shepperd K, Hicks J, et al. Spectroscopy of covalently functionalized graphene. *Nano letters* 2010;10(10):4061-4066.
- (28) Reis CP, Neufeld RJ, Ribeiro AJ, Veiga F. Nanoencapsulation I. Methods for preparation of drug-loaded polymeric nanoparticles. *Nanomedicine* 2006 Mar;2(1):8-21.
- (29) Tuerhong M, XU Y, YIN X. Review on Carbon Dots and Their Applications. *Chinese Journal of Analytical Chemistry* 2017 Jan;45(1):139-150.
- (30) Shen J, Zhu Y, Yang X, Li C. Graphene quantum dots: emergent nanolights for bioimaging, sensors, catalysis and photovoltaic devices. *Chemical communications* 2012;48(31):3686-3699.
- (31) Tuerhong M, Yang XU, Xue-Bo Y. Review on carbon dots and their applications. *Chinese Journal of Analytical Chemistry* 2017;45(1):139-150.
- (32) Vinci JC, Ferrer IM, Guterry NW, Colón VM, Destino JF, Bright FV, et al. Spectroscopic characteristics of carbon dots (C-dots) derived from carbon fibers and conversion to sulfur-bridged C-dots nanosheets. *Appl Spectrosc* 2015;69(9):1082-1090.
- (33) Swider JR, Hackley VA, Winter J. Characterization of Chinese ink in size and surface. *Journal of Cultural Heritage* 2003;4(3):175-186.
- (34) Yang S, Sun J, Li X, Zhou W, Wang Z, He P, et al. Large-scale fabrication of heavy doped carbon quantum dots with tunable-photoluminescence and sensitive fluorescence detection. *Journal of Materials Chemistry A* 2014;2(23):8660-8667.
- (35) Tao H, Yang K, Ma Z, Wan J, Zhang Y, Kang Z, et al. In vivo NIR fluorescence imaging, biodistribution, and toxicology of photoluminescent carbon dots produced from carbon nanotubes and graphite. *Small* 2012;8(2):281-290.
- (36) Ando Y, Zhao X. Synthesis of carbon nanotubes by arc-discharge method. *New diamond and frontier carbon technology* 2006;16(3):123-138.
- (37) Shi Z, Lian Y, Zhou X, Gu Z, Zhang Y, Iijima S, et al. Mass-production of single-wall carbon nanotubes by arc discharge method. *Carbon* 1999;37(9):1449-1453.

- (38) Hutchison JL, Kiselev NA, Krinichnaya EP, Krestinin AV, Loutfy RO, Morawsky AP, et al. Double-walled carbon nanotubes fabricated by a hydrogen arc discharge method. *Carbon* 2001;39(5):761-770.
- (39) Jiang H, Chen F, Lagally MG, Denes FS. New strategy for synthesis and functionalization of carbon nanoparticles. *Langmuir* 2010;26(3):1991-1995.
- (40) Ando Y, Zhao X, Sugai T, Kumar M. Growing carbon nanotubes. *Materials today* 2004;7(10):22-29.
- (41) Peng H, Travas-Sejdic J. Simple aqueous solution route to luminescent carbogenic dots from carbohydrates. *Chemistry of Materials* 2009;21(23):5563-5565.
- (42) Krysmann MJ, Kelarakis A, Giannelis EP. Photoluminescent carbogenic nanoparticles directly derived from crude biomass. *Green Chem* 2012;14(11):3141-3145.
- (43) Zhang Q, Sun X, Ruan H, Yin K, Li H. Production of yellow-emitting carbon quantum dots from fullerene carbon soot. *Science China Materials* 2017;60(2):141-150.
- (44) Qiao Z, Wang Y, Gao Y, Li H, Dai T, Liu Y, et al. Commercially activated carbon as the source for producing multicolor photoluminescent carbon dots by chemical oxidation. *Chemical Communications* 2010;46(46):8812-8814.
- (45) Hu S, Niu K, Sun J, Yang J, Zhao N, Du X. One-step synthesis of fluorescent carbon nanoparticles by laser irradiation. *Journal of Materials Chemistry* 2009;19(4):484-488.
- (46) Wang X, Feng Y, Dong P, Huang J. A mini review on carbon quantum dots: preparation, properties, and electrocatalytic application. *Frontiers in Chemistry* 2019:671.
- (47) Shen J, Zhu Y, Yang X, Zong J, Zhang J, Li C. One-pot hydrothermal synthesis of graphene quantum dots surface-passivated by polyethylene glycol and their photoelectric conversion under near-infrared light. *New Journal of Chemistry* 2012;36(1):97-101.
- (48) Ge G, Li L, Wang D, Chen M, Zeng Z, Xiong W, et al. Carbon dots: Synthesis, properties and biomedical applications. *Journal of Materials Chemistry B* 2021.
- (49) Zhu S, Meng Q, Wang L, Zhang J, Song Y, Jin H, et al. Highly photoluminescent carbon dots for multicolor patterning, sensors, and bioimaging. *Angewandte Chemie* 2013;125(14):4045-4049.
- (50) Zhang Z, Hao J, Zhang J, Zhang B, Tang J. Protein as the source for synthesizing fluorescent carbon dots by a one-pot hydrothermal route. *Rsc Advances* 2012;2(23):8599-8601.

- (51) Sahu S, Behera B, Maiti TK, Mohapatra S. Simple one-step synthesis of highly luminescent carbon dots from orange juice: application as excellent bio-imaging agents. *Chemical communications* 2012;48(70):8835-8837.
- (52) Bhunia SK, Saha A, Maity AR, Ray SC, Jana NR. Carbon nanoparticle-based fluorescent bioimaging probes. *Scientific reports* 2013;3(1):1-7.
- (53) Wang W, Xia J, Feng J, He M, Chen M, Wang J. Green preparation of carbon dots for intracellular pH sensing and multicolor live cell imaging. *Journal of Materials Chemistry B* 2016;4(44):7130-7137.
- (54) Li S, Zhou S, Li Y, Li X, Zhu J, Fan L, et al. Exceptionally high payload of the IR780 iodide on folic acid-functionalized graphene quantum dots for targeted photothermal therapy. *ACS applied materials & interfaces* 2017;9(27):22332-22341.
- (55) Fadeeva VP, Tikhova VD, Nikulicheva ON. Elemental analysis of organic compounds with the use of automated CHNS analyzers. *Journal of analytical chemistry* 2008;63(11):1094-1106.
- (56) Ludmerczki R, Mura S, Carbonaro CM, Mandity IM, Carraro M, Senes N, et al. Carbon dots from citric acid and its intermediates formed by thermal decomposition. *Chemistry—A European Journal* 2019;25(51):11963-11974.
- (57) Dong Y, Shao J, Chen C, Li H, Wang R, Chi Y, et al. Blue luminescent graphene quantum dots and graphene oxide prepared by tuning the carbonization degree of citric acid. *Carbon* 2012;50(12):4738-4743.
- (58) MacKenzie K, Dunens O, Harris AT. A review of carbon nanotube purification by microwave assisted acid digestion. *Separation and Purification Technology* 2009;66(2):209-222.
- (59) Schwenke AM, Hoepfner S, Schubert US. Synthesis and modification of carbon nanomaterials utilizing microwave heating. *Adv Mater* 2015;27(28):4113-4141.
- (60) Ng HM, Lim GK, Leo CP. Comparison between hydrothermal and microwave-assisted synthesis of carbon dots from biowaste and chemical for heavy metal detection: A review. *Microchemical Journal* 2021;165:106116.
- (61) Shen Z, Zhang C, Yu X, Li J, Wang Z, Zhang Z, et al. Microwave-assisted synthesis of cyclen functional carbon dots to construct a ratiometric fluorescent probe for tetracycline detection. *Journal of Materials Chemistry C* 2018;6(36):9636-9641.
- (62) Jiang K, Wang Y, Gao X, Cai C, Lin H. Facile, quick, and gram-scale synthesis of ultralong-lifetime room-temperature-phosphorescent carbon dots by microwave irradiation. *Angewandte Chemie International Edition* 2018;57(21):6216-6220.

- (63) Jiang Y, Wang Y, Meng F, Wang B, Cheng Y, Zhu C. N-doped carbon dots synthesized by rapid microwave irradiation as highly fluorescent probes for Pb²⁺ detection. *New Journal of Chemistry* 2015;39(5):3357-3360.
- (64) Liu R, Wu D, Liu S, Koynov K, Knoll W, Li Q. An aqueous route to multicolor photoluminescent carbon dots using silica spheres as carriers. *Angewandte Chemie International Edition* 2009;48(25):4598-4601.
- (65) Zong J, Zhu Y, Yang X, Shen J, Li C. Synthesis of photoluminescent carbogenic dots using mesoporous silica spheres as nanoreactors. *Chemical communications* 2011;47(2):764-766.
- (66) Yang Y, Wu D, Han S, Hu P, Liu R. Bottom-up fabrication of photoluminescent carbon dots with uniform morphology via a soft-hard template approach. *Chemical Communications* 2013;49(43):4920-4922.
- (67) Carbonaro CM, Corpino R, Salis M, Mocci F, Thakkar SV, Olla C, et al. On the emission properties of carbon dots: Reviewing data and discussing models. *C* 2019;5(4):60.
- (68) Sharma A, Gadly T, Neogy S, Ghosh SK, Kumbhakar M. Molecular origin and self-assembly of fluorescent carbon nanodots in polar solvents. *The journal of physical chemistry letters* 2017;8(5):1044-1052.
- (69) Aihara J. Weighted HOMO-LUMO energy separation as an index of kinetic stability for fullerenes. *Theoretical Chemistry Accounts* 1999;102(1):134-138.
- (70) Zheng XT, Ananthanarayanan A, Luo KQ, Chen P. Glowing graphene quantum dots and carbon dots: properties, syntheses, and biological applications. *small* 2015;11(14):1620-1636.
- (71) Shen J, Zhu Y, Chen C, Yang X, Li C. Facile preparation and upconversion luminescence of graphene quantum dots. *Chemical communications* 2011;47(9):2580-2582.
- (72) Liu R, Wu D, Liu S, Koynov K, Knoll W, Li Q. An aqueous route to multicolor photoluminescent carbon dots using silica spheres as carriers. *Angewandte Chemie* 2009;121(25):4668-4671.
- (73) Liu R, Wu D, Liu S, Koynov K, Knoll W, Li Q. An aqueous route to multicolor photoluminescent carbon dots using silica spheres as carriers. *Angewandte Chemie International Edition* 2009;48(25):4598-4601.
- (74) Carbonaro CM, Chiriu D, Stagi L, Casula MF, Thakkar SV, Malfatti L, et al. Carbon dots in water and mesoporous matrix: Chasing the origin of their photoluminescence. *The Journal of Physical Chemistry C* 2018;122(44):25638-25650.

- (75) Sun C, Zhang Y, Kalytchuk S, Wang Y, Zhang X, Gao W, et al. Down-conversion monochromatic light-emitting diodes with the color determined by the active layer thickness and concentration of carbon dots. *Journal of Materials Chemistry C* 2015;3(26):6613-6615.
- (76) Neikov OD, Yefimov NA. *Handbook of non-ferrous metal powders: technologies and applications.* : Elsevier; 2009.
- (77) Ming H, Ma Z, Liu Y, Pan K, Yu H, Wang F, et al. Large scale electrochemical synthesis of high quality carbon nanodots and their photocatalytic property. *Dalton transactions* 2012;41(31):9526-9531.
- (78) Zhang Y, He J. Facile synthesis of S, N co-doped carbon dots and investigation of their photoluminescence properties. *Physical Chemistry Chemical Physics* 2015;17(31):20154-20159.
- (79) Song Y, Zhu S, Zhang S, Fu Y, Wang L, Zhao X, et al. Investigation from chemical structure to photoluminescent mechanism: a type of carbon dots from the pyrolysis of citric acid and an amine. *Journal of Materials Chemistry C* 2015;3(23):5976-5984.
- (80) Shi L, Yang JH, Zeng HB, Chen YM, Yang SC, Wu C, et al. Carbon dots with high fluorescence quantum yield: the fluorescence originates from organic fluorophores. *Nanoscale* 2016;8(30):14374-14378.
- (81) Zhu S, Zhang J, Liu X, Li B, Wang X, Tang S, et al. Graphene quantum dots with controllable surface oxidation, tunable fluorescence and up-conversion emission. *Rsc Advances* 2012;2(7):2717-2720.
- (82) Cao L, Wang X, Meziani MJ, Lu F, Wang H, Luo PG, et al. Carbon dots for multiphoton bioimaging. *J Am Chem Soc* 2007;129(37):11318-11319.
- (83) Pan L, Sun S, Zhang L, Jiang K, Lin H. Near-infrared emissive carbon dots for two-photon fluorescence bioimaging. *Nanoscale* 2016;8(39):17350-17356.
- (84) Li D, Liang C, Ushakova EV, Sun M, Huang X, Zhang X, et al. Thermally activated upconversion near-infrared photoluminescence from carbon dots synthesized via microwave assisted exfoliation. *Small* 2019;15(50):1905050.
- (85) Lim SY, Shen W, Gao Z. Carbon quantum dots and their applications. *Chem Soc Rev* 2015;44(1):362-381.
- (86) Zheng H, Wang Q, Long Y, Zhang H, Huang X, Zhu R. Enhancing the luminescence of carbon dots with a reduction pathway. *Chemical communications* 2011;47(38):10650-10652.
- (87) Liu H, Ye T, Mao C. Fluorescent carbon nanoparticles derived from candle soot. *Angewandte chemie* 2007;119(34):6593-6595.

- (88) Agarwal GS, Harshawardhan W. Inhibition and enhancement of two photon absorption. *Phys Rev Lett* 1996;77(6):1039.
- (89) Wang J, Zhang Z, Zha S, Zhu Y, Wu P, Ehrenberg B, et al. Carbon nanodots featuring efficient FRET for two-photon photodynamic cancer therapy with a low fs laser power density. *Biomaterials* 2014;35(34):9372-9381.
- (90) Jiang K, Sun S, Zhang L, Lu Y, Wu A, Cai C, et al. Red, green, and blue luminescence by carbon dots: full-color emission tuning and multicolor cellular imaging. *Angewandte Chemie International Edition* 2015;54(18):5360-5363.
- (91) Wang Y, Anilkumar P, Cao L, Liu J, Luo PG, Tackett KN, et al. Carbon dots of different composition and surface functionalization: cytotoxicity issues relevant to fluorescence cell imaging. *Exp Biol Med* 2011;236(11):1231-1238.
- (92) Ray SC, Saha A, Jana NR, Sarkar R. Fluorescent carbon nanoparticles: synthesis, characterization, and bioimaging application. *The Journal of Physical Chemistry C* 2009;113(43):18546-18551.
- (93) Wang K, Gao Z, Gao G, Wo Y, Wang Y, Shen G, et al. Systematic safety evaluation on photoluminescent carbon dots. *Nanoscale research letters* 2013;8(1):1-9.
- (94) Soo Choi H, Liu W, Misra P, Tanaka E, Zimmer JP, Itty Ipe B, et al. Renal clearance of quantum dots. *Nat Biotechnol* 2007;25(10):1165-1170.
- (95) Huang X, Zhang F, Zhu L, Choi KY, Guo N, Guo J, et al. Effect of injection routes on the biodistribution, clearance, and tumor uptake of carbon dots. *ACS nano* 2013;7(7):5684-5693.
- (96) Sciortino A, Cannizzo A, Messina F. Carbon nanodots: a review—from the current understanding of the fundamental photophysics to the full control of the optical response. *C* 2018;4(4):67.
- (97) Li H, He X, Kang Z, Huang H, Liu Y, Liu J, et al. Water-soluble fluorescent carbon quantum dots and photocatalyst design. *Angewandte Chemie International Edition* 2010;49(26):4430-4434.
- (98) Zhang H, Ming H, Lian S, Huang H, Li H, Zhang L, et al. Fe₂O₃/carbon quantum dots complex photocatalysts and their enhanced photocatalytic activity under visible light. *Dalton Transactions* 2011;40(41):10822-10825.
- (99) Xie S, Su H, Wei W, Li M, Tong Y, Mao Z. Remarkable photoelectrochemical performance of carbon dots sensitized TiO₂ under visible light irradiation. *Journal of Materials Chemistry A* 2014;2(39):16365-16368.

- (100) Cao L, Sahu S, Anilkumar P, Bunker CE, Xu J, Fernando KS, et al. Carbon nanoparticles as visible-light photocatalysts for efficient CO₂ conversion and beyond. *J Am Chem Soc* 2011;133(13):4754-4757.
- (101) Wang X, Cao L, Lu F, Meziani MJ, Li H, Qi G, et al. Photoinduced electron transfers with carbon dots. *Chemical Communications* 2009(25):3774-3776.
- (102) Li H, He X, Kang Z, Huang H, Liu Y, Liu J, et al. Water-soluble fluorescent carbon quantum dots and photocatalyst design. *Angewandte Chemie International Edition* 2010;49(26):4430-4434.
- (103) Atchudan R, Edison TNJI, Perumal S, Vinodh R, Lee YR. In-situ green synthesis of nitrogen-doped carbon dots for bioimaging and TiO₂ nanoparticles@ nitrogen-doped carbon composite for photocatalytic degradation of organic pollutants. *J Alloys Compounds* 2018;766:12-24.
- (104) Kim JK, Kim SJ, Park MJ, Bae S, Cho S, Du QG, et al. Surface-engineered graphene quantum dots incorporated into polymer layers for high performance organic photovoltaics. *Scientific reports* 2015;5(1):1-10.
- (105) Vercelli B. The role of carbon quantum dots in organic photovoltaics: a short overview. *Coatings* 2021;11(2):232.
- (106) Gupta V, Chaudhary N, Srivastava R, Sharma GD, Bhardwaj R, Chand S. Luminescent graphene quantum dots for organic photovoltaic devices. *J Am Chem Soc* 2011;133(26):9960-9963.
- (107) Günes S, Neugebauer H, Sariciftci NS. Conjugated polymer-based organic solar cells. *Chem Rev* 2007;107(4):1324-1338.
- (108) Chapin DM, Fuller CS, Pearson GL. A new silicon p-n junction photocell for converting solar radiation into electrical power. *J Appl Phys* 1954;25(5):676-677.
- (109) Arjunan aT, Senthil TS. Dye sensitised solar cells. *Mater Technol* 2013;28(1-2):9-14.
- (110) Dou D, Duan J, Zhao Y, He B, Tang Q. Cubic carbon quantum dots for light-harvesters in mesoscopic solar cells. *Electrochim Acta* 2018;275:275-280.
- (111) Wang J, Wang C, Chen S. Amphiphilic egg-derived carbon dots: rapid plasma fabrication, pyrolysis process, and multicolor printing patterns. *Angewandte Chemie International Edition* 2012;51(37):9297-9301.
- (112) Zhu S, Meng Q, Wang L, Zhang J, Song Y, Jin H, et al. Highly photoluminescent carbon dots for multicolor patterning, sensors, and bioimaging. *Angewandte Chemie* 2013;125(14):4045-4049.

(113) Shabashini A, Panja SK, Nandi GC. Applications of carbon dots (CDs) in latent fingerprints imaging. *Chemistry–An Asian Journal* 2021;16(9):1057-1072.

(114) Fernandes D, Krysmann MJ, Kelarakis A. Carbon dot based nanopowders and their application for fingerprint recovery. *Chemical Communications* 2015;51(23):4902-4905.

(115) Yadav HA, Eraiah B, Basavaraj RB, Nagabhushana H, Darshan GP, Sharma SC, et al. Rapid synthesis of C-dot@ TiO₂ core-shell composite labeling agent: Probing of complex fingerprints recovery in fresh water. *J Alloys Compounds* 2018;742:1006-1018.

(116) Xiao L, Sun H. Novel properties and applications of carbon nanodots. *Nanoscale Horizons* 2018;3(6):565-597.

(117) Lu W, Qin X, Liu S, Chang G, Zhang Y, Luo Y, et al. Economical, green synthesis of fluorescent carbon nanoparticles and their use as probes for sensitive and selective detection of mercury (II) ions. *Anal Chem* 2012;84(12):5351-5357.

(118) Dong Y, Wang R, Li H, Shao J, Chi Y, Lin X, et al. Polyamine-functionalized carbon quantum dots for chemical sensing. *Carbon* 2012;50(8):2810-2815.

(119) Dong Y, Wang R, Li G, Chen C, Chi Y, Chen G. Polyamine-functionalized carbon quantum dots as fluorescent probes for selective and sensitive detection of copper ions. *Anal Chem* 2012;84(14):6220-6224.

(120) Zhu A, Qu Q, Shao X, Kong B, Tian Y. Carbon-dot-based dual-emission nanohybrid produces a ratiometric fluorescent sensor for in vivo imaging of cellular copper ions. *Angewandte Chemie International Edition* 2012;51(29):7185-7189.

(121) Farshbaf M, Davaran S, Rahimi F, Annabi N, Salehi R, Akbarzadeh A. Carbon quantum dots: recent progresses on synthesis, surface modification and applications. *Artificial cells, nanomedicine, and biotechnology* 2018;46(7):1331-1348.

(122) Yang S, Cao L, Luo PG, Lu F, Wang X, Wang H, et al. Carbon dots for optical imaging in vivo. *J Am Chem Soc* 2009;131(32):11308-11309.

(123) Wei X, Xu Y, Li Y, Yin X, He X. Ultrafast synthesis of nitrogen-doped carbon dots via neutralization heat for bioimaging and sensing applications. *RSC Advances* 2014;4(84):44504-44508.

(124) Andersson DI, Hughes D. Antibiotic resistance and its cost: is it possible to reverse resistance? *Nature Reviews Microbiology* 2010;8(4):260-271.

- (125) Varghese M, Balachandran M. Antibacterial efficiency of carbon dots against Gram-positive and Gram-negative bacteria: A review. *Journal of Environmental Chemical Engineering* 2021;9(6):106821.
- (126) Kumar VB, Natan M, Jacobi G, Porat Z, Banin E, Gedanken A. Ga@ C-dots as an antibacterial agent for the eradication of *Pseudomonas aeruginosa*. *International Journal of Nanomedicine* 2017;12:725.
- (127) Boobalan T, Sethupathi M, Sengottuvelan N, Kumar P, Balaji P, Gulyás B, et al. Mushroom-derived carbon dots for toxic metal ion detection and as antibacterial and anticancer agents. *ACS Applied Nano Materials* 2020;3(6):5910-5919.
- (128) O'Brien P, Carrasco-Pozo C, Speisky H. Boldine and its antioxidant or health-promoting properties. *Chem Biol Interact* 2006;159(1):1-17.
- (129) D'souza SL, Deshmukh B, Bhamore JR, Rawat KA, Lenka N, Kailasa SK. Synthesis of fluorescent nitrogen-doped carbon dots from dried shrimps for cell imaging and boldine drug delivery system. *RSC advances* 2016;6(15):12169-12179.
- (130) Schweiger C, Hartmann R, Zhang F, Parak WJ, Kissel TH, Rivera_Gil P. Quantification of the internalization patterns of superparamagnetic iron oxide nanoparticles with opposite charge. *Journal of nanobiotechnology* 2012;10(1):1-11.
- (131) Chatterjee K, Zhang J, Honbo N, Karliner JS. Doxorubicin cardiomyopathy. *Cardiology* 2010;115(2):155-162.
- (132) Wang Q, Huang X, Long Y, Wang X, Zhang H, Zhu R, et al. Hollow luminescent carbon dots for drug delivery. *Carbon* 2013;59:192-199.
- (133) Feng T, Ai X, An G, Yang P, Zhao Y. Charge-convertible carbon dots for imaging-guided drug delivery with enhanced in vivo cancer therapeutic efficiency. *ACS nano* 2016;10(4):4410-4420.
- (134) Wang Q, Zhang C, Shen G, Liu H, Fu H, Cui D. Fluorescent carbon dots as an efficient siRNA nanocarrier for its interference therapy in gastric cancer cells. *Journal of nanobiotechnology* 2014;12(1):1-12.
- (135) Zheng M, Liu S, Li J, Qu D, Zhao H, Guan X, et al. Integrating oxaliplatin with highly luminescent carbon dots: an unprecedented theranostic agent for personalized medicine. *Adv Mater* 2014;26(21):3554-3560.
- (136) Culy CR, Clemett D, Wiseman LR. Oxaliplatin. *Drugs* 2000;60(4):895-924.

- (137) Sánchez A, Vázquez A. Bioactive peptides: A review. *Food Quality and Safety* 2017;1(1):29-46.
- (138) Dixon H, Cornish-Bowden A, Liébecq C, Loening KL, Moss GP, Reedijk J, et al. Nomenclature and symbolism for amino acids and peptides. *Pure and Applied Chemistry* 1984;56(5):595-624.
- (139) Zamyatnin AA. Amino acid, peptide, and protein volume in solution. *Annu Rev Biophys Bioeng* 1984;13(1):145-165.
- (140) Polanco C, Samaniego JL, Buhse T, Mosqueira FG, Negron-Mendoza A, Ramos-Bernal S, et al. Characterization of selective antibacterial peptides by polarity index. *International journal of peptides* 2012;2012.
- (141) Tinker F. The microscopic structure of semipermeable membranes and the part played by surface forces in osmosis. *Proceedings of the Royal Society of London. Series A, Containing Papers of a Mathematical and Physical Character* 1916;92(641):357-372.
- (142) Lindgren M, Hällbrink M, Prochiantz A, Langel Ü. Cell-penetrating peptides. *Trends Pharmacol Sci* 2000;21(3):99-103.
- (143) Ruseska I, Zimmer A. Internalization mechanisms of cell-penetrating peptides. *Beilstein journal of nanotechnology* 2020;11(1):101-123.
- (144) Silva S, Almeida AJ, Vale N. Combination of cell-penetrating peptides with nanoparticles for therapeutic application: a review. *Biomolecules* 2019;9(1):22.
- (145) Madani F, Lindberg S, Langel Ü, Futaki S, Gräslund A. Mechanisms of cellular uptake of cell-penetrating peptides. *Journal of biophysics* 2011;2011.
- (146) Trabulo S, Cardoso AL, Mano M, De Lima MCP. Cell-penetrating peptides—mechanisms of cellular uptake and generation of delivery systems. *Pharmaceuticals* 2010;3(4):961-993.
- (147) Shai Y, Oren Z. From “carpet” mechanism to de-novo designed diastereomeric cell-selective antimicrobial peptides. *Peptides* 2001;22(10):1629-1641.
- (148) Mudhakar D, Harashima H. Learning from the viral journey: how to enter cells and how to overcome intracellular barriers to reach the nucleus. *The AAPS journal* 2009;11(1):65-77.
- (149) Alves ID, Jiao C, Aubry S, Aussedat B, Burlina F, Chassaing G, et al. Cell biology meets biophysics to unveil the different mechanisms of penetratin internalization in cells. *Biochimica et Biophysica Acta (BBA)-Biomembranes* 2010;1798(12):2231-2239.

(150) Copolovici DM, Langel K, Eriste E, Langel U. Cell-penetrating peptides: design, synthesis, and applications. *ACS nano* 2014;8(3):1972-1994.

(151) Bechara C, Sagan S. Cell-penetrating peptides: 20 years later, where do we stand? *FEBS Lett* 2013;587(12):1693-1702.

(152) Zhao F, Zhao Y, Liu Y, Chang X, Chen C, Zhao Y. Cellular uptake, intracellular trafficking, and cytotoxicity of nanomaterials. *small* 2011;7(10):1322-1337.

(153) Conner SD, Schmid SL. Regulated portals of entry into the cell. *Nature* 2003;422(6927):37-44.

(154) Chou LY, Ming K, Chan WC. Strategies for the intracellular delivery of nanoparticles. *Chem Soc Rev* 2011;40(1):233-245.

(155) Futaki S, Nakase I, Tadokoro A, Takeuchi T, Jones AT. Arginine-rich peptides and their internalization mechanisms. *Biochem Soc Trans* 2007;35(4):784-787.

(156) Xiang S, Tong H, Shi Q, Fernandes JC, Jin T, Dai K, et al. Uptake mechanisms of non-viral gene delivery. *J Controlled Release* 2012;158(3):371-378.

(157) Haucke V, Kozlov MM. Membrane remodeling in clathrin-mediated endocytosis. *J Cell Sci* 2018;131(17):jcs216812.

(158) Palade GE. The fine structure of blood capillaries. *J Appl Phys* 1953;24:1424.

(159) Kiss AL, Botos E. Endocytosis via caveolae: alternative pathway with distinct cellular compartments to avoid lysosomal degradation? *J Cell Mol Med* 2009;13(7):1228-1237.

(160) Branza-Nichita N, Macovei A, Lazar C. Caveolae-dependent endocytosis in viral infection. *Molecular regulation of endocytosis* 2012;31.

(161) Kirkham M, Parton RG. Clathrin-independent endocytosis: new insights into caveolae and non-caveolar lipid raft carriers. *Biochimica et Biophysica Acta (BBA)-Molecular Cell Research* 2005;1745(3):273-286.

(162) Wołczański G, Płóciennik H, Lisowski M, Stefanowicz P. A faster solid phase peptide synthesis method using ultrasonic agitation. *Tetrahedron Lett* 2019;60(28):1814-1818.

(163) Merrifield RB. Solid phase peptide synthesis. I. The synthesis of a tetrapeptide. *J Am Chem Soc* 1963;85(14):2149-2154.

(164) Amblard M, Fehrentz J, Martinez J, Subra G. Methods and protocols of modern solid phase peptide synthesis. *Mol Biotechnol* 2006;33(3):239-254.

- (165) Carpino LA, Han GY. 9-Fluorenylmethoxycarbonyl amino-protecting group. *J Org Chem* 1972;37(22):3404-3409.
- (166) Lloyd-Williams P, Albericio F, Giralt E. *Chemical approaches to the synthesis of peptides and proteins*. : CRC Press; 2020.
- (167) Sherrington DC. Preparation, structure and morphology of polymer supports. *Chemical Communications* 1998(21):2275-2286.
- (168) Sherrington DC. Preparation, structure and morphology of polymer supports. *Chemical Communications* 1998(21):2275-2286.
- (169) Mano M, Teodósio C, Paiva A, Simões S, Pedroso de Lima MC. On the mechanisms of the internalization of S413-PV cell-penetrating peptide. *Biochem J* 2005;390(2):603-612.
- (170) Koren E, Torchilin VP. Cell-penetrating peptides: breaking through to the other side. *Trends Mol Med* 2012;18(7):385-393.
- (171) Huang Y, Jiang Y, Wang H, Wang J, Shin MC, Byun Y, et al. Curb challenges of the "Trojan Horse" approach: smart strategies in achieving effective yet safe cell-penetrating peptide-based drug delivery. *Adv Drug Deliv Rev* 2013;65(10):1299-1315.
- (172) Grunwald J, Rejtar T, Sawant R, Wang Z, Torchilin VP. TAT peptide and its conjugates: proteolytic stability. *Bioconjug Chem* 2009;20(8):1531-1537.
- (173) Koren E, Apte A, Sawant RR, Grunwald J, Torchilin VP. Cell-penetrating TAT peptide in drug delivery systems: proteolytic stability requirements. *Drug Deliv* 2011;18(5):377-384.
- (174) Jiang T, Olson ES, Nguyen QT, Roy M, Jennings PA, Tsien RY. Tumor imaging by means of proteolytic activation of cell-penetrating peptides. *Proceedings of the National Academy of Sciences* 2004;101(51):17867-17872.
- (175) Kuai R, Yuan W, Qin Y, Chen H, Tang J, Yuan M, et al. Efficient delivery of payload into tumor cells in a controlled manner by TAT and thiolytic cleavable PEG co-modified liposomes. *Molecular pharmaceutics* 2010;7(5):1816-1826.
- (176) Gessner I, Neundorff I. Nanoparticles modified with cell-penetrating peptides: Conjugation mechanisms, physicochemical properties, and application in cancer diagnosis and therapy. *International journal of molecular sciences* 2020;21(7):2536.
- (177) Kumar S, Aaron J, Sokolov K. Directional conjugation of antibodies to nanoparticles for synthesis of multiplexed optical contrast agents with both delivery and targeting moieties. *Nature protocols* 2008;3(2):314-320.

- (178) Juang V, Chang C, Wang C, Wang H, Lo Y. pH-responsive PEG-shedding and Targeting peptide-modified nanoparticles for dual-delivery of Irinotecan and microRNA to enhance tumor-specific therapy. *Small* 2019;15(49):1903296.
- (179) Gao G, Jiang Y, Jia H, Sun W, Guo Y, Yu X, et al. From perinuclear to intranuclear localization: a cell-penetrating peptide modification strategy to modulate cancer cell migration under mild laser irradiation and improve photothermal therapeutic performance. *Biomaterials* 2019;223:119443.
- (180) dos Santos Rodrigues B, Lakkadwala S, Kanekiyo T, Singh J. Development and screening of brain-targeted lipid-based nanoparticles with enhanced cell penetration and gene delivery properties. *International journal of nanomedicine* 2019;14:6497.
- (181) Temming K, Schiffelers RM, Molema G, Kok RJ. RGD-based strategies for selective delivery of therapeutics and imaging agents to the tumour vasculature. *Drug resistance updates* 2005;8(6):381-402.
- (182) Yang L, Jiang W, Qiu L, Jiang X, Zuo D, Wang D, et al. One pot synthesis of highly luminescent polyethylene glycol anchored carbon dots functionalized with a nuclear localization signal peptide for cell nucleus imaging. *Nanoscale* 2015;7(14):6104-6113.
- (183) Yang L, Wang Z, Wang J, Jiang W, Jiang X, Bai Z, et al. Doxorubicin conjugated functionalizable carbon dots for nucleus targeted delivery and enhanced therapeutic efficacy. *Nanoscale* 2016;8(12):6801-6809.
- (184) Venkatesan R, Pichaimani A, Hari K, Balasubramanian PK, Kulandaivel J, Premkumar K. Doxorubicin conjugated gold nanorods: a sustained drug delivery carrier for improved anticancer therapy. *Journal of Materials Chemistry B* 2013;1(7):1010-1018.
- (185) Song Y, Li X, Cong S, Zhao H, Tan M. Nuclear-targeted of TAT peptide-conjugated carbon dots for both one-and two-photon fluorescence imaging. *Colloids and Surfaces B: Biointerfaces* 2019;180:449-456.
- (186) Chen W, Luo G, Zhang X. Recent advances in subcellular targeted cancer therapy based on functional materials. *Adv Mater* 2019;31(3):1802725.
- (187) Shen Y, Zhang X, Liang L, Yue J, Huang D, Xu W, et al. Mitochondria-targeting supra-carbon dots: Enhanced photothermal therapy selective to cancer cells and their hyperthermia molecular actions. *Carbon* 2020;156:558-567.
- (188) Ge J, Jia Q, Liu W, Guo L, Liu Q, Lan M, et al. Red-emissive carbon dots for fluorescent, photoacoustic, and thermal theranostics in living mice. *Adv Mater* 2015;27(28):4169-4177.

- (189) Moellering Jr RC. Discovering new antimicrobial agents. *Int J Antimicrob Agents* 2011;37(1):2-9.
- (190) Gough M, Hancock RE, Kelly NM. Antiendotoxin activity of cationic peptide antimicrobial agents. *Infect Immun* 1996;64(12):4922-4927.
- (191) Singh S, Nimmagadda A, Su M, Wang M, Teng P, Cai J. Lipidated α/α -AA heterogeneous peptides as antimicrobial agents. *Eur J Med Chem* 2018;155:398-405.
- (192) Rucker AL, Creamer TP. Polyproline II helical structure in protein unfolded states: lysine peptides revisited. *Protein science* 2002;11(4):980-985.
- (193) Richter S, Bouvet V, Wuest M, Bergmann R, Steinbach J, Pietzsch J, et al. ^{18}F -Labeled phosphopeptide-cell-penetrating peptide dimers with enhanced cell uptake properties in human cancer cells. *Nucl Med Biol* 2012;39(8):1202-1212.
- (194) Richter S, Bouvet V, Wuest M, Bergmann R, Steinbach J, Pietzsch J, et al. ^{18}F -Labeled phosphopeptide-cell-penetrating peptide dimers with enhanced cell uptake properties in human cancer cells. *Nucl Med Biol* 2012;39(8):1202-1212.
- (195) De Vuyst L, Vincent P, Makras E, Leroy F, Pot B. Peptide extracts from cultures of certain Lactobacilli inhibit *Helicobacter pylori*. *Probiotics and antimicrobial proteins* 2010;2(1):26-36.
- (196) Does patient age influence anti-cancer immunity? *Seminars in Immunopathology*: Springer; 2019.
- (197) Walther C, Meyer K, Rennert R, Neundorf I. Quantum dot- carrier peptide conjugates suitable for imaging and delivery applications. *Bioconjug Chem* 2008;19(12):2346-2356.
- (198) Colombo M, Bianchi A. Click chemistry for the synthesis of RGD-containing integrin ligands. *Molecules* 2010;15(1):178-197.
- (199) Carreiras F, Thiébot B, Leroy-Dudal J, Maubant S, Breton M, Darbeida H. Involvement of $\alpha\text{v}\beta 3$ integrin and disruption of endothelial fibronectin network during the adhesion of the human ovarian adenocarcinoma cell line IGROV1 on the human umbilical vein cell extracellular matrix. *International journal of cancer* 2002;99(6):800-808.
- (200) Folkman J. Angiogenesis. *Biology of endothelial cells* 1984:412-428.
- (201) Wang C, Chen Y, Xu Z, Chen B, Zhang Y, Yi X, et al. Fabrication and characterization of novel cRGD modified graphene quantum dots for chemo-photothermal combination therapy. *Sensors Actuators B: Chem* 2020;309:127732.

(202) Hoffman JR, Falvo MJ. Protein—which is best? *Journal of sports science & medicine* 2004;3(3):118.

(203) World Health Organization. Protein Quality Evaluation: Report of the Joint FAO/WHO Expert Consultation, Bethesda, Md., USA 4-8 December 1989. : Food & Agriculture Org.; 1991.

(204) Lemon PW, Tarnopolsky MA, MacDougall JD, Atkinson SA. Protein requirements and muscle mass/strength changes during intensive training in novice bodybuilders. *J Appl Physiol* 1992;73(2):767-775.

(205) Kratz F, Beyer U. Serum proteins as drug carriers of anticancer agents: a review. *Drug Deliv* 1998;5(4):281-299.

(206) Li S, Wang L, Chusuei CC, Suarez VM, Blackwelder PL, Micic M, et al. Nontoxic carbon dots potently inhibit human insulin fibrillation. *Chemistry of Materials* 2015;27(5):1764-1771.

(207) Li S, Peng Z, Dallman J, Baker J, Othman AM, Blackwelder PL, et al. Crossing the blood–brain–barrier with transferrin conjugated carbon dots: A zebrafish model study. *Colloids and Surfaces B: Biointerfaces* 2016;145:251-256.

(208) Young RJ, Lovell PA. *Introduction to polymers.* : CRC press; 2011.

(209) Carothers WH. Polymerization. *Chem Rev* 1931;8(3):353-426.

(210) Ueda M. Sequence control in one-step condensation polymerization. *Progress in polymer science* 1999;24(5):699-730.

(211) Flory PJ. Fundamental principles of condensation polymerization. *Chem Rev* 1946;39(1):137-197.

(212) McGrath JE. No title. *Chain reaction polymerization* 1981.

(213) Sanda F, Endo T. Radical ring-opening polymerization. *Journal of Polymer Science Part A: Polymer Chemistry* 2001;39(2):265-276.

(214) Thompson MS, Vadala TP, Vadala ML, Lin Y, Riffle JS. Synthesis and applications of heterobifunctional poly (ethylene oxide) oligomers. *Polymer* 2008;49(2):345-373.

(215) Nuyken O, Pask SD. Ring-opening polymerization—an introductory review. *Polymers* 2013;5(2):361-403.

(216) Hummers Jr WS, Offeman RE. Preparation of graphitic oxide. *J Am Chem Soc* 1958;80(6):1339.

- (217) Kuo W, Chang C, Huang K, Liu J, Shao Y, Yang C, et al. Amino-functionalized nitrogen-doped graphene-quantum-dot-based nanomaterials with nitrogen and amino-functionalized group content dependence for highly efficient two-photon bioimaging. *International journal of molecular sciences* 2020;21(8):2939.
- (218) Yudovin-Farber I, Golenser J, Beyth N, Weiss EI, Domb AJ. Quaternary ammonium polyethyleneimine: antibacterial activity. *Journal of nanomaterials* 2010;2010.
- (219) Lin J, Qiu S, Lewis K, Klivanov AM. Mechanism of bactericidal and fungicidal activities of textiles covalently modified with alkylated polyethylenimine. *Biotechnol Bioeng* 2003;83(2):168-172.
- (220) Arai T, Freddi G, Innocenti R, Kaplan DL, Tsukada M. Acylation of silk and wool with acid anhydrides and preparation of water-repellent fibers. *J Appl Polym Sci* 2001;82(11):2832-2841.
- (221) Nöding G, Heitz W. Amphiphilic poly (ethyleneimine) based on long-chain alkyl bromides. *Macromolecular Chemistry and Physics* 1998;199(8):1637-1644.
- (222) Lin J, Tiller JC, Lee SB, Lewis K, Klivanov AM. Insights into bactericidal action of surface-attached poly (vinyl-N-hexylpyridinium) chains. *Biotechnol Lett* 2002;24(10):801-805.
- (223) Shaker ZG, Browne RM, Stretz HA, Cassidy PE, Blanda MT. Epoxy-toughened, unsaturated polyester interpenetrating networks. *J Appl Polym Sci* 2002;84(12):2283-2286.
- (224) Soares BG, Silva AA, Livi S, Duchet-Rumeau J, Gerard J. New Epoxy/Jeffamine networks modified with ionic liquids. *J Appl Polym Sci* 2014;131(3).
- (225) Burton B, Alexander D, Klein H, Garibay-Vasquez A, Pekarik A, Henkee C. Epoxy formulations using Jeffamine® polyetheramines. *Huntsman Corp* 2005;1(1).
- (226) Yu R, de Saint-Cyr LC, Soussan L, Barboiu M, Li S. Anti-bacterial dynamic hydrogels prepared from O-carboxymethyl chitosan by dual imine bond crosslinking for biomedical applications. *Int J Biol Macromol* 2021;167:1146-1155.
- (227) Eelkema R, Pich A. Pros and cons: supramolecular or macromolecular: what is best for functional hydrogels with advanced properties? *Adv Mater* 2020;32(20):1906012.
- (228) Fleming S, Ulijn RV. Design of nanostructures based on aromatic peptide amphiphiles. *Chem Soc Rev* 2014;43(23):8150-8177.
- (229) Krakovský I, Martínez-Haya R, Ferrer GG, i Serra RS, Dodda JM. Epoxy networks and hydrogels prepared from α , ω -diamino terminated poly (oxypropylene)-b-poly (oxyethylene)-b-poly (oxypropylene) and polyoxypropylene bis (glycidyl ether). *European Polymer Journal* 2015;62:19-30.

- (230) Sinclair L, Brown J, Salim MG, May D, Guilvaiee B, Hawkins A, et al. Optimization of fluorescence and surface adsorption of citric acid/ethanolamine carbon nanoparticles for subsurface tracers. *Carbon* 2020;169:395-402.
- (231) Kim Y, Park Y, Han S, Park W, Kim M, Kim K, et al. Radiative and Non-Radiative Decay Pathways in Carbon Nanodots toward Bioimaging and Photodynamic Therapy. *Nanomaterials* 2022;12(1):70.
- (232) Franken LE, Boekema EJ, Stuart MC. Transmission electron microscopy as a tool for the characterization of soft materials: application and interpretation. *Advanced Science* 2017;4(5):1600476.
- (233) CCBER, CHEADLE CENTER FOD BIODIVERSITY AND ECOLOGICAL RESTORATION. The Transmission Electron Microscope. 2007; Available at: <https://www.ccber.ucsb.edu/ucsb-natural-history-collections-botanical-plant-anatomy/transmission-electron-microscope>.
- (234) Petroski JM, Wang ZL, Green TC, El-Sayed MA. Kinetically controlled growth and shape formation mechanism of platinum nanoparticles. *The Journal of Physical Chemistry B* 1998;102(18):3316-3320.
- (235) Serizawa T, Takehara S, Akashi M. Transmission Electron Microscopic Study of Cross-Sectional Morphologies of Core– Corona Polymeric Nanospheres. *Macromolecules* 2000;33(5):1759-1764.
- (236) Harris JR, Roos C, Djalali R, Rheingans O, Maskos M, Schmidt M. Application of the negative staining technique to both aqueous and organic solvent solutions of polymer particles. *Micron* 1999;30(4):289-298.
- (237) Dubochet J, Adrian M, Chang J, Homo J, Lepault J, McDowell AW, et al. Cryo-electron microscopy of vitrified specimens. *Q Rev Biophys* 1988;21(2):129-228.
- (238) Dutta A. Fourier transform infrared spectroscopy. *Spectroscopic methods for nanomaterials characterization* 2017:73-93.
- (239) Faix O. Fourier transform infrared spectroscopy. *Methods in lignin chemistry*: Springer; 1992. p. 83-109.
- (240) Fadeeva VP, Tikhova VD, Nikulicheva ON. Elemental analysis of organic compounds with the use of automated CHNS analyzers. *Journal of analytical chemistry* 2008;63(11):1094-1106.
- (241) Broido A. A simple, sensitive graphical method of treating thermogravimetric analysis data. *Journal of Polymer Science Part A-2: Polymer Physics* 1969;7(10):1761-1773.

- (242) Kumar L, Alam MS, Meena CL, Jain R, Bansal AK. Fexofenadine hydrochloride. Profiles of drug substances, excipients and related methodology: Elsevier; 2009. p. 153-192.
- (243) Schoonheydt RA. UV-VIS-NIR spectroscopy and microscopy of heterogeneous catalysts. Chem Soc Rev 2010;39(12):5051-5066.
- (244) Antonov L, Nedeltcheva D. Resolution of overlapping UV-Vis absorption bands and quantitative analysis. Chem Soc Rev 2000;29(3):217-227.
- (245) Bose A, Thomas I, Kavitha G, Abraham E. Fluorescence spectroscopy and its applications: A Review. International journal of advances in pharmaceutical analysis 2018;8(1):1-8.
- (246) Naresh K. Applications of fluorescence spectroscopy. J.Chem.Pharm.Sci 2014;974:2115.
- (247) Sadjadi S. Emerging Carbon Materials for Catalysis. 1st ed.: Elsevier 2020; 2020.
- (248) Shukla AK. Membrane Proteins—Production and Functional Characterization. : Academic Press; 2015.
- (249) Lawson-Wood K, Upstone S, Evans K. Determination of Relative Fluorescence Quantum Yields using the FL6500 Fluorescence Spectrometer. Fluoresc.Spectrosc 2018;4:1-5.
- (250) Hamai S, Hirayama F. Actinometric determination of absolute fluorescence quantum yields. J Phys Chem 1983;87(1):83-89.
- (251) Hu Y, Yang J, Jia L, Yu J. Ethanol in aqueous hydrogen peroxide solution: Hydrothermal synthesis of highly photoluminescent carbon dots as multifunctional nanosensors. Carbon 2015;93:999-1007.
- (252) Life Science. Time-resolved Fluorescence. Available at: <https://www.picoquant.com/applications/category/life-science/time-resolved-fluorescence>.
- (253) Yasuda R. Principle and application of fluorescence lifetime imaging for neuroscience: Monitoring biochemical signaling in single synapses using fluorescence lifetime imaging. Neurophotonics and Biomedical Spectroscopy: Elsevier; 2019. p. 53-64.
- (254) Jain A, Blum C, Subramaniam V. Fluorescence lifetime spectroscopy and imaging of visible fluorescent proteins. Advances in biomedical engineering: Elsevier; 2009. p. 147-176.
- (255) Masters JR. HeLa cells 50 years on: the good, the bad and the ugly. Nature Reviews Cancer 2002;2(4):315-319.
- (256) Ma HT, Poon RY. Synchronization of HeLa cells. Cell Cycle Synchronization: Springer; 2011. p. 151-161.

(257) Martuza RL, Malick A, Markert JM, Ruffner KL, Coen DM. Experimental therapy of human glioma by means of a genetically engineered virus mutant. *Science* 1991;252(5007):854-856.

(258) Terzioglu-Usak S, Nalli A, Elibol B, Ozek E, Hatiboglu MA. AnvirzelTMregulates cell death through inhibiting GSK-3 activity in human U87 glioma cells. *Neurol Res* 2020;42(1):68-75.

(259) Bassi R, Giussani P, Anelli V, Colleoni T, Pedrazzi M, Patrone M, et al. HMGB1 as an autocrine stimulus in human T98G glioblastoma cells: role in cell growth and migration. *J Neurooncol* 2008;87(1):23-33.

(260) Park W, Chang MS, Kim H, Choi HY, Yang WM, Park EH, et al. Cytotoxic effect of gallic acid on testicular cell lines with increasing H₂O₂ level in GC-1 spg cells. *Toxicology in Vitro* 2008;22(1):159-163.

(261) Gamborg OL, Phillips GC. Sterile techniques. *Plant Cell, Tissue and Organ Culture*: Springer; 1995. p. 35-42.

(262) Marco I, Feyerabend F, Willumeit-Römer R, Van der Biest O. Degradation testing of Mg alloys in Dulbecco's modified eagle medium: Influence of medium sterilization. *Materials Science and Engineering: C* 2016;62:68-78.

(263) Louis KS, Siegel AC. Cell viability analysis using trypan blue: manual and automated methods. *Mammalian cell viability*: Springer; 2011. p. 7-12.

(264) Klimanskaya I, McMahon J. Approaches for Derivation and Maintenance of Human Embryonic Stem Cells: Detailed Procedures and Alternatives. *Essentials of Stem Cell Biology*: Elsevier; 2009. p. 365-379.

(265) Bartlett JC, Radcliffe RJ, Convey P, Hughes KA, Hayward SA. The effectiveness of Virkon® S disinfectant against an invasive insect and implications for Antarctic biosecurity practices. *Antarct Sci* 2021;33(1):1-9.

(266) Sharma M, Kumar R, Sharma S, Thomas B, Kapatia G, Singh G, et al. Sustained exposure to trypsin causes cells to transition into a state of reversible stemness that is amenable to transdifferentiation. *bioRxiv* 2019:679928.

(267) Boncler M, Różalski M, Krajewska U, Podśędek A, Watala C. Comparison of PrestoBlue and MTT assays of cellular viability in the assessment of anti-proliferative effects of plant extracts on human endothelial cells. *J Pharmacol Toxicol Methods* 2014;69(1):9-16.

(268) Mosmann T. Rapid colorimetric assay for cellular growth and survival: application to proliferation and cytotoxicity assays. *J Immunol Methods* 1983;65(1-2):55-63.

- (269) Lall N, Henley-Smith CJ, De Canha MN, Oosthuizen CB, Berrington D. Viability reagent, PrestoBlue, in comparison with other available reagents, utilized in cytotoxicity and antimicrobial assays. *International journal of microbiology* 2013;2013.
- (270) Chwalek M, Lalun N, Bobichon H, Plé K, Voutquenne-Nazabadioko L. Structure–activity relationships of some hederagenin diglycosides: haemolysis, cytotoxicity and apoptosis induction. *Biochimica et Biophysica Acta (BBA)-General Subjects* 2006;1760(9):1418-1427.
- (271) Ishikawa-Ankerhold HC, Ankerhold R, Drummen GP. Advanced fluorescence microscopy techniques—Frap, Flip, Flap, Fret and flim. *Molecules* 2012;17(4):4047-4132.
- (272) Coons AH, Creech HJ, Jones RN. Immunological properties of an antibody containing a fluorescent group. *Proceedings of the society for experimental biology and medicine* 1941;47(2):200-202.
- (273) Douce G, Turcotte C, Cropley I, Roberts M, Pizza M, Domenghini M, et al. Mutants of *Escherichia coli* heat-labile toxin lacking ADP-ribosyltransferase activity act as nontoxic, mucosal adjuvants. *Proceedings of the National Academy of Sciences* 1995;92(5):1644-1648.
- (274) Nataro JP, Kaper JB. Diarrheagenic *Escherichia coli*. *Clin Microbiol Rev* 1998;11(1):142-201.
- (275) Lowy FD. *Staphylococcus aureus* infections. *N Engl J Med* 1998;339(8):520-532.
- (276) Cheng AG, Kim HK, Burts ML, Krausz T, Schneewind O, Missiakas DM. Genetic requirements for *Staphylococcus aureus* abscess formation and persistence in host tissues. *The FASEB Journal* 2009;23(10):3393.
- (277) Lessa FC, Mu Y, Davies J, Murray M, Lillie M, Pearson A, et al. Comparison of incidence of bloodstream infection with methicillin-resistant *Staphylococcus aureus* between England and United States, 2006–2007. *Clinical Infectious Diseases* 2010;51(8):925-928.
- (278) Langer R. Drug delivery. Drugs on target. *Science (New York, NY)* 2001;293(5527):58-59.
- (279) Moreno-Bautista G, Tam KC. Evaluation of dialysis membrane process for quantifying the in vitro drug-release from colloidal drug carriers. *Colloids Surf Physicochem Eng Aspects* 2011;389(1-3):299-303.
- (280) D'Souza S. A review of in vitro drug release test methods for nano-sized dosage forms. *Advances in Pharmaceutics* 2014;2014.
- (281) D'Souza SS, DeLuca PP. Methods to assess in vitro drug release from injectable polymeric particulate systems. *Pharm Res* 2006;23(3):460-474.

(282) Heng D, Cutler DJ, Chan H, Yun J, Raper JA. What is a suitable dissolution method for drug nanoparticles? *Pharm Res* 2008;25(7):1696-1701.

(283) Yan G, Zong R, Li L, Fu T, Liu F, Yu X. Anticancer drug-loaded nanospheres based on biodegradable amphiphilic ϵ -caprolactone and carbonate copolymers. *Pharm Res* 2010;27(12):2743-2752.

(284) Xu X, Al-Ghabeish M, Krishnaiah YS, Rahman Z, Khan MA. Kinetics of drug release from ointments: role of transient-boundary layer. *Int J Pharm* 2015;494(1):31-39.

(285) Bakalyar SR, McIlwrick R, Roggendorf E. Solvent selectivity in reversed-phase high-pressure liquid chromatography. *Journal of Chromatography A* 1977;142:353-365.

(286) Abdel Monaim SA, Jad YE, Ramchuran EJ, El-Faham A, Govender T, Kruger HG, et al. Lysine scanning of Arg10-teixobactin: deciphering the role of hydrophobic and hydrophilic residues. *ACS omega* 2016;1(6):1262-1265.

(287) Florance HV, Stopford AP, Kalapothakis JM, McCullough BJ, Bretherick A, Barran PE. Evidence for α -helices in the gas phase: A case study using Melittin from honey bee venom. *Analyst* 2011;136(17):3446-3452.

(288) Anderson ZT. No title. Peptide modified C-dots for bioimaging applications 2019.

(289) Krysmann MJ, Kellarakis A, Dallas P, Giannelis EP. Formation mechanism of carbogenic nanoparticles with dual photoluminescence emission. *J Am Chem Soc* 2012;134(2):747-750.

(290) Wei S, Yin X, Li H, Du X, Zhang L, Yang Q, et al. Multi-Color Fluorescent Carbon Dots: Graphitized sp² Conjugated Domains and Surface State Energy Level Co-Modulate Band Gap Rather Than Size Effects. *Chemistry—A European Journal* 2020;26(36):8129-8136.

(291) Rittner K, Benavente A, Bompard-Sorlet A, Heitz F, Divita G, Brasseur R, et al. New basic membrane-destabilizing peptides for plasmid-based gene delivery in vitro and in vivo. *Molecular Therapy* 2002;5(2):104-114.

(292) Lin H, Zhao Z, GARCIA-ECHEVERRIA C, Rich DH, Cooper SL. Synthesis of a novel polyurethane co-polymer containing covalently attached RGD peptide. *Journal of Biomaterials Science, Polymer Edition* 1992;3(3):217-227.

(293) Madejová J. FTIR techniques in clay mineral studies. *Vibrational spectroscopy* 2003;31(1):1-10.

(294) Kozak M, Domka L. Adsorption of the quaternary ammonium salts on montmorillonite. *Journal of Physics and Chemistry of Solids* 2004;65(2-3):441-445.

- (295) Jalageri MD, Puttaiahgowda YM, Parambil AM, Varadavenkatesan T. Synthesis and fabrication of highly functionalized Jeffamine antimicrobial polymeric coating. *Polym Adv Technol* 2019;30(7):1616-1627.
- (296) Mewada A, Pandey S, Shinde S, Mishra N, Oza G, Thakur M, et al. Green synthesis of biocompatible carbon dots using aqueous extract of *Trapa bispinosa* peel. *Materials Science and Engineering: C* 2013;33(5):2914-2917.
- (297) Liu X, Xie X, Du Z, Li B, Wu L, Li W. Aqueous self-assembly of arginine and K₈SiW₁₁O₃₉: fine-tuning the formation of a coacervate intended for sprayable anticorrosive coatings. *Soft Matter* 2019;15(45):9178-9186.
- (298) Shin YC, Lee JH, Kim MJ, Hong SW, Kim B, Hyun JK, et al. Stimulating effect of graphene oxide on myogenesis of C2C12 myoblasts on RGD peptide-decorated PLGA nanofiber matrices. *Journal of Biological Engineering* 2015;9(1):1-10.
- (299) Lu G, Wu D, Fu R. Studies on the synthesis and antibacterial activities of polymeric quaternary ammonium salts from dimethylaminoethyl methacrylate. *React Funct Polym* 2007;67(4):355-366.
- (300) Jalageri MD, Puttaiahgowda YM, Parambil AM, Varadavenkatesan T. Synthesis and fabrication of highly functionalized Jeffamine antimicrobial polymeric coating. *Polym Adv Technol* 2019;30(7):1616-1627.
- (301) Wang B, Jin J, Xu Z, Jiang Z, Li X, Jiang F, et al. Single-step synthesis of highly photoluminescent carbon dots for rapid detection of Hg²⁺ with excellent sensitivity. *J Colloid Interface Sci* 2019;551:101-110.
- (302) Liao S, Li X, Yang H, Chen X. Nitrogen-doped carbon dots rapid and selective detection of mercury ion and biothiol and construction of an IMPLICATION logic gate. *Talanta* 2019;194:554-562.
- (303) Choi Y, Kang B, Lee J, Kim S, Kim GT, Kang H, et al. Integrative approach toward uncovering the origin of photoluminescence in dual heteroatom-doped carbon nanodots. *Chemistry of Materials* 2016;28(19):6840-6847.
- (304) Reckmeier CJ, Schneider J, Xiong Y, Häusler J, Kasák P, Schnick W, et al. Aggregated molecular fluorophores in the ammonothermal synthesis of carbon dots. *Chemistry of Materials* 2017;29(24):10352-10361.
- (305) Behrman A, Hofmann AW. Ueber die Amide der Citronensäure; Umwandlung derselben in Pyridinverbindungen. *Berichte der deutschen chemischen Gesellschaft* 1884;17(2):2681-2699.

(306) Sell WJ, Easterfield TH. LXXIII.—Studies on citrazinic acid. Part I. *Journal of the Chemical Society, Transactions* 1893;63:1035-1051.

(307) Ludmerczki R, Malfatti L, Stagi L, Meloni M, Carbonaro CM, Casula MF, et al. Polymerization-Driven Photoluminescence in Alkanolamine-Based C-Dots. *Chemistry—A European Journal* 2021;27(7):2543-2550.

(308) Sun Y, Zhou B, Lin Y, Wang W, Fernando KS, Pathak P, et al. Quantum-sized carbon dots for bright and colorful photoluminescence. *J Am Chem Soc* 2006;128(24):7756-7757.

(309) Han Z, He L, Pan S, Liu H, Hu X. Hydrothermal synthesis of carbon dots and their application for detection of chlorogenic acid. *Luminescence* 2020;35(7):989-997.

(310) Ding H, Wei J, Xiong H. Nitrogen and sulfur co-doped carbon dots with strong blue luminescence. *Nanoscale* 2014;6(22):13817-13823.

(311) Gao F, Ma S, Li J, Dai K, Xiao X, Zhao D, et al. Rational design of high quality citric acid-derived carbon dots by selecting efficient chemical structure motifs. *Carbon* 2017;112:131-141.